frontiers | Research Topics

Recent developments in aerodynamics

Edited by
Arash Shams Taleghani, Farschad Torabi and Mohammad Mehdi Rashidi

Published in
Frontiers in Mechanical Engineering

ISSN 1664-8714
ISBN 978-2-8325-5930-7
DOI 10.3389/978-2-8325-5930-7

About Frontiers

Frontiers is more than just an open access publisher of scholarly articles: it is a pioneering approach to the world of academia, radically improving the way scholarly research is managed. The grand vision of Frontiers is a world where all people have an equal opportunity to seek, share and generate knowledge. Frontiers provides immediate and permanent online open access to all its publications, but this alone is not enough to realize our grand goals.

Frontiers journal series

The Frontiers journal series is a multi-tier and interdisciplinary set of open-access, online journals, promising a paradigm shift from the current review, selection and dissemination processes in academic publishing. All Frontiers journals are driven by researchers for researchers; therefore, they constitute a service to the scholarly community. At the same time, the *Frontiers journal series* operates on a revolutionary invention, the tiered publishing system, initially addressing specific communities of scholars, and gradually climbing up to broader public understanding, thus serving the interests of the lay society, too.

Dedication to quality

Each Frontiers article is a landmark of the highest quality, thanks to genuinely collaborative interactions between authors and review editors, who include some of the world's best academicians. Research must be certified by peers before entering a stream of knowledge that may eventually reach the public - and shape society; therefore, Frontiers only applies the most rigorous and unbiased reviews. Frontiers revolutionizes research publishing by freely delivering the most outstanding research, evaluated with no bias from both the academic and social point of view. By applying the most advanced information technologies, Frontiers is catapulting scholarly publishing into a new generation.

What are Frontiers Research Topics?

Frontiers Research Topics are very popular trademarks of the *Frontiers journals series*: they are collections of at least ten articles, all centered on a particular subject. With their unique mix of varied contributions from Original Research to Review Articles, Frontiers Research Topics unify the most influential researchers, the latest key findings and historical advances in a hot research area.

Find out more on how to host your own Frontiers Research Topic or contribute to one as an author by contacting the Frontiers editorial office: frontiersin.org/about/contact

Recent developments in aerodynamics

Topic editors

Arash Shams Taleghani — Aerospace Research Institute, Ministry of Science, Research and Technology, Iran

Farschad Torabi — K.N.Toosi University of Technology, Iran

Mohammad Mehdi Rashidi — University of Electronic Science and Technology of China, China

Citation

Shams Taleghani, A., Torabi, F., Rashidi, M. M., eds. (2025). *Recent developments in aerodynamics*. Lausanne: Frontiers Media SA. doi: 10.3389/978-2-8325-5930-7

Table of contents

frontiers | Frontiers in Mechanical Engineering

TYPE Editorial
PUBLISHED 15 January 2025
DOI 10.3389/fmech.2024.1537383

OPEN ACCESS

EDITED AND REVIEWED BY
Ram Balachandar,
University of Windsor, Canada

*CORRESPONDENCE
Arash Shams Taleghani,
arash.taleghani@gmail.com

RECEIVED 30 November 2024
ACCEPTED 31 December 2024
PUBLISHED 15 January 2025

CITATION
Shams Taleghani A and Torabi F (2025) Editorial: Recent developments in aerodynamics.
Front. Mech. Eng. 10:1537383.
doi: 10.3389/fmech.2024.1537383

Editorial: Recent developments in aerodynamics

Arash Shams Taleghani[1]* and Farschad Torabi[2]

[1]Aerospace Research Institute, Ministry of Science, Research and Technology, Tehran, Iran, [2]Battery an Energy Generators Research Lab, Department of Energy Systems, Faculty of Mechanical Engineering, K.N Toosi, University of Technology, Tehran, Iran

KEYWORDS

experimental aerodynamics, computational aerodynamics, flow control, applied aerodynamics, machine learning and AI, environmental aerodynamics, emerging technologies, novel materials and manufacturing

Editorial on the Research Topic
Recent developments in aerodynamics

This editorial paper examines the cutting-edge advancements in aerodynamics, a critical field within fluid mechanics, with wide-ranging applications in aviation, automotive engineering, wind energy, and beyond. As aerodynamics evolves, it influences the design of aircraft, turbines, vehicles, and energy systems, necessitating specialized tools and methods for in-depth research and application. Recent advancements in experimental techniques, computational methods, material science, and flow control technologies are driving significant changes in aerodynamic design and performance. Figure 1 presents a detailed chart illustrating the recent advancements in aerodynamic tools, methodologies, technologies, and applications.

Experimental aerodynamics, particularly through sub-scale and full-scale testing and flight experiments, will make significant strides with the development of advanced sensors, instruments, and measurement systems. For example, the future of time-resolved PIV is expected to be shaped by technological advancements in imaging, data processing, and integration with emerging techniques. Future developments could allow researchers to observe flows over multiple scales simultaneously, helping to link small-scale turbulent dynamics with large-scale flow structures and improve our understanding of turbulence at all scales. The combination of higher resolution, real-time analysis, multi-dimensional measurements, and the use of machine learning will make PIV an even more powerful tool for studying aerodynamics. Wind tunnel testing will remain a crucial method for assessing aircraft performance, particularly in different flight phases (Taleghani et al., 2020; Zhang et al., 2024; Arthur, 2024). Simultaneously, computational tools, such as CFD, will progress. More accurate simulations of airflow around complex geometries are now possible, with techniques like LES (Tonicello et al., 2022) and DNS (Chiarini and Quadrio, 2021) offering higher resolution but at the increased computational cost. Machine learning and artificial intelligence are also gaining importance in aerodynamics, enabling the optimization of designs, improving CFD accuracy, and developing new turbulence models (Sabater et al., 2022). CFD is anticipated to undergo a paradigm shift with the integration of artificial intelligence and machine learning, enabling faster, more accurate simulations of complex flows, including turbulent and hypersonic regimes.

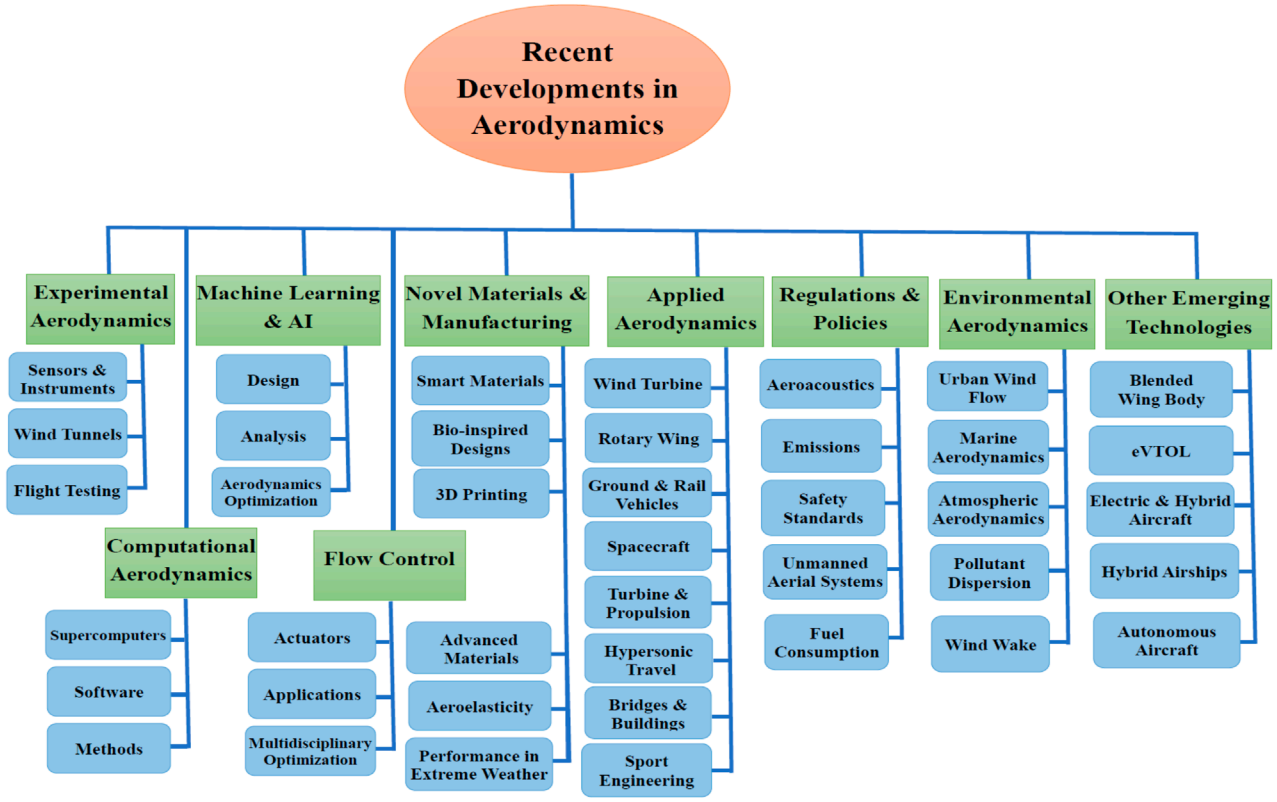

FIGURE 1
Chart of the key research domains in recent developments in aerodynamics.

Flow control technologies, which optimize aerodynamic performance by manipulating natural airflow around structures, have evolved considerably. Advances in actuators, including modulated pulse jets (Abdolahipour et al., 2022a; Abdolahipour et al., 2022b), plasma actuators (Taleghani et al., 2018), model-free closed-loop systems (Ren et al., 2024), and hybrid methods (Azadi et al., 2024), aim to enhance control, reduce energy consumption, and improve robustness. These technologies will become particularly useful in applications where efficient aerodynamic performance is critical under varying conditions. These innovations are expected to enhance both the performance and sustainability of next-generation aircraft. Material science will continue to play a pivotal role in improving aerodynamic performance. Lightweight composites, shape-memory alloys, and advanced materials like polymeric gyroid structures (Overbeck et al., 2024) are being developed to reduce weight, enhance structural integrity, and lower drag. Finally, smart materials with adaptive surface properties will enable real-time optimization of drag and lift, ushering in a new era of dynamic, responsive aerodynamic systems. These advancements, underpinned by computational, material, and environmental innovations, will redefine the role of aerodynamics in addressing global challenges and driving technological progress. Additionally, the rise of 3D printing technology has revolutionized the production of complex aerodynamic components, enabling the creation of intricate shapes previously difficult to manufacture. This capability will open new avenues for optimizing designs in aerospace and automotive applications.

Nature has long been a source of inspiration for aerodynamic design. Bio-inspired aerodynamics (De Manabendra et al., 2024), which studies natural flight patterns and fluid dynamics in animals, is expected to become an even more prominent field in engineering solutions. For example, the study of owl wings (Harbi Monfared et al., 2022) has led to the development of quieter flight mechanisms, which are particularly beneficial for urban air mobility applications. By mimicking the aerodynamic features of birds and fish, engineers are developing more efficient designs for both aircraft and wind energy systems. Biomimetic approaches inspired by natural systems, such as bird flight and marine locomotion, are expected to revolutionize aerodynamic design, enhancing energy efficiency and adaptability. Applied aerodynamics bridges theoretical fluid dynamics with practical engineering challenges. Researchers are increasingly focusing their efforts on the design of vehicles (including aircraft, spacecraft, drones, and cars) to withstand extreme weather conditions such as turbulence, crosswinds, and heavy rain. For aircraft, this involves developing systems to predict and manage weather-related disturbances. In automotive design, the focus is on optimizing aerodynamics for all-weather conditions, improving both safety and efficiency. Hypersonic vehicles, which face extreme aerodynamic and thermal stresses, will benefit from new materials and models designed to maintain stability at high speeds.

Hypersonic aerodynamics will see significant breakthroughs in thermal management and flow control, facilitating safer, more stable designs for high-speed vehicles. Recent innovations in wind energy, such as optimized blade aerodynamics and turbine layout, have made wind power generation more efficient and sustainable (Torabi, 2022). Renewable energy systems, particularly wind turbines, will benefit from refined blade aerodynamics to maximize energy capture while minimizing environmental impacts. These advancements will reduce the number of turbines needed, minimizing the environmental footprint of wind farms while increasing power output. Aerodynamics will also play a pivotal role in the optimization of fuel efficiency and stability for both ground vehicles and rail systems. Effective aerodynamic design is essential for minimizing air resistance, improving handling, and maximizing energy efficiency in vehicles such as trucks, buses, and electric cars.

Regulations and policies significantly influence aerodynamic design. Safety standards established by agencies like the FAA and EASA will drive innovations in structural integrity and aerodynamic efficiency. As concerns regarding climate change intensify, policies designed to reduce emissions and fuel consumption, such as the ICAO's Carbon Offsetting and Reduction Scheme for International Aviation (CORSIA), are likely to encourage the development of aircraft with enhanced aerodynamic efficiency (Taleghani et al., 2024). Regulations targeting noise pollution at urban airports will also lead to quieter aircraft designs, fostering advancements in technology and methodology. Additionally, policies supporting sustainable aviation technologies, including electric and hybrid propulsion systems, will encourage the development of novel aerodynamic solutions tailored to these emerging systems. In aviation, sustainable technologies will lead to ultra-efficient airframes optimized for electric and hydrogen propulsion, complemented by noise-reduction techniques critical for urban air mobility. Aerodynamics is also essential for understanding environmental phenomena such as air pollution, weather patterns, and climate change. By studying airflow and atmospheric dynamics, researchers can better predict and mitigate the impact of human activities on the environment (Christia et al., 2022). For example, urban airflow studies can inform city planning and improve pollution control strategies. The interdisciplinary field of environmental aerodynamics combines fluid dynamics, meteorology, and environmental science to address real-world challenges and enhance sustainability.

Innovative designs such as the blended wing-body concept (Gray and Zingg, 2024), which integrates the wings and fuselage into a single structure, will continue to improve aerodynamic efficiency by reducing drag and minimizing turbulence at the junction of wings and fuselage. This design is expected to allow for better lift-to-drag ratios, leading to reduced fuel consumption and increased efficiency. The exploration of electric and hybrid propulsion systems will drive further aerodynamic advancements. As electric aircraft become more viable, optimizing their aerodynamic performance will be essential for maximizing range and efficiency. Researchers will focus on designs that take into account the unique characteristics of electric motors and batteries, allowing for more efficient electric aircraft. Looking forward, several key areas are poised to shape the future of aerodynamics. One such area is the development of autonomous aircraft, which require innovative aerodynamic designs to ensure stability and control in real-time (Deniz et al., 2024). Advanced control surfaces and wing configurations are being studied to adapt to changing flight conditions autonomously. Another promising direction is the integration of renewable energy sources, such as solar-powered aircraft, which would require specialized aerodynamic designs to maximize energy efficiency and reduce reliance on fossil fuels. The growth of urban air mobility solutions, such as eVTOL aircraft (Simmons and Busan, 2024), presents unique aerodynamic challenges. The design of these vehicles must prioritize efficiency in urban environments, where concerns regarding noise and safety are particularly salient. Aerodynamic innovations will play a key role in ensuring the success of these emerging transportation solutions.

In conclusion, the field of aerodynamics continues to advance, driven by innovations in experimental methods, computational techniques, materials, and regulatory frameworks. As new challenges emerge in the design of autonomous, electric, and sustainable aircraft, aerodynamic research will remain central to addressing these issues and shaping the future of transportation and energy systems. The future evolution of aerodynamics is poised to be shaped by interdisciplinary innovation and sustainability imperatives, driving advancements across aviation, automotive, renewable energy, and space exploration. This Research Topic encompasses the latest developments in flow control, simulation methods, applied aerodynamics, and propulsion design, reflecting the multi-disciplinary nature of modern aerodynamic research.

Author contributions

AS: Investigation, Writing–original draft, Writing–review and editing. FT: Writing–original draft.

Funding

The author(s) declare that no financial support was received for the research, authorship, and/or publication of this article.

Conflict of interest

The authors declare that the research was conducted in the absence of any commercial or financial relationships that could be construed as a potential conflict of interest.

Generative AI statement

The author(s) declare that no Generative AI was used in the creation of this manuscript.

Publisher's note

References

Abdolahipour, S., Mani, M., and Shams Taleghani, A. (2022a). Experimental investigation of flow control on a high-lift wing using modulated pulse jet vortex generator. *J. Aerosp. Eng.* 35 (5), 05022001. doi:10.1061/(asce)as.1943-5525.0001463

Abdolahipour, S., Mani, M., and Shams Taleghani, A. (2022b). Pressure improvement on a supercritical high-lift wing using simple and modulated pulse jet vortex generator. *Flow. Turbul. Combust.* 109 (1), 65–100. doi:10.1007/s10494-022-00327-9

Arthur, J. K. (2024). Particle image velocimetry study of the flow control effects of singular and multiple curved serration models. *Front. Mech. Eng.* 10, 1452996. doi:10.3389/fmech.2024.1452996

Azadi, S., Abjadi, A., Vahdat Azad, A., Ahmadi Danesh Ashtiani, H., and Afshar, H. (2024). Experimental investigation of enhancement heat dissipation in a novel heat sink under simultaneous impact of impingement jet and magnetic field. *Front. Mech. Eng.* 10, 1450972. doi:10.3389/fmech.2024.1450972

Chiarini, A., and Quadrio, M. (2021). The turbulent flow over the BARC rectangular cylinder: a DNS study. *Flow. Turbul. Combust.* 107, 875–899. doi:10.1007/s10494-021-00254-1

Christiansen, N., Daewel, U., and Schrum, C. (2022). Tidal mitigation of offshore wind wake effects in coastal seas. *Front. Mar. Sci.* 9, 1006647. doi:10.3389/fmars.2022.1006647

De Manabendra, M., Sudhakar, Y., Gadde, S., Shanmugam, D., and Vengadesan, S. (2024). Bio-inspired flapping wing aerodynamics: a review. *J. Indian Inst. Sci.* 104, 181–203. doi:10.1007/s41745-024-00420-0

Deniz, S., Wu, Y., and Wang, Z. (2024). "Autonomous landing of eVTOL vehicles for advanced air mobility via deep reinforcement learning," in *AIAA SCITECH 2024 forum*, 2485. doi:10.2514/6.2024-2485

Gray, A. L., and Zingg, D. W. (2024). Blended-wing-body regional aircraft optimization with high-fidelity aerodynamics and critical design requirements. *J. Aircr.* 61, 1775–1792. doi:10.2514/1.C037876

Harbi Monfared, R., Taeibi Rahni, M., Zareh, M., Ahmadi, G., and Etemadi Haghighi, S. (2022). Aerodynamic and aeroacoustic performance of a wing with structured surface inspired by owl's wings. *J. Appl. Fluid Mech.* 15 (4), 1243–1253. doi:10.47176/jafm.15.04.33091

Overbeck, M., Heimbs, S., Kube, J., and Hühne, C. (2024). Energy absorption properties of 3D-printed polymeric gyroid structures for an aircraft wing leading edge. *Aerospace* 11, 801. doi:10.3390/aerospace11100801

Ren, F., Wen, X., and Tang, H. (2024). Model-free closed-loop control of flow past a bluff body: methods, applications, and emerging trends. *Actuators* 13, 488. doi:10.3390/act13120488

Sabater, C., Stürmer, P., and Bekemeyer, P. (2022). Fast predictions of aircraft aerodynamics using deep-learning techniques. *AIAA J.* 60 (9), 5249–5261. doi:10.2514/1.J061234

Simmons, B. M., and Busan, R. C. (2024). "Statistical wind-tunnel experimentation advancements for eVTOL aircraft aero-propulsive model development," in *AIAA SciTech 2024 forum*, 2482. doi:10.2514/6.2024-2482

Taleghani, A. S., Ghajar, A., and Masdari, Me. (2020). Experimental study of ground effect on horizontal tail effectiveness of a conceptual advanced jet trainer. *J. Aerosp. Eng.* 33. doi:10.1061/(ASCE)AS.1943-5525.0001140

Taleghani, A. S., Hesabi, A., and Esfahanian, V. (2024). Numerical study of flow control to increase vertical tail effectiveness of an aircraft by tangential blowing. *Int. J. Aeronaut. Space Sci.* doi:10.1007/s42405-024-00826-1

Taleghani, A. S., Shadaram, A., Mirzaei, M., and Abdolahipour, S. (2018). Parametric study of a plasma actuator at unsteady actuation by measurements of the induced flow velocity for flow control. *J. Braz. Soc. Mech. Sci. Eng.* 40 (4), 173. doi:10.1007/s40430-018-1120-x

Tonicello, N., Lodato, G., and Vervisch, L. (2022). Analysis of high-order explicit LES dynamic modeling applied to airfoil flows. *Flow. Turbul. Combust.* 108, 77–104. doi:10.1007/s10494-021-00273-y

Torabi, F. (2022). *Fundamentals of wind farm aerodynamic layout design*. Academic Press. doi:10.1016/C2019-0-05110-2

Zhang, S., Lin, Z., Gao, Z., Miao, S., Li, J., Zeng, L., et al. (2024). Wind tunnel experiment and numerical simulation of secondary flow systems on a supersonic wing. *Aerospace* 11, 618. doi:10.3390/aerospace11080618

frontiers | Frontiers in Mechanical Engineering

TYPE Original Research
PUBLISHED 30 August 2023
DOI 10.3389/fmech.2023.1266729

OPEN ACCESS

EDITED BY
Arash Shams Taleghani,
Aerospace Research Institute, Iran

REVIEWED BY
Ebrahim Afshari,
University of Isfahan, Iran
D. D. Ganji,
Babol Noshirvani University of Technology, Iran
Alireza Dehghanisanij,
University of Waterloo, Canada

*CORRESPONDENCE
Ali Abjadi,
a_abjadi@azad.ac.ir

RECEIVED 25 July 2023
ACCEPTED 16 August 2023
PUBLISHED 30 August 2023

CITATION
Azadi S, Abjadi A, Vahdat Azad A, Ahmadi Danesh Ashtiani H and Afshar H (2023), Enhancement of heat transfer in heat sink under the effect of a magnetic field and an impingement jet.
Front. Mech. Eng 9:1266729.
doi: 10.3389/fmech.2023.1266729

Enhancement of heat transfer in heat sink under the effect of a magnetic field and an impingement jet

Shervin Azadi[1], Ali Abjadi[1]*, Abazar Vahdat Azad[1], Hossein Ahmadi Danesh Ashtiani[1] and Hossein Afshar[2]

[1]Department of Mechanical Engineering, South Tehran Branch, Islamic Azad University, Tehran, Iran, [2]Department of Mechanical Engineering, East Tehran Branch, Islamic Azad University, Tehran, Iran

Improving the performance of heat sinks is very important in the development of cooling systems. In this study, the use of a novel combination method [magnetic field impingement jet (MF-IJ)] to improve the convective heat transfer coefficient in a designed heat sink is numerically investigated. To model heat transfer, a steady three-dimensional computational fluid dynamics (CFD) approach is employed. Numerical results including velocity and temperature contours, as well as the distribution of wall temperature of the heat sink and also the convective heat transfer coefficient are analyzed. The results show that the use of ferrofluid (Fe_3O_4/water) flow with an external magnetic field alone increases the heat transfer coefficient by 10%, while the use of an air impingement jet with pure water and without a magnetic field increases it by 22.4%. By using the MF-IJ method, a 32% enhancement of heat transfer coefficient is achieved compared to the case of pure water flow and without MF-IJ. Based on results, at a Reynolds number of 600, by applying the magnetic field intensities of 400, 800, and 1600 G, the average heat transfer coefficient increases by 5.35, 11.77, and 16.11%, respectively. It is also found that the cooling of the heat sink and temperature distribution is improved by increasing the Reynolds number and the inlet mass flow rate of the impingement jet. For instance, at z = 0.02 m, the application of an impingement jet with mass flow rates of 0.001, 0.004, and 0.005 kg/s results in a respective decrease of 0.36, 1.62, and 1.82% in wall temperature. The results of the current study suggest that the combination method of MF-IJ can be utilized for heat sinks with high heat flux generation as a flow control device.

KEYWORDS

flow control, impingement jet, magnetic field, heat sink, ferrofluid, enhancement of heat transfer

1 Introduction

The development of cooling systems in industries is of great importance (Pereira et al., 2015; Johnson and Go, 2016). Among them, Plate-fin heat sinks have broad applications in various industries to dissipate heat. Researchers have extensively studied and developed the use of plate-fin heat sinks in combination with jet and fan cooling systems (Bar-Cohen, 1993). Numerous investigations have been carried out to examine the performance of plate-fin heat sinks with impingement jet flow. However, heat sinks have limitations such as

bulkiness, but they are still widely used and effective for cooling electronic devices. Moreover, Considerations for efficient thermal management are crucial when using heat sinks.

Kotb et al. (2023) performed an experimental study on the jet impingement cooling of a flat plate. Biber (1997) conducted a numerical investigation to identify the effective parameters in the channels of a plate-fin heat sink and presented a correlation for the average Nusselt number. Kondo et al. (1998) investigated a plate-fin heat sink with six zones in a semi-empirical zonal manner and confirmed the values of thermal resistance and pressure drop. Forghan et al. (2001) conducted studies on two different types of heat sinks with plate fin, and pin fin, and found that for low air velocities, the thermal performance of the plate-fin heat sink was lower compared to the pin-fin heat sinks. Jang et al. (2003) performed an experimental study to examine the impact of an impingement jet on a heat sink equipped with parallel pin-fins. Their findings revealed that incorporating parallel pin-fins into an impingement jet system can enhance heat transfer by as much as 30%. Li et al. (2009) carried out a combined numerical and experimental investigation to explore how parameters such as fin width, fin height, and jet distance impact the thermal performance of plate-fin heat sinks. Their research revealed that these factors can exert a considerable influence on the thermal performance of the heat sinks. Cheong (Wong and Indran, 2013) studied the effect of a fillet profile on the thermal performance of the heat sink and observed adding a fillet profile at the bottom of the plate-fin heat sink can increase the thermal performance by up to 13%. Byon (2015) examined the effect of effective parameters in increasing the heat transfer of an aluminum heat sink under the influence of an impingement jet with uniform pumping power and provided an experimental correlation to predict the Nusselt number as a function of the pumping power and the dimensionless distance of the jet to the heat sink. Naphon et al. (2019) conducted a numerical and experimental analysis of the flow and heat transfer properties of nanofluid jets in microchannel heat sinks. This study utilized computational fluid dynamics and neural network optimization algorithms to create a model that could analyze both heat transfer and pressure drop in microchannel heat sinks. Gan et al. (2020) proposed a geometry that included inlet and outlet microchannels to improve the heat transfer of microchannel heat sinks using impingement jets. Researchers detected the proposed geometry increased heat transfer by 17.5% and decreased pressure drop by 22%. Froissart et al. (2021) used a heat sink with a humped cone structure and applied an impingement jet to it to increase heat transfer by 10% compared to a flat heat sink and reduce pressure drop. Pandey et al. (2022) conducted an experimental study on the thermal performance of a copper heat sink featuring two types of parallel microchannel heat sinks and pin-fin heat sinks. The investigators discovered that the thermal resistance decreased with increasing pumping power for both heat sink models. Additionally, they found that the pressure drop of the parallel heat sink was higher than that of the pin-fin heat sink.

Numerous researchers have explored the utilization of a magnetic field to enhance heat transfer (Jalili et al., 2023a; Jalili et al., 2023b; Jalili et al., 2023c; Sadighi et al., 2023; þSadighi et al., 2023; Sadighi et al., 2022a). A flow of ferrofluid is made up of magnetic nanoparticles and a base fluid, which could be oil or water. When subjected to an external magnetic field, these two components combine to create a fluid with improved magnetic characteristics (Bailey, 1983). The magnetic nanoparticles used in the studies are typically Fe_3O_4, Al_2O_3, CuO, and TiO_2, with water being the most common base fluid. It should be noted that in some studies, combinations of different nanoparticles have been used to improve the thermal conductivity of the ferrofluid. Ferrofluids are widely used in the heat sink and electronics industries due to their remarkable ability to regulate and enhance temperature through the application of an external magnetic field (Bahiraei and Hangi, 2013). In addition, when exposed to a magnetic field, ferrofluids demonstrate an increase in thermal conductivity. This characteristic makes them even more valuable in the heat sink and electronics industries where efficient heat dissipation is crucial (Karimi et al., 2015). In recent years, there have been numerous studies on the use of ferrofluids with an external magnetic field to control and enhance the thermal performance of heat sinks. Selvakumar and Suresh (2012) conducted an experimental study on the increase of heat transfer in a heat sink, achieving a 29.63% increase in heat transfer compared to DI water. Zamzamian et al. (2011) conducted an experimental study on the enhancement of the heat transfer coefficient using Al_2O_3/EG and CuO/EG nanofluids in a plate heat exchanger under turbulent flow. Li and Xuan (2009) experimentally investigated the characteristics of heat transfer in a magnetic fluid flow with Fe_3O_4/water around a heated fine wire under the influence of an external magnetic field. This study found an enhanced heat exchange between the wire and ferrofluid in the presence of a non-uniform magnetic field. (Ashjaee et al., 2015). investigated the effect of a magnetic field on forced convection heat transfer and pressure drop of Fe_3O_4 nanofluid in a microchannel heat sink. The results showed a 38% increase in heat transfer compared to the case without a magnetic field. Bahiraei and Hangi (2016) conducted a numerical investigation of the hydrothermal characteristics that affect the heat transfer of a magnetic nanofluid in a toroidal loop with two heat sources and heat sinks under the influence of a magnetic field. Bezaatpour and Goharkhah (2019) numerically investigated the effect of an external magnetic field on a porous fin heat sink with a ferrofluid flow consisting of Fe_3O_4 and water as the base fluid. This study found that high values of the volume fraction of the nanofluid, the porosity of the fins, and intensity of the magnetic field, cause an increased amount of heat transfer. Zhong et al. (2021) conducted a numerical investigation of the ferro-nanofluid flow within a porous ribbed microchannel heat sink using single-phase and two-phase approaches in the presence of a uniform magnetic field. Researchers observed parameters such as porosity percentage, Reynolds number, and Hartmann number have a direct relation with increasing heat transfer coefficient. El-Shorbagy et al. (2021) numerically investigated the effect of fin thickness on the mixed convection of a hybrid nanofluid (Al_2O_3/CuO) exposed to a magnetic field to enhance heat sink efficiency. The study revealed that CuO nanoparticles increase heat transfer more than Al_2O_3, and were able to investigate the effect of a hybrid nanofluid on the heat sink.

Sadighi et al. (2022b) analytically solved the MHD micropolar fluid flow and mixed convection characteristics using entropy production analysis of a sheet that is stretched with an inclined porous surface. Jalili et al. (2023d) carried out a numerical investigation of the magnetic field effect on the thermal behavior

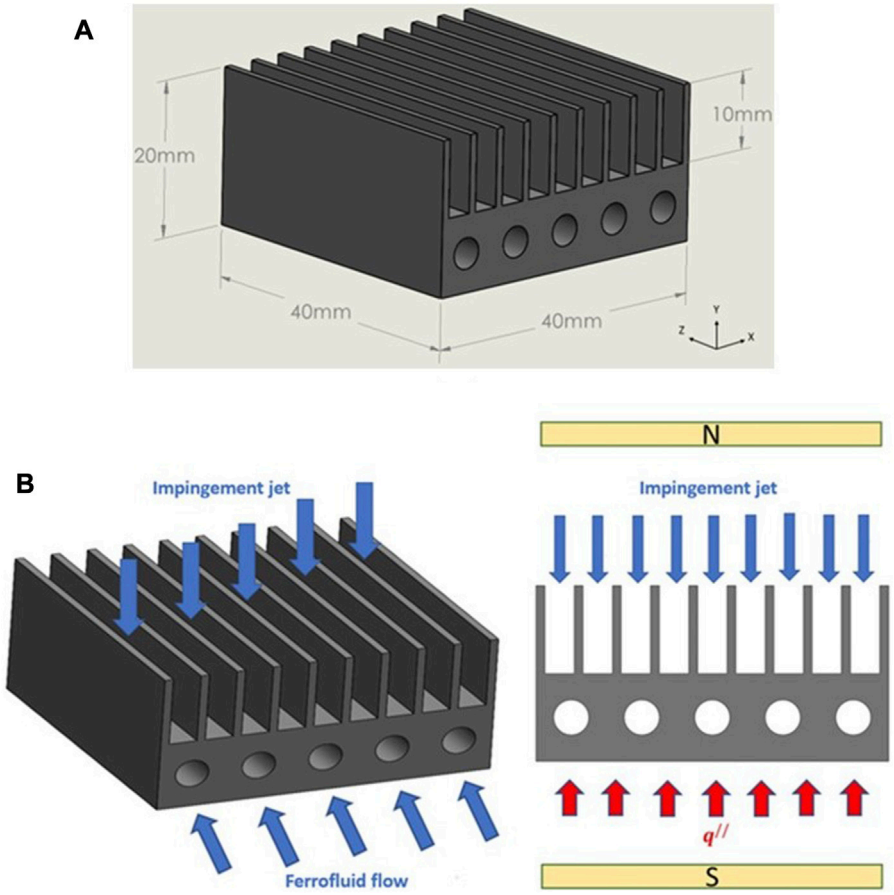

FIGURE 1
(A) The geometrical model of the designed heat sink. **(B)** Schematic of the flow direction of impingement jet and ferrofluid flow.

of a microchannel heat sink. This study used the Koo-Kleinstreuer model (KKL correlation) to obtain the viscosity and effective thermal conductivity of the nanofluid. The results showed that the magnetic field has a direct relation with the Nusselt number, indicating that the heat transfer rate increases with increasing magnetic field intensity. Active flow control techniques such as plasma actuators (Mirzaei and TaleghaniShadaram, 2012; Taleghani et al., 2012; Salmasi et al., 2013; Mohammadi and Taleghani, 2014; Taleghani et al., 2018), pulse blowing (Abdolahipour et al., 2021; Abdolahipour et al., 2022a; Abdolahipour et al., 2022b), surface acoustic waves (Sheikholeslam Noori et al., 2020a; Sheikholeslam Noori et al., 2020b; Noori et al., 2020; Sheikholeslam Noori et al., 2021; Taeibi Rahni et al., 2022), etc. are rapidly developing in fluid mechanics and aerodynamics. Desired goals in engineering can be achieved using Flow control such as lift enhancement, drag reduction, heat transfer enhancement, etc.

A review of past studies on cooling using heat sinks, especially in the electronics industry, shows that the main challenge is to achieve a uniform and low temperature distribution on the surface of the heat sink body, as well as a high convective heat transfer coefficient. With the increase in the use of electronic devices and subsequent heat generation, it is more important than ever to study and investigate new cooling methods in heat sinks. Advanced cooling technologies can have better thermal performance for heat sink cooling and as well as the potential to reduce greenhouse gas emissions and mitigate the environmental impact of cooling systems. However, despite the numerous studies conducted on heat sink cooling methods, the simultaneous effect of two flows with different regimes on the cooling of heat sinks has not been fully explored. Therefore, the main objectives and novelty of present work are as follows:

- Development of a new geometry for heat sink including the microchannel and plate fins.
- Obtaining the maximum improvement of the convective heat transfer coefficient of the designed heat sink by the proposed combination method of magnetic field and impingement jet (MF-IJ) as a flow control device.
- Obtaining the maximum improvement of the wall temperature distribution of the designed heat sink under the MF-IJ method.

2 Problem description

The objective of this section is to create a computational fluid dynamics (CFD) model that can analyze heat transfer in a heat sink when subjected to cooling with the proposed method (MF-IJ). The

TABLE 1 Dimensions of the designed heat sink (mm).

L	W	Y	N_f	∅	t	Z	C	d
40	40	20	10	4	1	10	10	3.3

aim is to investigate various parameters including wall temperature, heat transfer coefficient, Reynolds number of the nanofluid, and contour of temperature and velocity distribution of the designed heat sink. The heat sink being analyzed is made of aluminum and has 10 parallel pin-fins on the top and 5 circular microchannels at the bottom of it. Moreover, the thickness of the fins and the distance between them are both constant at 1 and 3.3 mm, respectively, along the entire length of the heat sink. The length, width, and height of this designed heat sink respectively are 40, 40, and 20 mm used in numerical simulation and shown in Figure 1A. All of the dimensions of the proposed design are condensed in Table 1.

As illustrated in Figures 1A, B uniform impingement jet flows along the *Y*-direction and strikes the top of the heat sink, after which it flows in the *Z*-direction and exits the heat sink. Furthermore, a ferrofluid (Fe_3O_4/water) flows through the microchannels of the heat sink simultaneously.

In this study, the designed heat sink was investigated under two uniform heat fluxes: 66,000 W/m^2 and 18,750 W/m^2, respectively, that were applied from the bottom of the heat sink. The rest of the surfaces were assumed to be insulated. Moreover, according to the reference (Ashjaee et al., 2015) assumed that the heat sink is located between the air gap of a U-form electromagnet. As shown in Figure 1B a uniform external magnetic field in Y- direction is designed at the core of the air gap and as well as, this external magnetic field applies with various intensities in the direction vertical to the orientation of moving the ferrofluid that flows in the *Z* direction.

3 Governing equations and boundary conditions

In this study, there are two flows with different regimes, therefore, in this section, the governing equations and boundary conditions of both regimes have been presented.

3.1 Impingement jet flow

To investigate of air impingement jet flow in the heat transfer process, it is requirement to verification the continuity, momentum, and energy equations with the assistance of the following assumptions:

1. The heat transfer is considered conjugate and three-dimensional.
2. The air flow is assumed to be steady state, in a turbulent regime, and incompressible.
3. Gravity and heat loss terms, are ignored.
4. All properties of the heat sink body are assumed to be constant.
5. All properties of the air are depending on the mean temperature which is expressed according to the following equation:

$$\mathbf{T_m} = \frac{(\mathbf{T_{avg}} + \mathbf{T_b})}{\mathbf{2}} \tag{1}$$

Where T_{avg} is the average temperature and is given by (Hussain et al., 2019):

$$\mathbf{T_{avg}} = \frac{(\mathbf{T_{out}} + \mathbf{T_{in}})}{\mathbf{2}} \tag{2}$$

The continuity equation can be expressed in the following form:

$$\frac{\partial \mathbf{u}}{\partial \mathbf{x}} + \frac{\partial \mathbf{v}}{\partial \mathbf{y}} + \frac{\partial \mathbf{w}}{\partial \mathbf{z}} = \mathbf{0} \tag{3}$$

Navier-Stokes equations in x, y, and z directions in Cartesian coordinates are given as followings:

$$\begin{aligned}
\boldsymbol{\rho}\left(\mathbf{u}\frac{\partial \mathbf{u}}{\partial \mathbf{x}} + \mathbf{v}\frac{\partial \mathbf{u}}{\partial \mathbf{y}} + \mathbf{w}\frac{\partial \mathbf{u}}{\partial \mathbf{z}}\right) &= -\frac{\partial \mathbf{p}}{\partial \mathbf{x}} + \boldsymbol{\mu}\left(\frac{\partial^2 \mathbf{u}}{\partial \mathbf{x}^2} + \frac{\partial^2 \mathbf{u}}{\partial \mathbf{y}^2} + \frac{\partial^2 \mathbf{u}}{\partial \mathbf{z}^2}\right) \\
\boldsymbol{\rho}\left(\mathbf{u}\frac{\partial \mathbf{v}}{\partial \mathbf{x}} + \mathbf{v}\frac{\partial \mathbf{v}}{\partial \mathbf{y}} + \mathbf{w}\frac{\partial \mathbf{v}}{\partial \mathbf{z}}\right) &= -\frac{\partial \mathbf{p}}{\partial \mathbf{y}} + \boldsymbol{\mu}\left(\frac{\partial^2 \mathbf{v}}{\partial \mathbf{x}^2} + \frac{\partial^2 \mathbf{v}}{\partial \mathbf{y}^2} + \frac{\partial^2 \mathbf{v}}{\partial \mathbf{z}^2}\right) \\
\boldsymbol{\rho}\left(\mathbf{u}\frac{\partial \mathbf{w}}{\partial \mathbf{x}} + \mathbf{v}\frac{\partial \mathbf{w}}{\partial \mathbf{y}} + \mathbf{w}\frac{\partial \mathbf{w}}{\partial \mathbf{z}}\right) &= -\frac{\partial \mathbf{p}}{\partial \mathbf{z}} + \boldsymbol{\mu}\left(\frac{\partial^2 \mathbf{w}}{\partial \mathbf{x}^2} + \frac{\partial^2 \mathbf{w}}{\partial \mathbf{y}^2} + \frac{\partial^2 \mathbf{w}}{\partial \mathbf{z}^2}\right)
\end{aligned} \tag{4}$$

The energy equation is expressed as follows:

$$\begin{aligned}
\boldsymbol{\rho}\left(\mathbf{u}\frac{\partial \mathbf{T}}{\partial \mathbf{x}} + \mathbf{v}\frac{\partial \mathbf{T}}{\partial \mathbf{y}} + \mathbf{w}\frac{\partial \mathbf{T}}{\partial \mathbf{z}}\right) &= \frac{\partial}{\partial \mathbf{x}}\left(\frac{\mathbf{k_f}}{\mathbf{c_P}}\frac{\partial \mathbf{T}}{\partial \mathbf{x}}\right) + \frac{\partial}{\partial \mathbf{y}}\left(\frac{\mathbf{k_f}}{\mathbf{c_P}}\frac{\partial \mathbf{T}}{\partial \mathbf{y}}\right) \\
&\quad + \frac{\partial}{\partial \mathbf{z}}\left(\frac{\mathbf{k_f}}{\mathbf{c_P}}\frac{\partial \mathbf{T}}{\partial \mathbf{z}}\right) + \mathbf{s_h}
\end{aligned} \tag{5}$$

In this equation, ρ is the density and s_h is the source term (Hussain et al., 2019).

3.2 Turbulent flow modeling

The Reynolds number for the impingement jet at the highest mass flow rate in this designed heat sink is approximately 1,550, it is in the turbulent range, which is above the critical Reynolds number of 1,400. Furthermore, the Reynolds number is calculated according to the following equation (Fox et al., 2020):

$$\mathbf{Re} = \frac{\boldsymbol{\rho}\mathbf{v_m}\mathbf{D_h}}{\boldsymbol{\mu}} \tag{6}$$

Where ρ is density, v_m is average velocity, D_h is hydraulic diameter and μ is viscosity. The hydraulic diameter is calculated according to the following equation:

$$\mathbf{D_h} = \frac{\mathbf{4A}}{\mathbf{p}} \tag{7}$$

In between the types of RANS turbulent models, the two-equation k-ε model introduced by Launder and Spalding is known as a standard turbulent model today (Spalding, 1974). RANS equations are derived by replacing the Reynolds decomposition terms in the conservation of momentum equations.

Studies have shown that the realizable k-ε model has the best performance in between all sorts of the k-ε model for flows with separation as well as complex secondary flows, and therefore, in this study, this model is used to model the impingement jet flow. The

transport equations for the k and ε in the Realizable model are as equations (8) and (9) (Singh et al., 2021):

$$\frac{\partial}{\partial x_i}(\rho k u_i) = \frac{\partial}{\partial x_j}\left[\left(\mu + \frac{\mu_t}{\sigma_k}\right)\frac{\partial k}{\partial x_j}\right] + G_k + G_b - \rho\varepsilon - Y_M + S_k \quad (8)$$

$$\frac{\partial}{\partial x_i}(\rho \varepsilon u_i) = \frac{\partial}{\partial x_j}\left[\left(\mu + \frac{\mu_t}{\sigma_\varepsilon}\right)\frac{\partial \varepsilon}{\partial x_j}\right] + C_{1\varepsilon}\frac{\varepsilon}{k}(G_k + C_{3\varepsilon}G_b) - C_{2\varepsilon}\rho\frac{\varepsilon^2}{k} + S_\varepsilon \quad (9)$$

Where Y_M is the fluctuating dilatation, G_k is the turbulent kinetic energy produced since of the mean velocity gradient, G_b is the turbulent kinetic energy generated by the buoyancy, and $C_{1\varepsilon}, C_{2\varepsilon}, C_{3\varepsilon}$ are the constant of the k-ε model, σ_k and σ_ε are the turbulence Prandtl numbers for k and ε (Singh et al., 2021).

3.3 Ferrofluid flow

Continuity, momentum, and energy equations assuming a 3D, laminar, incompressible, homogeneous and steady-state form, for fluid and solid regions are as follows (Bezaatpour and Goharkhah, 2019):

$$\nabla.(\rho_f V) = 0 \quad (10)$$

$$\frac{\rho_f}{\varepsilon}\frac{(\nabla.\nabla)V}{\varepsilon} = -\nabla P + \frac{\mu}{\varepsilon}\nabla^2 V - \frac{\mu}{k_P}V - \frac{c_f\rho_f}{k_P^{1/2}}|V|V + (M.\nabla)B \quad (11)$$

The energy equation of the fluid region is written as follows:

$$(\rho c_P)_{eff} V.\nabla T = \nabla.(k_{eff}\nabla T) \quad (12)$$

Where ε is porosity, k_p is the permeability of porous media, B is magnetic flux density, c_f, and c_p are quadratic drag factor and specific heat, respectively and M is the magnetization.

Considering that in this study, the microchannels of ferrofluid flow are solid, the porosity in Eq. 11 is 0. Additionally, the third and fourth terms on the right-hand side of Eq. 11 represent the Darcy and Forchheimer terms respectively, and the last term represents the magnetic volume force. Since the fluid and solid regions are in thermal equilibrium, the energy equation for the solid region can be expressed as follows (Bezaatpour and Goharkhah, 2019).

$$k_s\left(\frac{\partial^2 T_s}{\partial x^2} + \frac{\partial^2 T_s}{\partial y^2} + \frac{\partial^2 T_s}{\partial z^2}\right) = 0 \quad (13)$$

3.3.1 The computing of the magnetic volume force

In this study, the Fe_3O_4/water is used as a ferrofluid, therefore maxwell equations can be written as (Xie et al., 2021):

$$\nabla.B = 0 \quad (14)$$

$$\nabla \times H = 0 \quad (15)$$

The following relation is available from (Bezaatpour and Goharkhah, 2019):

$$B = \mu_0(M + H) \quad (16)$$

Where μ_0 is the permeability of free space and H is magnetic field intensity.

According to (Ganguly et al., 2004) it is possible that the magnetization vector is compliant with the magnetic field, for that reason:

$$M = x_m H \quad (17)$$

Considering that the variation of x_m is dependent on the temperature, thus according to (Ganguly et al., 2004). x_m can be written as follows:

$$x_m = x_m(T) = \frac{x_0}{(1 + \beta(T - T_0))} \quad (18)$$

As a result, the magnetic volume force (kelvin body force) is obtained from Bezaatpour and Goharkhah (2019):

$$F_k = \frac{1}{2}\mu_0 x_m(1 + x_m)\nabla(H.H) + \mu_0 x_m H((H.\nabla)x_m) \quad (19)$$

The first term in the magnetic volume force equation is similar to the pressure term in the momentum equation. According to Ref. (Ganguly et al., 2004), when a heat sink is placed at the center of the electromagnet air gap, there is a uniform element in the *Y*-direction (Selvakumar and Suresh, 2012). As a result, the magnetic volume force equation can be written as Eq. 20 (Bezaatpour and Goharkhah, 2019).

$$F_k = \mu_0\chi_m H^2\frac{-\chi_0\beta}{[1 + \beta(T - T_0)]^2}\frac{\partial T}{\partial y}\vec{j} \quad (20)$$

3.4 Boundary conditions

The air impingement jet flow with a constant inlet temperature of 298 K and inlet mass flow rates of 0.001, 0.003, 0.004, and 0.005 kg/s entrance the plate-fins, and simultaneously ferrofluid flow with a constant inlet temperature of 298 K and uniform velocity flow into the microchannels of ferrofluid.

The uniform heat flux from the bottom surface of the heat sink is 66,000 W/m^2 and 18,750 W/m^2, Additionally, the no-slip condition exists between the fluid and solid body of the heat sink, hence:

$$V = 0, T_s = T_f, -k_{eff}\frac{\partial T_f}{\partial n} = -k_s\frac{\partial T_s}{\partial n} \quad (21)$$

The walls of the heat sink are assumed to be insulated:

$$\frac{\partial T}{\partial n} = 0 \quad (22)$$

In this study, the properties of aluminum and Fe_3O_4 particles are written in Table 2. (Bezaatpour and Goharkhah, 2019).

3.5 Thermophysical properties of the nanofluid

In this study, the nanofluid consists of water and iron oxide (Fe_3O_4). According to Ref. (Xuan and Roetzel, 2000), for a two-phase mixture, the properties of the nanofluid as a function of the nanoparticle volume fraction and temperature can be written as follows:

TABLE 2 Properties of Aluminum and Fe_3O_4 particles.

Material	Diameter (mm)	k (W/m.k)	c_p (J/kg.K)	ρ (kg/m^3)
Fe_3O_4	0.00002	7	640	4,950
Aluminum	0.1	202.4	871	2,719

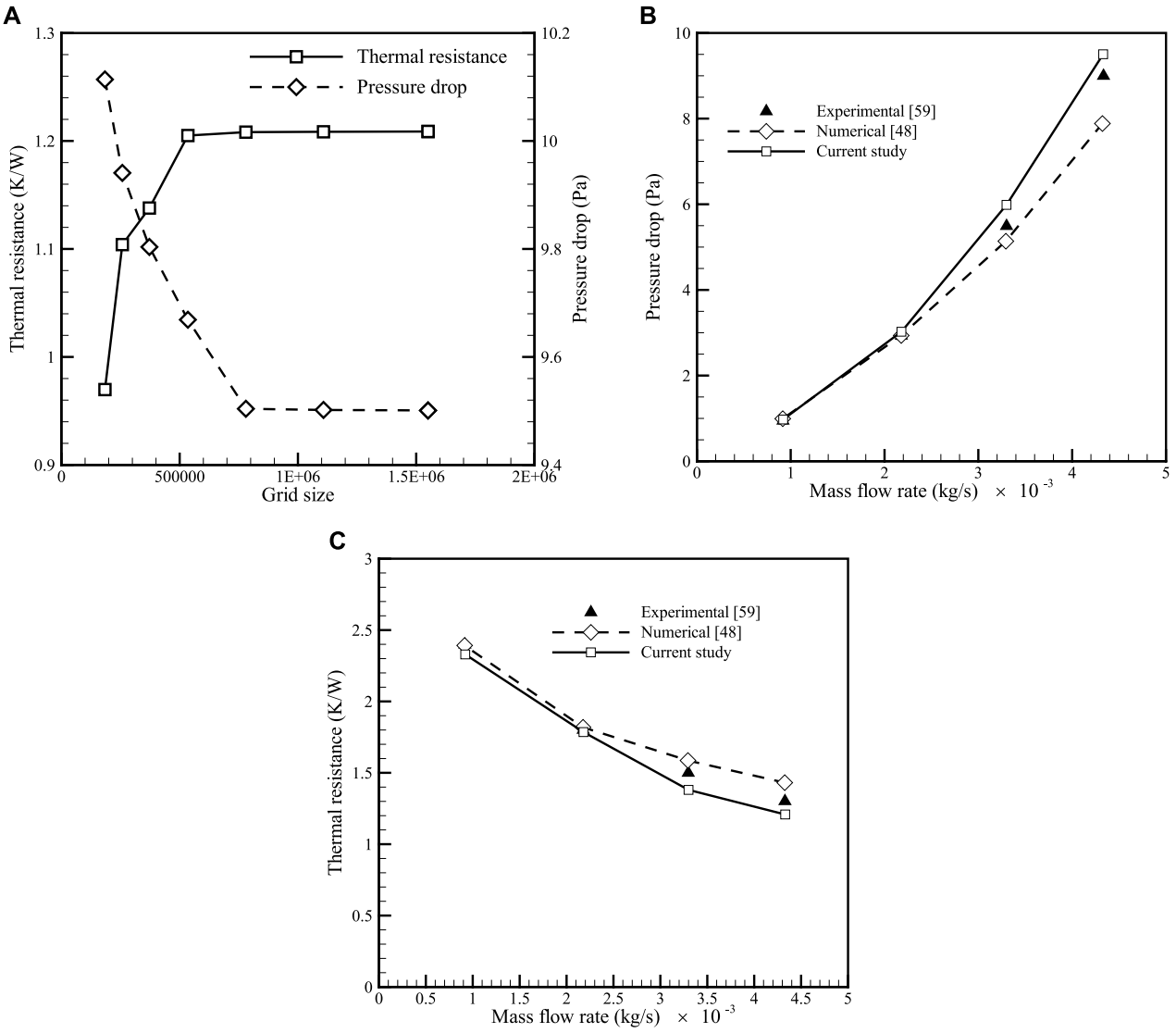

FIGURE 2
(A) Comparison of mesh size changes based on thermal resistance and pressure drop. **(B)** Validation of CFD results for pressure drop at various mass flow rates. **(C)** Validation of CFD results for thermal resistance at various mass flow rates.

$$\rho_{nf} = (1-\varphi)\rho_{bf} + \varphi\rho_{np} \tag{23}$$

$$(\rho c_p)_{nf} = (1-\varphi)(\rho c_p)_{bf} + \varphi(\rho c_p)_{np} \tag{24}$$

Moreover, for volume fractions less than or equal to 2%:

$$\mu_{nf} = \mu_{bf}(1 + 2.5\varphi) \tag{25}$$

And as well, for volume fraction greater than 2% (Bezaatpour and Goharkhah, 2019):

$$\mu_{nf} = \frac{\mu_{bf}}{(1-\varphi)^{2.5}} \tag{26}$$

The thermal conductivity of nanofluid is mainly due to Brownian motion, which is the random movement of particles in a fluid. Brownian motion in nanofluids causes micro-mixing, thus micro-mixing effect enhances the thermal conductivity of the nanofluid by increasing effective contact between the nanoparticles and the fluid molecules, which facilitates heat

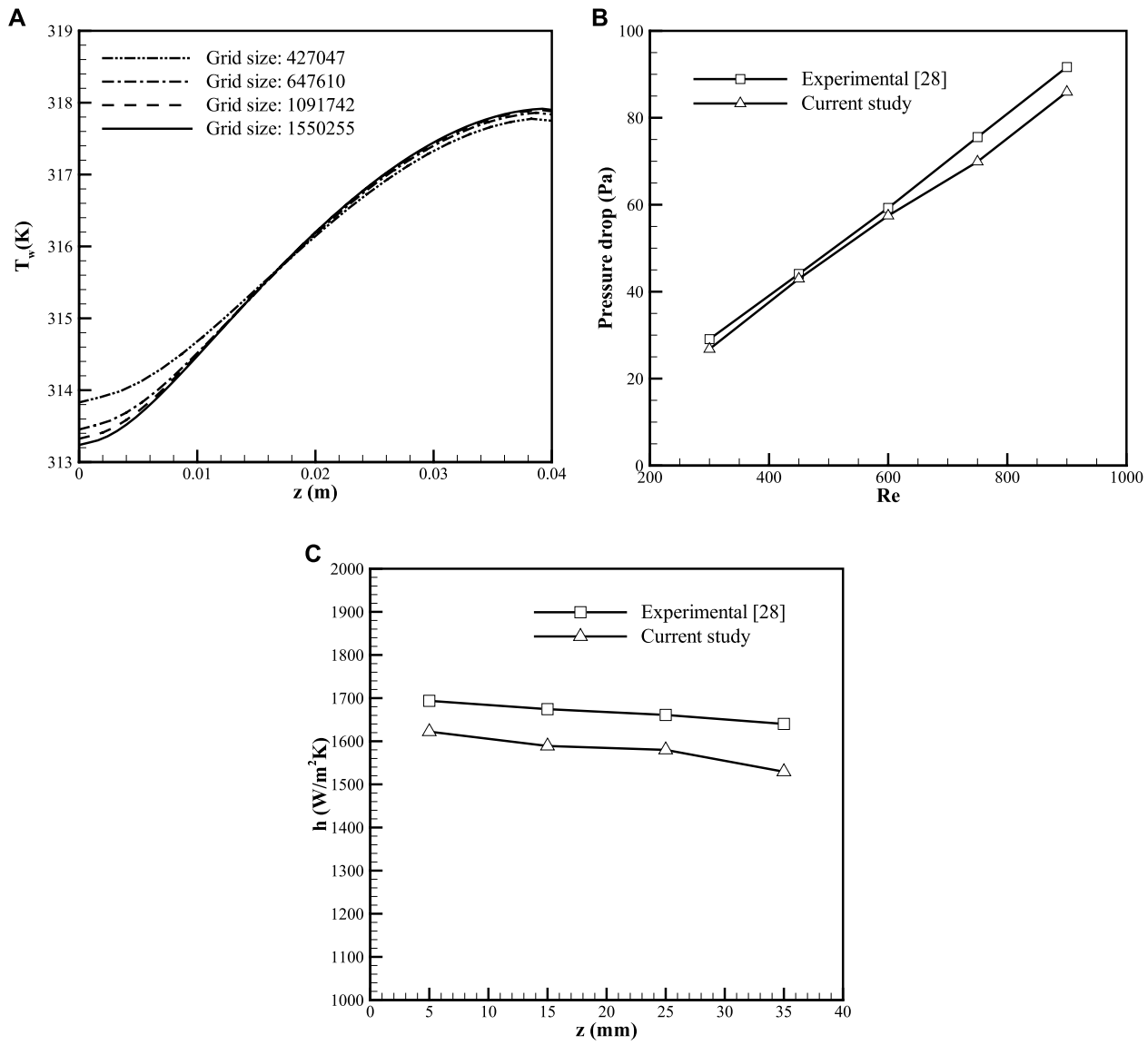

FIGURE 3
(A) Bottom wall temperature variation of the heat sink along the channels. **(B)** Comparison between experimental and numerical results of pressure drop at B = 800 G and φ = 2%. **(C)** Comparison between experimental and numerical results of local convective heat transfer coefficient at B = 1,200, Re = 600, and φ = 3%.

transfer (Koo and Kleinstreuer, 2004). Therefore, from (Koo and Kleinstreuer, 2004) k_{nf} can be written as:

$$\mathbf{k_{nf}} = \mathbf{k_{static}} + \mathbf{k_{Brownian}} \quad (27)$$

Where, k_{static} and $k_{Brownian}$ are the thermal conductivity of a static dilute suspension and thermal conductivity due to Brownian motion, respectively (Koo and Kleinstreuer, 2004).

4 Numerical modeling and validation of the numerical method

In this study, the grid independency of numerical results of the impingement jet flow was investigated for the maximum input mass flow rate of air. The appropriate mesh was selected, and numerical simulations were performed for other mass flow rates, and ultimately the validation of the numerical results was achieved.

The energy and momentum equations were discretized using the second-order upwind method (Jazmi et al., 2021), and the SIMPLE algorithm was used for pressure-velocity coupling (Mohammadzadeh et al., 2018). In this research, $y^+ < 96$, and scalable wall functions are used. These wall functions are designed to prevent the degradation of standard wall functions when the grid is refined to a level where y+ < 30. By doing so, the scalable wall functions produce reliable and consistent results for grids of any level of refinement. For grids that are not as refined, with y+ > 30, the standard wall functions remain unchanged. The aim of using scalable wall functions is to ensure that the log law is integrated with the standard wall functions approach (ANSYS Fluent 17.2, 2016).

To validate the numerical results of the impingement jet, a mass flow rate of 0.00433 kg/s was considered. To check the grid independence of the impingement jet, primary simulations were

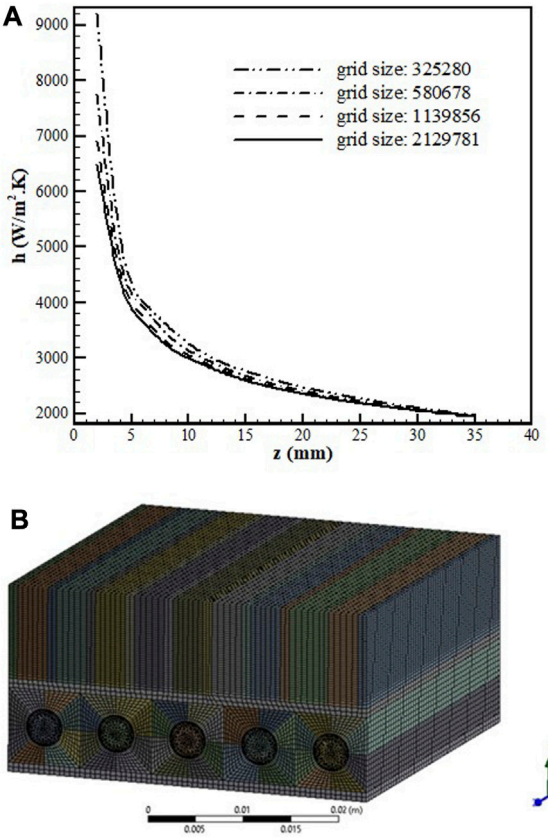

FIGURE 4
(A) Grid study of local convective heat transfer coefficient along the channels at heat flux = 18,750 W/m^2, Re = 900, φ = 3%, B = 1200 G, and $\dot{m}$_jet = 0.005 kg/s. **(B)** The mesh of the proposed design with 1,139,856 elements.

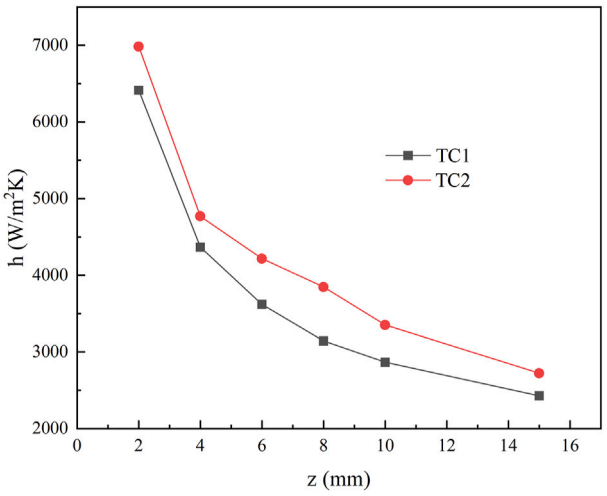

FIGURE 5
The local convective heat transfer coefficient of TC1 and TC2 along the heat sink length at a heat flux of 18,750 W/m^2.

carried out using grid sizes of 184,000, 257,588, 372,000, 534,660, 780,800, 1,108,080, and 1,550,000. The grid sizes were selected such that the skewness, smoothness, aspect ratio, and orthogonality were within the appropriate range. Additionally, to enhance the accuracy of the numerical results, a bias factor of 1.4 was applied to the meshes near the walls.

The thermal resistance and pressure drop results for various grid sizes are presented in Figure 2A Based on these results, a grid size with 780,800 elements was selected to reduce computation time for the validation of the impingement jet flow. The current study results for the validation of the impingement jet flow are compared with the experimental results of (Kim et al., 2009) and the numerical results of Hussain et al. (2019). Figures 2B, C depict the pressure drop and thermal resistance for different mass flow rates, respectively. Based on Figure 2B, the pressure drop increases as the inlet mass flow rate rises, which results in increased friction and losses due to the increase in the Reynolds number. Moreover, as shown in Figure 2C, the thermal resistance decreases with an increase in the mass flow rate. As can be seen, the maximum errors of pressure drops and thermal resistance are 5.6% and 7.2%, respectively, compared to the experimental results of (Kim et al., 2009).

To validate the numerical method for simulation of ferrofluid flow under the influence of a magnetic field, the grid independence of the model was investigated using computational grids of 427,047, 647,610, 1,091,742, and 1,550,255 grid sizes, as shown in Figure 3A. The results for the bottom wall temperature along the channels, which were subjected to a heat flux of 66,000 W/m^2, φ = 2%, and Reynolds number of 830 are presented in Figure 3A. The results show that the grid with 1,091,742 and 1,550,255 elements are close to each other. Therefore, the grid with 1,091,742 elements will be used for the validation of the ferrofluid flow under the influence of a magnetic field. The pressure drop values for different Reynolds numbers and the local convective heat transfer coefficient along the channels were compared with the experimental results of Ashjaee et al. (2015), as

TABLE 3 The studied test cases.

Test case number	Re	B(G)	φ	$\dot{m}$_ jet(kg/s)	Heat flux(W/m^2)
TC1	900	0	0	0	18,750
TC2	900	0	0	0.005	18,750
TC3	900	1,600	0.03	0	18,750
TC4	900	1,600	0.03	0.005	18,750
TC5	900	0	0	0	66,000
TC6	900	1,600	0.03	0.005	66,000

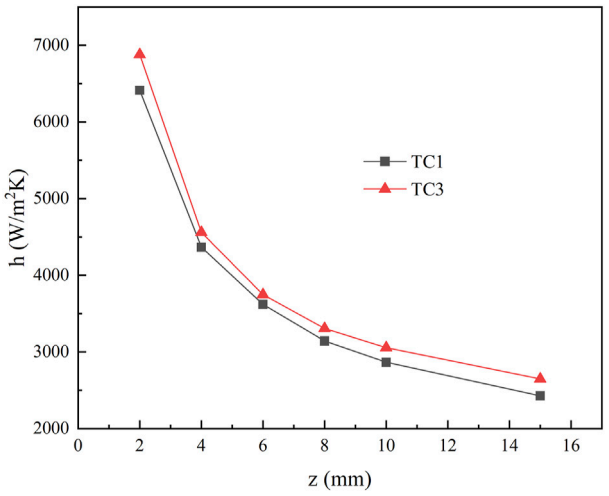

FIGURE 6
The local convective heat transfer coefficient of TC1 and TC3 along the heat sink length at a heat flux of 18,750 W/m^2.

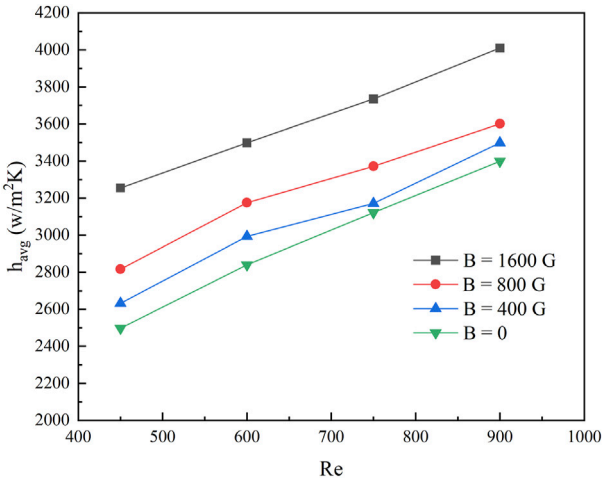

FIGURE 8
Effect of magnetic field utilizing impingement jet on the average heat transfer coefficient of ferrofluid at a heat flux of 18,750 W/m^2, $\dot{m}$_jet = 0.005 kg/s and φ = 3%.

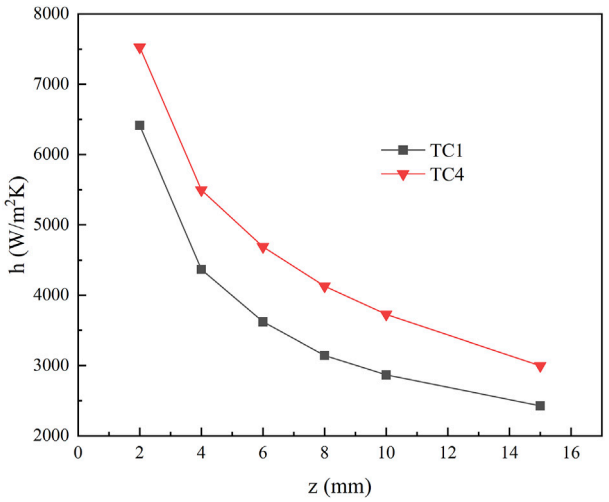

FIGURE 7
The local convective heat transfer coefficient of TC1 and TC4 along the heat sink length at a heat flux of 18,750 W/m^2.

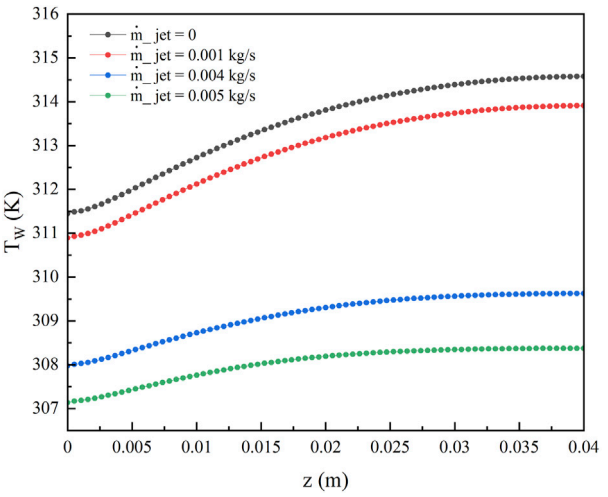

FIGURE 9
Wall temperature variation of the heat sink at B = 1,600 G, φ = 3%, Re = 900, and heat flux of 66,000 W/m^2 for different inlet mass flow.

shown in Figures 3B, C, respectively. The results indicate a maximum discrepancy of 7.83% for pressure drop and 6.75% for the local convective heat transfer coefficient. Therefore, it can be concluded that there is a good agreement between the numerical results of the current study and the experimental results of Ashjaee et al. (2015).

5 Mesh generation

In this section, a coupled algorithm was used to solve the pressure-velocity coupling for the numerical simulation of a heat sink under the effect of MF-IJ. The equations of momentum and energy were discretized using the second-order upwind method, and the residual values for the continuity, momentum, and energy equations were set to 10^{-4}, 10^{-6}, and 10^{-9}, respectively. To investigate the grid independence of the numerical results for the heat sink under the effect of MF-IJ, the variations of the local convective heat transfer coefficient for grid sizes 325,280, 580,678, 1,139,856, and 2,129,781 were obtained, as shown in Figure 4A, for the maximum Reynolds number (Re = 900) of the nanofluid. Based on Figure 4A, it can be observed that the results obtained for the grid size of 1,139,856 and 2,129,781 elements are close to each other. Therefore, to reduce the computation time the grid size with 1,139,856 elements will be used for the rest of the simulations of the heat sink under the effect of MF-IJ.

Figure 4B shows by hybrid mesh with structured and unstructured meshes was used to mesh the designed geometry

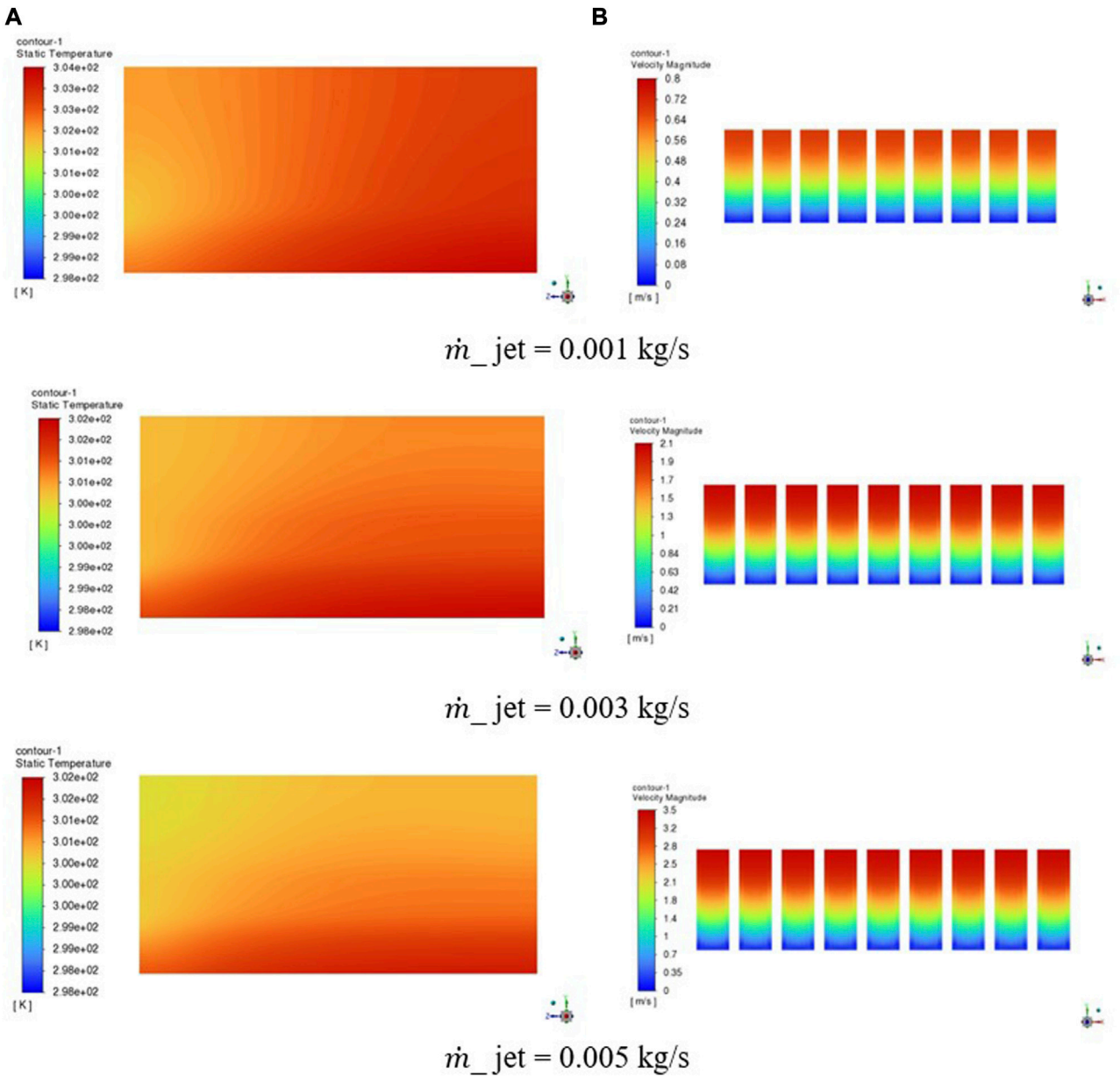

FIGURE 10
Study on the effect of increasing the inlet mass flow rate of impingement jet on the velocity of the jet and wall temperature of the heat sink at B = 1,600 G, Re = 900, φ = 3% and heat flux of 18750W/m^2 **(A)** Temperature contour of the heat sink wall **(B)** Velocity contour at the middle channel of the heat sink.

under the effect of MF-IJ. In this geometry, due to the high gradient variation of temperature and velocity, mesh refinement was applied with a bias factor of 1.4 near the walls. This approach was adopted to ensure accurate capture of the flow and temperature fields near the walls.

6 Results and discussion

In this section, numerical simulations have been carried out for heat flux values of 18,750 W/m^2 and 66,000 W/m^2. In addition, a comparison has been made between the convective heat transfer coefficient of TC1 with TC2, TC3, and TC4. The details of these Test cases are shown in Table 3. Based on the numerical results presented in Figure 5, it can be concluded that the cooling of the heat sink is done at a higher rate in case TC2 than in case TC1.

The maximum enhancement of the local convective heat transfer coefficient in case TC2 was obtained at 22.4% relative to TC1. The comparison between the results of TC1 and TC2 revealed that the impingement jet increases the velocity gradient in the plate-fins region of the heat sink, which led to a more effective exchange of heat between the air and the heat sink, resulting in the heat transfer coefficient enhancement relative to TC1.

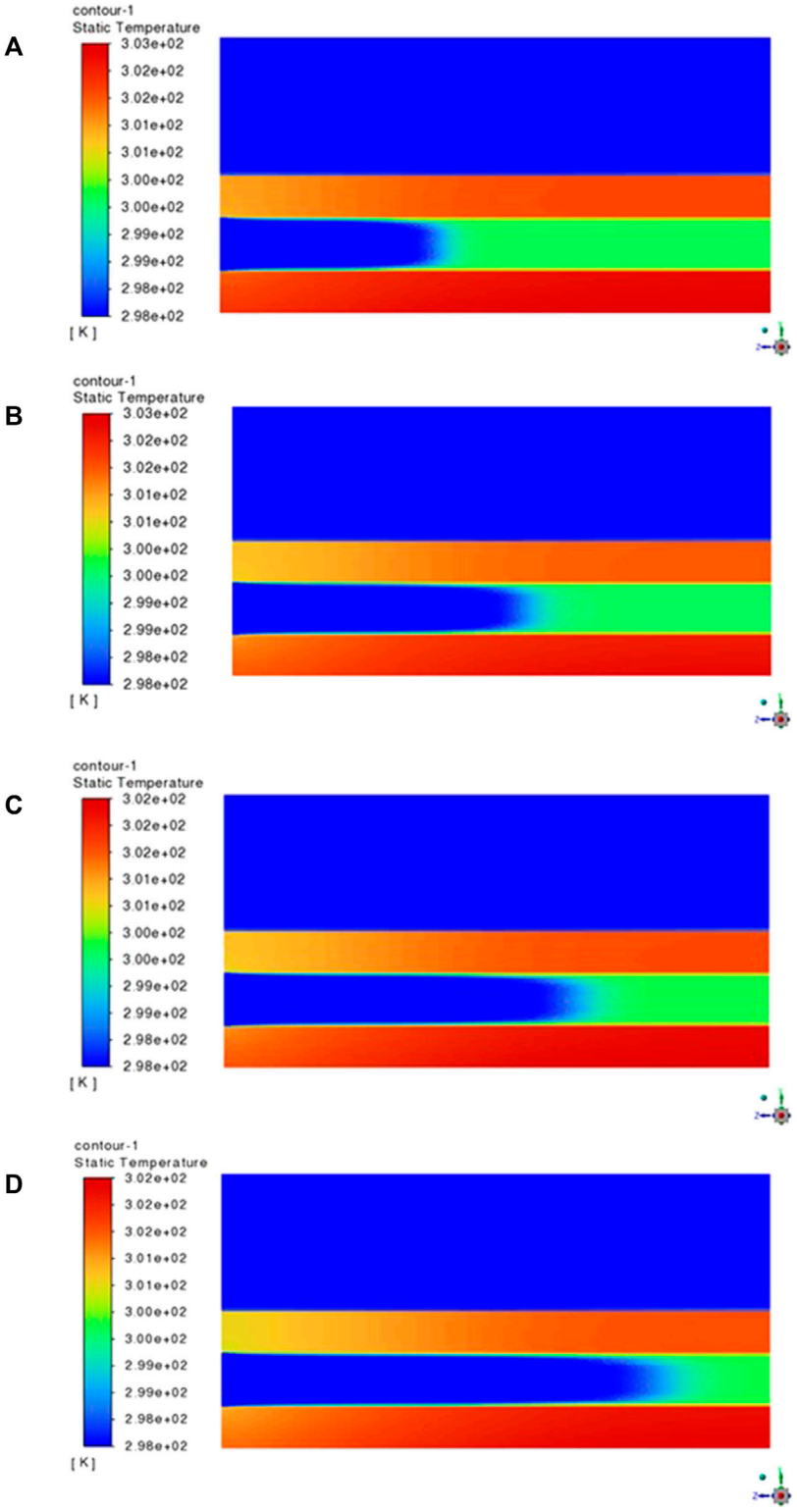

FIGURE 11
Temperature contour of the longitudinal section of the microchannel heat sink at heat flux of 18,750 W/m^2, B = 1,600 G, φ = 3%, $\dot{m}$ _ jet = 0.005 kg/s: **(A)** Re = 450; **(B)** Re = 600; **(C)** Re = 750; **(D)** Re = 900.

The effect of using a magnetic field in the designed heat sink, is presented in Figure 6. As can be seen, the maximum increase in the local convective heat transfer coefficient in comparison to heat sink cooling using the case of TC3 versus the case of TC1 is almost 10%. The reason for the increase in heat transfer rate is that the magnetic field induces fluid motion, which increases the mixing in the fluid.

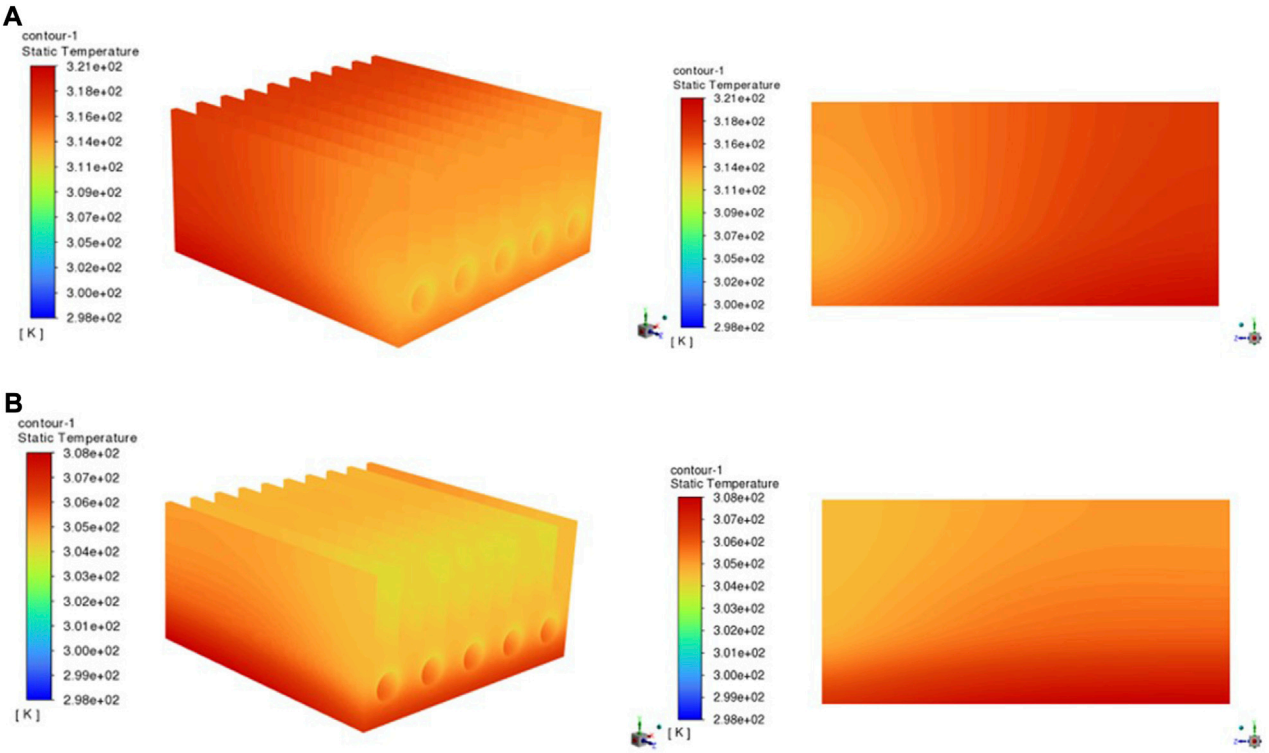

FIGURE 12
Wall temperature contour of the heat sink wall subject to a heat flux of 66,000 W/m^2: **(A)** TC5 **(B)** TC6.

This enhanced mixing, causes the fluid to come into closer contact with the heat sink surface, resulting in a more effective transfer of heat from the surface to the fluid. On the other hand, when an external magnetic field is applied to a ferrofluid flow, the magnetic nanoparticles within the fluid become magnetized and align themselves in the direction of the magnetic field. This alignment of the magnetic nanoparticles can induce a convective flow within the ferrofluid, which can enhance the heat transfer rate of the heat sink. In addition, the aligned magnetic nanoparticles can act as a thermal conductor, facilitating the transfer of heat away from the heat sink. Finally, in this section, the effect of MF-IJ on the improvement of the local convective heat transfer coefficient in the designed heat sink is investigated. The simulation results for cooling of the heat sink utilizing the case of TC4 compared to cooling of the heat sink utilizing the case of TC1 are presented in Figure 7. As can be seen, based on the results, the maximum improvement local convective heat transfer coefficient for the designed heat sink increased by approximately 32% under the influence of MF-IJ compared to the pure water state (TC1). Therefore, the simultaneous use of ferrofluid flows inside the microchannels under the effect of magnetic field and the air impingement jet flow on the plate-fins of the heat sink, increases the heat transfer rate.

The effect of magnetic field intensity has been investigated on the improvement of the average heat transfer coefficient at an inlet mass flow rate of 0.005 kg/s, heat flux of 18,750 W/m^2, and φ = 3% in Figure 8. Based on Figure 8, the average heat transfer coefficient increases with increasing magnetic field intensity. For example, at a Reynolds number of 600, by applying magnetic field intensities B = 400, 800, and 1600 G, the average heat transfer coefficient increases by 5.35, 11.77, and 16.11%, respectively. Furthermore, it is observed that the effect of the magnetic field on heat transfer was more pronounced at lower Reynolds numbers, suggesting that the magnetic field may be particularly effective in low fluid velocity applications. This observation is consistent with previous studies (Ashjaee et al., 2015) and may be because the magnetic field disrupts the thermal boundary layer and enhances the mixing of the fluid, leading to more effective heat transfer.

The ferrofluid flow under the influence of the magnetic field increases the mixing of the fluid as well as, increasing the fluid's thermal conductivity and decreasing the thermal boundary layer thickness. On the other hand, according to the results of Figures 9, 10, the air impingement jet flow induces turbulence and mixing in the boundary layer, and promotes the vortex shedding, by increasing the fluid velocity near the heat sink surface, which can reduce the wall temperature of the heat sink. For example, in the location of z = 0.02 m, by applying the impingement jet with the mass flow rates of 0.001, 0.004, and 0.005 kg/s, the wall temperature increases by 0.36, 1.62%, and 1.82%, respectively. Therefore, the combination of these two effects leads to a significant enhancement in heat transfer performance, as demonstrated by the observed increase in the local convective heat transfer coefficient.

The effect of the value of inlet mass flow rate of the impingement jet along the channel at a heat flux of 66,000 W/m^2, Reynolds number of 900, B = 1,600 G, and φ = 3% is shown in Figure 9. It can be observed that the wall temperature of the heat sink at different cases has a similar trend, which decreased gradually as

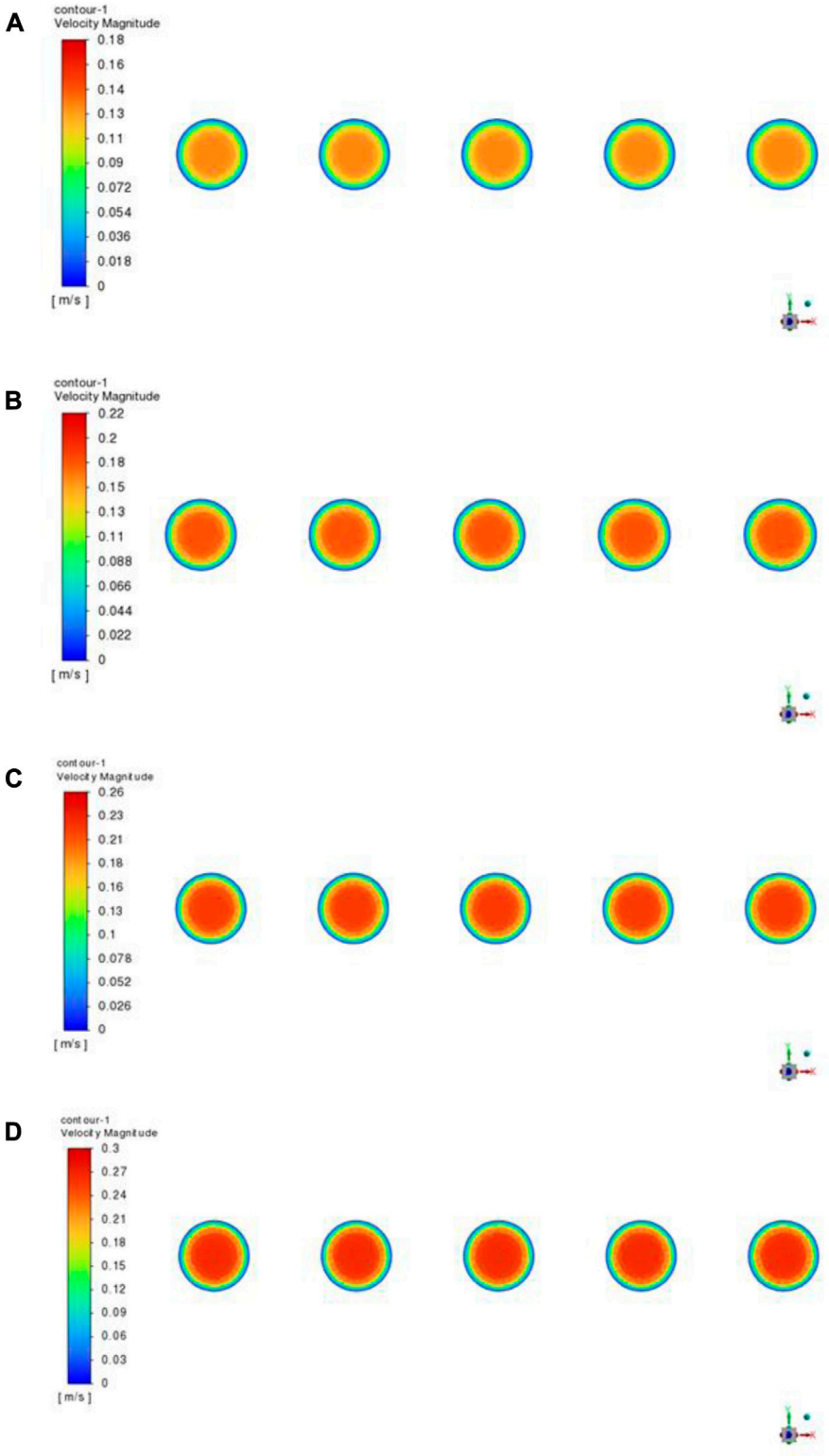

FIGURE 13
Velocity contour at the middle channel of the heat sink at a heat flux of 18,750 W/m^2, B = 1,600 G and φ = 3% for ferrofluid flow: **(A)** Re = 450; **(B)** Re = 600; **(C)** Re = 750; **(D)** Re = 900.

the inlet mass flow rate increased. The reason for this reduction is due to the increase in the convective heat transfer coefficient associated with the air flow. As the inlet mass flow rate is increased, the velocity of the air flow over the heat sink surface also increases, which creates more air motion inside the plate fins of the heat sink. Figure 11 shows the temperature contour of the

longitudinal section of the microchannel heat sink at a heat flux of 18,750 W/m^2, B = 1600 G, φ = 3%, $\dot{m}$_jet = 0.005 kg/s for various Reynolds numbers. Based on Figure 11, ferrofluid with a constant inlet temperature of 298 K enters the microchannel at different Reynolds numbers. The thermal boundary layer formed inside the microchannel becomes thinner as the Reynolds number increases. The length of the thermal entrance region increases and grows along the channel by increasing the Reynolds number. In addition, due to the heat transfer from the heat sink walls, the ferrofluid is heated and its temperature increases at the outlet of the microchannels.

Figure 12 shows the results of two cases of TC5 and TC6 on the wall temperature of the designed heat sink at a heat flux of 66,000 W/m^2. As can be seen, in Figure 12A, where the cooling is only with pure water passing through the microchannels, the maximum temperature of the heat sink wall has reached 321 K, while for Figure 12B, where the cooling is done using a combination method of MF-IJ, the maximum temperature of the heat sink wall has been reduced to 308 K. Also, in Figure 12B, due to the presence of an impingement jet and magnetic field, the cooling of the upper and middle parts of the heat sink is done better than in Figure 12A, where there is no magnetic field and impingement jet. Therefore, using the proposed combination method of MF-IJ is more effective at high heat fluxes.

The effect of increasing the inlet mass flow rate of the impingement jet on the velocity of the impingement jet is shown in Figure 10B. Also, the effect of increasing the inlet mass flow rate of the impingement jet on the wall temperature of the heat sink is shown in Figure 10A. As can be seen, in Figure 10B, with the increase of inlet mass flow of the impingement jet, the maximum velocity inside the channels of the plate-fins increases. Therefore, according to Figure 10A, the wall temperature of the heat sink decreases. Moreover, according to Figure 10A, it can be seen that with moving from the top to the bottom of the heat sink, due to approaching the stagnation point, the velocity of the impingement jet gradually decreases.

Based on the findings presented in Figure 13, it can be observed that the velocity contours at the middle channel of the heat sink are affected by the variation of Reynolds numbers. By comparing Figures 11, 13, it is revealed that as the Reynolds number increases, the flow separation is delayed, and the velocity in the center of the microchannels of ferrofluid increases. Therefore, it is recommended that for the designed heat sink, increasing the Reynolds number can enhance heat transfer and lead to a decrease in the temperature of the heat sink wall. For example, the maximum wall temperature of the heat sink for a Reynolds number of 900 is approximately 301 K. These results highlight the importance of considering the Reynolds number as a key parameter for optimizing the design of microchannel heat sinks for efficient thermal management.

7 Conclusion

In this study, the simultaneous effect of the impingement jet and an external magnetic field with magnetite ferrofluid flowing are numerically investigated on the improvements of the convective heat transfer coefficient of the proposed heat sink using a steady three-dimensional CFD approach. In this study, the impingement jet and the magnetic ferrofluid flows are considered to be turbulent and laminar, respectively. Finally, the following results are obtained:

- The cooling utilizing TC2 versus the heat sink cooling utilizing TC1 has the maximum improvement of convective heat transfer coefficient of 22.4%, and this amount of heat sink cooling using TC3 resulted in a 10% improvement.
- The use of the combination cooling method of MF-IJ could increase the maximum improvement of the convective heat transfer coefficient for this designed heat sink by 32% compared to the TC1.
- The average heat transfer coefficient of ferrofluid increases with increasing magnetic field intensity when subjected to the combination cooling method of MF-IJ. For example, at Re = 600, by applying magnetic fields B = 400 G, B = 800 G, and B = 1,600 G, the average heat transfer coefficient increases by 5.35, 11.77, and 16.11%, respectively.
- Increasing the Reynolds number of the ferrofluid and inlet mass flow of the impingement jet improved the cooling of the heat sink. At z = 0.02 m, the use of an impingement jet at different mass flow rates (0.001, 0.004, and 0.005 kg/s) causes a corresponding decrease in wall temperature (0.36%, 1.62%, and 1.82%, respectively).
- Using the proposed combination method (MF-IJ) for two heat flux values of 18,750 and 66,000 W/m^2 in this study, it was concluded that MF-IJ can also be utilized for heat sinks with high heat flux generation.

This study investigated the effects of the combination of an external magnetic field and an impingement jet (MF-IJ) on the heat transfer process in a designed heat sink. It can be concluded that this combination has a significant effect on the cooling of the heat sink, leading to enhanced heat transfer performance. Implementation of advanced cooling techniques, such as the MF-IJ, can help reduce the use of harmful refrigerants that contribute to ozone depletion and global warming, promoting the use of more environmentally friendly cooling solutions. This discovery could have significant practical implications for a wide range of electronic cooling devices. By incorporating this new understanding into the design of heat transfer devices, engineers could potentially create more efficient and effective cooling systems, which in turn could have a greater effect on the cooling of heat sinks.

As a suggestion for future works, the following improvements can be considered:

- Using porous fins instead of solid fins.
- Using pin fin instead of plate fin.
- Using a non-uniform jet instead of a uniform jet.
- Using a non-uniform magnetic field instead of a uniform magnetic field.

Data availability statement

The original contributions presented in the study are included in the article/Supplementary Material, further inquiries can be directed to the corresponding author.

Author contributions

SA: Methodology, Data curation, Writing–original draft. AA: Supervision, and project administration, Writing–review and editing. AV: writing–original draft. HAh: Data curation, Supervision. HAf: Formal Analysis, Writing–original draft.

Funding

The author(s) declare that no financial support was received for the research, authorship, and/or publication of this article.

Acknowledgments

I hereby express my sincere acknowledgment to Islamic Azad University-South Tehran Branch-Tehran-Iran for its unwavering support and invaluable assistance throughout the entire duration of my research Ph.D. project.

Conflict of interest

The authors declare that the research was conducted in the absence of any commercial or financial relationships that could be construed as a potential conflict of interest.

Publisher's note

All claims expressed in this article are solely those of the authors and do not necessarily represent those of their affiliated organizations, or those of the publisher, the editors and the reviewers. Any product that may be evaluated in this article, or claim that may be made by its manufacturer, is not guaranteed or endorsed by the publisher.

References

Abdolahipour, S., Mani, M., and Shams Taleghani, A. (2022b). Experimental investigation of flow control on a high-lift wing using modulated pulse jet vortex generator. *J. Aerosp. Eng.* 35 (Issue 5), 2022. doi:10.1061/(ASCE)AS.1943-5525.0001463

Abdolahipour, S., Mani, M., and Shams Taleghani, A. (2021). Parametric study of a frequency-modulated pulse jet by measurements of flow characteristics. *Phys. Scr.* 96 (No. 12), 125012. doi:10.1088/1402-4896/ac2bdf

Abdolahipour, S., Mani, M., and Shams Taleghani, A. (2022a). Pressure improvement on a supercritical high-lift wing using simple and modulated pulse jet vortex generator. *Flow. Turbul. Combust.* 109, 65–100. doi:10.1007/s10494-022-00327-9

ANSYS Fluent 17.2 (2016). *ANSYS fluent theory guide*. Southpointe, Canonsburg, PA: ANSYS Inc.

Ashjaee, M., Goharkhah, M., Khadem, L. A., and Ahmadi, R. (2015). Effect of magnetic field on the forced convection heat transfer and pressure drop of a magnetic nanofluid in a miniature heat sink. *Heat Mass Transf.* 51, 953–964. þ. doi:10.1007/s00231-014-1467-1

Bahiraei, M., and Hangi, M. (2016). Automatic cooling by means of thermomagnetic phenomenon of magnetic nanofluid in a toroidal loop. *Appl. Therm. Eng.*, 107, 700–708.þdoi:10.1016/j.applthermaleng.2016.07.021

Bahiraei, M., and Hangi, M. (2013). Investigating the efficacy of magnetic nanofluid as a coolant in double-pipe heat exchanger in the presence of magnetic field. *Energy Convers. Manag.* 76, 1125–1133. þ. doi:10.1016/j.enconman.2013.09.008

Bailey, R. L. (1983). Lesser known applications of ferrofluids. *J. magnetism magnetic Mater.* 39 (1-2), 178–182. þ. doi:10.1016/0304-8853(83)90428-6

Bar-Cohen, A. (1993). Thermal management of electronic components with dielectric liquids. *JSME Int. J. Ser. B Fluids Therm. Eng.* 36 (1), 1–25. þ. doi:10.1299/jsmeb.36.1

Bezaatpour, M., and Goharkhah, M. (2019). Effect of magnetic field on the hydrodynamic and heat transfer of magnetite ferrofluid flow in a porous fin heat sink. *J. Magnetism Magnetic Mater.* 476, 506–515. þ. doi:10.1016/j.jmmm.2019.01.028

Biber, C. R. (1997). Pressure drop and heat transfer in an isothermal channel with impinging flow. *IEEE Trans. Components, Packag. Manuf. Technol. Part A* 20 (4), 458–462. þ. doi:10.1109/95.650935

Byon, C. (2015). Heat transfer characteristics of aluminum foam heat sinks subject to an impinging jet under fixed pumping power. *Int. J. Heat Mass Transf.* 84, 1056–1060. þ. doi:10.1016/j.ijheatmasstransfer.2015.01.025

El-Shorbagy, M. A., Algehyne, E. A., Ibrahim, M., Ali, V., and Kalbasi, R. (2021). Effect of fin thickness on mixed convection of hybrid nanofluid exposed to magnetic field-Enhancement of heat sink efficiency. *Case Stud. Therm. Eng.*, 26, 101037. doi:10.1016/j.csite.2021.101037

Forghan, F., Goldthwaite, D., Ulinski, M., and Metghalchi, H.(2001). "Experimental and theoretical investigation of thermal performance of heat sinks," in *Annual meeting for ISME* (United States: þ).

Fox, R. W., McDonald, A. T., and Mitchell, J. W. (2020). *Fox and McDonald's introduction to fluid mechanics*. þHoboken, New Jersey: John Wiley & Sons.

Froissart, M., Ziółkowski, P., Dudda, W., and Badur, J. (2021). Heat exchange enhancement of jet impingement cooling with the novel humped-cone heat sink. *Case Stud. Therm. Eng.* 28, 101445. þ. doi:10.1016/j.csite.2021.101445

Gan, T., Ming, T., Fang, W., Liu, Y., Miao, L., Ren, K., et al. (2020). Heat transfer enhancement of a microchannel heat sink with the combination of impinging jets, dimples, and side outlets. *J. Therm. Analysis Calorim.* 141, 45–56. þ. doi:10.1007/s10973-019-08754-z

Ganguly, R., Sen, S., and Puri, I. K. (2004). Thermomagnetic convection in a square enclosure using a line dipole. *Phys. Fluids* 16 (7), 2228–2236. þ. doi:10.1063/1.1736691

Hussain, A. A., Freegah, B., Khalaf, B. S., and Towsyfyan, H. (2019). Numerical investigation of heat transfer enhancement in plate-fin heat sinks: effect of flow direction and fillet profile. *Case Stud. Therm. Eng.* 13, 100388. þ. doi:10.1016/j.csite.2018.100388

Jalili, B., Rezaeian, A., Jalili, P., Ommi, F., and Ganji, D. D. (2023d). Numerical modeling of magnetic field impact on the thermal behavior of a microchannel heat sink. *Case Stud. Therm. Eng.* 45, 102944. þ. doi:10.1016/j.csite.2023.102944

Jalili, B., Roshani, H., Jalili, P., Jalili, M., Pasha, P., and Ganji, D. D. (2023b). The magnetohydrodynamic flow of viscous fluid and heat transfer examination between permeable disks by AGM and FEM. *Case Stud. Therm. Eng.* 45, 102961. doi:10.1016/j.csite.2023.102961

Jalili, P., Azar, A. A., Jalili, B., and Ganji, D. D. (2023a). Study of nonlinear radiative heat transfer with magnetic field for non-Newtonian Casson fluid flow in a porous medium. *Results Phys.* 48, 106371. doi:10.1016/j.rinp.2023.106371

Jalili, P., Narimisa, H., Jalili, B., and Ganji, D. D. (2023c). Micro-polar nanofluid in the presence of thermophoresis, hall currents, and Brownian motion in a rotating system. *Mod. Phys. Lett. B* 37 (01), 2250197. doi:10.1142/s0217984922501974

Jang, S. P., Kim, S. J., and Paik, K. W. (2003). Experimental investigation of thermal characteristics for a microchannel heat sink subject to an impinging jet, using a micro-thermal sensor array. *Sensors Actuators A Phys.* 105 (2), 211–224. þ. doi:10.1016/s0924-4247(03)00103-1

Jazmi, Ramin, Mohammadzadeh, Kazem, Hassan, Khaleghi, and Maddahian, Reza (2021). Numerical investigation of water droplet behavior in anode channel of a PEM fuel cell with partial blockage. *Archive Appl. Mech.* 91 (4), 1391–1406. doi:10.1007/s00419-020-01828-7

Johnson, M. J., and Go, D. B. (2016). Impingement cooling using the ionic wind generated by a low-voltage piezoelectric transformer. *Front. Mech. Eng.* 2, 7. doi:10.3389/fmech.2016.00007

Karimi, A., Goharkhah, M., Ashjaee, M., and Shafii, M. B. (2015). Thermal conductivity of $$\mathrm{Fe}_{2}\mathrm{O}_{3}$$ Fe 2 O 3 and $$\mathrm{Fe}_{3}\mathrm{O}_{4}$$ Fe 3 O 4 magnetic nanofluids under the influence of magnetic field. *Int. J. Thermophys.* 36, 2720–2739. þ. doi:10.1007/s10765-015-1977-1

Kim, D. K., Kim, S. J., and Bae, J. K. (2009). Comparison of thermal performances of plate-fin and pin-fin heat sinks subject to an impinging flow. *Int. J. Heat Mass Transf.* 52 (15-16), 3510–3517. þ. doi:10.1016/j.ijheatmasstransfer.2009.02.041

Kondo, Y., Behnia, M., Nakayama, W., and Matsushima, H. (1998). *Optimization of finned heat sinks for impingement cooling of electronic packages*, 259–266þ.

Koo, J., and Kleinstreuer, C. (2004). A new thermal conductivity model for nanofluids. *J. Nanoparticle Res.* 6, 577–588. þ. doi:10.1007/s11051-004-3170-5

Kotb, A., Askar, H., and Saad, H. (2023). On the impingement of heat transfer using swirled air jets. *Front. Mech. Eng.* 9, 1120985. doi:10.3389/fmech.2023.1120985

Li, H. Y., Chen, K. Y., and Chiang, M. H. (2009). Thermal-fluid characteristics of plate-fin heat sinks cooled by impingement jet. *Energy Convers. Manag.* 50 (11), 2738–2746. þ. doi:10.1016/j.enconman.2009.06.030

Li, Q., and Xuan, Y. (2009). Experimental investigation on heat transfer characteristics of magnetic fluid flow around a fine wire under the influence of an external magnetic field. *Exp. Therm. Fluid Sci.* 33 (4), 591–596. þ. doi:10.1016/j.expthermflusci.2008.12.003

Mirzaei, M., and TaleghaniShadaram, A. S. A. (2012). Experimental study of vortex shedding control using plasma actuator. *Appl. Mech. Mater.* 186, 75–86. doi:10.4028/www.scientific.net/amm.186.75

Mohammadi, M., and Taleghani, A. S. (2014). Active flow control by dielectric barrier discharge to increase stall angle of a NACA0012 airfoil. *Arab. J. Sci. Eng.* 39, 2363–2370. doi:10.1007/s13369-013-0772-1

Mohammadzadeh, K., Khaleghi, H., Khadem Abolfazli, H. R., and Seddiq, M. (2018). Effects of gas cross-over through the membrane on water management in the cathode and anode sides of PEM fuel cell. *J. Appl. Fluid Mech.* 11 (4), 861–875. doi:10.29252/jafm.11.04.28559

Naphon, P., Wiriyasart, S., Arisariyawong, T., and Nakharintr, L. (2019). ANN, numerical and experimental analysis on the jet impingement nanofluids flow and heat transfer characteristics in the micro-channel heat sink. *Int. J. Heat Mass Transf.* 131, 329–340. þ. doi:10.1016/j.ijheatmasstransfer.2018.11.073

Noori, S. M. S., Taeibi Rahni, M., and Shams Taleghani, S. A. (2020). Numerical analysis of droplet motion over a flat plate due to surface acoustic waves. *Microgravity Sci. Technol.* 32 (4), 647–660. doi:10.1007/s12217-020-09784-1

Pandey, J., Husain, A., Ansari, M. Z., and Al-Azri, N. (2022). Comparison of the parallel microchannel and Pin-Fin heat Sinks: an experimental study. *Mater. Today Proc.* 56, 845–850. doi:10.1016/j.matpr.2022.02.503

Pereira, P. R., Varga, S., Oliveira, A. C., and Soares, J. (2015). Development and performance of an advanced ejector cooling system for a sustainable built environment. *Front. Mech. Eng.* 1, 7. doi:10.3389/fmech.2015.00007

Sadighi, S., Afshar, H., Jabbari, M., and Ahmadi Danesh Ashtiani, H. (2022b). An analytical approach to entropy production in MHD mixed convection micropolar fluid flow over an inclined porous stretching sheet. *Front. Mech. Eng.* 8, 900316. doi:10.3389/fmech.2022.900316

Sadighi, S., Afshar, H., Jabbari, M., and Ashtiani, H. A. D. (2023). Heat and mass transfer for MHD nanofluid flow on a porous stretching sheet with prescribed boundary conditions. *Case Stud. Therm. Eng.* 49, 103345. doi:10.1016/j.csite.2023.103345

Sadighi, S., Jabbari, M., Afshar, H., and Ashtiani, H. A. D. (2022a). MHD heat and mass transfer nanofluid flow on a porous cylinder with chemical reaction and viscous dissipation effects: benchmark solutions. *Case Stud. Therm. Eng.* 40, 102443. doi:10.1016/j.csite.2022.102443

Salmasi, A., Shadaram, A., and Shams Taleghani, A. (2013). Effect of plasma actuator placement on the airfoil efficiency at poststall angles of attack. *IEEE Trans. Plasma Sci.* 41 (10), 3079–3085. doi:10.1109/tps.2013.2280612

Selvakumar, P., and Suresh, S. (2012). Convective performance of CuO/water nanofluid in an electronic heat sink. *Exp. Therm. Fluid Sci.* 40, 57–63. doi:10.1016/j.expthermflusci.2012.01.033

Sheikholeslam Noori, M., Shams Taleghani, A., and Taeibi Rahni, M. (2020a). Phenomenological investigation of drop manipulation using surface acoustic waves. *Microgravity Sci. Technol.* 32 (6), 1147–1158. doi:10.1007/s12217-020-09839-3

Sheikholeslam Noori, M., Shams Taleghani, A., and Taeibi Rahni, M. (2021). Surface acoustic waves as control actuator for drop removal from solid surface. *Fluid Dyn. Res.* 53 (4), 045503. doi:10.1088/1873-7005/ac12af

Sheikholeslam Noori, M., Taeibi Rahni, M., and Shams Taleghani, A. (2020b). Effects of contact angle hysteresis on drop manipulation using surface acoustic waves. *Theor. Comput. Fluid Dyn.* 34 (1), 145–162. doi:10.1007/s00162-020-00516-0

Singh, R., Ahmed, R., Karami, H., Nasser, M., and Hussein, I. (2021). CFD analysis of turbulent flow of power-law fluid in a partially blocked eccentric annulus. *Energies*, 14(3), 731.þdoi:10.3390/en14030731

Spalding, D. B. (1974). The numerical computation of turbulent flow. *Comp. Methods Appl. Mech. Eng.*, 3, 269.þ

Taeibi Rahni, M., Shams Taleghani, A., Sheikholeslam, M., and Ahmadi, G. (2022). Computational simulation of water removal from a flat plate, using surface acoustic waves. *Wave Motion* 111, 102867, 102867. doi:10.1016/j.wavemoti.2021.102867

Taleghani, A. S., Shadaram, A., Mirzaei, M., and Abdolahipour, S. (2018). Parametric study of a plasma actuator at unsteady actuation by measurements of the induced flow velocity for flow control. *J. Braz. Soc. Mech. Sci. Eng.* 40 (No. 4), 173–213. doi:10.1007/s40430-018-1120-x

Taleghani, A. S., Shadaram, A., and Mirzaei, M. (2012). Effects of duty cycles of the plasma actuators on improvement of pressure distribution above a NLF0414 airfoil. *IEEE Trans. Plasma Sci.* 40 (5), 1434–1440. doi:10.1109/tps.2012.2187683

Wong, K. C., and Indran, S. (2013). Impingement heat transfer of a plate fin heat sink with fillet profile. *Int. J. Heat Mass Transf.* 65, 1–9. þ. doi:10.1016/j.ijheatmasstransfer.2013.05.059

Xie, Y., Jiang, C., Zheng, P., Cao, Z., and Luo, M. (2021). Ferrohydrodynamic and magnetohydrodynamic effects on jet flow and heat transfer of Fe_3O_4-H_2O nanofluid in a microchannel subjected to permanent magnets. *Symmetry* 13 (11), 2051. þ. doi:10.3390/sym13112051

Xuan, Y., and Roetzel, W. (2000). Conceptions for heat transfer correlation of nanofluids. *Int. J. heat Mass Transf.* 43 (19), 3701–3707. þ. doi:10.1016/s0017-9310(99)00369-5

Zamzamian, A., Oskouie, S. N., Doosthoseini, A., Joneidi, A., and Pazouki, M. (2011). Experimental investigation of forced convective heat transfer coefficient in nanofluids of Al2O3/EG and CuO/EG in a double pipe and plate heat exchangers under turbulent flow. *Exp. Therm. Fluid Sci.* 35 (3), 495–502. þ. doi:10.1016/j.expthermflusci.2010.11.013

Zhong, J. F., Sedeh, S. N., Lv, Y. P., Arzani, B., and Toghraie, D. (2021). Investigation of Ferro-nanofluid flow within a porous ribbed microchannel heat sink using single-phase and two-phase approaches in the presence of constant magnetic field. *Powder Technol.* 387, 251–260. doi:10.1016/j.powtec.2021.04.03

þSadighi, S., Afshar, H., Ashtiani, H. A. D., and Jabbari, M. (2023). MHD flow and conductive heat transfer on a permeable stretching cylinder: benchmark solutions. *Case Stud. Therm. Eng.* 44, 102886. doi:10.1016/j.csite.2023.102886

Appendix A

$$R_{th} = \frac{1}{h_{avg} A_T}$$

$$A_T = WL + 2N_f C[L + t] + 2Z[L + W]$$

Nomenclature

A_T	Total area of heat transfer, m^2
R_{th}	Thermal resistance, K/W
h_{avg}	Average heat transfer coefficient, W/m^2K
Re	Reynolds number
T	Temperature, K
W	Width of the heat sink, m
L	Length of the heat sink, m
Y	Height of the heat sink, m
Z	Base height, m
C	Height of fin, m
N_f	Number of fins
t	Thickness of fin, m
ø	Microchannel diameter, m
d	Distance between fins, m
B	Magnetic flux density, N. A^{-1}. m^{-1}
C_f	Quadratic drag factor
C_p	Specific heat, KJ. Kg^{-1}. K^{-1}
F_k	Kelvin body force, N/m^3
h	Local heat transfer coefficient, $W/m^2.K$
H	Magnetic field intensity, A m^{-1}
k	Thermal conductivity, W m^{-1}. K^{-1}
M	Magnetization, A m^{-1}
n	Normal direction
P	Pressure, Pa
q''	Heat flux, W/m^2
V	Velocity, m s^{-1}

Greek

φ	Volume fraction
χ_m	Magnetic susceptibility
χ_0	Reference magnetic susceptibility
ρ	Density, kg/m^3
μ	Dynamic viscosity, N s/m^2
μ_0	Permeability of free space, N/A^2
β	Liquid volume fraction, k^{-1}

Subscripts

b	Base
m	Mean
in	Inlet
out	Outlet
avg	Average
eff	Effective
nf	Nanofluid
np	Nanoparticle
bf	Base fluid
f	Fluid
s	Solid
0	At reference (300 K)

frontiers | Frontiers in Mechanical Engineering

TYPE Original Research
PUBLISHED 15 November 2023
DOI 10.3389/fmech.2023.1207894

OPEN ACCESS

EDITED BY
Farschad Torabi,
K. N. Toosi University of Technology, Iran

REVIEWED BY
Ebrahim Afshari,
University of Isfahan, Iran
Azadeh Shahidian,
K. N. Toosi University of Technology, Iran

*CORRESPONDENCE
D. D. Ganji,
ddg_davood@yahoo.com

RECEIVED 18 April 2023
ACCEPTED 24 October 2023
PUBLISHED 15 November 2023

CITATION
Jalili B, Jalili P, Ommi F and Ganji DD (2023), Experimental study on the nozzle-shape effect on liquid jet characteristics in gaseous crossflow. *Front. Mech. Eng* 9:1207894. doi: 10.3389/fmech.2023.1207894

Experimental study on the nozzle-shape effect on liquid jet characteristics in gaseous crossflow

B. Jalili[1], P. Jalili[1], F. Ommi[2] and D. D. Ganji[3]*

[1]Department of Mechanical Engineering, North Tehran Branch, Islamic Azad University, Tehran, Iran,
[2]Department of Mechanical Engineering, Tarbiat Modares University, Tehran, Iran,
[3]Department of Mechanical Engineering, Babol Noshirvani University of Technology, Babol, Iran

This study presents experimental findings on the crossflow injection of a liquid jet into a gaseous flow. Crossflow injection is favored over co-axial trajectory injection because of its potential to enhance atomization, promote the formation of smaller droplets, and improve injection parameters, mainly due to the differing trajectory of fuel injection within the transverse airflow. The study's experiments use two circular and four elliptical nozzles with varying aspect ratios. The research investigates the influential factors that affect the trajectory and breakup of the liquid jet, specifically analyzing the impact of the nozzle geometry, Weber number, and momentum ratio of the liquid jet to the air crossflow. Additionally, equations are derived to describe the trajectory for both elliptical and circular nozzles. The relationship between breakup height and length is explored, with the observation that breakup length remains constant for both nozzle shapes. Furthermore, the study investigates the analysis of breakup regimes and establishes a direct correlation between the Weber number and the breakup regime. Column, bag, and multimode breakup are observed at Weber numbers 4, 38, and 82, respectively. The experimental error for the liquid jet trajectory obtained is approximately 2%. Importantly, the experimental results align with previously published experimental and numerical data, confirming the validity and reliability of the findings.

KEYWORDS

experimental study, crossflow, liquid jet, elliptical nozzle, breakup regime

1 Introduction

The flow field associated with injecting a transverse fluid jet into a crossflow can be divided into two main categories. The first type of gas jet (or liquid) within the transverse gas flow (or liquid) is called a "single-phase flow". The second type of gas jet (or liquid) within the transverse flow of liquid (or gas) is known as a "two-phase flow." Crossflow jet applications have various uses in industry, environmental systems, and nature. Examples of these applications include airborne engines (such as diluted air jets, turbine blast cooling, and fuel injection in jet and scramjet systems), rocket motors (for thrust vector control), environmental control systems (including smoke from chimneys and from ship or train funnels), and natural phenomena (like volcanic lava in crosswinds). There has been initial research on the environmental applications of transverse flow, such as the dispersion of exhaust or chimney outlet smoke or liquid wastewater in the airflow (Gurevich et al., 2018; Wen et al., 2020; Niu et al., 2022; Jalili and Jalili, 2023).

The thrust vector control of rocket motors using a row of crossflow jets is used to disperse the nozzle fluid for gas and liquid jets. This jet structure is also used to control lift and thrust vectors during lifting, stationary, and wing-borne flight (Li et al., 2022). Better jet mixing properties are more attractive for engineering applications than jets in stationary air, especially where fast mixing is essential. Additionally, the dilution of gas jets in the primary or secondary combustion chamber is used to reduce the temperature of combustion products before entering the turbine area, making it an application of crossflow jets (Ukamanal et al., 2020). Transversely injecting liquid fuel into a crossflow is commonly used in ground and air power generation systems, where rapid fuel penetration, evaporation, combustion, and, ultimately, stable combustion processes are considered (Keramaris and Pechlivanidis, 2020). Cross-injection of the jet is one of the most advanced methods for fuel injection systems, thanks to proper atomization and a high evaporation rate. Moreover, the momentum ratio and adjustable injection angles, or even a swirl injector, can be used to achieve the desired fuel-to-air ratio. These elements are crucial in achieving the desired air and fuel mixture quality. Ultimately, all of those mentioned previously contribute to reducing the production of environmental pollutants, increasing combustion efficiency, and decreasing fuel consumption (Cerri et al., 2007).

The nature of crossflow is volatile. These instabilities are due to the boundary layer near the walls and turbulence in the flow. Physical complexities arise from the strong vortex structure, small-scale waveforms, the separation of tiny droplets from the jet surface, and the formation of ligaments and droplets of different sizes. Theoretical studies have generally been used to obtain initial information on the formation of a jet and its trajectory. Empirical studies have also obtained information about changes in jet trajectory and jet breakup mechanisms. Iyogun et al. (2006) showed that a larger injector diameter would increase penetration depth at the same momentum ratio. They also showed that an increase in the momentum ratio results in deeper penetration for a constant injector diameter. Lakhamraju (2003) studied the effect of ambient temperature on the jet trajectory and penetration depth and found that the latter decreases with increasing ambient temperature. They also observed that, with an increasing momentum ratio, the breakup length does not change and remains constant. Bellofiore et al. (2007) experimentally studied transverse airflow with high temperature and pressure. They showed that the liquid-to-gas momentum ratio, Reynolds gas number, and aerodynamic Weber number are essential for determining the breakup point. Wang et al. (2011) studied the injection of plate jets in a gas crossflow. They experimentally examined the penetration and diffusion of the liquid jet and obtained relationships for the liquid column's penetration, breakup time, and instability frequency. Bai et al. (2009) investigated the effects of different angles of swirl jets on the mixing ratio of gas and liquid phases. They discovered that increased gas turbulence increases the mixing rate. Birouk et al. (2007) studied the effect of liquid viscosity on jet penetration and trajectory in a low-speed gas crossflow.

This paper is an experimental and comprehensive study of effective parameters on the trajectory and penetration of a liquid jet in the gaseous crossflow. It investigates the effect of nozzle output geometry, momentum ratio, and Weber number. The main focus of this study is nozzle geometry, which considers elliptic and circular nozzles of different diameters. It also investigates its effect on the liquid jet's trajectory, penetration, and initial rupture length. Most previous studies have used a limited range of Weber numbers and momentum ratios (essentially representing the liquid jet velocity and transverse air velocity). However, this paper employs a more extensive range for examination.

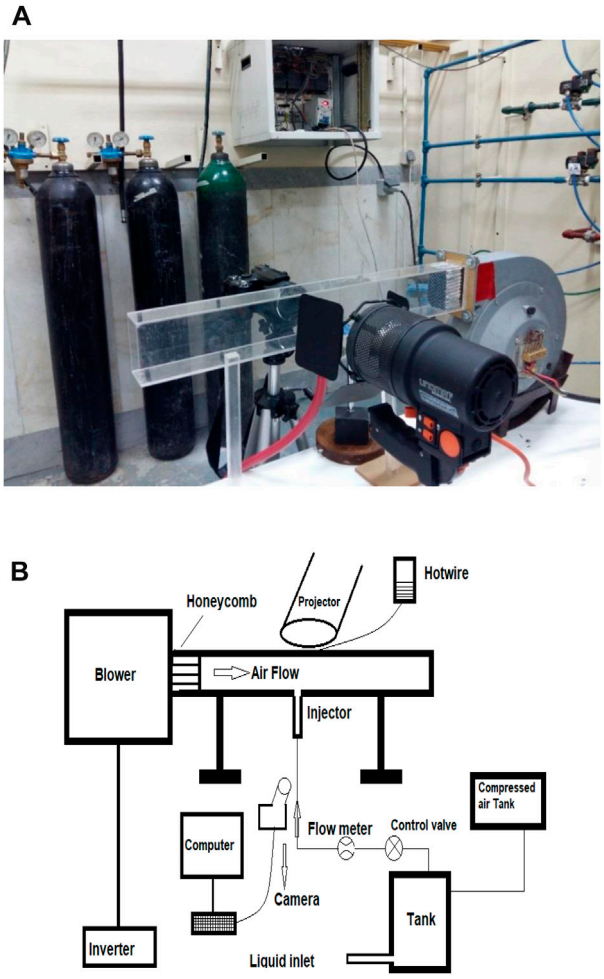

FIGURE 1
(A) Experimental setup. **(B)** Schematic diagram.

1.1 Experiment apparatus

Equipment used in the laboratory test, as shown in Figure 1, could be classified into three main categories: the air supply system, fuel system, and imaging and detection system.

1.2 Air supply system

The airflow generation in this setup involved using a Gebhardt company centrifugal blower, operating at a speed of 2,750 rpm, with the capacity to generate up to 35% of a cubic meter per second (Figure 2A). The LS company employs a converter (Figure 2B) capable of modulating the blower's speed to control and adjust flow rates within the channel. This converter achieves different channel velocities by altering the motor's input frequency, ranging from 0 to

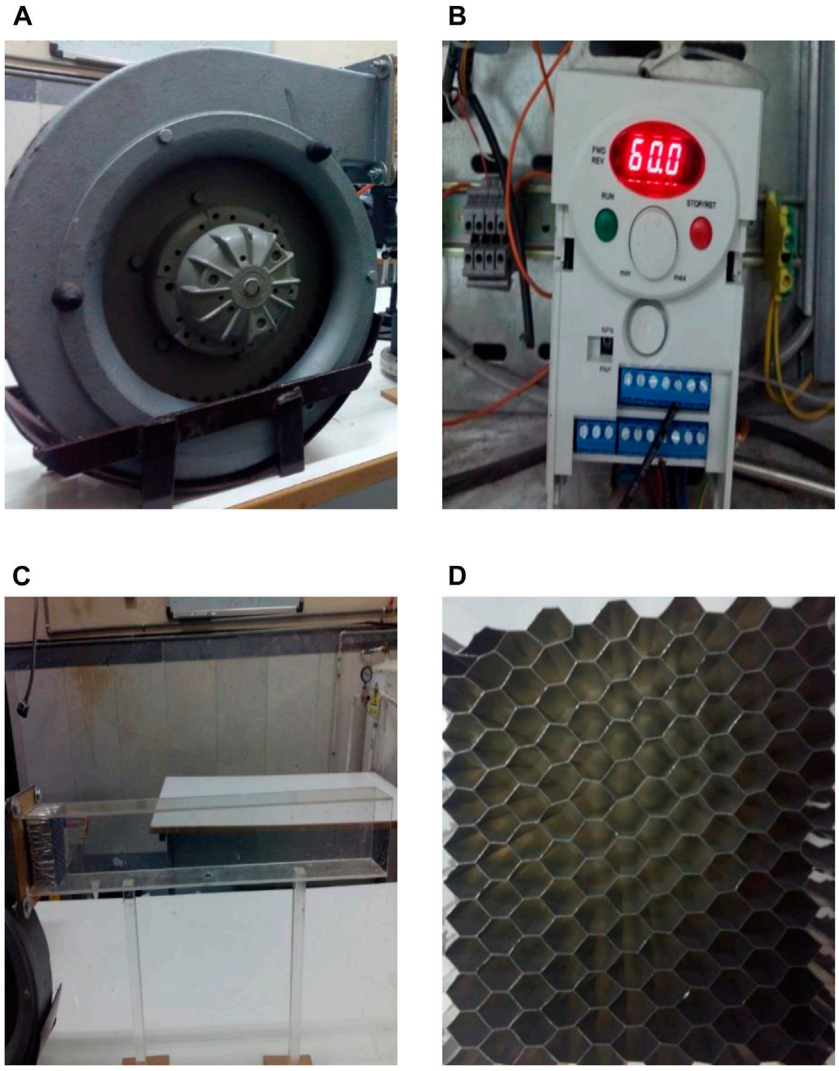

FIGURE 2
(A) Blower, **(B)** converter, **(C)** duct, and **(D)** honeycomb.

60 Hz, changing the engine's speed from 0 to 2,750 rpm, and the flow speed from 0 to approximately 53 m/s.

The primary structure of the wind tunnel was crafted from Plexiglas. It possessed a cross-section measuring 50 × 80 mm and extended over a length of 60 cm. The transparent nature of Plexiglas enables optical measurements during testing. The Plexiglas sheet was 2-mm-thick, and the nozzle was positioned 30 cm into the channel. The initial 30 cm of the channel streamlined and smoothed the flow (Figure 2C).

A honeycomb composed of hexagonal aluminum cells (Figure 2D) was employed to enhance flow stability and minimize vertical velocity components. These hexagonal cells comprised multiple tubes that effectively reduced the intrusion of large-scale eddies into the airflow. The honeycomb structure utilized in this study was 35-mm-long and was characterized by 6-mm regular hexagons.

To ensure the stability of the channel and prevent unwanted vibrations, two solid Plexiglass base holders with a cross-section of 20 × 20 mm were employed. Additionally, 100 × 100 mm Plexiglass sheets were used to maintain balance on the base and table. Furthermore, a support holder was covered with fiber and polystyrene to prevent vibrations in the blower.

1.3 Fuel supply system

Injecting a liquid jet vertically into the air stream requires a specific route for fuel injection at the desired speed by the jet supply system. Due to natural fuel limitations, water was used as a fluid injected into the stream. Injections of fluid into the transverse airflow at the desired speed required increased pressure behind the fluid using a pressurized tank (Figure 3A). The tanker was partially filled with liquid and pressurized by a gas. We could then adjust the flow rate in the nozzle outlet using a regulator valve. A flow meter was used to obtain the rate of the fluid jet in the nozzle outlet. The outlet speed of the nozzle was easily calculated by measuring the inlet flow and the nozzle area. The Besta Company made the flowmeter used, in the range of 0.16–1.6 L per minute (Figure 3B). The nozzle used here was a simple orifice,

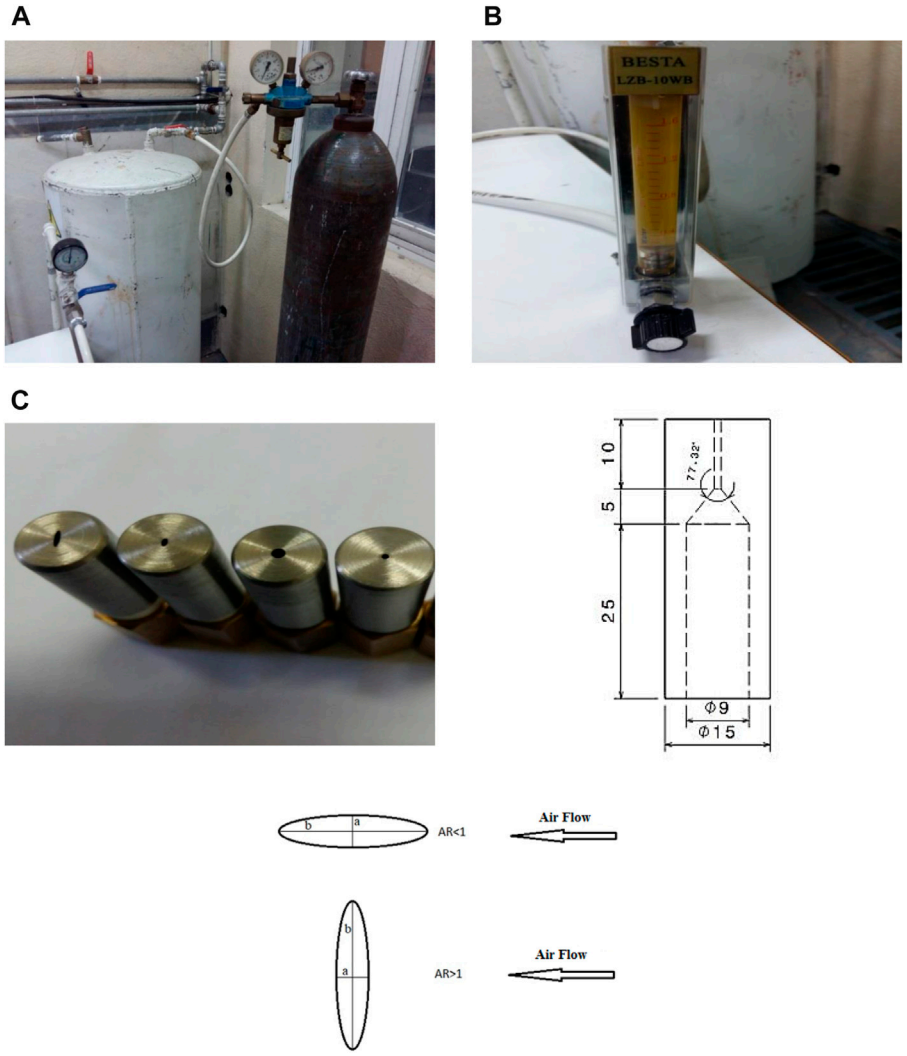

FIGURE 3
(A) Pressurized tank, **(B)** flowmeter, and **(C)** view of the nozzles used and nozzle structure.

and was circular and elliptical in different dimensions (Figure 3C). Four configurations for the nozzle outlet were considered. In two cases, the nozzle outlet was circular with diameters of 1 and 2 mm, and in the other two cases, elliptical nozzles with major and minor radii of 1 and 2, and 1 and 4 mm, respectively, were constructed. These nozzles were fabricated using a super drill and wire cutter and were specifically designed for this paper. When the smaller diameter faced the wind direction, the aspect ratio was less than 1, and when the same nozzle had its larger diameter facing the wind, the aspect ratio became greater than 1. Thus, depending on its orientation relative to the wind, two aspect ratios smaller and greater than 1 could be achieved with a single nozzle.

1.4 Image processing and detection system

In this study, shadowgraphy was used to detect crossflow. We required detection and imaging systems to capture relatively good-quality images for crossflow analysis. The camera used in this test was a Casio EX-F1 camera that can take pictures at 1,200 frames per second.

This study used 25-micron-long time exposure photography, which is the maximum time that could be achieved with the present camera. Due to the low time exposure, it needed a vital light source, as explained in the following paragraphs. The most important effect of the time exposure on the photographs was that the lower the number, the less light the camera sensor needed. For example, if the droplets were flowing, they could be depicted with a relatively low resolution with low lightning time.

For a light source, a projector with an Onomat 1000-W bulb was used due to the type of lens mounted on it and the surrounding protections; its light output was relatively uniform (Figure 4A). To measure the speed of the incoming air, a hot wire anemometer model 1,340, manufactured by Tess Corporation with an error of less than 3% was used. (Figure 4B).

Measurement of the velocity profile in the test's transverse section showed that this section's velocity profile was uniform. The speed of blown air varied from 7.6 to 51.8 (ms^{-1}). The fluid

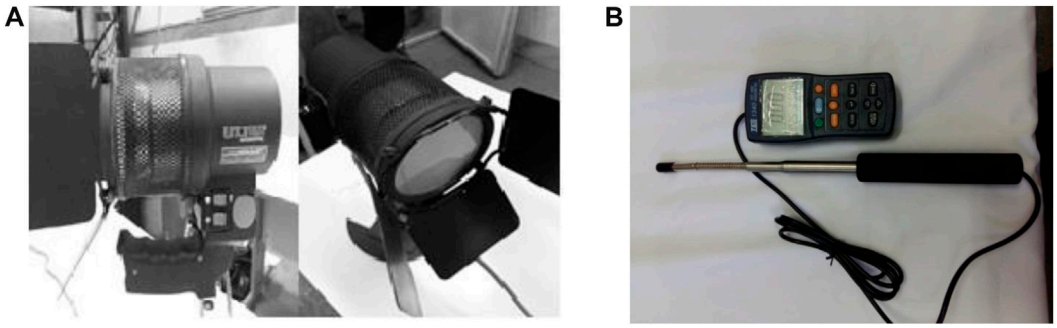

FIGURE 4
(A) View of the projector. **(B)** Hot wire.

TABLE 1 Experimental conditions.

Parameter	Quantity
Water density ($\frac{m^3}{s}$)	998
Crossflow velocity ($\frac{m}{s}$)	7–50
Liquid jet velocity ($\frac{m}{s}$)	3–23
Water viscosity ($N.\frac{s}{m^2}$)	0.00089
Surface tension ($\frac{N}{m}$)	0.073
Gas Weber number	6–88
Momentum ratio	10–500
Circular nozzle diameter (mm)	1,2
Elliptic nozzle aspect ratio	0.25, 0.5, 2, 4

tested was water; the use of water instead of fuel is routine and was used as the scavenged fluid. Since nozzles with different openings were used in this experiment, the speed of the outlet water of the nozzle was different. However, water velocity generally varied from 1.06 to 33.95. The test temperature was an ambient 25 °C (Table 1).

Because this is a study on crossflow, there are many non-dimensional numbers in the problem. The following are the dimensionless numbers used in this experiment (Ashgriz, 2011). The momentum ratio number is defined as the ratio of the liquid jet momentum to the gas momentum (liquid jet dynamic pressure to the dynamic gas pressure):

$$q = \frac{\rho_l v_l^2}{\rho_g v_g^2} \tag{1}$$

In relation (1), ρ_l is the liquid density, v_l is the liquid velocity (jet) in the y-direction, ρ_g is the density of the gas (air), and v_g is the gas velocity (air) in the x-direction. The gas Weber number is defined as the force of inertia to the surface tension force:

$$we_g = \frac{\rho_g v_g^2 d}{\sigma_l}. \tag{2}$$

In relation (2), d is the diameter of the nozzle and σ_l is the liquid's surface tension.

The liquid Weber number is defined as the gas Weber number:

$$we_l = \frac{\rho_l v_l^2 d}{\sigma_l}. \tag{3}$$

The gas Reynolds number is defined as the ratio of inertia to the viscous force:

$$Re_g = \frac{\rho_g v_g l}{\mu_g}, \tag{4}$$

where l is the characteristic length and μ_g is the viscosity of the air.

The liquid Reynolds number is also defined as follows:

$$Re_l = \frac{\rho_l v_l l}{\mu_l}. \tag{5}$$

Eqs 1–5 were used to obtain the Mach number for gas and liquid, as well as the Reynolds number for gas and liquid and the momentum ratio. As can be seen, the dimensionless numbers are determined after plugging the values obtained from Table 1 into these equations.

2 Results and discussion

2.1 Penetration and trajectory of liquid jet

The trajectory and penetration of a liquid jet into a transverse gas flow are critical parameters for a fluid jet. They directly influence the distribution of fuel injection within the combustion chamber, the process of evaporation, and the rate of mixing with the oxidizing agent. It is also essential to design the combustion chamber to prevent the liquid jet from impacting the chamber walls. The observations from this study reveal that, when a liquid jet is injected into calm air, it maintains a straight trajectory and does not collide with the upper wall of the test section. It is important to note that these observations are based on small-scale dimensions. In larger-scale scenarios, the fluid jet may indeed deflect and not reach the upper surface of the channel.

A schematic representation of the fluid jet being sprayed into the transverse air is shown in Figure 5. The liquid separates from the

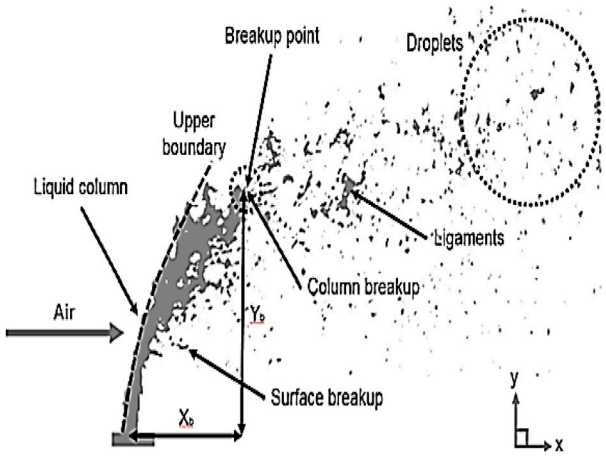

FIGURE 5
View of injection of the liquid jet structure (Stenzler et al., 2006).

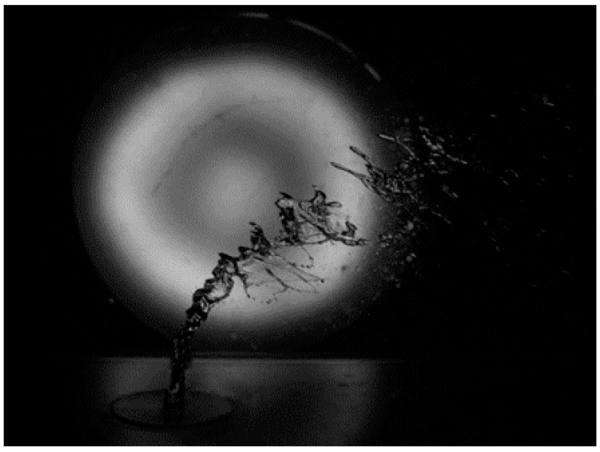

FIGURE 6
View of a liquid jet in crossflow.

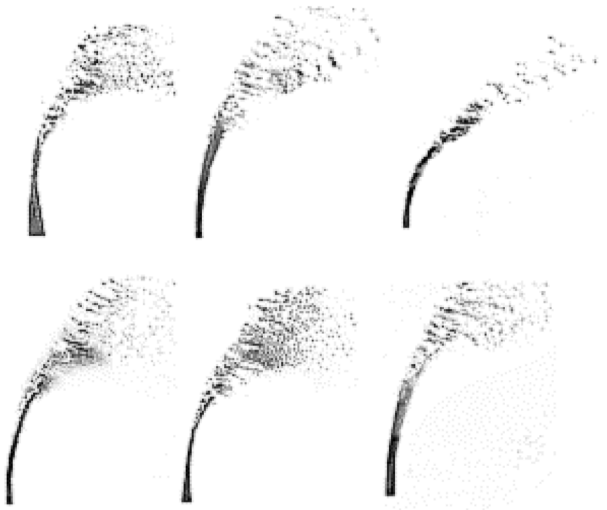

FIGURE 7
View of a liquid jet in crossflow with a different nozzle geometry.

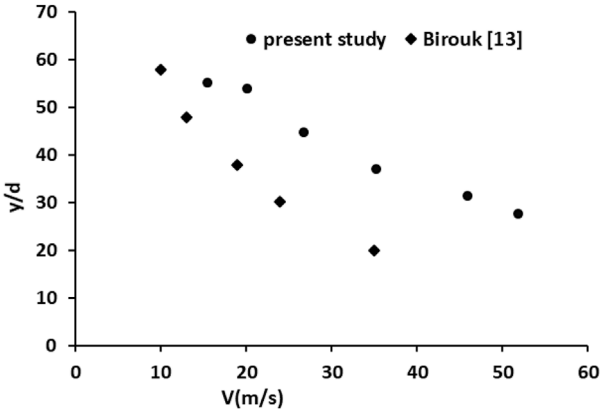

FIGURE 8
Effect of air velocity on liquid jet penetration.

surface of the jet column in the form of a liquid strip. Due to hydrodynamic instability, the liquid jet, which initially leaves the nozzle as a continuous column, becomes unstable along its length, leading to its eventual breakup into ligaments—a "column breakup." Subsequently, the separated liquid pieces along this trajectory transform into smaller droplets that enter the combustion chamber.

Figure 6 shows the injected fluid jet in the transverse airflow for circular nozzles. The overall process of the liquid jet breaking into the airflow and forming the spray in different nozzles is the same, and, depending on the geometry used, the length of penetration and breakup will be different.

Figure 7 shows the liquid jet trajectory for the geometry of different nozzles. In each geometry, liquid velocity, and the different air velocities, several photographs were taken at the time, with a total of 2,100 photographs. To better detect the boundaries of the liquid jet column and detect the breakup point, we took the average of photographs at the same conditions using MATLAB software (Supplementary Appendix SA).

Figure 8 illustrates the impact of transverse air velocity on the penetration depth of the liquid jet. It is evident from the figure that, as the air velocity quantified by the Weber number increases, the penetration depth of the liquid jet decreases. This is due to the increased drag force caused by the higher velocity, which prompts the liquid jet to deviate from its earlier path, resulting in a reduced penetration depth.

The observed change in penetration depth aligns with findings from other studies. However, it is important to note that this study differs from previous research regarding the fluid used, which is not oil. Additionally, the velocities employed in this study are distinct. The primary objective of this research is to examine how variations in transverse air velocity affect the penetration depth of

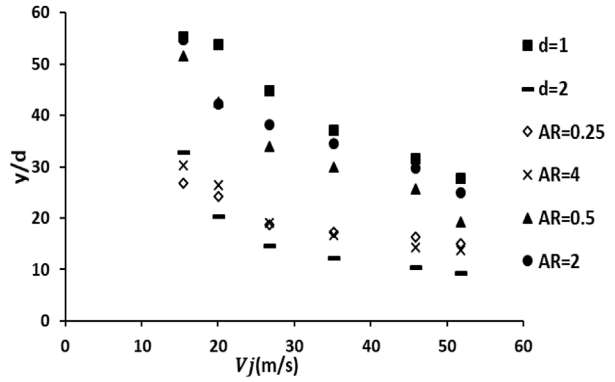

FIGURE 9
Effect of air velocity on liquid jet penetration for different nozzle geometry.

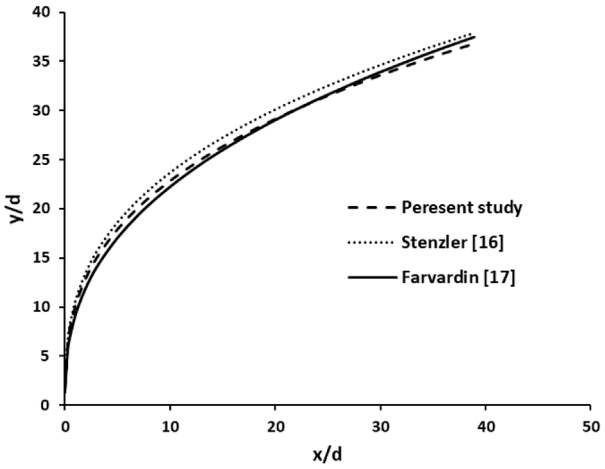

FIGURE 11
Liquid jet trajectory for a circular nozzle.

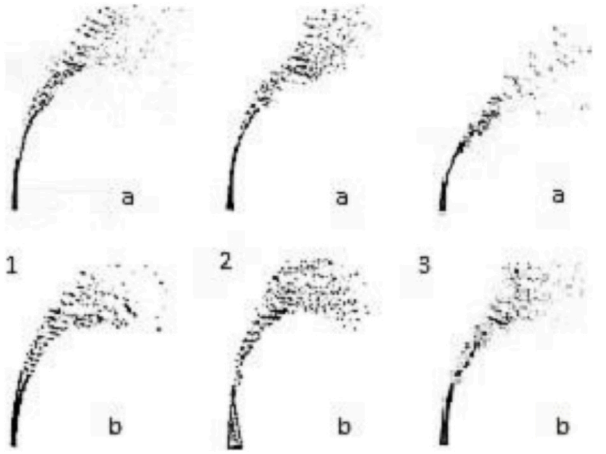

FIGURE 10
Effect of nozzle geometry on liquid jet penetration, 1. **(a)** AR= 4, **(b)** AR = 0.25; 2. **(a)** AR = 2, **(b)** AR = 0.5; 3. **(a)** d = 2 mm, **(b)** d = 1 mm.

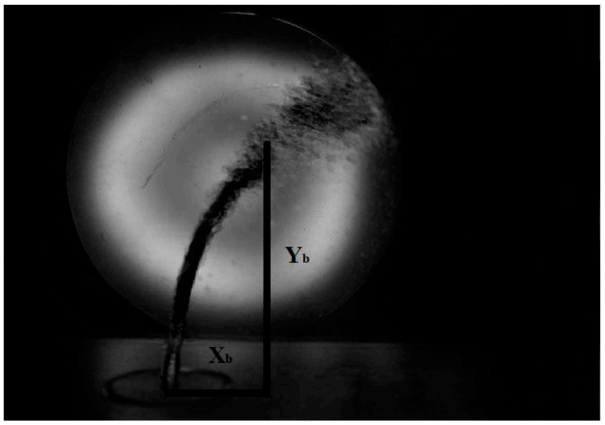

FIGURE 12
Length and height of breakup.

liquid jets, particularly when dealing with nozzles of different geometries.

In this research, two circular nozzles with diameters of 1 and 2 mm, two elliptical horizontal nozzles with a small diameter of 1 mm and large diameters of 2 and 4 mm, and two elliptical vertical nozzles with a small diameter of 1 mm and large diameters of 2 and 4 mm were used. Laboratory tests were first performed with a circular nozzle with a diameter of 1 mm, and then, a circular nozzle with a diameter of 2 mm was used. Oval nozzles performed another part of the laboratory tests. The results are shown in the following diagrams. As shown in Figure 9, the behavior of the liquid jet is the same for all nozzles, so the liquid jet penetration decreases with the increasing amount of transverse air velocity, assuming that other parameters are constant.

The impact of nozzle geometry on the penetration of the liquid jet can be studied while maintaining a constant Weber number and momentum ratio. Figure 10 demonstrates that the velocity of incoming air decreases for circular geometries with increasing diameter while holding the Weber number constant. Conversely, at a constant momentum ratio, the velocity of the inlet liquid increases due to the momentum ratio formula (q). With lower air velocity at a larger diameter, a reduced drag force is exerted on the liquid. The increased fluid velocity also results in higher momentum, leading to a greater penetration depth. Similar principles apply to elliptic nozzles, meaning that the penetration depth increases as the ratio of the larger to smaller diameters increases while keeping Weber's number and momentum ratio constant. When there are the same areas but with opposite dimensions, where the smaller diameter is aligned with the flow direction and the larger diameter is oriented perpendicularly to the transverse flow, it is evident that the penetration depth is greater. In cases where the minor diameter is aligned perpendicular to the transverse flow, the airflow encounters less surface area, resulting in reduced drag force on the liquid jet and, consequently, deeper penetration of the liquid jet.

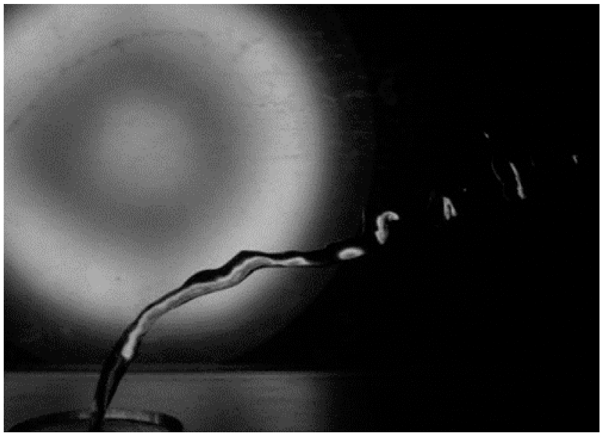

FIGURE 13
Column breakup.

Considering the upper boundary of the liquid jet trajectory for the circular nozzle, we can determine the equation of the liquid injection trajectory using linear regression. Considering the circular nozzle with a diameter of 1 mm, the equation of the liquid jet trajectory was obtained as follows:

$$\left(\frac{y}{d}\right) = 3.94\left(\frac{x}{d}\right)^{0.35} q^{0.33}. \tag{6}$$

As shown in Figure 11, the liquid-jet injection trajectory agrees very well with previous research, and the difference may be due to factors such as the experimental equipment, the difference between the momentum ratio, and Weber numbers.

Linear regression can also be used to obtain the elliptical nozzle injection trajectory. The direction equation for the elliptical nozzle is obtained as follows:

$$\left(\frac{y}{d_{eq}}\right) = 2.051\left(\frac{x}{d_{eq}}\right)^{0.34} q^{0.52}. \tag{7}$$

A specific diameter should be used to make the jet spray trajectory dimensionless and the diameter used in the Weber number into an elliptical nozzle. For this purpose, it should be considered equivalent to the following diameter:

$$d_{eq} = \sqrt{ab}, \tag{8}$$

where a is a large diameter, b is a small diameter oval, and d_{eq} is the equivalent diameter.

2.2 Length and height of breakup

As mentioned, two distinct breakup processes exist for liquid jets in transverse flow: surface and column breakup. The liquid forms a continuous column between the nozzle outlet and the breakup point. Determining the exact location of this breakup is crucial for modeling fluid jets in transverse airflow. However, obtaining a precise location can be challenging, primarily due to the presence of high-density droplets. As shown in Figure 12, the length of the breakup x_b and its height y_b are equal to the trajectory that the liquid jet passes in the trajectory of the transverse flow to break.

To determine the breakup length, it is necessary to identify the coordinates of the breakup point by examining various combinations of momentum ratios and Weber numbers for a given nozzle. This process allows for the derivation of relevant relationships. Interestingly, the difference in breakup length is minimal when considering various values of q and Weber numbers less than 10, essentially making it a constant value for these scenarios. Similarly, another constant value can be established for different q values and Weber numbers exceeding 10. As a result, we can derive the following fixed values for the breakup length:

$$\left(\frac{x_b}{d}\right) = 4.1 \pm 0.5we < 10$$
$$\left(\frac{x_b}{d}\right) = 10.3 \pm 0.6we < 10. \tag{9}$$

To obtain the height of the breakup, the height should be calculated by considering the momentum ratio and different Weber numbers. Then, the height of the breakup equation is obtained, which is as follows for the Weber number greater and smaller than 10:

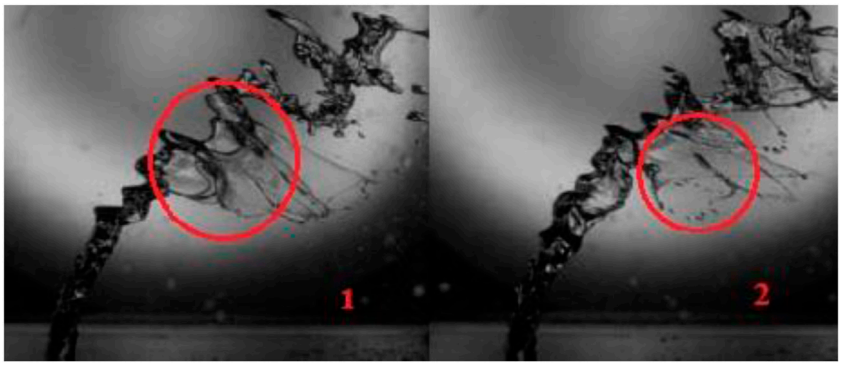

FIGURE 14
Bag breakup.

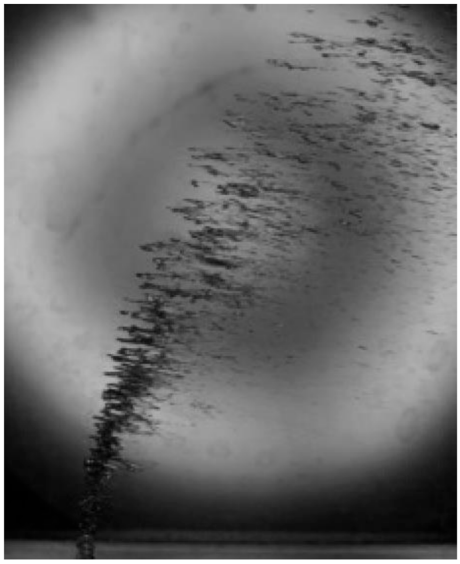

FIGURE 15
Multimode breakup.

$$\left(\frac{y_b}{d}\right) = 10.419\left(\frac{x}{d}\right)^{0.278} \quad we < 10$$
$$\left(\frac{y_b}{d}\right) = 4.77\left(\frac{x}{d}\right)^{0.387} \quad we < 10. \tag{10}$$

2.3 Breakup regimes

Much research (Mazallon et al., 1999; Sallam et al., 2004; Zhang et al., 2013; Song et al., 2017) has demonstrated that the Weber number influences the breakup pattern of a liquid jet. The initial phase in a liquid jet's breakup involves the formation of a strip-like ligament. The presence of vortices in the crossflow induces waves on the surface of the liquid column jet. These waves gradually grow, ultimately leading to the fragmentation of the liquid jet into ligaments. These separated segments are exposed to the dynamic air pressure, causing them to break into smaller droplets. This force leads to the dispersion of the liquid jet column, transforming it into a bean-like shape. The phenomenon where a liquid jet breaks into ligaments is commonly referred to as "column breakup" (Figure 13).

Another kind of breakup appears with the increase in the Weber number. In this kind of breakup, a hollow layer of liquid is formed as a bag shape. The time of its formation is brief because aerodynamic force overcomes surface tension, and bags change to small particles. The bag breakup is shown in Figure 14. In Part 1, bag breakup is produced and, in Part 2, changes to small particles.

The bag breakup has vanished to increase the Weber number, and small particles (much smaller than the nozzle diameter) are separated from the liquid column. This step combines a different kind of breakup called multimode breakup. In this regime, particles separate from the bottom part before the breakup because of increasing aerodynamic force (Figure 15).

As shown in Figure 16, the breakup pattern changes when increasing the Weber number while maintaining an equal momentum ratio and nozzle diameter. Specifically, Weber numbers 2, 16.6, and 62 are considered for different sections. At Weber number 2, the growth of surface instability is prolonged, allowing sufficient time for forming ligaments. In the case of Weber number 16.6, dynamic pressure increases, leading to the growth of waves on the liquid jet's surface and resulting in a "bag breakup". After a period, aerodynamic forces overcome surface tension, causing the bags to break and form small particles. These bags represent only a portion of the liquid jet, with the remainder transforming into ligaments or larger particles. With the Weber number increasing to 62, the aerodynamic forces applied to the column jet intensify. These forces surpass the surface tension in each segment, and particles separate from the jet's surface. In this scenario, bag breakup is minimal and quickly transitions into small particles. A comparison of these results with previous studies is presented in Table 2.

2.4 Error analysis

In this article, the variance method is used to obtain the uncertainty of the test results. Considering the w function as follows,

$$W = w(x_1, x_2, x_3, ..., x_n). \tag{11}$$

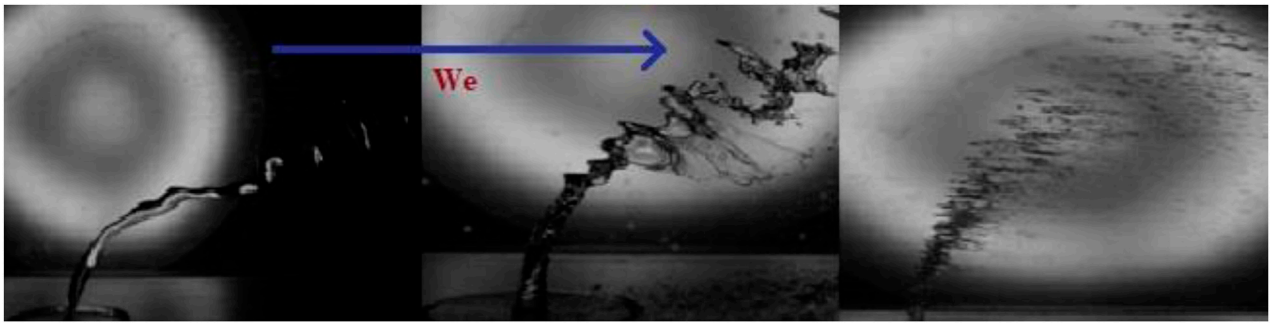

FIGURE 16
Breakup regimes based on the Weber number increase.

TABLE 2 Breakup regimes based on Weber's number.

Breakup regime	Mazallon et al. (1999)	Sallam et al. (2004)	Present study
Column breakup	5	4	4
Bag breakup	60	30	38
Multimode breakup	110	110	82

The error propagation for the function given in relation 11 is calculated using the variance method thus:

$$\delta(w) = \sqrt{\left[\frac{\partial(w)}{\partial(x_1)}\delta(x_1)^2\right] + \left[\frac{\partial(w)}{\partial(x_2)}\delta(x_2)^2\right] + \left[\frac{\partial(w)}{\partial(x_3)}\delta(x_3)^2\right] + \ldots} \tag{12}$$

In relation 11, all parameters from x_1 to x_n are independent of each other. Uncertainty about any of the parameters can result from systematic or inherent errors. For example, the liquid trajectory is obtained from Eq. 6. Using Eq. 11, the error expression for $\frac{y}{d}$ function can be expressed based on all other quantities.

$$\delta\left(\frac{y}{d}\right) = \left\{\left[\frac{\partial\left(\frac{y}{d}\right)}{\partial\left(\frac{x}{d}\right)}\delta\left(\frac{x}{d}\right)\right]^2 + \left[\frac{\partial\left(\frac{y}{d}\right)}{\partial(q)}\delta(q)\right]^2\right\}^{\frac{1}{2}}. \tag{13}$$

Now the error is obtained for each of the aforementioned sentences separately.

$$\delta\left(\frac{x}{d}\right) = \left\{\left[\frac{\partial\left(\frac{x}{d}\right)}{\partial(x)}\delta(x)\right]^2 + \left[\frac{\partial\left(\frac{x}{d}\right)}{\partial(d)}\delta(d)\right]^2\right\}^{\frac{1}{2}} \tag{14}$$

$$\delta\left(\frac{x}{d}\right) = \left\{\left[\frac{1}{d}\delta(x)\right]^2 + \left[\frac{-x}{d^2}\delta(d)\right]^2\right\}^{\frac{1}{2}}. \tag{15}$$

The momentum ratio error (Eq. 1) can be obtained from the following equation.

$$\delta(q) = \left\{\left[\frac{\partial(q)}{\partial(\rho_l)}\delta(\rho_l)\right]^2 + \left[\frac{\partial(q)}{\partial(\rho_g)}\delta(\rho_g)\right]^2 + \left[\frac{\partial(q)}{\partial(v_l)}\delta(v_l)\right]^2 + \left[\frac{\partial(q)}{\partial(v_g)}\delta(v_g)\right]^2\right\}^{\frac{1}{2}}. \tag{16}$$

After derivation from relationship q and placing it in the aforementioned equation, we derive a relation as follows.

$$\delta(q) = \left\{\left[\frac{v_l^2}{\rho_g v_g}\delta(\rho_l)\right]^2 + \left[\frac{-\rho_l v_l^2}{\rho_g^2 v_l^2}\delta(\rho_g)\right]^2 + \left[\frac{\rho_l v_l}{\rho_g v_g^2}\delta(v_l)\right]^2 + \left[\frac{\rho_l v_l^2}{\rho_g v_g^3}\delta(v_g)\right]^2\right\}^{\frac{1}{2}}. \tag{17}$$

In the aforementioned relationship, v_g is the gas or air velocity obtained using a speedometer. The liquid velocity is obtained from the following equation:

$$Q = \frac{v}{t} = \frac{\pi}{4} \times d^2 \times v_l \Rightarrow v_l = \frac{4v}{\pi d^2 t}. \tag{18}$$

The liquid velocity error can be obtained thus:

$$\delta(v_l) = \left\{\left[\frac{4}{\pi d^2 t}\delta(v)\right]^2 + \left[\frac{-8v}{\pi d^3 t}\delta(d)\right]^2 + \left[\frac{-4v}{\pi d^2 t^2}\delta(t)\right]^2\right\}^{\frac{1}{2}}. \tag{19}$$

To obtain the approximate error for Eq. 11, it is necessary to know the error of each of the primary quantities. All errors are shown in Table 3.

TABLE 3 Error percentage.

	Error percentage (%)
$\delta\left(\frac{x}{d}\right)$	0.11
$\delta(\rho_l)$	0
$\delta(\rho_g)$	2
$\delta(v_l)$	5
$\delta(v_g)$	2

Considering the aforementioned error values, the error value $\frac{y}{d}$ is 2%. Similarly, the error can be obtained in each step (Zhang et al., 2013).

3 Conclusion

Jet cross-injection, due to proper atomization and high evaporation rate, is one of the most advanced methods for a fuel injection system, and its study is of great importance due to its extensive application in various industries. This paper investigated the effect of nozzle geometry on a liquid jet trajectory, and the trajectory equation was obtained for circular and elliptic jets. The following summary results were obtained.

- By increasing the circular nozzle diameter, the penetration depth increases. For example, we take into account the drag force for a 2-mm and a 1-mm-diameter nozzle, considering that the wetted cross-sectional area for calculating the drag force is proportional to the nozzle diameter and that the gas velocity squared power for the 2 mm nozzle is twice that of the 1 mm nozzle. Consequently, the drag force remains unchanged when the nozzle cross-sectional area increases. On the other hand, for the momentum produced by the liquid jet, since momentum is related to the cross-sectional area and the inlet velocity of the nozzle, the inlet velocity becomes $\frac{\sqrt{2}}{2}$ times lower, but the area becomes four times larger, resulting in $2\sqrt{2}$ times the total momentum. Now, because the momentum is greater, the penetration is also greater.
- The penetration depth in the elliptic nozzle increases as the aspect ratio increases. Increasing the ratio of the larger to smaller diameters in a given Weber number and a specified momentum ratio results in greater liquid jet penetration; this applies similarly to a circular nozzle. As the area ratio increases while keeping the Weber number constant, the drag force for an area ratio of 2 is equal to the drag force for an area ratio of 4. On the other hand, the momentum force increases because the

area doubles and the velocity doubles. As a result, with the increased momentum force and decreased back pressure, the penetration depth also increases.
- The penetration depth decreases with increasing transverse air velocity for both circular and elliptical nozzles.
- For different momentum ratios and Weber numbers, the breakup length is almost constant, and the breakup height is related to the momentum ratio, which is different for Weber numbers less than and more than 10.

Data availability statement

The raw data supporting the conclusion of this article will be made available by the authors, without undue reservation.

Author contributions

All authors listed have made a substantial, direct, and intellectual contribution to the work and approved it for publication.

Conflict of interest

The authors declare that the research was conducted in the absence of any commercial or financial relationships that could be construed as a potential conflict of interest.

Publisher's note

All claims expressed in this article are solely those of the authors and do not necessarily represent those of their affiliated organizations, or those of the publisher, the editors, and the reviewers. Any product that may be evaluated in this article, or claim that may be made by its manufacturer, is not guaranteed or endorsed by the publisher.

Supplementary material

The Supplementary Material for this article can be found online at: https://www.frontiersin.org/articles/10.3389/fmech.2023.1207894/full#supplementary-material

References

Ashgriz, N. (2011). *Handbook of atomization and sprays*. New York, NY, USA: Springer, 657–665.

Bai, B., Zhang, H., Liu, L., and Sun, H. J. (2009). Experimental study on turbulent mixing of spray droplets in crossflow. *Exp. Therm. Fluid Sci.* 33, 1012–1020. doi:10.1016/j.expthermflusci.2009.05.002

Bellofiore, A., Cavaliere, A., and Ragucci, R. (2007). Air density effect on the atomization of liquid jets in crossflow. *Combust. Sci. Technol.* 179, 319–342. doi:10.1080/00102200600809563

Birouk, M., Iyogun, C. O., and Popplewell, N. (2007). Role of viscosity on trajectory of liquid jets in a cross-airflow. *Atomization Sprays* 17 (3), 267–287. doi:10.1615/atomizspr.v17.i3.30

Cerri, G., Giovannelli, A., Battisti, L., and Fedrizzi, R. (2007). Advances in effusive cooling techniques of gas turbines. *Appl. Therm. Energy* 27, 692–698. doi:10.1016/j.applthermaleng.2006.10.012

Farvardin, E., Johnson, M., Alaee, H., Martinez, A., and Dolatabadi, A. (2013). Comparative study of biodiesel and diesel jets in gaseous crossflow. *J. Propuls. Power* 29 (6), 1292–1302. doi:10.2514/1.b34743

Gurevich, A. Y., Goman, M. G., Gurevich, Y. G., and Lopez, A. M. (2018). Synthetic turbulence modeling for evaluation of ultrasonic cross-correlation flow measurement. *Flow Meas. Instrum.* 60, 134–143. doi:10.1016/j.flowmeasinst.2017.12.013

Iyogun, C. O., Birouk, M., and Popplewell, N. (2006). Trajectory of water jet exposed to low subsonic crossflow. *Atomization Sprays* 16 (8), 963–980. doi:10.1615/atomizspr.v16.i8.70

Jalili, B., and Jalili, P. (2023). Numerical analysis of airflow turbulence intensity effect on liquid jet trajectory and breakup in two-phase cross flow. *Alexandria Eng. J.* 68 (2023), 577–585. doi:10.1016/j.aej.2023.01.059

Keramaris, E., and Pechlivanidis, G. (2020). Boundary effects of vertical buoyant jets in a stagnant fluid in a crossflow. *Exp. Tech.* 44 (2), 149–158. doi:10.1007/s40799-019-00320-4

Lakhamraju, R. R. (2003). *Liquid jets in subsonic airstream at elevated temperatures*. PhD Thesis. Ohio, OH, USA: University of Cincinnati.

Li, S., Wu, J., and Ma, F. (2022). Choking flow characteristics of the rectangular slot-type flip bucket. *Exp. Tech.* 47, 211–222. doi:10.1007/s40799-021-00532-7

Mazallon, J., Dai, Z., and Faeth, G. M. (1999). Primary breakup of nonturbulent round liquid jets in gas crossflows. *At. Sprays* 9, 291–312. doi:10.1615/atomizspr.v9.i3.40

Niu, H., Yi, S., Liu, X., Huo, J., and Zheng, W. (2022). Experimental study of hypersonic traveling crossflow instability over a yawed cone. *Acta Astronaut.* 193, 173–181. doi:10.1016/j.actaastro.2021.12.016

Sallam, K. A., Aalburg, C., and Faeth, G. M. (2004). Breakup of round nonturbulent liquid jets in gaseous crossflow. *AIAA J.* 42, 2529–2540. doi:10.2514/1.3749

Song, Y., Hwang, D., and Ahn, K. (2017). "Effect of orifice geometry on spray characteristics of liquid jet in crossflow," in Proceedings of the 55th AIAA Aerospace Sciences Meeting, Grapevine, Texas, USA, January, 2017.

Stenzler, J., Lee, J., Santavica, D., and Lee, W. (2006). Penetration of liquid jets in a crossflow. *Atomization Sprays* 16 (8), 887–906. doi:10.1615/atomizspr.v16.i8.30

Ukamanal, M., Mishra, P. C., and Sahoo, A. K. (2020). Effects of spray cooling process parameters on machining performance AISI 316 steel: a novel experimental technique. *Exp. Tech.* 44 (1), 19–36. doi:10.1007/s40799-019-00334-y

Wang, Q., Mondragon, U. M., Brown, C. T., and McDonell, V. G. (2011). Characterization of trajectory, break point, and break point dynamics of a plain liquid jet in a crossflow. *Atomization Sprays* 21 (3), 203–219. doi:10.1615/atomizspr.2011002848

Wen, J., Hu, Y., Nakanishi, A., and Kurose, R. (2020). Atomization and evaporation process of liquid fuel jets in crossflows: a numerical study using Eulerian/Lagrangian method. *Int. J. Multiph. Flow* 129, 103331. doi:10.1016/j.ijmultiphaseflow.2020.103331

Zhang, H., Bai, B., Liu, Li, Sun, H., and Yan, J. (2013). Experimental study of the mixing of two impinging pressure-swirl sprays in crossflow. *Exp. Therm. fluid Sci.* 49, 67–74. doi:10.1016/j.expthermflusci.2013.04.002

frontiers | Frontiers in Mechanical Engineering

TYPE Original Research
PUBLISHED 22 November 2023
DOI 10.3389/fmech.2023.1290074

OPEN ACCESS

EDITED BY
Farschad Torabi,
K. N. Toosi University of Technology, Iran

REVIEWED BY
Ebrahim Afshari,
University of Isfahan, Iran
Hossein Afshar,
Islamic Azad University, Iran

*CORRESPONDENCE
Soheila Abdolahipour,
sabdolahi@ari.ac.ir

RECEIVED 06 September 2023
ACCEPTED 07 November 2023
PUBLISHED 22 November 2023

CITATION
Abdolahipour S (2023), Effects of low and high frequency actuation on aerodynamic performance of a supercritical airfoil.
Front. Mech. Eng 9:1290074.
doi: 10.3389/fmech.2023.1290074

Effects of low and high frequency actuation on aerodynamic performance of a supercritical airfoil

Soheila Abdolahipour*

Aerospace Research Institute, Ministry of Science, Research, and Technology, Tehran, Iran

The main objective of this study is to investigate the effects of low and high frequency actuation in improving the aerodynamic performance of the supercritical airfoil with the approach of using it in a high-lift or flight control device. For this purpose, a flow control numerical simulation is performed on a supercritical airfoil with NASA SC(2)-0714 cross section using a pulsed jet at the chord-based Reynolds number of 1×10^6. The pulsed jet actuation with different reduced frequencies of 0.2, 1, 1.2, 2.4, 4, 6, and 12 is implemented on the upper side of the airfoil surface upstream of the separation point of the uncontrolled case. The aerodynamic efficiency improvements are investigated by extracting the results of time-averaged and instantaneous aerodynamic forces for all cases. The study compares the flow streamline, Q-criterion contour, and surface pressure distribution to examine how the separated flow configuration over the airfoil responds to different actuation frequencies. The results indicate that pulsed jet actuation effectively postpones the flow separation. A comparison of the time-averaged aerodynamic coefficients at different actuation frequencies revealed that utilizing a low actuation frequency range maximizes lift, while a high frequency range minimizes drag. In addition, the aerodynamic efficiency of the supercritical airfoil improves across all controlled scenarios, with the optimal increase in aerodynamic efficiency of 28.62% achieved at an actuation frequency of $F^+ = 1$.

KEYWORDS

flow control, pulsed jet actuator, actuation frequency, aerodynamic performance, vortex dynamics, reduced frequency, vorticity, supercritical airfoil

1 Introduction

Flow control techniques for lifting surfaces have largely concentrated on reducing or eliminating flow separation, which is usually induced by an adverse pressure gradient. All separation control strategies aim to increase the momentum content of the boundary layer flow, allowing it to cope with stronger adverse pressure gradients than would be naturally possible. Depending on the flow control strategy, different physical mechanisms are considered to achieve the desired results. In fluidic actuators, the flow control strategy is classified into steady (Radespiel et al., 2016) and unsteady (McManus et al., 1995; Sheikholeslam Noori et al., 2021) methods based on whether momentum or mass flux is added continuously or periodically. In the steady method, fluid with high momentum and energy is continuously injected into the boundary layer. Thus, achieving the desired result requires a considerable amount of mass and momentum. In contrast, unsteady actuation produces vortical structures in the flow that increase the mixing rate throughout the flow field (Wu et al., 1998). As a result, the turbulence mixing is improved and the momentum is

more efficiently transferred between high-momentum region in the cross-flow and low-momentum region near the wall (Greenblatt and Wygnanski, 2000). It is noteworthy that flow control with unsteady actuation is based on the phenomenon of natural flow instability, which has the potential to reduce the mass flux requirement and enhance flow control efficiency (Bernardini et al., 2014). Therefore, unsteady flow control has been widely considered due to the lower power and momentum requirements compared to the steady flow control method. In unsteady flow control, several parameters affect the separation control on lifting surfaces, including geometric and physical parameters (Bauer, 2015; Hipp et al., 2016) of the main flow (Seifert et al., 2004; Haucke and Nitsche, 2013; Wild, 2015) and the actuation system (Stalnov and Seifert, 2010; Taleghani et al., 2012; Hecklau et al., 2013; Feero et al., 2017; Munday and Taira, 2018; Walker et al., 2018).

One of the most important parameters of unsteady actuation is the actuation frequency. The actuation frequency is usually presented as a reduced frequency F^+, which is defined as $F^+ = fL/V$ where f is the actuation frequency, V is the freestream velocity, and L is the length scale of the flow domain. Different frequency ranges were identified for maximum control effect depending on the physical flow control mechanism used in the flow (Mirzaei et al., 2012; Mohammadi and Taleghani, 2014; Sheikholeslam Noori et al., 2020; Taeibi et al., 2022). The literature has reported that the strategy of coupling periodic actuation with natural flow unsteadiness improves flow control efficiency significantly. However other works have demonstrated that aerodynamic efficiency can be improved over a much wider range of actuation frequencies that are at least an order of magnitude higher than the natural shedding frequencies in separated shear layer (Glezer et al., 2005).

Some previous studies have shown that the optimal separation control can be achieved by utilizing actuation frequencies within the range of natural instability frequencies found in the separated shear layer. The flow over the lifting surfaces is usually characterized by two dominant natural instabilities depending on the angle of attack. At low angles of attack when the flow attaches over the lifting surface, vortex shedding in the wake is dominant. At high angles of attack when flow separation is severe, the flow is characterized by roll-up vortices in the shear layer and large scale vortex shedding in the separated wake (Boutilier and Yarusevych, 2012; Feero, 2018). Wu et al. (1998) performed a numerical simulation of separation control on NACA-0012 airfoil using a local unsteady excitation located near the leading edge at post-stall angles of attack and Reynolds number 5×10^5. They found that the effective actuation frequency range at post-stall angles of attack 20–30° was about 0.3–2.0 times the natural shedding frequency. Duvigneau and Visonneau (2006) used 2D unsteady Reynolds-averaged Navier–Stokes equations to simulate aerodynamic stall control through a synthetic jet actuator located at the leading edge of a NACA 0015 airfoil at Reynolds number 8.96×10^5. They utilized the automatic optimization of the control parameters to maximize the lift enhancement at angles of attack between 12 and 24°. They found that the optimal lift enhancement was obtained at $F^+ = 0.85$ for all angles of attack in the range of 14–20° and $F^+ = 0.25$ for angles of attack 22. For the same configuration and Reynolds number, You and Parviz (2008) conducted a 3D LES study. They reported that the unsteady actuation on the airfoil at an angle of attack of 16.6°, can increase lift up to 70% when $F^+ = 1.284$. The separation control on a NACA-0015 airfoil was also experimentally studied at Reynolds number 3×10^4 and angle of attack of 18° (Tuck and Soria, 2008; Buchmann et al., 2013). The results indicated that maximum lift can be obtained by actuation frequency at the range of vortex shedding frequency in the separated wake $F^+ = 0.65$ and its superharmonic $F^+ = 1.3$.

Glezer et al. (2005) proposed a novel method to control separation on an airfoil through fluidic modifications of the apparent aerodynamic shape, aiming to alter the pressure gradient to reduce or eliminate separation. They utilized actuation frequencies significantly higher than those of natural vortex shedding. In this approach, the high actuation frequency ensures that the interaction between the unsteady actuation and the crossflow is perceived as a time-invariant phenomenon within the flow's timescale. Therefore, the interaction area over the surface produces a displacement of the crossflow that induces a virtual change in the shape of the surface and alters the streetwise pressure gradient over the airfoil. All of the modifications can lead to mitigation or elimination of boundary layer separation. Glezer et al. (2005) employed this control approach to study the flow field of a stalled airfoil and circular cylinder that undergo boundary layer separation. Yarusevych and Kotsonis (2017) investigated the response of a laminar separation bubble to excitation with low and high frequencies in the range of $2 \leq F^+ \leq 10$ and $F^+ = 100$ at $Re = 1.3 \times 10^5$. The study findings indicated that the greatest impact on the average decrease in the size of the laminar separation bubble occurred at $F^+ = 6$. Several researchers have studied the role of actuation frequency in separation control over a stalled airfoil. Their investigations showed the flow reattachment and the aerodynamic performance improvement on an airfoil for both high and low reduced frequency $F^+ = O(1)$ and $F^+ = O(10)$ (Amitay and Glezer, 2002a; Amitay and Glezer, 2002b; Glezer, 2011; Salmasi et al., 2013; Feero et al., 2015; Taleghani et al., 2018).

A review of literature reveals that the use of pulsed jet actuators to actively control flow separation over airfoils and wings has been a developing topic for several decades. In recent years, pulsed jet actuators have been widely utilized as flow separation control techniques to enhance the aerodynamic performance of high-lift devices in short take-off and landing (STOL) transportation airplanes (Abdolahipour et al., 2022a; Abdolahipour et al., 2022b). This method allows for an increase in aerodynamic efficiency of wings by eliminating the need for airfoil profile geometry changes or additional complex and heavy components. In addition, flow control can be utilized to offset the decreased aerodynamic efficiency of the damaged wing (Abdolahipour et al., 2007; Abdolahipour et al., 2011). Despite significant advancements in pulsed jet flow control methods over an aircraft's wing, this technology has not yet been utilized in civil aircraft due to insufficient control power for effective operation. Most studies examining the impact of different parameters on enhancing the performance of pulsed jet flow control have focused on airfoils used in low Reynolds number flows. For effective implementation of this flow control technology in airplane wings for practical and industrial purposes, it is crucial to conduct further studies on airplane wing sections operating in Reynolds numbers similar to real flight conditions. The aforementioned studies pointed out the lack of data available on this issue. Considering this research gap, this study

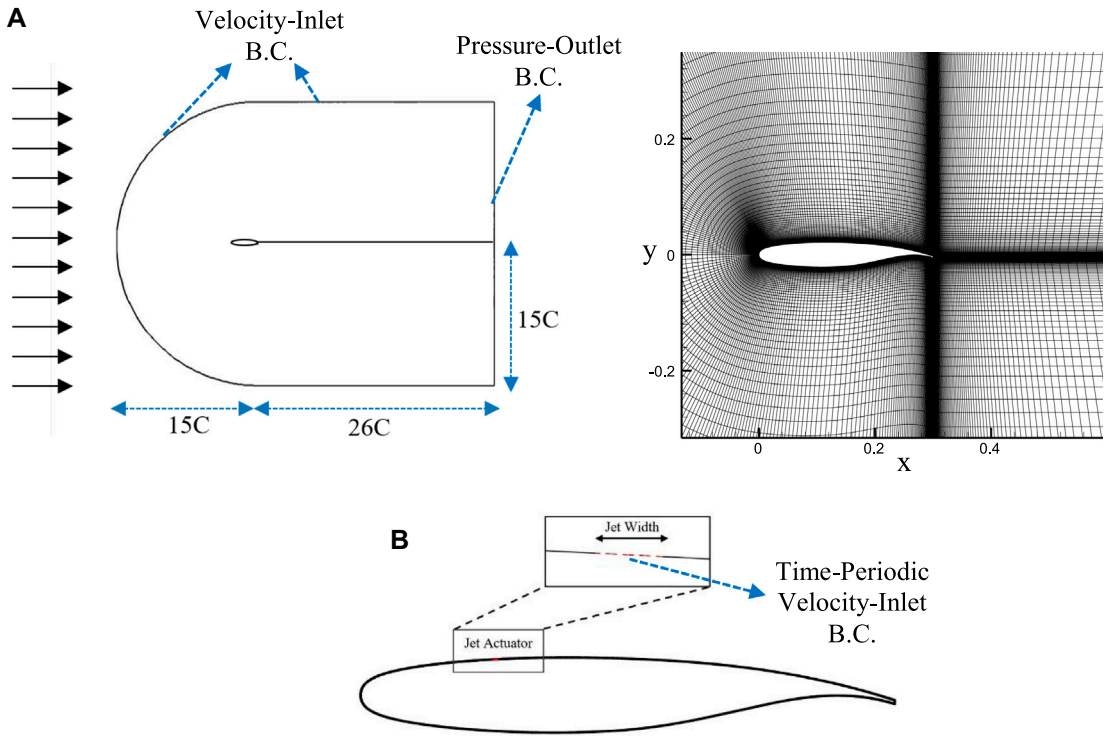

FIGURE 1
Schematic of **(A)** the physical model and the computational domain **(B)** the pulsed jet actuator on the model.

is an attempt to investigate the effect of actuation frequency on the actively controlling separation from the shoulder of a supercritical airfoil at incompressible high Reynolds number. The purpose of this study is to provide information about the substantially different responses of a separated flow over a supercritical airfoil to different ranges of actuation frequency from $F^+ = 0.2$ to 12. The results include time-averaged and instantaneous aerodynamic force coefficients, streamlines, vorticity contour, and pressure distribution generated through a numerical simulation. Subsequently, a comparison was made between the results.

2 Physical model and numerical methodology

The model used in this study is a supercritical airfoil with NASA SC(2)-0714 cross-section, which is numerically simulated in turbulent flow with Reynolds number 1×10^6 based on chord length. This investigation is provided at angle of attack of 16° as a situation of configuration near the stall condition. Figure 1 shows the geometry of the C-type computational domain around the airfoil discretized by a structured grid. After conducting the grid independence study, the total number of cells was considered to be about 47,000. The mesh quality near the wall is such that Y^+ is calculated within a range of 1. The velocity-inlet and pressure-outlet are considered as boundary conditions for the computational domain.

As shown in Figure 1, the pulsed jet actuator is modeled as a gap with a width of 0.002 m on the upper surface of the airfoil at 25% of the chord location upstream of the mean separation point. The curvature of the surface at the point where the actuator exits and intersects with the airfoil demonstrates a discontinuity. The pulsed air jet is simulated by the time-periodic velocity boundary condition at the exit of the actuator with an angle of 25° to the *x*-axis. The pulsed jet velocity changes from zero (jet-off) to the maximum value of 120 m/s (jet-on) as a square wave by duty cycle of 50% and specified actuation frequency. Therefore, an actuation cycle consists of two phases; the blowing phase (jet-on) from t/T = 0 to t/T < 0.5 and the closing phase (jet-off) from t/T = 0.5 to t/T < 1. The maximum jet velocity of 120 m/s is selected in the range of data obtained from the experiments of a solenoid valve actuator (Abdolahipour et al., 2021). The actuation reduced frequency is set to low values of $F^+ = 0.2$, 1, and 1.2 and high values of $F^+ = 2.4$, 4, 6, and 12.

In this numerical simulation, an approach based on solving unsteady two-dimensional Reynolds-averaged Navier–Stokes (URANS) equations was used. The governing equations including mass (Eq. 1) and momentum (Eq. 2) are considered as follows.

$$\frac{\partial u_j}{\partial x_j} = 0 \tag{1}$$

$$\frac{\partial u_i}{\partial t} + \frac{\partial}{\partial x_j}\left(u_i u_j\right) = -\frac{1}{\rho}\frac{\partial P}{\partial x_i} + \frac{\partial}{\partial x_j}\left[\upsilon\left(\frac{\partial u_i}{\partial x_j} + \frac{\partial u_j}{\partial x_i}\right)\right] + \frac{\partial}{\rho \partial x_j}\left(-\rho \acute{u_i} \acute{u_j}\right) \tag{2}$$

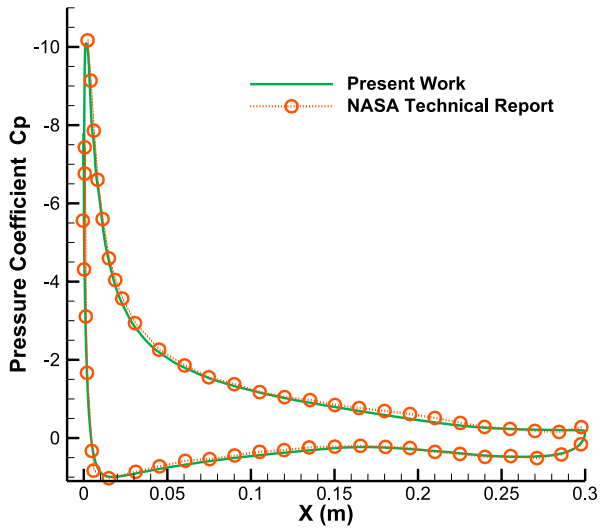

FIGURE 2
Comparing the pressure coefficients on the airfoil surface obtained from numerical analysis and NASA wind tunnel experiments (NASA Technical Memorandum 81912, 2013) in a flow with Reynolds number of 2 × 10^6 and AOA = 16°.

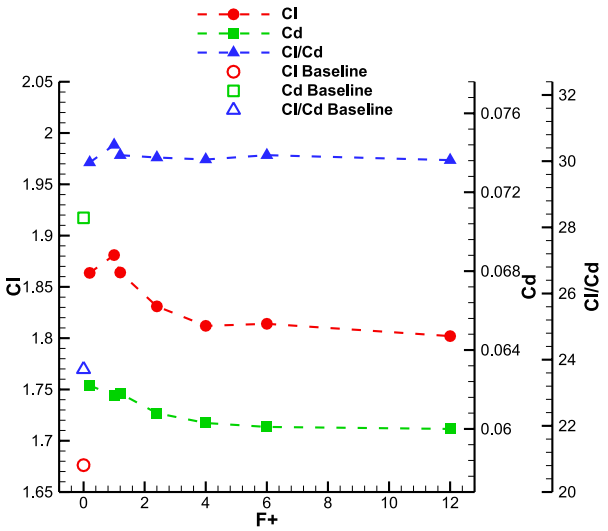

FIGURE 3
Variation of time-averaged aerodynamic forces for different actuation frequencies at AOA = 16°.

TABLE 1 Comparing the lift coefficients of the airfoil obtained from numerical analysis and NASA wind tunnel experiments (NASA Technical Memorandum 81912, 2013) in a flow with Reynolds number of 2 × 10^6.

AOA	Present work	NASA technical report (NASA Technical Memorandum 81912, 2013)
14°	1.7560	1.7784
16°	1.8033	1.8417
17.76°	0.954	0.9699

The equations are solved by using the pressure-based method and a second-order accurate numerical technique. The flow is considered viscous, incompressible, and turbulent in which κ-ω sst model has been used for turbulence modeling. The time step size is 2.0 × 10^{-5} in all simulations reported here. This time step size is chosen based on the time independence of the aerodynamic coefficients.

To validate the numerical simulation in this study, the results of the numerical analysis were compared with the data provided in the NASA technical report for the baseline case (NASA Technical Memorandum 81912, 2013). The aerodynamic characteristics described in this report are derived from model tests conducted at the wind tunnel with Reynolds 2 × 10^6. To ensure precision, the numerical solution was also performed in the validation phase at a free flow velocity of 100 m/s, which corresponds to Reynolds 2 × 10^6. Figure 2 presents the comparison of the pressure coefficient distribution on the airfoil surface from the numerical solution results and the wind tunnel results (NASA Technical Memorandum 81912, 2013) in the Reynolds 2 × 10^6 at the angle of attack of 14°. Table 1 presents a comparison of the lift coefficients obtained from the numerical solution and the wind tunnel test. The results indicate high accuracy.

3 Results

Pulsed jet actuation applied upstream of the mean separation point on the supercritical airfoil at high angle of attack results in notable enhancements in the airfoil's aerodynamic characteristics. Figure 3 displays the time-averaged aerodynamic force coefficients for both the baseline and actuated scenarios at an angle of attack of 16°. Upon initial examination, the data from all actuated cases show that the pulsed jet actuator significantly improves lift and aerodynamic efficiency and reduces drag compared to the baseline case. As shown, the highest time-averaged lift of 1.88 is achieved in the actuated case with F^+ = 1, which is an increase of 12.2% compared to the baseline case. As the frequency of actuation increases up to F^+ = 4, the lift that can be achieved decreases to 1.81 and then remains almost constant for higher actuation frequencies. Similarly, this trend is also observed for the drag coefficient, so that by increasing the actuation frequency up to F^+ = 12, the drag value decreases from 0.070 to 0.059 (a decrease of 15.7% compared to the baseline case). Slight variations in aerodynamic coefficients are observed between actuation frequencies F^+ = 4 and F^+ = 12. As a result of these variations in the lift and drag coefficients, the aerodynamic efficiency varies slightly among all actuation frequencies. However, the largest aerodynamic efficiency increase of 28.62% occurs at F^+ = 1.

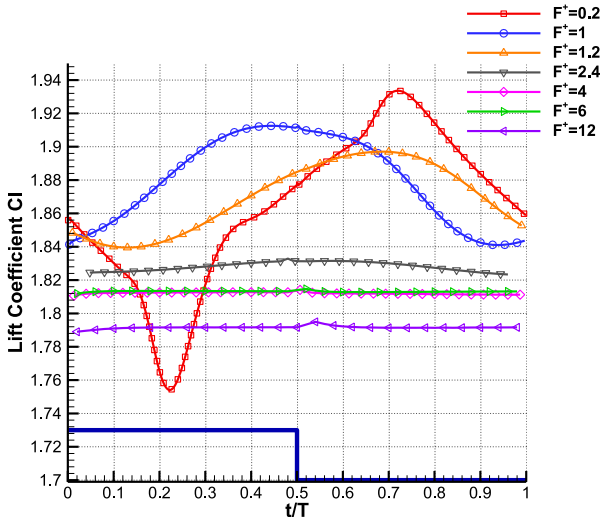

FIGURE 4
Temporal evolution of the lift coefficient during an actuation cycle at different reduced frequencies, AOA = 16° (The sketch of the corresponding actuation cycle is shown by the solid line and its amplitude is not in scale).

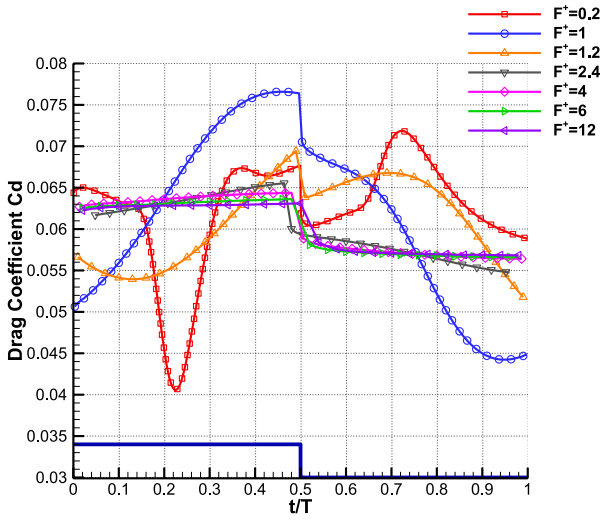

FIGURE 5
Temporal evolution of the drag coefficient during an actuation cycle at different reduced frequencies, AOA = 16° (The sketch of the corresponding actuation cycle is shown by the solid line and its amplitude is not in scale).

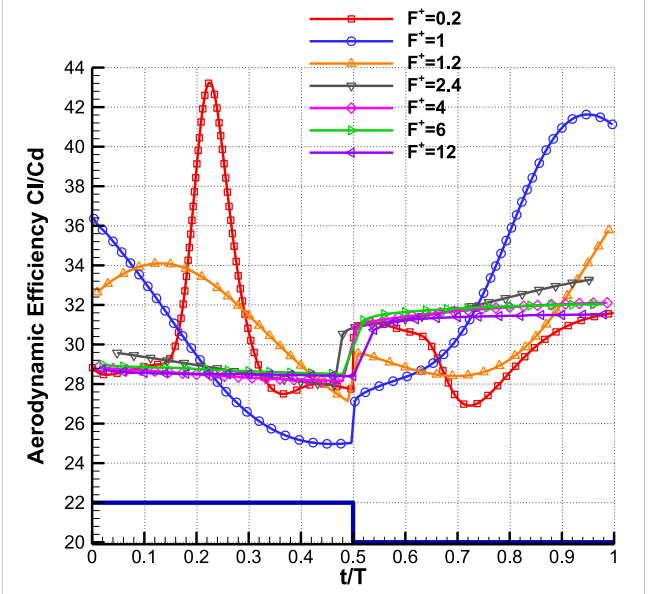

FIGURE 6
Temporal evolution of the aerodynamic efficiency during an actuation cycle at different reduced frequencies, AOA = 16° (The sketch of the corresponding actuation cycle is shown by the solid line and its amplitude is not in scale).

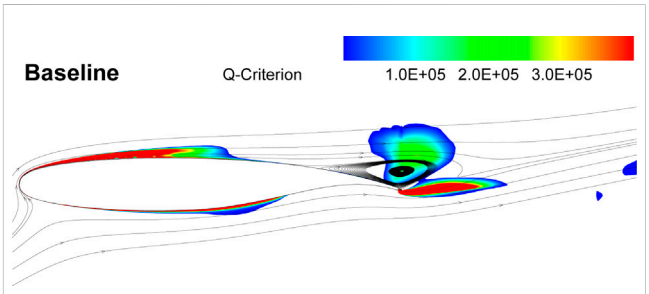

FIGURE 7
Streamlines and Q-criterion contour for baseline case at AOA = 16°.

Figures 4–6 show the evolution of the aerodynamic coefficients of the airfoil during a single cycle of pulsed jet actuation at various actuation frequencies. In these figures, the jet-on and jet-off phases of the pulsed jet actuation are sketched by solid line. The data show that pulsed jet actuation at different reduced frequencies significantly improves lift and aerodynamic efficiency compared to baseline, even in the jet-off phase of the actuation cycle. At the beginning of the jet-off phase, a sudden drop in drag value is observed at all actuation reduced frequencies. This drag is related to the presence of the jet actuator in the flow, which disappears when the jet is turned off. The main point of interest in these data is a fundamental difference in aerodynamic coefficient variations observed between the low and high-frequency actuation approaches. As can be seen in Figures 4, 5, the flow actuations with low frequencies of $F^+ = 0.2$, 1, and 1.2 produce time-dependent aerodynamic forces that oscillate around the mean values. Whereas, high frequencies of $F^+ = 2.4$, 4, 6, and 12 generate almost time-invariant aerodynamic forces during each phase in a cycle.

For the reduced frequency of $F^+ = 0.2$, after the onset of the actuation, the lift and drag coefficients follow a reduction trend until they reach minimum values at t/T = 0.22 and then start to increase. In the second phase, when the actuator is turned off, both the lift and drag forces maintain their increasing trend (except for the turn-off point, where a sharp drop in drag coefficient is seen). In almost the last quarter of the actuation cycle, the lift and drag forces start to

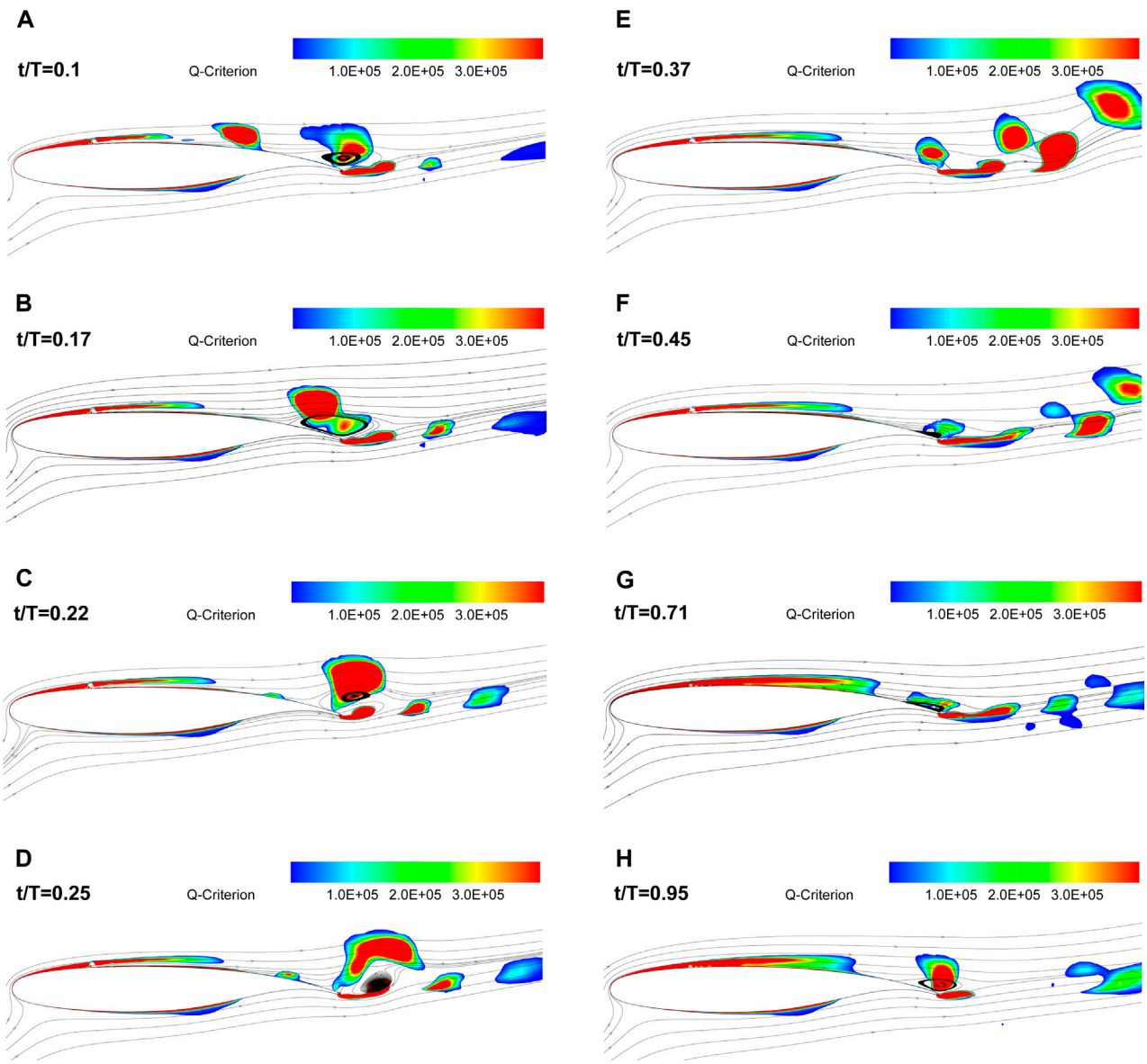

FIGURE 8
The evolution of the streamlines and Q-criterion for the actuated case at AOA = 16° with reduced frequency of F^+ = 0.2 at different time instants in an actuation cycle, t/T= (A) 0.1, (B) 0.17, (C) 0.22, (D) 0.25, (E) 0.37, (F) 0.45, (G) 0.71, (H) 0.95.

decrease again and create a maximum value at t/T = 0.72. Actuation frequency of F^+ = 0.2 greatly increases the rate of the aerodynamic forces variation during one cycle compared to reduced frequencies of F^+ = 1 and 1.2. The highest value of lift and the lowest value of drag both occurred at an actuation frequency of F^+ = 0.2. Upon closer inspection, it appears that the oscillation of lift and drag forces gradually subsides as the reduced frequency increases. For high reduced frequencies ranging from F^+ = 2.4 to 12, the lift and drag coefficients display similar variations throughout each cycle. Particularly, the lift coefficient remains quasi-time-invariant, and the drag coefficient changes slightly during each jet-on and jet-off phase. Meanwhile, as previously shown in Figure 3, the time-averaged values of the aerodynamic forces for all reduced frequencies are still improved compared to the baseline case with increased lift and reduced drag. To elucidate the reason why different actuation frequencies produce different force variations during a cycle, a coupled analysis of the vorticity field, streamlines, and pressure distribution around the airfoil is provided below.

Figure 7 shows the streamlines and specified Q-criterion contour for the baseline case at angle of attack of 16°. The Q-criterion identifies vortices as areas where the vorticity magnitude surpasses the strain rate magnitude. The presence of an adverse pressure gradient causes separation of the turbulent flow over the airfoil's suction side in the last third of the chord, as evident from the streamlines. This flow separation is characterized as a reverse flow with a low-velocity region.

Figure 8 shows the evolution of the streamline and Q-criterion for the actuated case with a reduced frequency of F^+ = 0.2 at various time instances during one actuation cycle. The analyzed phases in Figure 8 are represented by the time evolution of the lift increment in Figure 9

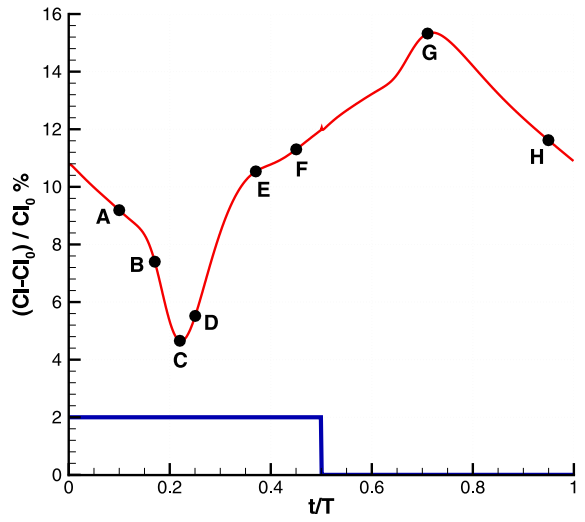

FIGURE 9
The instants from (A-H) are represented on the time evolution of the lift increment for the reduced frequency of $F^+ = 0.2$ (The sketch of the corresponding actuation cycle is shown by solid line and its amplitude is not in scale).

between the controlled airfoil and the baseline case. As explained earlier, an actuation cycle consists of two phases; the blowing phase (jet-on) from t/T = 0 to t/T < 0.5 and the closing phase (jet-off) from t/T = 0.5 to t/T < 1. The jet flow injection over the suction side of the airfoil creates a region of high vorticity flow just downstream of the actuator chord location. As can be seen in Figure 8A for t/T = 0.1, this region grows and is energized by the jet flow and generates a patch of vorticity detaching from the airfoil surface. This patch of vorticity is transported downstream by cross flow until it reaches the separation region near the trailing edge of the airfoil in Figure 8B. Then, it pushes separated flow away from the upper surface of the airfoil between t/T = 0.22 to 0.37, as shown in Figures 8C–E. During these instants, the lift increment starts to increase as shown in Figure 9. The pulsed jet actuation provides momentum flux and additional vorticity in the flow over the suction surface. This mechanism enables the flow to dynamically overcome the unfavorable pressure gradient, ultimately delaying and reducing the area of flow separation. This phenomenon continues until t/T = 0.71 in Figure 8G when the flow separation region reaches its minimum area. During the jet-off phase, as the momentum and vorticity injection are turned off, the flow tends to separate again due to the dominance of the adverse pressure gradient. As can be seen in Figure 8H, at t/T = 0.95, the separation point is moved upstream, but not as much as the baseline case. It is worth noting that despite the increase in the separation region after the jet is turned off, the flow separation region is still smaller than that of the baseline case. This phenomenon can be seen by comparing the streamline at time t/T = 0.95 in Figure 8H with the baseline in Figure 7.

For further analysis, Figure 10 presents the variation of the pressure coefficient C_p-C_{p0} on the airfoil surface, where C_{p0} represents the pressure coefficient of the baseline case. The effects induced by the pulsed jet are not limited to the downstream area of the actuator but involve the flow field throughout the entire airfoil. The new pressure distribution exhibits a larger suction peak at the leading edge.

As seen in Figure 8, the pulsed jet actuation generates a patch of additional vorticity detaching from the airfoil surface. This patch of vorticity moving towards the trailing edge can be seen as a region of higher suction pressure in Figure 10A. When the patch of vorticity encounters the separation flow at t/T = 0.17 (Figure 10B), a pressure increase is observed at the airfoil surface just in front of it (Figure 10B). The curvature of the streamlines upstream of the separation is also consistent with this pressure increase on the airfoil. This higher pressure region leads to a reduction in lift. The maximum pressure increment along the upper surface is observed at t/T = 0.22 in Figure 10C where a minimum lift increment is also obtained in Figure 9. Then the separated flow moves away from the airfoil surface (Figure 10D) and an increase in the suction pressure on the upper surface of the airfoil is observed (Figure 10E). Due to the advantageous modifications in the flow field, the flow separation on the airfoil surface is delayed and the separation region is reduced. Finally, the flow that is separated interacts with the flow that comes from the pressure side of the airfoil, resulting in a new vortex shedding pattern in the wake (see Figure 8F). It is responsible for reducing the suction pressure in the vicinity of the trailing edge on the upper surface of the airfoil as shown in Figures 10F, G.

During the jet-off phase, by turning off the momentum and vorticity injection, the flow field changes again and the separation point is moved upstream, but not as much as the baseline case. The new separation region is observed as a constant pressure area on the upper airfoil surface. Upstream of the separation point, a region of negative pressure increase extends along the airfoil due to the flow attaching to the streamlined body. The time-periodic advection of these pressure variations contributes to oscillations in the airfoil's lift and drag forces.

In summary, compared to the baseline when the jet is activated, the separation point moves toward the trailing edge. The suction pressure increment occurred along the upper surface followed by gradual pressure recovery toward the trailing edge. These lead to a reduction in flow separation and an increase in lift.

Figure 11 shows the evolution of streamlines and Q-criterion for the controlled case with reduced frequency of $F^+ = 1$ at different time instants in an actuation cycle. This figure illustrates a noticeable difference between the flow under actuation at the reduced frequency of $F^+ = 1$ compared to $F^+ = 0.2$, due to the difference in the duration of the jet-on and jet-off phases. As can be seen in Figure 11A, the interaction of the patch of vorticity with the separated flow, occurs before t/T = 0.05. It is much earlier than the controlled case with $F^+ = 0.2$. Actually, the phenomenon observed in Figure 11A is equivalent to that in Figure 8D at t/T = 0.25 for controlled case of $F^+ = 0.2$. Therefore, unlike the previous case, in the controlled case with reduced frequency of 1, the lift starts to increase almost at the beginning of the jet-on phase as shown in Figure 4. Then the maximum lift is obtained at t/T = 0.45. As can be seen in Figure 11B at t/T = 0.45, the flow separation is delayed and the separation region is reduced compared to the baseline case but is larger than the controlled case with $F^+ = 0.2$ at the corresponding instant. The larger separation area can be attributed to the shorter blowing phase, resulting in less promotion of the maximum lift (Cl_{max} = 1.9125 at t/T = 0.45) by the pulsed jet actuator's effects (as compared to Cl_{max} = 1.9336 for controlled case F^+ = 0.2 at t/T = 0.72). The larger size of the separation region is mainly due to the shorter duration of the blowing phase so that maximum lift (Cl_{max} = 1.9125 at t/T = 0.45) is less promoted by the effects provided by

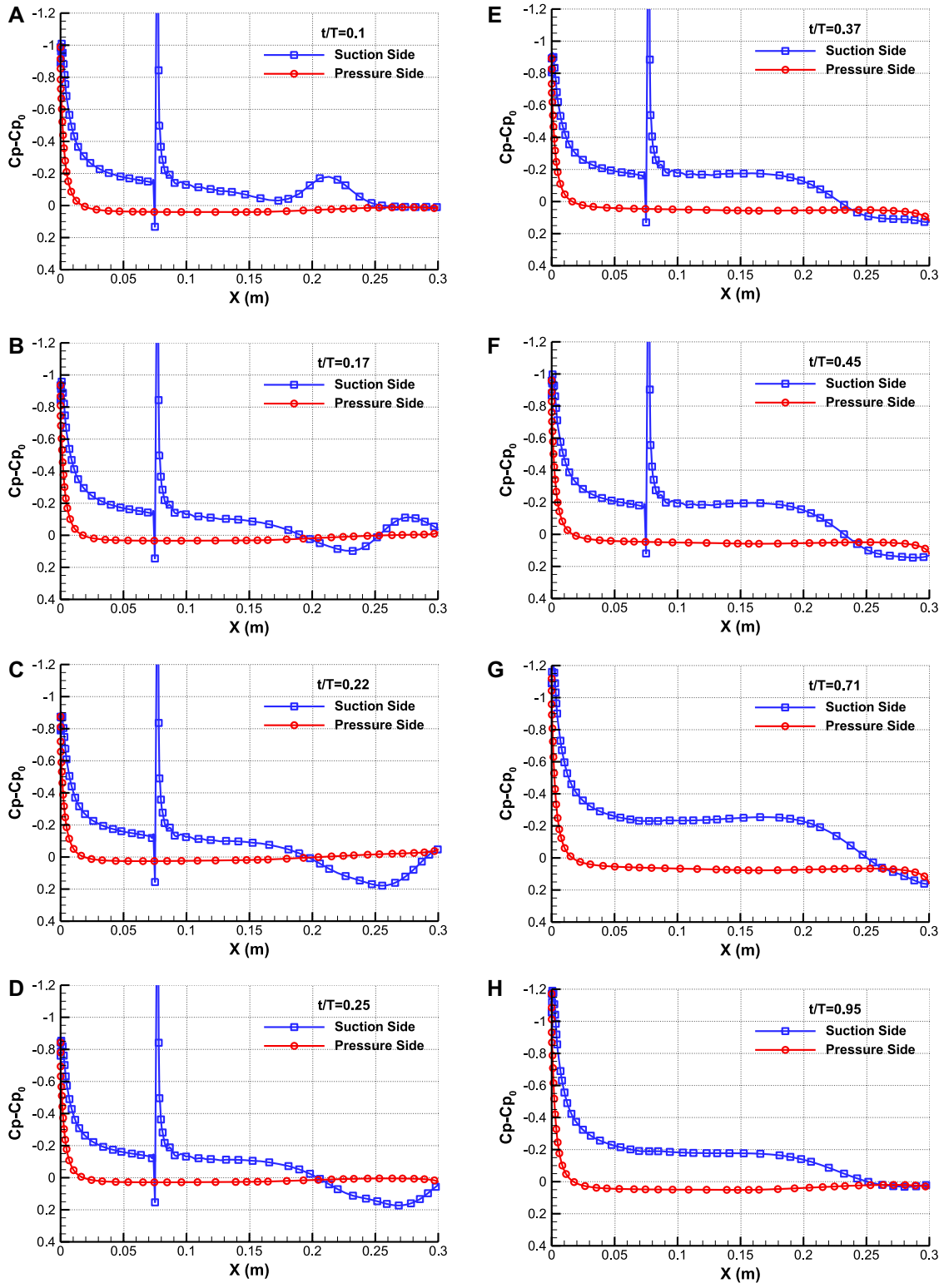

FIGURE 10
Variation of the pressure coefficient around the airfoil for reduced frequency of $F^+ = 0.2$ at different time instants in an actuation cycle, t/T= (A) 0.1, (B) 0.17, (C) 0.22, (D) 0.25, (E) 0.37, (F) 0.45, (G) 0.71, (H) 0.95.

the pulsed jet actuator (compared to $Cl_{max} = 1.9336$ for controlled case $F^+ = 0.2$ at t/T = 0.72). After the jet is turned off, due to hysteresis, the positive effects of jet injection in reducing flow separation and increasing lift are still observed at t/T = 0.55 in Figures 4, 11C. At the end of the jet-off phase at t/T = 0.95 in Figure 11D, the flow separation is growing, but unlike the controlled case with $F^+ = 0.2$ in

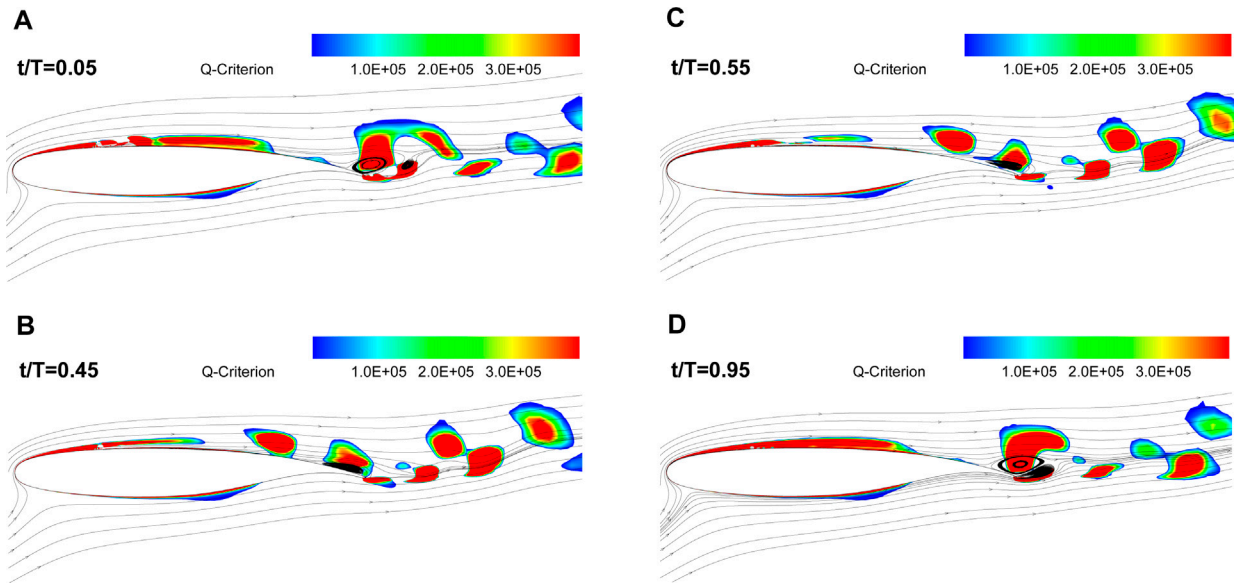

FIGURE 11
The evolution of the streamlines and Q-criterion for the actuated case at AOA = 16° with reduced frequency of $F^+ = 1$ at different time instants in an actuation cycle, t/T= (A) 0.05, (B) 0.45, (C) 0.55, (D) 0.95.

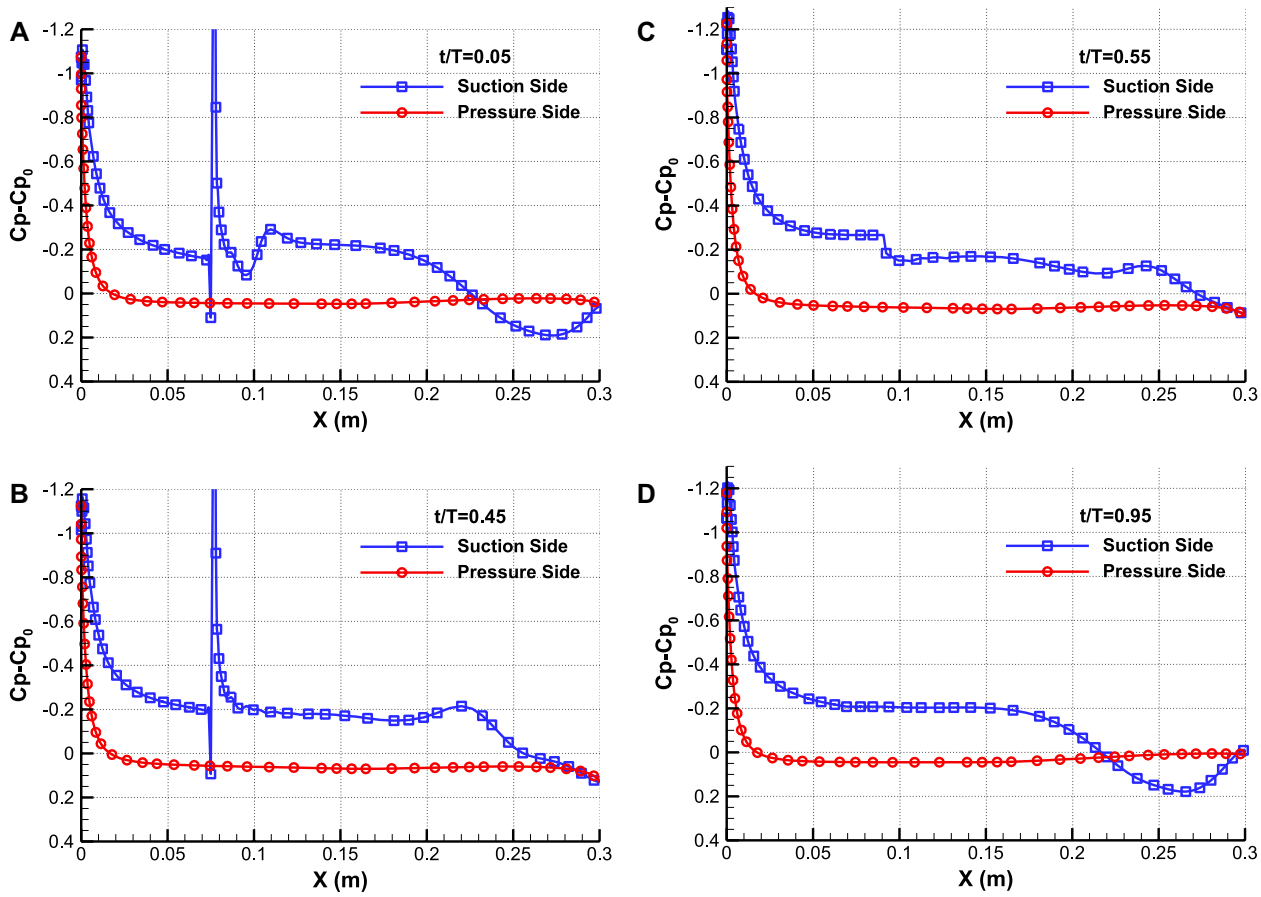

FIGURE 12
Variation of the pressure coefficient around the airfoil for reduced frequency of $F^+ = 1$ at different time instants in an actuation cycle, t/T= (A) 0.05, (B) 0.45, (C) 0.55, (D) 0.95.

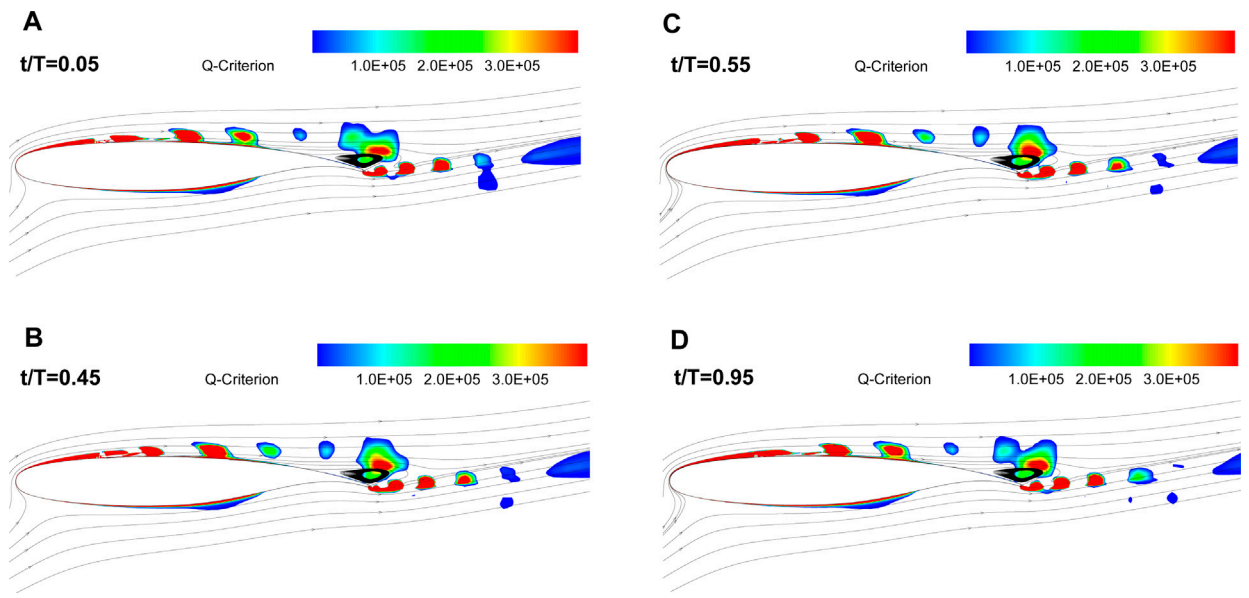

FIGURE 13
The evolution of the streamlines and Q-criterion for the actuated case at AOA = 16° with reduced frequency of $F^+ = 6$ at different time instants in an actuation cycle, t/T= (A) 0.05, (B) 0.45, (C) 0.55, (D) 0.95.

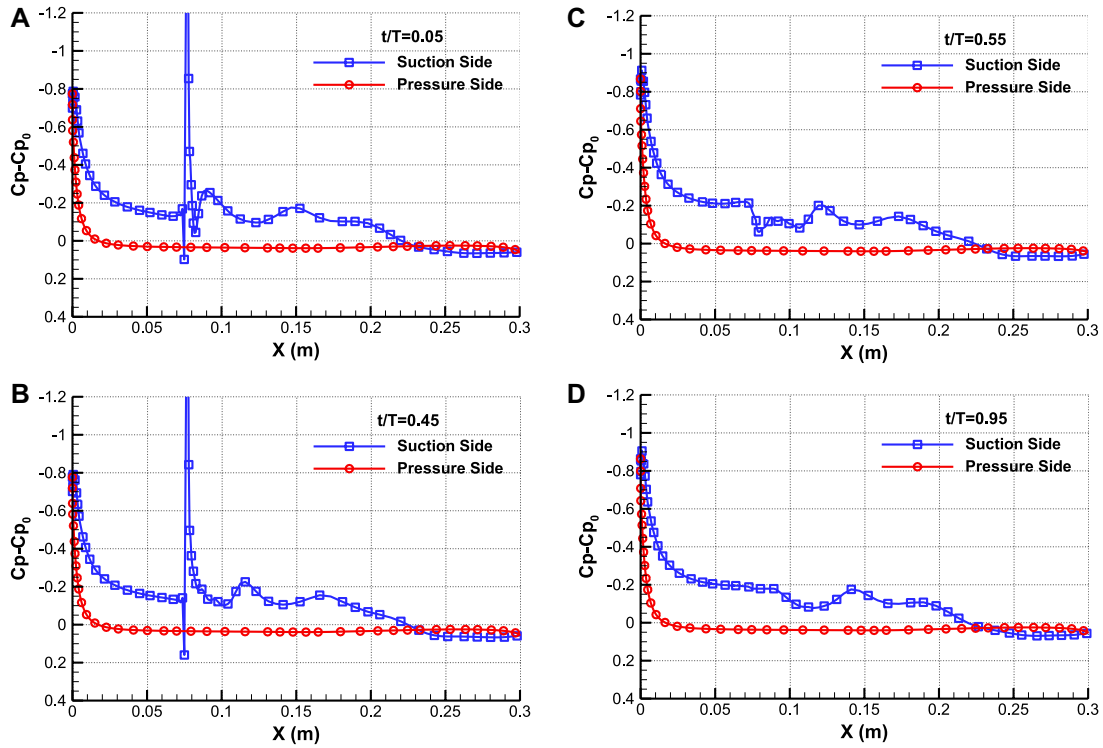

FIGURE 14
Variation of the pressure coefficient around the airfoil for reduced frequency of $F^+ = 6$ at different time instants in an actuation cycle, t/T= (A) 0.05, (B) 0.45, (C) 0.55, (D) 0.95.

Figure 8H, the separation region is not fully formed. The variation of the pressure coefficient C_p-C_{p0} on the airfoil surface for $F^+ = 6$ at the times corresponding to the Figure 11, is presented in Figure 12. On average, the pressure difference between the upper and lower surfaces is greater for the majority of time intervals in Figure 12 compared to Figure 10.

The unsteady flow structure and dynamics of vortices around the controlled airfoil under the influence of actuation with high frequencies $F^+ = 2.4, 4, 6$, and 12 compared to the actuation with low frequencies $F^+ = 0.2$, 1, 1.2 have completely different patterns. Figure 13 shows the evolution of the streamline and Q-criterion for actuation frequency of $F^+ = 6$ at different time instants in one cycle of actuation. Since the duration of each actuation cycle is shorter than the advection time scale on the airfoil, a series of small patches of vorticity shedding from the actuator can be observed at any instant. However, unlike reduced frequencies of 0.2 and 1 in Figures 8, 11, these patches of vorticity appear smaller and less intense. The small size of the patches of vorticity is mainly due to the very short duration of the blowing phase. As a consequence, actuation at high frequency is not strong enough to eliminate flow separation during a cycle and it only leads to slight downstream migration of the separation point compared to baseline. This leads to the reduction of the separation region and thus to the improvement of the aerodynamic forces.

In contrast to the low-frequencies actuation, the high-frequency actuation exhibits a similar flow structure at different time instants during an actuation cycle, resulting in relatively time-invariant aerodynamic forces. It seems that the time duration of each actuation cycle is so short that the cross flow does not sense significant changes in terms of turning the actuator on or off.

The variation of the pressure coefficient C_p-C_{p0} on the airfoil surface for $F^+ = 6$ at the times corresponding to the Figure 13, is presented in Figure 14. The pressure distributions for an actuation frequency of $F^+ = 6$, which exceeds the natural frequency of flow by an order of magnitude, exhibit marked differences from previously discussed cases. In general, high-frequency actuation yields a lower suction peak at the leading edge of the airfoil. After the suction peak, the pressure difference between the upper and lower surfaces decreases compared to corresponding low-frequency actuation cases, resulting in lower lift. Furthermore, the area with a constant suction pressure exhibits a larger separated flow over the upper surface of the airfoil compared to the low-frequency actuation cases.

4 Conclusion

Numerical simulations were conducted to investigate the impact of different pulsed jet actuation frequencies on improving the performance of separation control on a supercritical airfoil with a NASA SC(2)-0714 cross-section. The actuation frequency varies between the low range of $F^+ = 0.2$ and the high range of $F^+ = 12$, which respectively correspond to the natural instability frequencies of the separated shear layer and higher order frequencies ($0.2 \leq F^+ \leq 12$). The study was conducted under incompressible flow conditions, with a high Reynolds number of 1×10^6, and an angle of attack of 16°, where the maximum lift was obtained. This study aimed to enhance aerodynamic efficiency and maximum lift through an unsteady flow investigation. Furthermore, it aimed to increase knowledge regarding the mechanisms that are effective in augmenting instantaneous lift and diminishing instantaneous drag.

The study demonstrated that utilizing pulsed jet actuation upstream of the separation point over the supercritical airfoil at a high angle of attack effectively postponed flow separation for all actuation frequencies. This led to an enhanced lift-to-drag ratio for all controlled cases with a maximum lift-to-drag increase of 28.62% at $F^+ = 1$. In this study, the low reduced frequency of $F^+ = 1$ produced the greatest time-averaged lift increment of 12.21%, while the high reduced frequency of $F^+ = 12$ resulted in the highest time-averaged drag reduction of 15.7%. Furthermore, the aerodynamic forces experienced slight changes with the actuation frequencies in controlled cases at reduced frequencies exceeding $F^+ = 4$, suggesting that the enhancement of aerodynamic characteristics becomes restricted when actuation frequency is high enough.

Temporal evolution of lift coefficient during an actuation cycle at different reduced frequencies showed that the controlled cases with low actuation frequencies of $F^+ = 0.2$, 1, and 1.2 produced time-dependent aerodynamic forces that oscillated around the mean values. Therefore, it can increase the load fluctuations on the airfoil. The results showed that the oscillation of lift and drag forces gradually disappeared from low to high reduced frequency. Therefore, high actuation frequencies of $F^+ = 2.4, 4, 6$, and 12 generated almost time-invariant aerodynamic forces during each phase in a cycle.

Investigating the evolution of the streamline and vorticity field for different reduced frequencies in an actuation cycle showed that in all the controlled cases, the interaction of the pulsed air jet with the crossflow generated patches of vorticity near the airfoil surface and within the turbulent boundary layer. Therefore, in addition to increasing the momentum of the near-wall flow, the patches of vorticity enhanced the momentum exchange between the outer parts of the boundary layer with high momentum flow and the region near the surface with low momentum flow. It was also found that the patches of vorticity were smaller and less intense in the controlled cases with high frequencies compared to the low frequencies due to the short duration of the blowing phase. However, in controlled cases with high frequencies, the high shedding sequence of patches of vorticity and the hysteresis effect had a positive impact on reducing fluctuation of aerodynamic coefficients compared to the low frequencies.

Data availability statement

The original contributions presented in the study are included in the article/Supplementary Material, further inquiries can be directed to the corresponding author.

Author contributions

SA: Investigation, Methodology, Software, Writing–original draft, Writing–review and editing.

Funding

The author(s) declare that no financial support was received for the research, authorship, and/or publication of this article.

Conflict of interest

The author declares that the research was conducted in the absence of any commercial or financial relationships that could be construed as a potential conflict of interest.

Publisher's note

References

Abdolahipour, S., Mani, M., and Ahmadi Dehaghi, G. M. (2011). Numerical and experimental study of the influence of damage on the aerodynamic characteristics of a finite wing. *Fluids Eng. Div. Summer Meet.* 44403, 1441–1447. doi:10.1115/AJK2011-03055

Abdolahipour, S., Mani, M., and Render, P. M. (2007). "Numerical investigation into the aerodynamic characteristics of wings with triangular shape damage in different span positions," in Proceedings of the 15th Annual Conference of the CFD Society of Canada, Toronto, Ontario, May 2007, 27–31.

Abdolahipour, S., Mani, M., and Shams Taleghani, A. (2022a). Experimental investigation of flow control on a high-lift wing using modulated pulse jet vortex generator. *J. Aerosp. Eng.* 35 (5), 05022001. doi:10.1061/(asce)as.1943-5525.0001463

Abdolahipour, S., Mani, M., and Shams Taleghani, A. (2022b). Pressure improvement on a supercritical high-lift wing using simple and modulated pulse jet vortex generator. *Flow, Turbul. Combust.* 109 (1), 65–100. doi:10.1007/s10494-022-00327-9

Abdolahipour, S., Mani, M., and Taleghani, A. S. (2021). Parametric study of a frequency-modulated pulse jet by measurements of flow characteristics. *Phys. Scr.* 96 (12), 125012. doi:10.1088/1402-4896/ac2bdf

Amitay, M., and Glezer, A. (2002a). Controlled transients of flow reattachment over stalled airfoils. *Int. J. Heat Fluid Flow* 23 (5), 690–699. doi:10.1016/s0142-727x(02)00165-0

Amitay, M., and Glezer, A. (2002b). Role of actuation frequency in controlled flow reattachment over a stalled airfoil. *AIAA J.* 40 (2), 209–216. doi:10.2514/2.1662

Bauer, M. (2015). *Design and application of a fluidic actuator system for high lift flow control*. Ph.D. Dissertation. Berlin, Germany: Technical University of Berlin.

Bernardini, C., Benton, S. I., Chen, J. P., and Bons, J. P. (2014). Pulsed jets laminar separation control using instability exploitation. *AIAA J.* 52 (1), 104–115. doi:10.2514/1.j052274

Boutilier, M. S., and Yarusevych, S. (2012). Parametric study of separation and transition characteristics over an airfoil at low Reynolds numbers. *Exp. Fluids* 52 (6), 1491–1506. doi:10.1007/s00348-012-1270-z

Buchmann, N. A., Atkinson, C., and Soria., J. (2013). Influence of ZNMF jet flow control on the spatio-temporal flow structure over a NACA-0015 airfoil. *Exp. Fluids* 54, 1–14. doi:10.1007/s00348-013-1485-7

Duvigneau, R., and Visonneau, M. (2006). Optimization of a synthetic jet actuator for aerodynamic stall control. *Comput. fluids* 35 (6), 624–638. doi:10.1016/j.compfluid.2005.01.005

Feero, M. A. (2018). *Investigation of synthetic jet flow control parameters for the mitigation of laminar boundary layer separation*. Ph.D. Dissertation. Toronto, Canada: University of Toronto.

Feero, M. A., Goodfellow, S. D., Lavoie, P., and Sullivan, P. E. (2015). Flow reattachment using synthetic jet actuation on a low-Reynolds-number airfoil. *AIAA J.* 53 (7), 2005–2014. doi:10.2514/1.j053605

Feero, M. A., Lavoie, P., and Sullivan, P. E. (2017). Influence of synthetic jet location on active control of an airfoil at low Reynolds number. *Exp. Fluids* 58 (8), 99. doi:10.1007/s00348-017-2387-x

Glezer, A. (2011). Some aspects of aerodynamic flow control using synthetic-jet actuation. *Philosophical Trans. R. Soc. A Math. Phys. Eng. Sci.* 369 (1940), 1476–1494. doi:10.1098/rsta.2010.0374

Glezer, A., Amitay, M., and AndrewHonohan, M. (2005). Aspects of low-and high-frequency actuation for aerodynamic flow control. *AIAA J.* 43 (7), 1501–1511. doi:10.2514/1.7411

Greenblatt, D., and Wygnanski, I. J. (2000). The control of flow separation by periodic excitation. *Prog. Aerosp. Sci.* 36 (7), 487–545. doi:10.1016/s0376-0421(00)00008-7

Haucke, F., and Nitsche, W. (2013). "Active separation control on a 2D high-lift wing section towards high Reynolds number application," in Proceedings of the The 31st AIAA Applied Aerodynamics Conference, California, June 2013.

Hecklau, M., Salazar, D. P., and Nitsche, W. (2013). "Influence of the actuator jet angle on the reattachment process with pulsed excitation," in *New results in numerical and experimental fluid Mechanics VIII* (Berlin: Springer Verlag), 143–150.

Hipp, K. D., Walker, M. M., Benton, S. I., and Bons, J. P. (2016). Control of poststall airfoil using leading-edge pulsed jets. *AIAA J.* 55 (2), 365–376. doi:10.2514/1.j055223

McManus, K., Joshi, P., Legner, H., and Davis, S. (1995). "Active control of aerodynamic stall using pulsed jet actuators," in Proceedings of the Fluid Dynamics Conference, San Diego,CA,U.S.A., June 1995, 2187.

Mirzaei, M., Taleghani, A. S., and Shadaram, A. (2012). Experimental study of vortex shedding control using plasma actuator. *Appl. Mech. Mater.* 186, 75–86. doi:10.4028/www.scientific.net/amm.186.75

Mohammadi, M., and Taleghani, A. S. (2014). Active flow control by dielectric barrier discharge to increase stall angle of a NACA0012 airfoil. *Arabian J. Sci. Eng.* 39, 2363–2370. doi:10.1007/s13369-013-0772-1

Munday, P. M., and Taira, K. (2018). Effects of wall-normal and angular momentum injections in airfoil separation control. *AIAA J.* 56 (5), 1830–1842. doi:10.2514/1.j056303

NASA Technical Memorandum 81912 (2013). *Low-speed aerodynamic characteristics of a 14-percent-thick NASA phase 2 supercritical airfoil designed for a lift coefficient of 0.7*.

Radespiel, R., Burnazzi, M., Casper, M., and Scholz, P. (2016). Active flow control for high lift with steady blowing. *Aeronautical J.* 120 (1223), 171–200. doi:10.1017/aer.2015.7

Salmasi, A., Shadaram, A., and Taleghani, A. S. (2013). Effect of plasma actuator placement on the airfoil efficiency at poststall angles of attack. *IEEE Trans. Plasma Sci.* 41 (10), 3079–3085. doi:10.1109/tps.2013.2280612

Seifert, A., Greenblatt, D., and Wygnanski, I. J. (2004). Active separation control: an overview of Reynolds and mach numbers effects. *Aerosp. Sci. Technol.* 8 (7), 569–582. doi:10.1016/j.ast.2004.06.007

Sheikholeslam Noori, S. M., Shams Taleghani, S. A., and Taeibi, M. (2020). Phenomenological investigation of drop manipulation using surface acoustic waves. *Microgravity Sci. Technol.* 32, 1147–1158. doi:10.1007/s12217-020-09839-3

Sheikholeslam Noori, S. M., Shams Taleghani, S. A., and Taeibi, M. (2021). Surface acoustic waves as control actuator for drop removal from solid surface. *Fluid Dyn. Res.* 53 (4), 045503. doi:10.1088/1873-7005/ac12af

Stalnov, O., and Seifert, A. (2010). On amplitude scaling of active separation control. *Act. Flow Control II , Notes Numer. Fluid Mech. Multidiscip. Des.* 108, 63–80. doi:10.1007/978-3-642-11735-0_5

Taeibi, M., Shams Taleghani, S. A., Sheikholeslam Noori, S. M., and Ahmadi, G. (2022). Computational simulation of water removal from a flat plate, using surface acoustic waves. *Wave Motion* 111, 102867. doi:10.1016/j.wavemoti.2021.102867

Taleghani, A. S., Shadaram, A., and Mirzaei, M. (2012). Effects of duty cycles of the plasma actuators on improvement of pressure distribution above a NLF0414 airfoil. *IEEE Trans. Plasma Sci.* 40 (5), 1434–1440. doi:10.1109/tps.2012.2187683

Taleghani, A. S., Shadaram, A., Mirzaei, M., and Abdolahipour, S. (2018). Parametric study of a plasma actuator at unsteady actuation by measurements of the induced flow velocity for flow control. *J. Braz. Soc. Mech. Sci. Eng.* 40 (4), 173. doi:10.1007/s40430-018-1120-x

Tuck, A., and Soria, J. (2008). Separation control on a NACA 0015 airfoil using a 2D micro ZNMF jet. *Aircr. Eng. Aerosp. Technol.* 80 (2), 175–180. doi:10.1108/00022660810859391

Walker, M. M., Hipp, K. D., Benton, S. I., and Bons, J. P. (2018). Effect of jet spacing on swept-wing leading-edge separation control. *AIAA J.* 56 (7), 2907–2910. doi:10.2514/1.j056352

Wild, J. (2015). Mach-, Reynolds- and sweep effects on active flow separation control effectivity on a 2-element airfoil wing. *Act. Flow Combust. Control* 127, 87–100. doi:10.1007/978-3-319-11967-0_6

Wu, J.-Z., Lu, X.-Y., Denny, A. G., Fan, M., and Wu, J.-M. (1998). Post-stall flow control on an airfoil by local unsteady forcing. *J. Fluid Mech.* 371, 21–58. doi:10.1017/s0022112098002055

Yarusevych, S., and Kotsonis, M. (2017). Steady and transient response of a laminar separation bubble to controlled disturbances. *J. Fluid Mech.* 813, 955–990. doi:10.1017/jfm.2016.848

You, D., and Parviz, M. (2008). Active control of flow separation over an airfoil using synthetic jets. *J. Fluids Struct.* 24 (8), 1349–1357. doi:10.1016/j.jfluidstructs.2008.06.017

Nomenclature

f	actuation frequency (Hz)
F^+	Nondimensional frequency, reduced frequency, $F^+ = f\ L/V$
L	Length scale of the flow domain (m)
C	Chord Length (m)
V	Freestream velocity (m/s)
Cp	Pressure coefficient
Cp_0	Pressure coefficient of baseline case
Cl	Lift coefficient
Cl_0	Lift coefficient of baseline case
Cl_{max}	Maximum lift coefficient
Cd	Drag coefficient
Cl/Cd	Aerodynamic efficiency
T	Time period of actuation (s)
t/T	Nondimensional time
AOA	Angle of attack (Degree)

frontiers | Frontiers in Mechanical Engineering

TYPE Original Research
PUBLISHED 29 November 2023
DOI 10.3389/fmech.2023.1300967

OPEN ACCESS

EDITED BY
Arash Shams Taleghani,
Ministry of Science, Research and Technology, Iran

REVIEWED BY
Ebrahim Afshari,
University of Isfahan, Iran
Soheila Abdolahipour,
Aerospace Research Institute, Iran

*CORRESPONDENCE
Barat Ghobadian,
ghobadib@modares.ac.ir

RECEIVED 23 September 2023
ACCEPTED 13 November 2023
PUBLISHED 29 November 2023

CITATION
Baratian I, Ghobadian B and Banakar A (2023), Parametric comparison of different lobe rotor geometry for positive displacement turbine in water distribution network.
Front. Mech. Eng 9:1300967.
doi: 10.3389/fmech.2023.1300967

Parametric comparison of different lobe rotor geometry for positive displacement turbine in water distribution network

Iman Baratian, Barat Ghobadian* and Ahmad Banakar

Biosystems Engineering Department, Tarbiat Modares University, Tehran, Iran

The application of hydro turbines for harnessing water energy within distribution networks, as an alternative to pressure relief valves, is steadily increasing. These turbines are particularly suitable for recovering energy from incompressible subsonic fluid flows. In this research paper, three models of positive displacement lobe machine designed to function as water turbines were extensively examined and compared. The three selected turbine types included the circular lobe turbine, the cycloidal arc lobe turbine and the epicycloid arc lobe turbine. These turbines were meticulously designed and developed for their respective applications. Under identical operational conditions, optimization processes were applied to enhance volumetric efficiency and power efficiency for all three turbine variants, each having a different number of blades. A computer program was devised to facilitate the optimization and calculation of blade geometries under various operating conditions. This research delved into the impact of blade geometry type and the number of blades on turbine efficiency and size. The data obtained from the present investigation were systematically analyzed, and the performance of the different turbines were compared. Notably, the circular lobe turbine was found to be the largest among the three, occupying more space. The cycloidal arc requiring a greater amount of material resulting in rotor volume, which subsequently resulted in a higher overall cost. In contrast, the cycloidal arc lobe turbine emerged as the smallest variant, demanding less space for operation. Efficiency-wise, the cycloidal arc lobe turbine exhibited the highest efficiency with two blades, while the circular lobe turbine displayed the lowest efficiency with six blades. Moreover, among the turbines with the same number of lobes, the cycloidal arc lobe turbine consistently demonstrated superior efficiency compared to the circular lobe turbine.

KEYWORDS

incompressible flow, positive displacement turbine, lobe pump as turbine, geometric analysis, lobe rotor analysis

1 Introduction

Hydrodynamics and aerodynamics have similar behavior in many engineering cases. The application of airfoils is important in both fields of aerodynamics (Taleghani et al., 2012; Salmasi et al., 2013; Shams Taleghani et al., 2020; Abdolahipour et al., 2022a; Abdolahipour et al., 2022b) and hydrodynamics (Ouro and Stoesser, 2019; Bagal and Bhardwaj, 2022; Zhang, 2022; ElHelew et al., 2023; Ferretti et al., 2023), and some airfoils such as NACA0012 and NACA 4412 are generally used in both fields (Mirzaei et al., 2012;

Mohammadi and Taleghani, 2014). In many cases such as low-speed aerodynamics, the fluid flow equations are also used in hydrodynamics. This has caused some aerodynamic designers in the car industry and aeronautics to use water tunnel tests instead of wind tunnels to measure the drag coefficient (Erm and Ol, 2012; Sibilski et al., 2020; Lis et al., 2021).

In recent decades, optimizing and efficiently managing water distribution and transmission systems has become a critical concern due to growing human needs for both water resources and energy. One key factor in enhancing the performance of these systems is the efficient utilization of energy within the flowing water. This optimization holds significant importance as it not only improves the efficiency of water distribution and transmission networks but also contributes to energy conservation.

In this regard, Positive Displacement Lobe Turbines have emerged as an effective tool for energy conversion in these systems. Their utilization as intelligent alternatives to pressure-reducing valves in water distribution and transmission networks is gaining prominence. This substitution not only leads to energy savings and operational cost reduction but also offers an opportunity for harnessing renewable energy resources.

Unlike large power plants, small-scale hydropower installations often consist of a wide range of designs, layouts, and various equipment options, offering numerous choices for applications (Zhoua and Denga, 2017). However, the discussed technologies are often outdated and lack the required credibility and efficiency for in-network water distribution and conduit applications (IEA-ETSAP and IRENA, 2015).

A fundamental hydropower unit comprises a turbine and a generator. Despite their diversity, many turbines are categorized into reaction, impulse, and hydrokinetic turbines based on operational principles. Reaction turbines like Francis and Kaplan utilize water pressure and motion to generate hydrodynamic force for turbine blade rotation. Impulse turbines like Pelton, Turgo and cross-flow turbines use blades driven by high-velocity water flow. Reaction turbines are typically suited for low head systems, while impulse turbines are more suitable for medium head conditions. Nevertheless, practical applications of these turbines often involve significant overlap (McKinney, 1983). For instance, some newer impulse turbines like hydrodynamic screw turbines can also operate in low-head flows. Besides reaction and impulse turbines, there is growing interest in developing and installing hydrokinetic turbines that harness energy from water motion. Commercial hydrokinetic units are typically deployed in rivers, natural and man-made channels, and marine environments (Saria et al., 2018). The use of pumps instead of turbines (PAT) is a feasible solution but using a pump instead of a turbine reduces the overall efficiency of the machine (Liu et al., 2022).

Phommachanh et al. (2006) recommended the use of positive displacement micro-turbines for converting water energy into electricity in low-flow, high-head conditions. In their study, they compared a positive displacement turbine with an impulse turbine in a water distribution system. The results indicated that the positive displacement turbine significantly outperformed similar turbines under a wide range of operating conditions.

Yao et al. (2005) investigated the effect of the number of lobes in positive displacement pump turbines on the rotor's input force. They utilized an epicycloidal geometry in their research, developed it and provided a higher-degree geometric equation for the tip end of the rotor to reduce pulsation and improve rotor rotation. According to their findings for an epicycloidal lobe pump, increasing the number of lobes reduces output flow pulsation, resulting in a more uniform output flow.

Li et al. (2018); Li et al. (2019); Li et al. (2020) developed a geometry for a cycloidal lobe and presented a combined geometry of convex and concave arc cycloidal for a root blower. They studied and examined this geometry in their research and developed cycloidal arc lobe geometry.

Sonawat et al. (2020) studied the use of a positive displacement turbine in a district heating water network to replace pressure reducing valves. In this study, a specific 4-lobe turbine model was investigated both theoretically and experimentally. Various factors such as pulsation and efficiency were examined, focusing on a single turbine model as chosen by the researchers.

Rotor geometry significantly influences the efficiency and performance of a lobe turbine, and it varies with the changes in geometry specifications and lobe types (Kang and Vu, 2014).

In the most previous researches, the use of a lobed machine as a pump in the network has been explored and only a few studies considered positive displacement machines as turbines within the network. Additionally, the optimal design of positive displacement machines has not been thoroughly explored and the impact of geometry and the number of lobes on their output efficiency has not been investigated. Therefore, in the current research work three different geometries of lobe positive displacement machines were investigated. Considering the use of these machines as turbines in water transmission networks, a method for optimizing blade and rotor geometry was developed. Furthermore, geometry optimization under identical operating conditions examined the effects of the number of blades and geometry type on turbine efficiency. Ultimately, the priority of using different geometries and blade counts was determined.

2 Materials and methods

2.1 Blade design geometry

The principles of operation in a turbine are such that two rotor blades rotate around their central fixed axis and rolling over without contacting each other. This study focuses on "circular lobe turbines". Circular turbines have various types, all of which follow the same general principles but differ in the details of the blade curvature. The basic principles of designing circular and non-circular lobe turbines are the same, with the main difference being the variation in timing gears and the different rotational and linear speeds of the blades. In a lobe turbine and pumps, unlike gear types, there is no contact between the blades, and the blades are connected to a gear axis that rotates at a specific speed, allowing the blades to rotate without contacting each other. In general, the shape of the blades in a turbine can be either uniform or non-uniform. In this study, a circular turbine with uniform blades has been investigated.

2.2 Basic principles of rotor design for lob machine

Figure 1 displays a schematic cross-section of the lobe turbine rotor. In this figure, $r_1(\theta_1)$ and $r_2(\theta_2)$ are the curvature equations

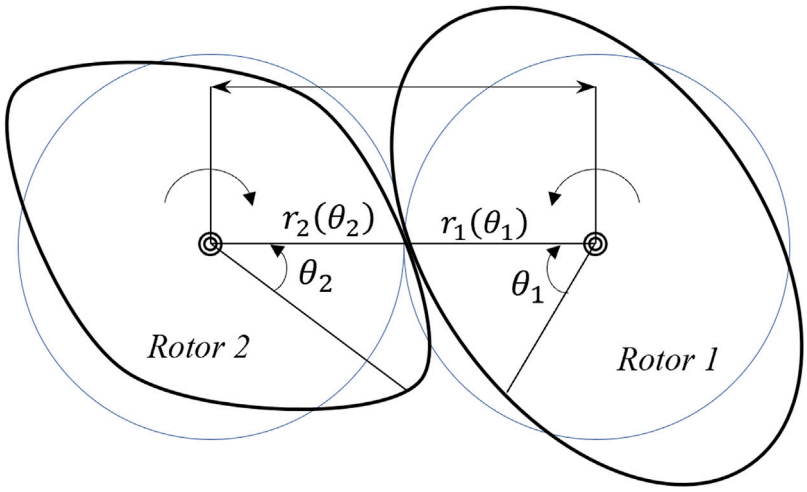

FIGURE 1
General view of the rotor and circular pitch circle.

for rotor 1 and rotor 2, respectively. The parameter " l " signifies the distance between the centers of these two rotors. Additionally, θ_1 and θ_2 represent the angular rotation of rotor 1 and rotor 2, respectively. Given that the only relative motion between the turbine blades is rolling, Eq. 1 is upheld:

$$r_2(\theta_2) = l - r_1(\theta_1) \tag{1}$$

Therefore, the rotational position of rotor 2 can be determined using Eq. 2:

$$\theta_2 = \int \frac{r_1}{l - r_1} d\theta_1 \tag{2}$$

If the values for l and $\theta_2 = f(\theta_1)$ are given, then the curve for the second blade can be derived using the previously mentioned equation. In a Lobe machine, it is crucial that the blades have relative rotation to each other without any contact, slippage, or excessive pressure. Under these conditions, the instantaneous velocity at the blade contact point remains constant, leading to Eqs 3, 4:

$$r_1 \frac{d\theta_1}{dt} = r_2 \frac{d\theta_2}{dt} \tag{3}$$

$$r_1 = r_2 \frac{d\theta_2}{d\theta_1} \tag{4}$$

By combining the above equations, the equations of the airfoil curve can be represented in the following form, Eqs 5, 6:

$$r_1(\theta_1) = \frac{f'l}{1 + f'} \tag{5}$$

$$r_2(\theta_1) = \frac{l}{1 + f'} \tag{6}$$

Under the conditions of uniform rotation, the absence of oscillation, slip, and circular motion of the rotor, the curves of each rotor are simple and closed. This implies that the equations r_1 and r_2 will also be simple and closed equations. In this scenario, the conditions are met based on Eq. 7:

$$\theta_2 = 2n\pi \quad when\ \theta_1 = 2\pi \tag{7}$$

In the above relation, the variable "n" is a real number that represents the ratio of the number of blades on rotor 1 to the number of blades on rotor 2 which is showed in Eq. 8.

$$n = \frac{Number\ of\ Lobes\ of\ Rotor1}{Number\ of\ Lobes\ of\ Rotor2} \tag{8}$$

This study focuses on the examination of the circular base curve propeller in a lobe machine. The circular lobe machine features a circular pitch, and both of its rotors share the same rotational speed. Additionally, the radii of the pitch circles in the rotors are identical. In this specific lobe type, the rotor blades are uniform in size and shape due to the consistent base circle size and rotational speed. Typically, this rotor profile is referred to as "circular" in the lobe machine context.

2.3 Circular lobe design

A circular-toothed lobe represents one of the fundamental and widely used geometries for rotor blades, forming the basis for numerous designs. The profile of the rotor's circular-toothed section is defined as part of a circular curve with a radius of ρ_1, centered at point C. Point C is situated at a distance " a " from the center of the rotor base, which corresponds to the center of rotor rotation. By computing the tip section of the tooth, i.e., the convex part of the blade, the profile of the convex section of the tooth can also be determined using Eq. 1.

Figure 2 provides an illustration of the specifications for two-blade and three-blade lobes, which serve as the basis for deriving the governing equations. In a three-blade lobe, the overlap angle of the rotor tooth section is 60°, while it is 90° in a two-blade lobe. Generally, when the rotor has N number of blades, the overlap angle of the tooth circle section can be determined using Eq. 9:

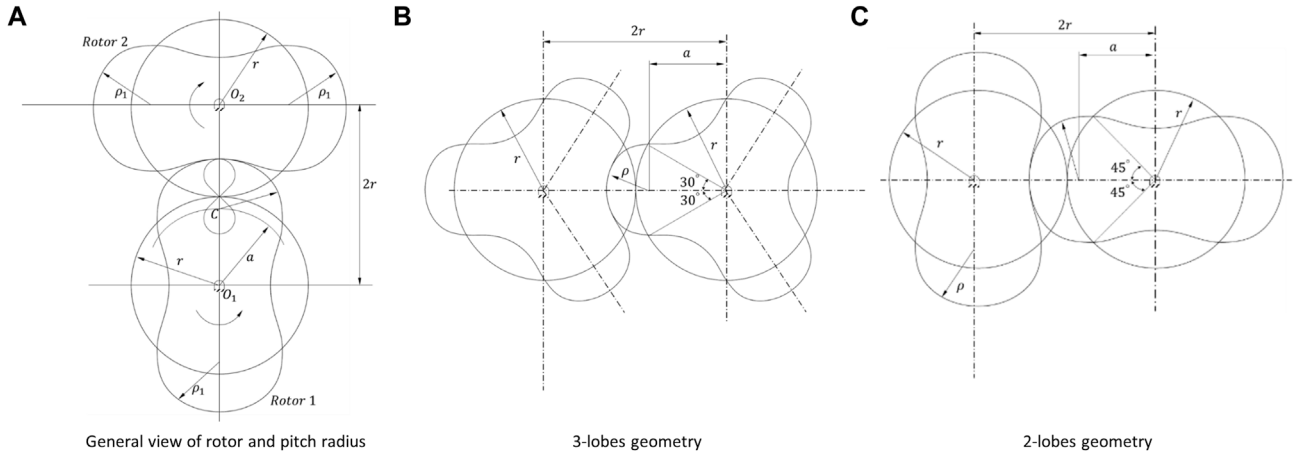

FIGURE 2
General View and lobe Geometry of circular lobe tooth profile for deriving equation.

$$\alpha = \frac{2\pi}{N} \tag{9}$$

The trigonometric relation that governs the lob turbine design is shown in Eq. 10 (Litvin and Fuentes, 2004):

$$r^2 + a^2 - 2ar\cos(\alpha) = \rho^2 \tag{10}$$

This equation allows to determine the radius of the tooth circle based on the values of r and a, which are adjustable design variables. So, Eq. 1 can be used to calculate the profile of the convex section of the rotor's tooth.

The profile of the rotor's tooth is an essential factor in the design of lob turbines, and by adjusting r and a, the shape and performance of the rotor blades can be controlled.

The equation governing the blade tooth section is established as follows in Eq. 11 (Litvin and Fuentes, 2004):

$$\begin{aligned} x_1 &= \rho\sin\theta \\ y_1 &= a + \rho\cos\theta \\ -\frac{(a+\rho)^2 - r^2}{\sqrt{2}ar} \le \tan\left(\frac{\theta}{2}\right) &\le \frac{(a+\rho)^2 - r^2}{\sqrt{2}ar} \end{aligned} \tag{11}$$

Using the method for calculating the coordinates of contact points between the rotors, the equation describing the rotor's tooth profile can be derived as Eq. 12 (Litvin and Fuentes, 2004):

$$f(\theta, \varnothing) = r\sin(\theta - \varnothing) - a\sin(\theta) = 0 \tag{12}$$

By solving the above equation for angle ϕ, the angle θ can be calculated. Using the equations mentioned earlier, the equation governing the convex section of the blade can be derived as Eq. 13 (Litvin and Fuentes, 2004):

$$\begin{aligned} x_2 &= \rho\sin(\theta - 2\varnothing) - a\sin(2\varnothing) + 2r\sin(\varnothing) \\ y_2 &= \rho\cos(\theta - 2\varnothing) + a\cos(2\varnothing) - 2r\cos(\varnothing) \\ & r\sin(\theta - \varnothing) - a\sin(\theta) = 0 \end{aligned} \tag{13}$$

The maximum radius or tooth radius of the rotor can also be determined using Eq. 14 (Litvin and Fuentes, 2004):

$$R_t = a + \rho \tag{14}$$

Additionally, the relationship between the tooth radius and the minimum profile radius, which is showed on Eq. 15 is established based on Eq. 1 as follows:

$$R_t + R_{min} = l \tag{15}$$

With these equations, the rotor profile can be calculated. The input parameters for geometry design are values of "a" and " r." Various combinations of "a" and " r " leads to different rotor profiles, as explained in subsequent sections.

2.4 Cycloidal arc lobe design

The Cycloidal Arc Lobe is derived from plotting the trajectory of a point on a circle as it rotates along another line or circle. This point can typically be situated on the outer edge or inside the circumference of the rotating circle.

The ratio of the pitch circle's radius to the rolling circle's radius leads to the creation of different shapes, and this approach is extensively employed in lobe rotor design. The same principle underlies the design of epicycloid rotors. In this research, two rotors with epicycloidal bases but differing geometries at the rotor tips are employed. Previous work by Yao and others has focused on epicycloidal rotors with the goal of minimizing issues related to slipping and mutual interaction between the two rotors. Drawing from their prior experiences, they divided the convex tooth section of the rotor into two parts (Yao et al., 2005): one with an epicycloidal profile and the other with a circular profile, while the concave tooth section is treated as a circular segment. Unlike the circular lobe design, the center of the convex tooth circle is positioned on the circumference of the base circle.

In Figure 3, a cross-sectional view of a three-bladed arc-cycloidal rotor is illustrated. It is evident that each tooth is composed of one convex epicycloidal section, one concave epicycloidal section and two circular arc segments. Two coordinate systems are established

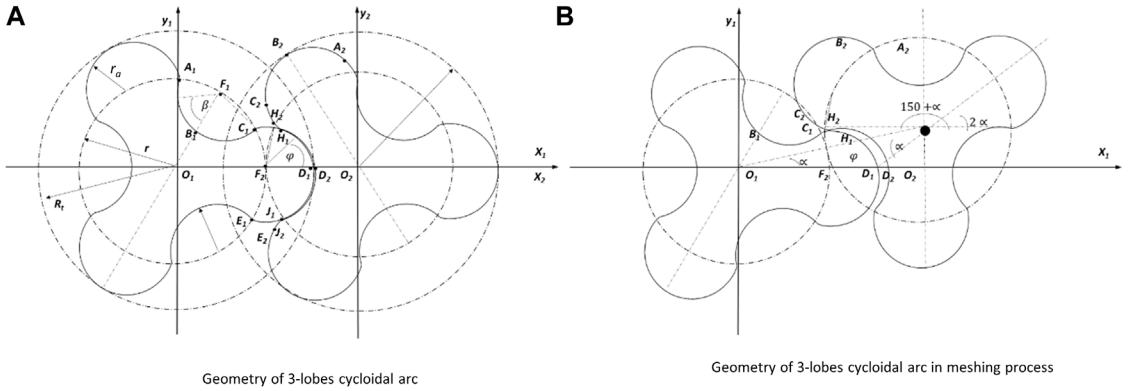

FIGURE 3
Geometry and cross-sectional view of a three-lobe cycloidal arc rotor.

for the two rotors, with each rotor rotating in the opposite direction about its axis. The convex and concave arc sections have their own distinct equations. Fundamentally the primary relationships between the lobe rotors, as detailed in Section 2.2 are applicable here as well, with the only difference being in the curvature equations of the curved sections.

Equation 16 shows the relationship between the angles depicted in Figure 3 and is valid for this particular rotor geometry (Yao et al., 2005):

$$\begin{aligned} &\angle B_2O_2H_2 = \angle H_2O_2F_2 = \angle D_1O_1C_1 = \angle C_1O_1B_1 = \frac{\pi}{2N} \\ &F_2H_2 = r_a = 2r\,sin\left(\frac{\pi}{2N}\right) \end{aligned} \tag{16}$$

In this rotor geometry, the maximum radius is equal to the sum of the base circle radius and the radius of curvature at the rotor tip. This is because the center of the rotor tip circle is positioned on the base circle which is shown in Eq. 17:

$$R_t = r + r_a \tag{17}$$

The equation for the curvature of the convex arc section of the rotor, curvature HDJ, can be also obtained based on Figure 3 as Eq. 18 (Yao et al., 2005):

$$\begin{aligned} x_{1ce} &= r + r_a\,cos(\varphi) \\ y_{1ce} &= r_a\,sin(\varphi) \\ -cos^{-1}\left(\frac{r_a}{2r}\right) &\le \varphi \le cos^{-1}\left(\frac{r_a}{2r}\right) \end{aligned} \tag{18}$$

Furthermore, by using the aforementioned equations and the general equations for designing lobe rotors, the equation for the curvature of the concave section of the rotor, curvature ABC, can be derived as Eq. 19 (Yao et al., 2005):

$$\begin{aligned} x_{1ca} &= r\,sin\left(\frac{\pi}{2N}\right) - r_a\,sin\left(\beta + \frac{\pi}{2N}\right) \\ y_{1ca} &= r\,cos\left(\frac{\pi}{2N}\right) - r_a\,cos\left(\beta + \frac{\pi}{2N}\right) \\ -cos^{-1}\left(\frac{r_a}{2r}\right) &\le \beta \le cos^{-1}\left(\frac{r_a}{2r}\right) \end{aligned} \tag{19}$$

Yao et al. aimed to enhance rotor performance by incorporating a circular curvature at the termination of the convex arc section and extending the cycloidal arc with a circular segment. To achieve this, they employed an inverse computational approach based on Figure 3, resulting in the following equation that governs the cycloidal section, curvature CH as Eq. 20 (Yao et al., 2005):

$$\begin{aligned} x_{1cy} &= 2r\,cos(\theta) + r\,cos\left(2\theta + \frac{5\pi}{2N}\right) \\ y_{1cy} &= 2r\,sin(\theta) + r\,sin\left(2\theta + \frac{5\pi}{2N}\right) \\ 0 &\le \theta \le \frac{\pi}{2N} \end{aligned} \tag{20}$$

Using the equations provided above, the complete geometry of the arc-cycloidal rotor can be accurately determined.

2.5 Epicycloid arc lobe design

Another type of lobe rotor examined in this study is the rotor with an epicycloidal geometry. This rotor is also a subset of cycloidal lobe rotors and follows the general principles and equations of lobe rotor geometry. In this type of lobe turbine, both convex and concave curvatures of the blade are formed by tracing a point on one circle as it rolls along another circle. Additionally, to minimize the issues of rotor slippage and mutual interaction between the blades, Li et al. have used higher-degree curves at the connection point of the convex and concave sections, leading to the development of this rotor type (Li et al., 2020).

Figure 4, illustrates the design principles and the formation of the rotor curve. Sections AB and CD represent the cycloidal regions of the rotor, while section BC is the curved area with higher degrees of curvature.

This type of rotor, with its unique geometry, offers its own advantages and characteristics, which make it suitable for specific applications within the broader category of the lobe rotors.

The curve for the tip section of the rotor; the curvature of section AB is obtained from Eq. 21 (Li et al., 2020):

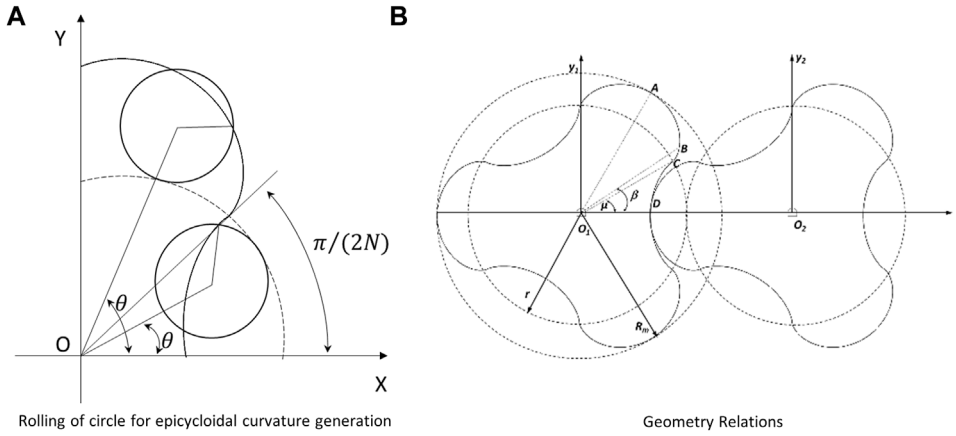

FIGURE 4
Geometric relation of epicycloidal lobe rotors.

$$x = \frac{(2N+1)R_t}{2(N+1)}cos(\theta) + \frac{R_t}{2(N+1)}cos[(1+2N)\theta]$$
$$y = \frac{(2N+1)R_t}{2(N+1)}sin(\theta) + \frac{R_t}{2(N+1)}sin[(1+2N)\theta] \quad (21)$$
$$\frac{\pi}{2N} \le \theta \le \frac{\pi}{N}$$

Furthermore, the curve for the convex section of the rotor; the curvature of section CD is obtained from Eq. 22 (Li et al., 2020):

$$x = \frac{(2N-1)R_t}{2(N+1)}cos(\theta) - \frac{R_t}{2(N+1)}cos[(1-2N)\theta]$$
$$y = \frac{(2N-1)R_t}{2(N+1)}sin(\theta) - \frac{R_t}{2(N+1)}sin[(1-2N)\theta] \quad (22)$$
$$0 \le \theta \le \frac{\pi}{2N}$$

The equation governing the curve of the higher-degree section of the rotor; section BC is also developed as Eq. 23 (Li et al., 2020):

$$\mu(\varphi) = k_0 + k_1\varphi + k_2\varphi^2 + k_3\varphi^3 + k_4\varphi^4 + k_5\varphi^5 + k_6\varphi^6 \quad (23)$$

In the equation above, k_0 to k_6 are design variables, and the objective is to minimize the pulsation while maximizing the rotational acceleration of the rotor and avoiding any interference during the rotor's motion. Eq. 24 represents an optimization problem whenever it is necessary to find the values of these design variables to satisfy these objectives (Li et al., 2020):

$$min\, W_1|J_{max}| + max\, W_2|k_{max}| \quad (24)$$

To optimize the above equation constraints are utilized based on Eq. 25 (Li et al., 2020):

$$\varphi(0) = \overline{OB}$$
$$\varphi(\beta-\mu) = \overline{OC}$$
$$\nu(0) = \nu(\beta-\mu) = k(\beta-\mu) = k(0) = J(\beta-\mu) = J(0) = 0 \quad (25)$$

In the above equations, $k(\mu) = \frac{d\mu}{d_\varphi}$ represents the angular velocity of the rotor, while $k(\varphi) = \frac{d^2\mu}{d_{\varphi^2}}$ denotes the angular acceleration, impacting the radial force on the rotor. Additionally, $J(\varphi) = \frac{d^3\mu}{d_{\varphi^3}}$ signifies the pulsation and noise of the rotor system.

With these equations, the complete geometry of the epicycloidal rotor can be calculated and designed.

2.6 Optimization of rotors

The calculation of the rotor's geometric profile was explained in the previous section. For a given volume, there are thousands of different turbine designs with various geometric dimensions that can be used. To design an appropriate rotor and turbine, it is essential to relate geometric parameters to relevant performance parameters. The most critical performance parameters for hydraulic machines are the volumetric efficiency and the output power. Initially, functional parameters must be linked to the machine's efficiency to perform the design based on higher efficiency.

In the previous section, the process of calculating the geometric profile of the rotor was discussed. When designing a turbine, it is crucial to establish a connection between geometric parameters and key performance indicators. Among the most critical performance parameters for hydraulic machines are volumetric efficiency and output power. To initiate the design process, it is essential to establish a relationship between geometric parameters and efficiency, with an emphasis on achieving higher efficiency.

The power efficiency of the machine, denoted as η_p, can be defined as the ratio of the turbine's output power to its input power, expressed by Eq. 26:

$$\eta_p = \frac{Output\ Power}{Input\ Power} = \frac{Q_r\Delta P}{Q_r\Delta P + W_f} \quad (26)$$

In the above equation, Q_r represents the actual fluid flow rate, ΔP is the pressure difference between the turbine's inlet and outlet, and W_f is the frictional losses within the machine.

Efficiency is a crucial factor in the design process, as it directly impacts the performance and effectiveness of the hydraulic turbine. Optimizing geometric parameters with a focus on enhancing efficiency can lead to more effective and energy-efficient turbines.

The equation for volumetric efficiency η_v, provided here is a fundamental parameter in evaluating the performance of hydraulic

turbines. This parameter shows that how well the actual outlet flow rate is and how leakage affect performance.

The goal in turbine design is to maximize volumetric efficiency, which means achieving a high ratio of actual flow rate to ideal flow rate bases on Eq. 27. High volumetric efficiency indicates that the turbine is effectively converting the incoming fluid into mechanical energy, minimizing losses and waste.

$$\eta_v = \frac{Q_r}{Q_i} \tag{27}$$

where, Q_r of the turbine compares to the ideal flow rate Q_i, which represents the flow rate that would be achieved under perfect ideal conditions. Q_r represents the actual flow rate of fluid exiting the turbine. It is the real-world flow rate experienced in the operating turbine. Q_i, The ideal flow rate, represents the theoretical maximum flow rate that could be achieved under perfect conditions, without losses or inefficiencies and Q_l is the leakage rate from the turbine.

The actual turbine flow rate is calculated from the difference between the inlet and outlet flow rates which is showed on Eq. 28:

$$Q_r = Q_i - Q_l \tag{28}$$

The ideal turbine flow rate can be written as Eq. 29:

$$Q_i = nq_i \tag{29}$$

The lobe machine uses a structure, identical to that of a pump for power generation purposes with the only difference being in the analysis and operation. Therefore, essentially a pump instead of a turbine is used with different design objectives. However, pump design parameters can also be used in turbine design. For this purpose, the dimensionless parameter called the "pumping ratio" is used, which depends only on rotor geometry.

The concept of the "pumping ratio" is an important parameter in the design and analysis of lobe machines that are used as pumps or turbines. This dimensionless parameter is primarily determined by the geometry of the rotor and provides valuable insights into the machine's performance. The pumping ratio itself is a dimensionless quantity, and it quantifies the machine's ability to transfer fluid from the inlet to the outlet. It depends on rotor geometry and is a key factor in assessing the machine's performance.

By calculating the pumping ratio, can gain insights into how the machine's geometry and configuration affect its fluid-handling capabilities and helping to optimize performance for specific applications, such as a pump or a turbine.

The equation provided defines the pumping ratio (r_p) and its relationship with various geometric parameters of the rotor is shown on Eq. 30:

$$r_p = \frac{q_i}{V} \tag{30}$$

The relationship described in the provided Eqs 19, 20 highlights an essential aspect of the design and performance of lobe machines that function as pumps or turbines.

Based on this relationship, it can be observed that if two pumps have the same size and rotor speed and the pump with a higher pumping ratio has a greater water output. This observation holds true for turbines as well. By combining Eqs 19, 20, Eq. 31 is obtained:

$$Q_i = nVr_p \tag{31}$$

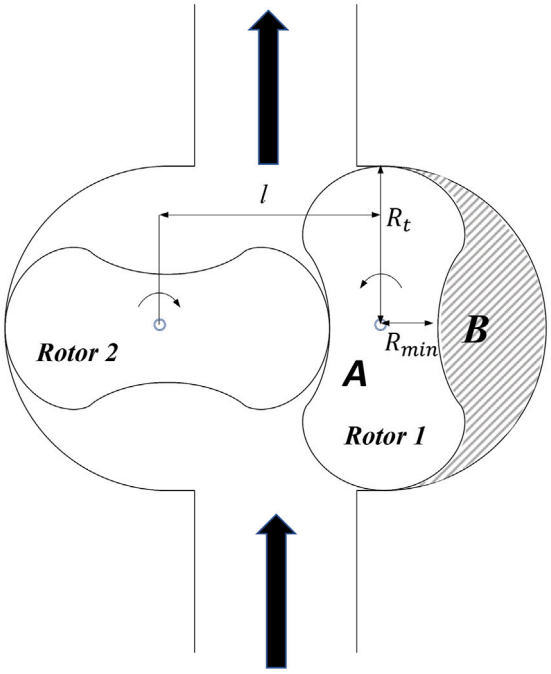

FIGURE 5
Schematic of fluid sections in lobe turbine.

To use the dimensionless pumping ratio in rotor design, the mathematical relationship between them needs to be determined. In Figure 5, the area of the region exiting the turbine in each rotor rotation is denoted as B. The ideal output volume in each rotor rotation can be calculated as Eq. 32:

$$q_i = 2NBw = 2\left(\pi R_t^2 - A\right)w \tag{32}$$

In the above equation, N represents the number of rotor blades, and w is the blade length. The rotor area is denoted as A. Now, by using the above relationship, the pumping ratio can be rewritten as Eq. 33:

$$r_p = \frac{q_i}{V} = \frac{2NB}{\pi R_t^2 + 2R_t l} = \frac{2\left(\pi R_t^2 - A\right)}{\pi R_t^2 + 2R_t l} \tag{33}$$

Using the equation above, the effects of changing the geometric profile of the rotor on the pumping ratio can be studied. To do this, the efficiency equations using r_p is rewritten. By substituting the above equations into Eq. 16, the power efficiency is rewritten as Eq. 34:

$$\eta_p = \frac{Q_r \Delta P}{Q_r \Delta P + W_f} = \frac{\left(r_p nV - Q_l\right)\Delta P}{\left(r_p nV - Q_l\right)\Delta P + W_f} = \frac{\left(r_p n - Q_l/V\right)\Delta P}{\left(r_p n - Q_l/V\right)\Delta P + W_f/V} \tag{34}$$

This equation represents the power efficiency η_p as a function of the pumping ratio r_p, the frictional losses W_f/V, and the leakage rate Q_l/V. It allows to study that how changes in the geometric profile of the rotor (which affect r_p) impact the power efficiency of

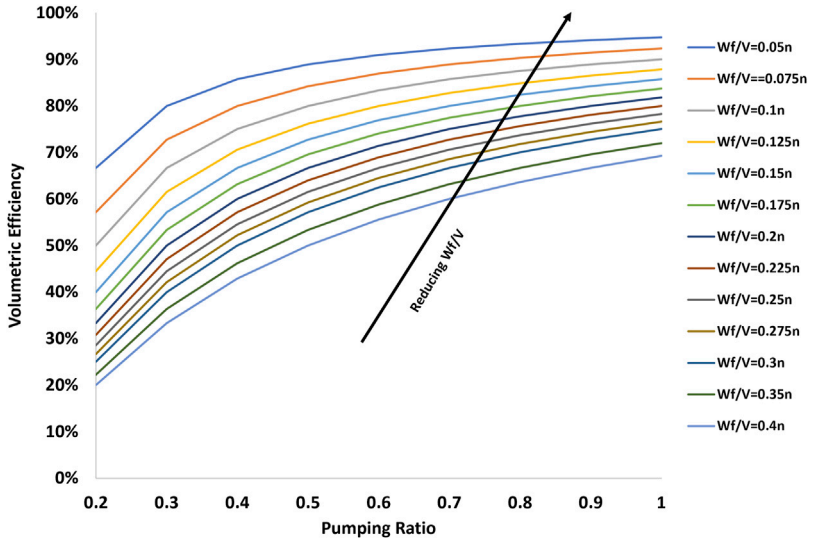

FIGURE 6
Variation of η_v with respect to r_p for different values of Q_l/V.

the turbine, while considering the influence of frictional losses and leakage which is shown on Eq. 35:

$$\eta_v = \frac{Q_r}{Q_i} = \frac{nVr_p - Q_l}{nVr_p} = \frac{nr_p - Q_l/V}{nr_p} \tag{35}$$

So, the volumetric efficiency, η_v, can be expressed as a function of the pumping ratio, r_p , and specific leakage ratio (Q_l/V). Similar to Eq. 34, this equation allows to study how changes in the geometric profile of the rotor (which affect r_p) impact the volumetric efficiency while considering the influence of leakage.

To investigate the effects of altering the geometric profile of the rotor on the pumping ratio (r_p), specific operating conditions are initially assumed. These conditions maintain constant pressure difference, rotor speed, leakage, and frictional losses. An examination of the efficiency equations reveals that increasing the pumping ratio leads to higher efficiency.

In Figure 6, the relationship between volumetric efficiency (η_v) and r_p is depicted for various values of Q_l/V. Regardless of the Q_l/V values, it is evident that increasing r_p consistently results in improved volumetric efficiency. Moreover, as r_p increases, the influence of Q_l/V on volumetric efficiency diminishes, reducing the impact of leakage. This trend emphasizes the importance of maximizing r_p during rotor design.

Figure 7 illustrates the variation in power efficiency (η_p) concerning r_p for different values of W_f/V. This graph similarly demonstrates that increasing r_p enhances power efficiency across all W_f/V values, mitigating the impact of friction on efficiency.

These observations highlight the crucial role of selecting appropriate geometric parameters for the rotor to optimize efficiency and overall turbine performance under specified operating conditions.

To enhance the rotor design, a computer program was devised for determining the geometric parameters of the rotor. The objective was to maximize the output efficiency while considering the specified input conditions at the design point. The program takes into account the crucial input factors such as the maximum runner speed, the maximum fluid flow rate, and the desired number of lobes. Using these initial conditions, the program calculates both the pitch circle radius and the maximum tips radius to ensure that the turbine achieves peak output efficiency.

By inputting these parameters into the computer program, the geometric specifications of the runner, including the base circle radius and maximum radius are calculated to create an optimized turbine with the highest efficiency under the specified input conditions. SQP algorithm which is a versatile and effective method for solving nonlinear constrained optimization problems, have been used in this research.

The results indicate that using this computer program and adjusting the input parameters, it is possible to achieve the design of turbines with maximum efficiency under specific input conditions. It was assumed uniform operating conditions, including a maximum runner speed of 40 rotations per minute and a maximum fluid flow rate of 0.5 cubic meters per minute as design boundary conditions. Furthermore, the width of the runner is assumed to be 0.8 times the maximum length of the runner, with a constant length-to-width ratio of the runner.

By providing these parameters as input to the computer program, it performs calculations to determine the rotor's geometric specifications, which include the pitch circle radius and the maximum radius. This process results in an optimized turbine configuration that can achieve the highest efficiency while operating under the specified input conditions.

The algorithm of optimization is briefly as follow:

- Input initial conditions and design parameters including: rotation speed, flow rate, lobe number, geometry
  nput first evaluation of geometry design (pitch radius and tip radius)
- Geometry calculation for desire point

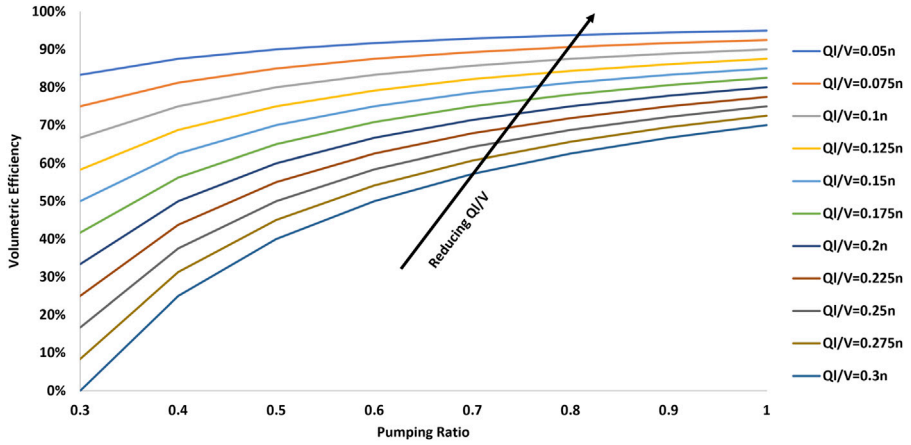

FIGURE 7
Variation of η_p with respect to r_p for different values of W_t/V.

- r_p calculation
- Maximize r_p using SQP algorithm and calculate pitch radius and tip radius based on the optimum design
- Geometry design for optimum point

The research findings suggest that using this computer program and the adjustment of input parameters, it becomes feasible to design turbines that can operate with maximum efficiency under specific input conditions. The study maintained consistent operating conditions, including a maximum runner speed of 40 rpm and a maximum fluid flow rate of 0.5 cubic meters per minute, serving as the design boundary conditions. Additionally, the width of the runner was assumed to be 0.8 times the maximum length of the runner, maintaining a constant length-to-width ratio for the rotor.

3 Results and discussion

The optimization process and design of Circular lobe turbines ranging from 2 to 6 lobes have been systematically carried out. In this particular turbine configuration, two parameters, namely, the pitch circle radius and the radius of blade curvature (tips radius), are fundamental in the comprehensive rotor design. It's important to note that for each parameter, there exists a multitude of potential rotor designs, resulting in a vast design space. By adjusting one of these parameters while maintaining the other constant, it leads to the creation of diverse rotor designs, which, in turn, can yield entirely distinct turbine configurations. Figure 8 visually portrays a selection of these rotor designs, each characterized by different ratios of the base circle radius to the radius of blade curvature.

The optimization process for the designated design point was executed through utilization of a specialized computer program. Figure 9 offers graphical representations of the rotor designs across varying blade counts.

This approach not only facilitates the exploration of an extensive spectrum of rotor designs for circular lobe turbines but also enables the fine-tuning of their performance characteristics to align with specific lobe counts by adjusting the pitch circle radius and radius of blade curvature while preserving the other pertinent factors as constants.

In the realm of Cycloidal Arc lobe rotor configuration, the interplay between the number of blades and the base circle radius serves as the cornerstone for the comprehensive rotor calculation. Consequently, for each distinctive shell and corresponding pitch circle radius, there exists a singular and unique rotor configuration.

The design of Cycloidal Arc lobe rotors, tailored to a specific design point, was diligently executed while accommodating a range of blade counts. For each design point, the optimal rotor geometry was meticulously calculated and devised. Figure 10 furnishes visual depictions of the resulting rotor designs across varying blade counts.

This strategic approach not only empowers the fine-tuning of Cycloidal Arc lobe rotor designs in accordance with predefined design points but also offers the flexibility to adapt differing blade counts, thereby generating distinct and tailored geometries for each configuration.

Figure 11 offers graphical depictions of the geometry for diverse design configurations within Epicycloidal Arc rotor category. This strategic approach empowers the fine-tuning of Epicycloidal Arc lobe rotor designs based on the defined design point and varying blade counts. The result is a collection of unique geometries for each configuration, setting them apart from the cycloidal lobe with distinctive design features. Epicycloidal Arc lobe and Cycloidal Arc lobe, though both falling within the same category of rotors, exhibit distinct variations in the curvature of their blade tips. Similar to the cycloidal lobe, this rotor type's blade geometry can be precisely determined by specifying the base circle radius and the number of blades. Each combination of radius and blade count yields a one-of-a-kind rotor design, distinguished by its unique design nuances compared to the cycloidal lobe. Furthermore, adhering to the parameters of a designated design point and encompassing various rotor blade counts, an optimization process was conducted to refine the design of this turbine.

For a specific design point, an examination of three distinct types of lobe turbine rotors was conducted investigating each rotor model across a range of lobe counts thoroughly, spanning from two to six

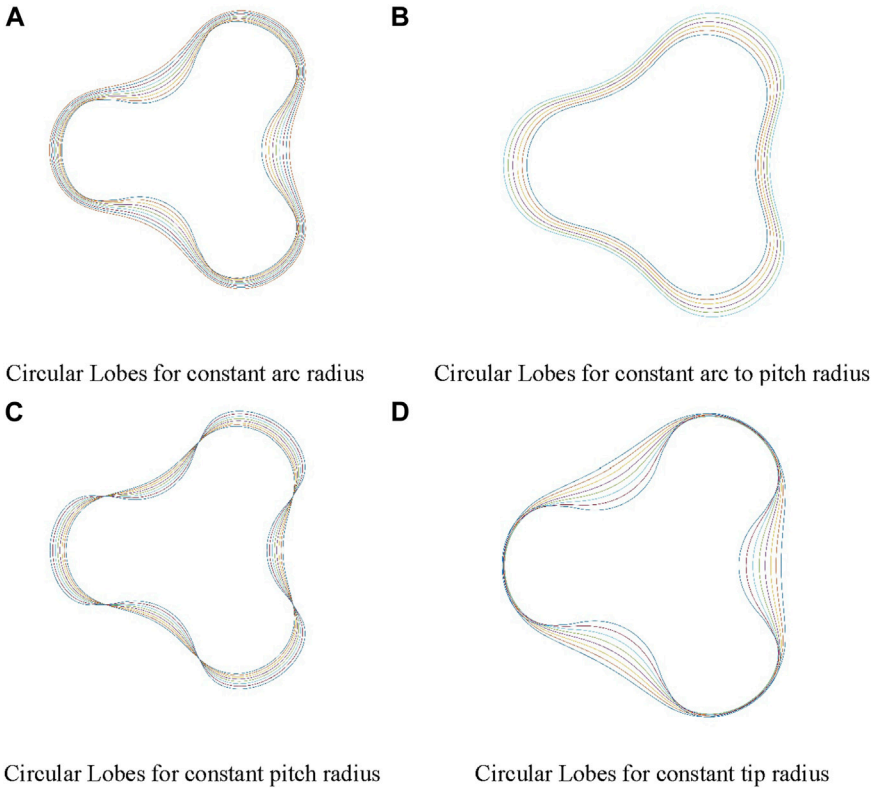

FIGURE 8
Various design of circular lobe based on different pitch radius and arc radius **(A)** Circular lobes for constant arc radius **(B)** Circular lobes for constant arc to pitch radius **(C)** Circular lobes for constant pitch radius **(D)** Circular lobes for constant tip radius.

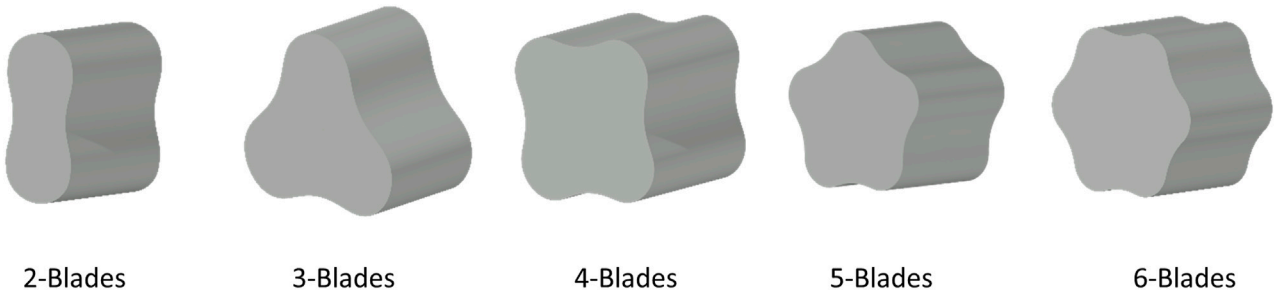

FIGURE 9
Circular rotor designs across varying lobes counts.

blades. This comprehensive research resulted in a total of 15 unique optimized designs, all sharing consistent input parameters but differing in rotor type and blade count. Figure 12, provides graphical representation offers a detailed overview of the obtained outcomes, particularly focusing on the pump ratio (r_p), which serves as the primary parameter optimized for rotor geometry. As established by prior sections, it becomes evident that an elevated r_p corresponds to superior turbine efficiency. For a comprehensive view of r_p values during various rolling processes, The findings of this study point towards the Cycloid rotor with two blades as the top-performer, boasting the highest efficiency. Conversely, the Circular rotor with six blades registers the lowest output efficiency among the considered designs.

In brief, the results shed light on a notable trend: an increase in the number of blades within lobe turbine rotors tends to correlate with reduced efficiency. Additionally, it is observed that, overall, the Cycloidal Arc rotor outperforms the Epicycloidal Arc rotor in terms of efficiency, with the Circular rotor exhibiting lower efficiency levels in comparison to both of these alternatives.

However, when comparing different rotor lobe counts, the general order of increasing efficiency is not always consistent, and the sequence of optimal designs can vary. Figure 12

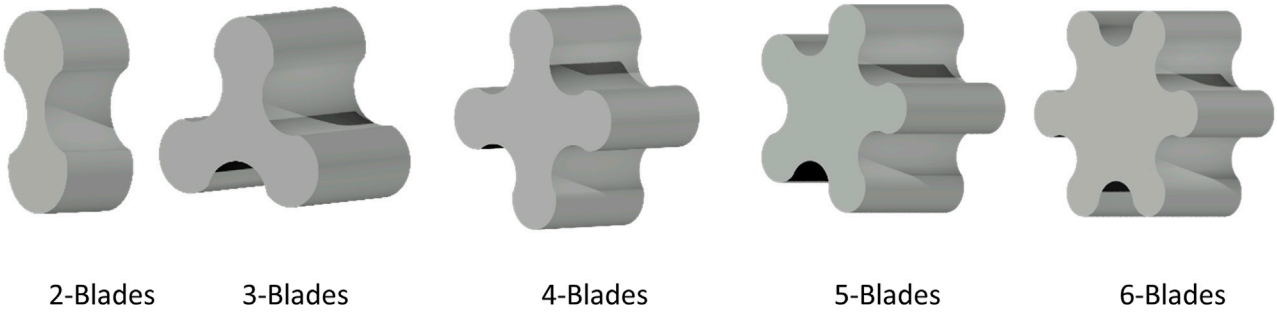

FIGURE 10
Cycloidal arc rotor designs across varying lobes counts.

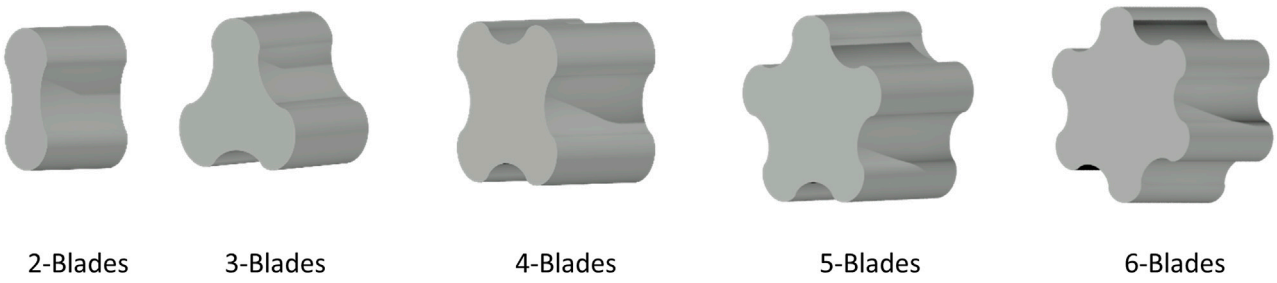

FIGURE 11
Epicyloidal arc rotor designs across varying lobes counts.

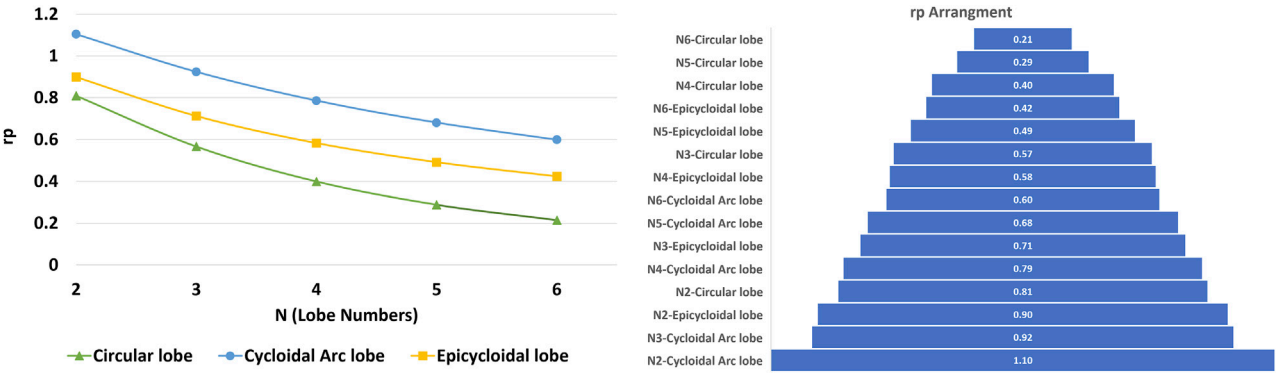

FIGURE 12
Changes in r_p for different rotors based on the number of blades.

illustrates the arrangement of various optimal designs based on rotor type and blade count, sorted by their efficiency levels. As observed, the Cycloidal Arc rotor with two blades attains the highest efficiency, followed by the same rotor with three blades. In the next position, the epicycloidal rotor with two blades, despite being of a different rotor type, exhibits higher efficiency than both Cycloidal Arc and Circular rotor types, followed by the Circular rotor with two blades. This demonstrates that the number of rotor blades holds greater significance compared to the rotor geometry type.

Based on Figure 12, it can be summarized that as the number of rotor blades increases, the geometric efficiency of the rotor decreases. Therefore, the Cycloidal Arc rotor with two blades achieves the highest efficiency, while the Circular rotor with six blades demonstrates the lowest efficiency.

Figure 13 illustrates the variation in Rm for different optimal rotor design. The maximum rotor radius represents the volume occupied by the rotor and the rotor shell. Therefore, a smaller rotor blade tip radius occupies less space and is more favorable both

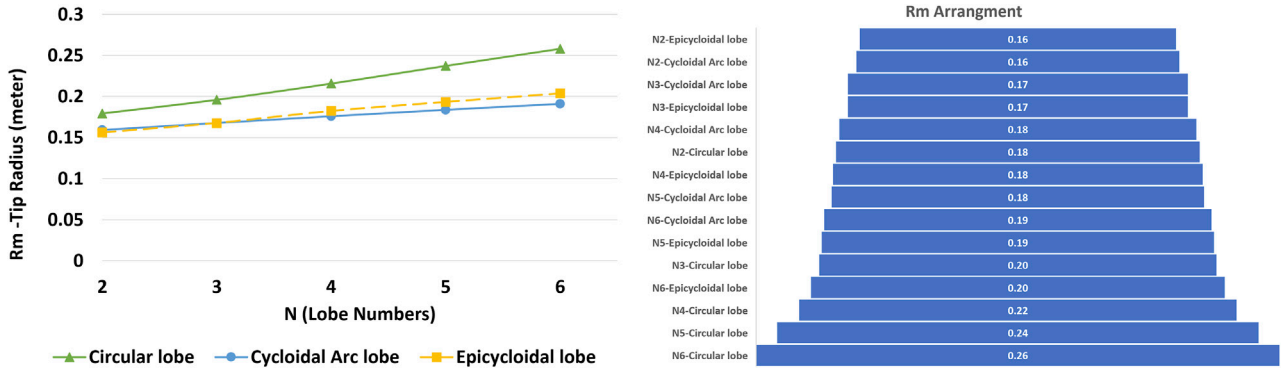

FIGURE 13
Changes in R_m for different rotors based on the number of blades.

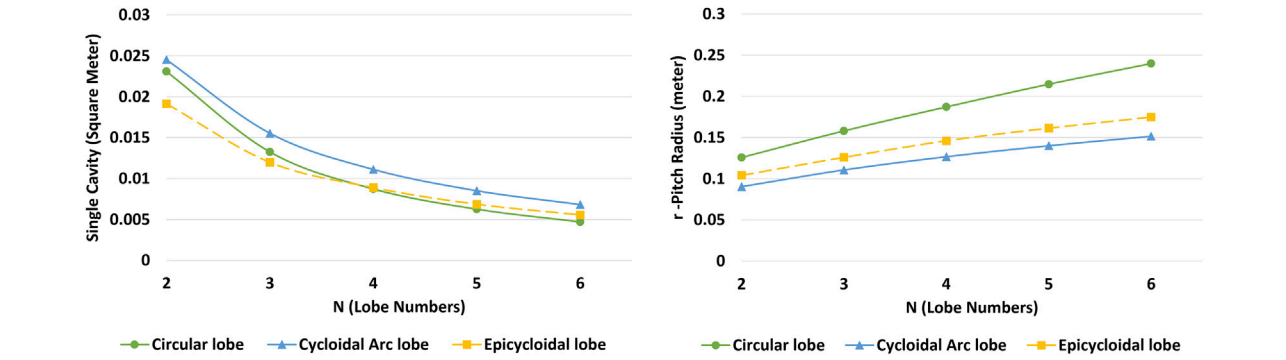

FIGURE 14
Changes in pitch radius and single cavity for different rotors based on the number of blades.

physically and economically. As observed, the Circular lobe rotor has the largest rotor radius, while the Cycloidal arc lobe rotor exhibits the smallest maximum radius and is the preferred choice in the first priority. Additionally, for a lower number of lobes, especially in the case of two lobes, this parameter is relatively similar for various blade geometries, and as the number of lobes increases, both the rotor radius and the spacing between different rotor types increase.

The order of rotor radii in the 15 optimal configurations, is shown in Figure 13. This graph illustrates that as the number of rotor lobes increases, the maximum radius and the space occupied by the turbine also increase. Furthermore, upon examining this parameter, it becomes evident that the 2-lobe rotor with cycloidal arc and epicycloidal geometry has the smallest Rm and, consequently, the best design. Conversely, the 6-blade circular rotor has the largest Rm, which should be avoided.

The examination of rotor radius results shows a strong correlation with rotor efficiency. The prioritization of rotors based on efficiency aligns closely with their prioritization based on maximum radius. The trend governing the maximum rotor radius remains consistent with that of the pitch circle radius. The variation in pitch circle radius for different optimal designs is illustrated in Figure 14. The pitch circle radius directly affects the rotor's efficiency and the occupied cross-sectional area, although it does not have a direct impact on the efficiency or volume occupied by the rotor.

Another factor indirectly influencing the selection of an optimal design is the "single cavity". This factor affects the choice of the optimal geometry by influencing r_p and efficiency. The variation in "single cavity" for various cases is depicted in Figure 14. It can be observed that the "Cycloidal arc lobe" has the largest value of "single cavity," and this value decreases as the number of rotor blades increases. This trend aligns with the definition of "single cavity" and is expected accordingly. In addition to functional and efficiency factors, economic considerations also play a crucial role in selecting the optimal rotor design. These economic factors include the amount of raw material consumption and the total cost of the rotor. The quantity of materials used in rotor construction can be assessed based on the rotor's volume, assuming uniform material properties.

Figure 15 illustrates the variations in rotor volume. As observed, the cycloidal arc lobe rotor has the highest volume and, consequently, the highest material consumption, while the epicycloidal rotor has the lowest material consumption.

An examination of the rotor volume change chart reveals that there is no specific correlation between turbine efficiency, weight,

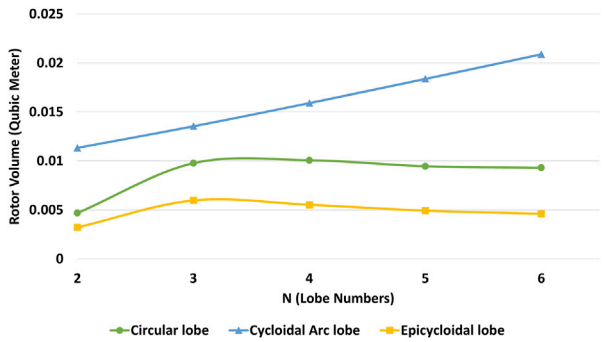

FIGURE 15
Changes in rotor volume for different rotors based on the number of blades.

volume, and material consumption. Therefore, to make an informed choice for the optimal design, real-world design should rely on techno-economic optimization based on actual operating conditions and the type of raw material used. Given the diversity of raw materials and different operating conditions, especially operational costs and income from work, this decision should be investigated for specific conditions, and it cannot be universally optimized and analyzed.

4 Conclusion

In this paper, three different geometries of lobe turbines, including circular lobe, circular arc lobe, and epicycloidal arc lobe, have been examined, optimized, and compared. Specific operating conditions were defined and based on these conditions, the optimum rotor blade design for each geometry with different blade numbers was carried out to maximize turbine efficiency. In total, 15 different optimized geometries were designed and calculated, and the results were compared. The findings of this research can be summarized as follows:

- For all different geometries, increasing the number of rotor blades leads to a decrease in volumetric efficiency and hydraulic efficiency of the turbine. Increasing in the number of blades, leads to decrease in pumping ratio from 1.1 to 0.6 for Cycloidal Arc lobe while it varies from 0.9 to 0.49 for Epicycloidal Arc lobe and from 0.81 to 0.21 for Circular Lobe.
- The cycloidal arc lobe turbine has a higher overall efficiency compared to the circular lobe and epicycloidal arc lobe turbines. This relationship holds true even for the same number of lobes. Maximum value of pumping ratio resulting maximum efficiency has been calculated for 2-Lobe Cycloidal Arc lobe and is equal to 1.1 which is higher than 0.90 for 2-Lobe Epicyloial Arc lobe and the lowest value for 2-Lobe is 0.81 for Circular lobe.
- The cycloidal arc lobe turbine with two lobes has the highest efficiency, while the circular lobe turbine with six lobes has the lowest efficiency. The highest pumping ratio is 1.1 for 2-Lobe Cycloidal Arc lobe and the lowest is 0.21 for 6-Lobe Circular lobe.
- Circular lobe turbines occupy more space, while cycloidal arc lobe turbines occupy less space compared to the other turbines. Tip radius of rotor, which is the index for spacing, has highest value for 6-Lobe circular lobe equal to 0.26, while the minimum amount is 0.16 for 2-lobe epicyloidal lobe.
- The "Cycloidal arc lobe" rotor has the highest volume, which is equal to 0.0113 cubic meter for 2-Lobe rotor and, consequently, the highest material consumption, while the epicycloidal rotor has the lowest volume which is equal to 0.0032 cubic meter and, consequently, the least material consumption.
- Considering factors such as available space, economic considerations, operating fluid properties, and specific working conditions such as pulse problems, the optimal design point and the suitable model and number of blades should be selected.
- In conclusion, this research work highlights the importance of selecting the right turbine geometry and blade count based on specific operational and fluid properties. The findings emphasize the need for careful consideration of these factors to optimize turbine design for various applications and conditions.

Data availability statement

The raw data supporting the conclusion of this article will be made available by the authors, without undue reservation.

Author contributions

IB: Conceptualization, Data curation, Formal Analysis, Methodology, Project administration, Resources, Software, Supervision, Validation, Visualization, Writing–original draft, Writing–review and editing. BG: Conceptualization, Data curation, Methodology, Project administration, Supervision, Writing–original draft, Writing–review and editing. AB: Conceptualization, Data curation, Methodology, Project administration, Supervision, Writing–original draft, Writing–review and editing.

Funding

The author(s) declare that no financial support was received for the research, authorship, and/or publication of this article.

Conflict of interest

The authors declare that the research was conducted in the absence of any commercial or financial relationships that could be construed as a potential conflict of interest.

Publisher's note

References

Abdolahipour, S., Mani, M., and Shams Taleghani, A. (2022a). Experimental investigation of flow control on a high-lift wing using modulated pulse jet vortex generator. *J. Aerosp. Eng.* 35 (5), 05022001. doi:10.1061/(asce)as.1943-5525.0001463

Abdolahipour, S., Mani, M., and Shams Taleghani, A. (2022b). Pressure improvement on a supercritical high-lift wing using simple and modulated pulse jet vortex generator. *Flow, Turbul. Combust.* 109 (1), 65–100. doi:10.1007/s10494-022-00327-9

Bagal, N. L., and Bhardwaj, D. (2022). 48V EGR pump system development and fuel benefit evaluation. *Front. Mech. Eng.* 8, 673134. doi:10.3389/fmech.2022.673134

ElHelew, W. K., Abdelmaqsoud, A. M., ElBagoury, K. F., and Shanan, H. A. (2023). Technical and economic evaluation of an engine and irrigation pump using a T-type mixer for natural gas. *Front. Mech. Eng.* 8, 1081659. doi:10.3389/fmech.2022.1081659

Erm, L. P., and Ol, M. V. (2012). *An assessment of the usefulness of water tunnels for aerodynamic investigations*. Australia: Defence Science And Technology Organisation Victoria.

Ferretti, P., Pagliari, C., Montalti, A., and Liverani, A. (2023). Design and development of a peristaltic pump for constant flow applications. *Front. Mech. Eng.* 9, 1207464. doi:10.3389/fmech.2023.1207464

IEA-ETSAP and IRENA (2015). *Hydropower: Technology brief*. Available at: http://www.irena.org/DocumentDownloads/Publications/IRENAETSAP_Tech_Brief_E06_Hydropower.pdf (Accessed July 31, 2017).

Kang, Y. H., and Vu, H. (2014). A newly developed rotor profile for lobe pumps: generation and numerical performance assessment. *J. Mech. Sci. Technol.* 28 (3), 915–926. doi:10.1007/s12206-013-1159-7

Li, Y., Du, J., and Guo, D. S. (2019). Numerical research on viscous oil flow characteristics inside the rotor cavity of rotary lobe pump. *J. Braz. Soc. Mech. Sci. Eng.* 41, 274. doi:10.1007/s40430-019-1781-0

Li, Y., Guo, D., Fan, Z., and Du, J. (2020). Effects of different blade numbers on radial exciting force of lobe pump rotor. *Int. J. Fluid Mach. Syst.* 13 (No. 2), 281–291. doi:10.5293/ijfms.2020.13.2.281

Li, Y., Guo, D. S., and Li, X. (2018). Mitigation of radial exciting force of rotary lobe pump by gradually varied gap. *Eng. Appl. Comput. Fluid Mech.* 12, 711–723. doi:10.1080/19942060.2018.1517053

Lis, D., Januszko, A., and Dobrocinski, T. (2021). A flow analysis using a water tunnel of an innovative unmanned aerial vehicle. *Appl. Sci.* 11 (13), 5772. doi:10.3390/app11135772

Litvin, L. F., and Fuentes, A. (2004). *Gear Geometry and applied theory*. Cambridge: Cambridge University Press.

Liu, M., Tan, L., and Cao, S. (2022). Performance prediction and geometry optimization for application of pump as turbine: a review. *Front. Energy Res.* 9. Article 818118. doi:10.3389/fenrg.2021.818118

McKinney, J. D. (1983). *Microhydropower handbook*. Idaho Falls, Idaho: Technical Information Center - U.S. Department of Energy.

Mirzaei, M., Taleghani, A. S., and Shadaram, A. (2012). Experimental study of vortex shedding control using plasma actuator. *Appl. Mech. Mater.* 186, 75–86. doi:10.4028/www.scientific.net/amm.186.75

Mohammadi, M., and Taleghani, A. S. (2014). Active flow control by dielectric barrier discharge to increase stall angle of a NACA0012 airfoil. *Arabian J. Sci. Eng.* 39, 2363–2370. doi:10.1007/s13369-013-0772-1

Ouro, P., and Stoesser, T. (2019). Impact of environmental turbulence on the performance and loadings of a tidal stream turbine. *Flow. Turbul. Combust.* 102, 613–639. doi:10.1007/s10494-018-9975-6

Phommachanh, D., Kurokawa, J., Choi, Y.-D., and Nakajima, N. (2006). Development of a positive displacement micro-hydro turbine. JSME Int. J. *Ser. B* 49 (No. 2), 482–489. doi:10.1299/jsmeb.49.482

Salmasi, A., Shadaram, A., and Taleghani, A. S. (2013). Effect of plasma actuator placement on the airfoil efficiency at poststall angles of attack. *IEEE Trans. Plasma Sci.* 41 (10), 3079–3085. doi:10.1109/tps.2013.2280612

Saria, M. M., Badruzzamana, M., Cherchia, C., Swindleb, M., Ajamic, N., and Jacangeloa, J. G. (2018). Recent innovations and trends in in-conduit hydropower technologies and their applications in water distribution systems. *J. Environ. Manag.* 228, 416–428. doi:10.1016/j.jenvman.2018.08.078

Shams Taleghani, A., Ghajar, A., and Masdari, M. (2020). Experimental study of ground effect on horizontal tail effectiveness of a conceptual advanced jet trainer. *J. Aerosp. Eng.* 33 (4), 05020001. doi:10.1061/(asce)as.1943-5525.0001140

Sibilski, K., Nowakowski, M., Rykaczewski, D., Paweł, S., Żyluk, A., Sibilska-Mroziewicz, A., et al. (2020). Identification of fixed-wing micro aerial vehicle aerodynamic derivatives from dynamic water tunnel tests. *Aerospace* 7 (8), 116. doi:10.3390/aerospace7080116

Sonawat, A., Kim, S. J., Yang, H. M., Choi, Y. S., Kim, K. M., Lee, Y. K., et al. (2020). Positive displacement turbine - a novel solution to the pressure differential control valve failure problem and energy utilization. *Energy* 190, 116400. doi:10.1016/j.energy.2019.116400

Taleghani, A. S., Shadaram, A., and Mirzaei, M. (2012). Effects of duty cycles of the plasma actuators on improvement of pressure distribution above a NLF0414 airfoil. *IEEE Trans. Plasma Sci.* 40 (5), 1434–1440. doi:10.1109/tps.2012.2187683

Yao, L., Ye, Z., Dai, J. S., and Cai, H. (2005). Geometric analysis and tooth profiling of a three-lobe helical rotor of the Roots blower. *J. Mater. Process. Technol.* 170, 259–267. doi:10.1016/j.jmatprotec.2005.05.020

Zhang, W. (2022). Effect of streamline curvature on three-dimensionality of transitional near-wall flow in a linear hydrofoil cascade: a dns investigation. *Flow. Turbul. Combust.* 109, 603–625. doi:10.1007/s10494-022-00359-1

Zhoua, D. B., and Denga, Z. (2017). Ultra-low-head hydroelectric technology: a review. *Renew. Sustain. Energy Rev.* 78, 23–30. doi:10.1016/j.rser.2017.04.086

Nomenclature

r	Pitch Rotor Radius, m
l	Rotors Center Distance, m
t	The time
n	Ratio of the number of blades
f	Function of rotor radius based on the rotation angle, m
a	Tip curvature center distance to rotor center, m
N	Lobe numbers
X	X-axis position, m
Y	Y-axis position, m
R,r	Rotor radius, m
R_t	Maximum Radius of Rotor, m
R_{min}	Minimum Radius of Rotor, m
ABC	Concave arc of the rotor
$BCHD$	1/6 part of cross section of the rotor
CH	Cycloidal of the rotor
EJ	Cycloidal of the rotor
HDJ	Convex arc of the rotor
r_a	Radius of tooth curvature, m
k	Design variable
W	Weighted function for optimization
Q	Flow rate, m^3/min
ΔP	Pressure difference, N/m^2
W_f	the frictional losses, $N.m/min$
q	Displaced flow of a rotation, $m^3/rotation$
V	Volume of turbine shell, m^3
$k(\mu)$	The angular velocity of the rotor, $\frac{d\mu}{d_\varphi}$
$k(\varphi)$	The angular acceleration, $\frac{d^2\mu}{d_{\varphi^2}}$
$J(\varphi)$	The factor of pulsation and noise of the rotor, $\frac{d^3\mu}{d_{\varphi^3}}$
r_p	Pumping ratio
B	Aria of Single cavity, m^2
w	Blade length, m
A	Rotor aria, m^2

Greek Letters

α	Overlap angle of the tooth circle section, Degree
∅	Rotation angle of rotor, Degree
θ	Geometry parameter and start rotation angle of rotor, Degree
ρ	Tip curvature radius, m
η_p	Power efficiency
η_v	Volume efficiency

Subscripts or Superscripts

1	Rotor 1
2	Rotor 2
t	Tip
Min	Minimum
Max	Maximum
r	Real
i	Ideal
l	Loosed
ca	Component of the concave arc
ce	Component of the convex arc
cy	Component of the cycloidal

frontiers | Frontiers in Mechanical Engineering

TYPE Original Research
PUBLISHED 19 January 2024
DOI 10.3389/fmech.2023.1334830

OPEN ACCESS

EDITED BY
Arash Shams Taleghani,
Aerospace Research Institute, Iran

REVIEWED BY
Mahdi Sheikholeslam,
K.N.Toosi University of Technology, Iran
Soheila Abdolahipour,
Aerospace Research Institute, Iran

*CORRESPONDENCE
Ghazala Nazeer,
ghazala.nazeer@gscwu.edu.pk,
ghazala.nazeer@yahoo.com

RECEIVED 07 November 2023
ACCEPTED 29 December 2023
PUBLISHED 19 January 2024

CITATION
Gul F, Nazeer G, Sana M, Shigri SH and Islam SU (2024), Extensive study of flow characters for two vertical rectangular polygons in a two-dimensional cross flow.
Front. Mech. Eng 9:1334830.
doi: 10.3389/fmech.2023.1334830

Extensive study of flow characters for two vertical rectangular polygons in a two-dimensional cross flow

Farheen Gul[1], Ghazala Nazeer[1]*, Madiha Sana[2], Sehrish Hassan Shigri[3] and Shams Ul Islam[4]

[1]Department of Mathematics, The Government Sadiq College Women University, Bahawalpur, Pakistan, [2]Department of Mathematics, The Islamia University, Bahawalpur, Pakistan, [3]Department of Sciences and Humanities, National University of Computer and Emerging Sciences, Islamabad, Pakistan, [4]Department of Mathematics, Fast Nuces, Islamabad, Pakistan, [5]Comsats University, Islamabad, Pakistan

Fluid dynamics problems have a significant impact on the growth of science and technologies all over the world. This study investigates viscous fluid's behavior when interacting with two rectangular polygons positioned vertically and aligned in a staggered configuration. Two physical parameters, Reynolds Number and Gap spacings, are discussed using the Lattice Boltzmann Method for two-dimensional flow. Results are discussed in vortex snapshots, time trace histories of drag and lift coefficient, and power spectra analysis of lift coefficient. Nine distinct flow vortex streets are identified based on increasing gap spacings between the pair of two rectangular polygons. The vortex shedding mechanism is disturbed at small gap spacings and becomes optimal at large gap spacings. Different physical parameters of practical importance, like mean drag coefficient, root mean square values of drag coefficient, root mean square values of lift coefficient, and Strouhal number, approach the single rectangular polygon value at large gap spacings.

KEYWORDS

fluid dynamical system, flow control, vortex shedding mechanism, viscous fluid flow, vertical rectangular polygons, staggered arrangement

1 Introduction

Fluid forces play a vital role in engineering applications, such as when an object is moving in a fluid, and energy is required to move that object. The engineers are mainly concerned with resistance to this movement through reducing drag force (CD) and transverse fluctuating force (CL); such force acts on a body that produces vertical vibration and may cause damage to the structure of an object. Effective flow control is essential to save energy and reduce vibrations to avoid damaging the structure. In this regard, a comprehensive analysis of the delay of the vortex shedding mechanism and the reduced fluid forces adjacent to the bluff body has attracted significant attention from researchers in the last few decades because of its great significance. The investigation of bluff body fluxes is essential to science and engineering due to their diverse flow characteristics and applications. Circular, square, or rectangular objects are typical examples of bluff bodies. Chimneys, tall structures, overhead power-line packages, wind tunnels, chemical reactions in towers, microelectromechanical systems (MEMS), and fiber cooling are just a few practical uses for the flow past bluff bodies. Numerous fluid dynamic phenomena,

including vortex shedding, flow separation, and reattachment, frequently occur in the flows around bluff bodies. Fluid dynamics are drastically altered when the number and alignment of multiple bluff bodies are changed.

Many theoretical, experimental, and numerical studies are performed in these aspects to analyze wake structure under the effects of different parameters. Researchers (Gad-el-Hak, 2000; Salmasi et al., 2013; Mohammadi and Taleghani, 2014; Abdolahipour et al., 2022a; Rahni et al., 2022; Shams Taleghani and Sheikholeslam Noori, 2022) investigated flow control basics and strategies to achieve transition delay, detachment prevention, lift augmentation, drag reduction, vortex suppression, noise reduction, and heat and mass transfer enhancements. Taleghani, A. S., et al. (Bajalan et al., 2011; Mirzaei et al., 2012; Taleghani et al., 2018; Noori et al., 2020; Abdolahipour et al., 2021; Noori et al., 2021; Abdolahipour et al., 2022a; Abdolahipour et al., 2022b) investigated different phenomena like ionic wind velocity in quiescent air at atmospheric pressure caused by a dielectric barrier discharge plasma actuator, effect of modulated pulse jet vortex generator, Enhancing pressure on a supercritical high-lift wing by applying a Modular and Simple Pulse Jet Vortex Generator, flow field properties of a baseline single pulsed jet actuator, airfoil's active flow control using a plasma actuator, acoustic streaming in a drop created by surface acoustic waves, a sessile drop's dynamic behavior, and behavior of a circular cylinder with an airfoil through experimental methods. Luo, X et al. (Luo et al., 2021) provided a feature analysis on flow characteristics in the laminar unsteady incompressible flow regime when fluid flows past an oscillating circular cylinder. Incoming flows are affected by the drag force, while the lift force acts perpendicular to the drag force. As the flow field changes, the lift force coefficient, influenced by vortex shedding, becomes a valuable descriptor for the vortex condition. Wang, F., & Lam, K. M (Wang and Lam, 2021). presented a comprehensive study on the complex turbulent wake around a short wall-mounted cylinder immersed in a thick, turbulent boundary layer with an aspect ratio (AR = 2). The study highlighted an excellent comparison of the low-order statistics of velocity fields between PIV and LES, which does not necessarily guarantee a satisfactory reproduction of the coherent structures. Shahab, M., et al. (Shahab et al., 2021) presented a systematic study on a T-shaped control plate's influence on fluid flow characteristics around a square cylinder at Re = 100–250 with varying lengths. The results revealed the existence of an optimum length for the T-shaped control plate that leads to a reduction in fluid forces. For Re = 100, 150, and 200, the optimum length is 0.5; for Re = 250, the optimum length is 2. Ahmad, S., et al. (Ahmad et al., 2021) presented a two-dimensional numerical study on the wake characteristics and Strouhal number (St) discontinuity in the flow past a rectangular cylinder. They observed different flow patterns with AR ranging from 0.05–1 and Re ranging from 75 to 150. They found that an aspect ratio exists where the St exhibited a discontinuity. Specifically, for Re = 145 and 150, a discontinuity in the St is observed at $0.5 \leq AR \leq 0.6$. In a study by Shui, Q., et al. (Shui et al., 2021), numerical simulations were employed to investigate the flow characteristics across a pair of square cylinders arranged in tandem at Re = 100. Their research involved an in-depth exploration of the flow structures within the far-wake regions behind the downstream square cylinders, enabling the identification of the mechanisms responsible for their formation. Abbasi, W. S., et al. (Abbasi et al., 2021) numerically studied the flow control around two square cylinders using a flat plate set in the wake to investigate the optimum conditions for modifying vortex shedding and reducing fluid forces. The gap spacing varied between $0.5 \leq G \leq 10$, with fixed Re = 150. They reported that the control plate did not always suppress fluid forces and control vortex shedding, as its presence in the wake could have critical effects on fluid forces and vortex shedding. Kumar, D., & Sen, S (Kumar and Sen, 2021). numerically investigated the flow-induced vibrations of two tandem square cylinders using a stabilized space-time finite-element algorithm at Re = 100 with mass ratio $m^* = 10$. Both cylinders are placed in the co-shedding pattern gap spacing 5. In contrast, hysteresis is only detected around the onset of the lock-in regime. Seyed-Aghazadeh, B. et al. (Seyed-Aghazadeh et al., 2021) experimentally studied Flow-induced vibration (FIV) of the high-mass ratio of isolated and tandem flexible cylinders with fixed boundary conditions subjected to uniform flow. They examined the dynamic response of the cylinder for a range of center-to-center gap spacing, covering 3 to 9 times the cylinder diameter. Qiu, T. et al. (Qiu et al., 2021) conducted a numerical study on the spacing effects in 2D vortex-induced vibrations of tandem square cylinders at Re = 150 and $2 \leq X^G \leq 6$. They find four distinct wake patterns in the lock-in regime: 2S pattern with chaotic wake flow, the 2S pattern of the reattachment regime, the two-row vortex pattern of the reattachment regime, and the two-row vortex pattern of the co-shedding regime. Zhou, C. Y (Zhou et al., 2021). investigated the wake and force statistics of flow past two tandem rectangles at four different Reynolds numbers (75, 100, 125, and 150) with $0.5 \leq X^G \leq 10$. The authors presented detailed wake patterns and force coefficient results for different geometrical configurations and Reynolds numbers. Islam, S. U., et al. (Islam et al., 2018) presented a comprehensive numerical investigation into the aerodynamic behavior of three inline rectangular cylinders with varying AR = 0.25 to 3 and X^G = 0.5 to 7 with Re = 150. They indicated that the AR significantly influences the flow behavior around the rectangular cylinders. The study reveals that some specific aspect ratios may lead to vortex shedding, while others exhibit more stable flow patterns. Rahimi, H., et al. (Rahimi et al., 2020) numerically presented a comprehensive study of flow behavior between two side-by-side (SBS) circular cylinders at large Reynolds number 1×10^6 with eleven different gaps spacing to cover both laminar and turbulent flow regimes. They observed that for different gap spacing of cylinders led to variations in the vortex shedding frequency and intensity, impacting the aerodynamic forces experienced by the cylinders. Zia ul, I., et al. (Zia ul et al., 2021) discussed the study of fluid flow past two square cylinders positioned SBS and explored using dual splitter plates as a flow control technique. They declared that an increase in splitter plate length influences the wake structure by enhancing the wake length by stabilizing the shear layers before their roll-up. Rahman, H., et al. (Rahman et al., 2022) investigated the fluid flow dynamics around two SBS square cylinders with and without a splitter plate with the help of LBM. Fixed Reynolds number (Re = 150) with various gap spacing ($0 \leq Y^G \leq 4$) and configurations of the square cylinders are considered to explore different flow regimes and conditions. Additionally, at intermediate gap spacings, these values are reduced for all values of splitter heights. Chatterjee, D.,

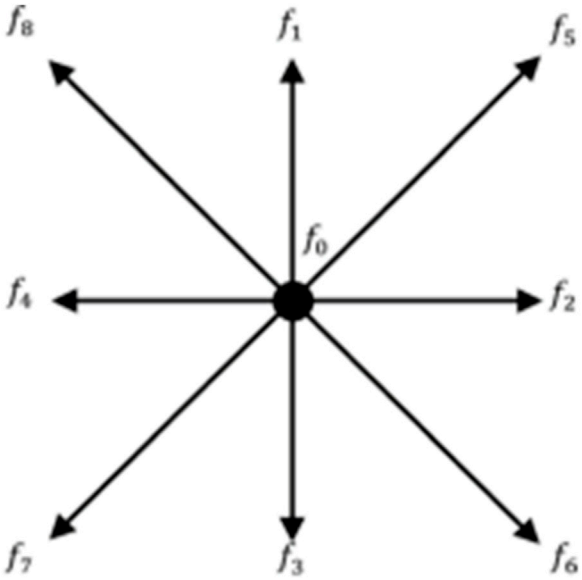

FIGURE 1
D2Q9 model.

et al. (Chatterjee et al., 2010) numerically investigated the flow across a row of five square cylinders set SBS and normal to the oncoming flow at Re = 150 and four gap spacings (1.2, 2, 3, and 4). They examined that at small gaps values, the flow exhibited chaotic behavior with prominent secondary frequencies. Aboueian, J. et al. (Aboueian and Sohankar, 2017) numerically investigated the flow across two square cylinders arranged in staggered alignment. In the modulated periodic regime, it was found that the multiple frequencies observed in the global forces acting on the downstream cylinder were more closely related to differences in the vortex-shedding frequencies of individual cylinders rather than individual shear layers. Hishikar, P. et al. (Hishikar et al., 2021) analyzed the influence of different flow parameters past two circular cylinders in an affected region using different CFD simulations at $40 \leq Re \leq 5 \times 10^6$. They determined that for different Re and G the Strouhal number does not increase linearly in the tandem alignment of the cylinders. Nazeer, G., et al. (Nazeer et al., 2019) focused on the flow characteristics around a configuration of seven square cylinders arranged in a staggered pattern using SRT-LBM to simulate the flow behavior. They analyzed vortex-shedding mechanisms occurring in the wake of the downstream row of cylinders. They also found that the secondary cylinder interaction frequency had a considerable impact on the hydrodynamic forces experienced by the cylinders. Islam, S. U., et al. (Islam et al., 2019) presented a numerical exploration of the flow behavior around multiple staggered rows of square cylinders. The study investigates the combined effects of Reynolds number and gap spacing on the two-dimensional cross-flow across the staggered configuration. At higher Reynolds numbers and specific gap spacings, the primary vortex shedding frequency dominates the flow behavior, while the secondary frequency becomes negligible. Fezai, S., et al. (Fezai et al., 2021) conducted a numerical examination of flow behavior around a configuration of three-square cylinders staggered in two triangular arrangements at $1 \leq Re \leq 110$. Their research establishes the critical Reynolds number for both triangular configurations and highlights the substantial impact of the arrangement type on the bifurcation point. Abdolahipour, S (Abdolahipour, 2023). numerically examined the influence of low and high-frequency actuation on enhancing the aerodynamic capabilities of the supercritical airfoil for potential integration into a high-lift or flight control mechanism. The results of the study indicated that employing pulsed jet actuation upstream of the separation point on the supercritical airfoil at a high angle of attack successfully delayed flow separation across all actuation frequencies.

After conducting an extensive review of existing research, it has been observed that previous studies have predominantly focused on circular and square cylinders. The present study aims to contribute to understanding the flow past rectangles arranged in a staggered configuration. This research aims to open new drag reduction and flow control possibilities in practical engineering applications.

2 Lattice Boltzmann Method

In the present study, the Lattice Boltzmann method (LBM) is employed as a numerical technique to solve the governing equations of fluid flow. LBM is a relatively new computational fluid dynamics (CFD) method compared to traditional approaches like finite difference, finite volume, and finite element methods (Mohammad, 2011a). It has gained popularity in the last 2 decades due to its numerous advantages, including easy implementation, sufficient accuracy, handling complex geometries, and parallel computation [(Chopard et al., 2002)–39]. LBM is considered a powerful tool for investigating fluid flow problems numerically.

In LBM, different lattice models are used based on the specific problem under consideration (Mohammad, 2011b). For two-dimensional (2D) problems, the two-dimensional nine-velocity-

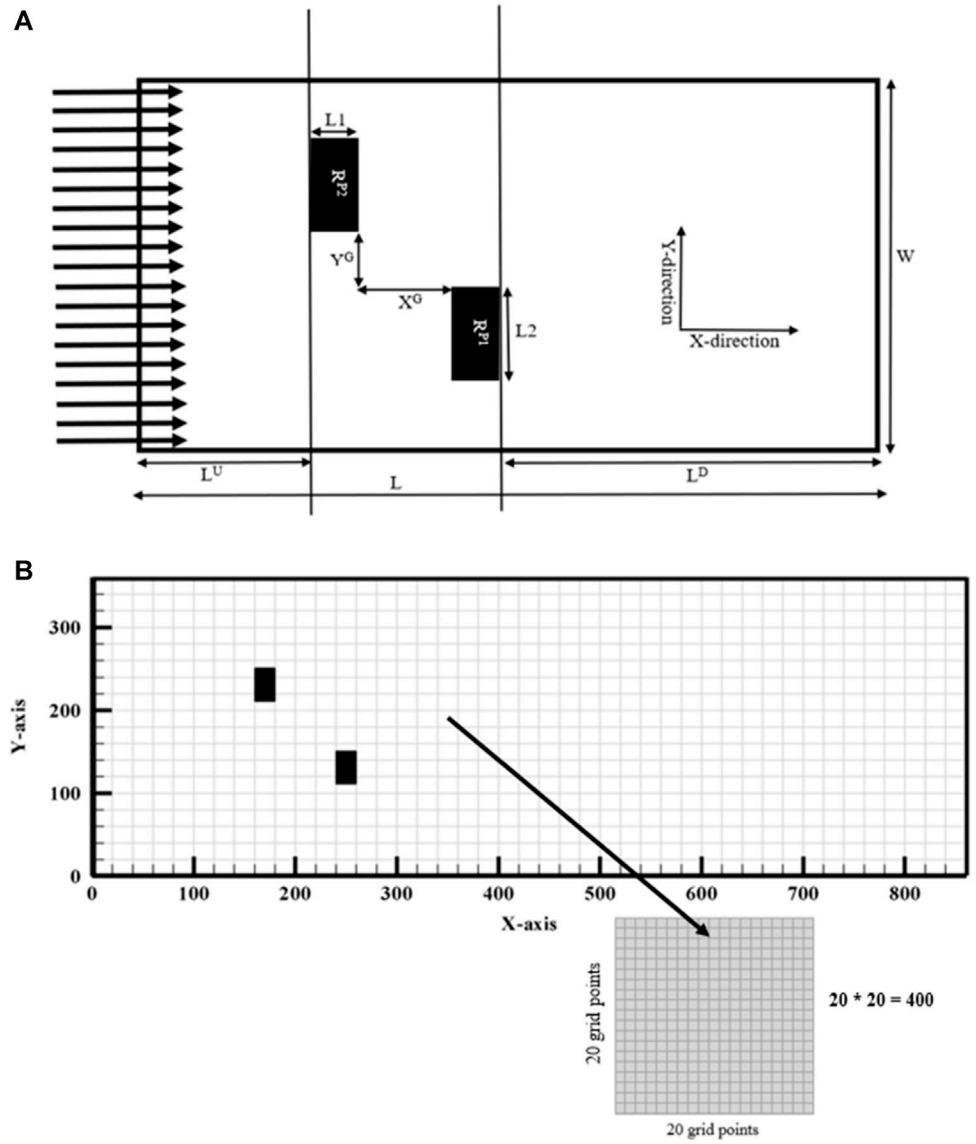

FIGURE 2
(A, B) Physical description of geometr.

particles model (D2Q9) is commonly used and employed in the current study. This model consists of nine discrete velocity directions, eight moving particles along the axis and diagonal directions, and one stationary rest particle at the model's center (see Figure 1).

The above equations (1) and (2) can be derived from the Boltzmann equation, which describes the behavior of particles in a gas using the Chapman-Enskog expansion (Viggen, 2009). However, in LBM, a simplified form of the Boltzmann equation, known as the lattice Boltzmann equation, is used to simulate fluid flow instead of directly solving the Navier-Stokes equations.

$$f_i(x + e_i, t + 1) - f_i(x, t) = -\frac{\left[f_i(x, t) - f_i^{(eq)}(x, t)\right]}{\tau} \quad (3)$$

The lattice Boltzmann equation (LBE) represents the evolution of discrete distribution functions, f_i, which indicate the position of particles in the lattice at time t, $\nu = c_s^2(\tau - 0.5)$ is the non-dimensional (SRT) parameter which controls the stability of the system, {cs = 1// $\sqrt{3}$} is the dimensionless speed of sound. The equilibrium distribution function, $f_i^{(eq)}$, is defined based on the weighting functions (w_i) specific to the D2Q9 model (Okajima, 1982):

$$f_i^{(eq)} = \rho w_i\left[1 + 3(\mathbf{e}_i \cdot \mathbf{u}) - \frac{3}{2}u^2 + \frac{9}{4}(\mathbf{e}_i \cdot \mathbf{u})^2\right] \quad (4)$$

Where, ρ is the density, w_i are the weighting functions and $\mathbf{e}_i$ are the discrete velocity directions.

The constraints for density and velocity are expressed as follows (Okajima, 1982):

$$\rho(\mathbf{x}, t) = \sum_i f_i = \sum_i f_i^{(eq)} \quad (6)$$

$$\rho(\mathbf{x}, t)\mathbf{u}(\mathbf{x}, t) = \sum_i e_i f_i = \sum_i e_i f_i^{(eq)} \quad (7)$$

TABLE 1 Mesh Configuration.

Sr. No.	G	L × W	Sr. No.	G	L × W
1	0	801 × 301	9	2.5	851 × 351
2	0.1	803 × 303	10	3	861 × 361
3	0.25	806 × 306	11	3.5	871 × 371
4	0.5	811 × 311	12	4	881 × 381
5	0.75	816 × 316	13	4.5	891 × 391
6	1	821 × 321	14	5	901 × 404
7	1.25	831 × 331	15	5.5	911 × 411
8	2	841 × 341	16	6	921 × 421

TABLE 2 Grid Independence study.

d	CDMEAN1	CDMEAN2
10	1.9286	1.5002
20	1.8700	1.4917
30	1.8223	1.4777

The lattice Boltzmann equation (Eq. 3) involves streaming (LHS) and collision (RHS) steps, representing the movement and interactions of particles in different directions. The LBM approach allows for efficient and accurate simulation of nearly incompressible flows, making it suitable for various applications in fluid dynamics research and modeling.

3 Problem description

This numerical study aims to investigate the variation in flow characteristics between two rectangular polygons, R^{P1} and R^{P2}, due to varying parameters of practical significance. In the geometry illustration see Figure 2A, two rectangular polygons, R^{P1} and R^{P2}, are aligned vertically and placed along the center line of a rectangular flow stream. Here, vertical alignment defines the difference in length and width of the polygons. The length "L1″ of the polygon is the side parallel to the X-axis, whereas the width "L2″ of the polygon is the side parallel to the Y-axis. When L2 ≥ L1, polygons are aligned vertically so that the flow separation region is much larger than the flow reattachment region. L1 is d, L2 is 2d, with an aspect ratio (AR) of 0.5, where AR is the length-to-width ratio. d represents the dimensions of a rectangular polygon. "L" represents the total length of the channel, while "W" represents the total width of the rectangular flow stream. Upstream distance "L^U" is the distance from the inlet to the R^{P2} polygon, where the flow is laminar and continuous. Downstream distance "L^D" is the distance from the R^{P1} polygon to the outlet, where the flow is rotational and turbulent. In general, "G" represents the distance between two polygons. In this investigation, the X-direction gap "X^G" and the Y-direction gap "Y^G" have the same value. G = G*/d gives the dimensionless distance between two polygons. The total length of the rectangular computing channel is now $L = L^U + L1 + X^G + L1 + L^D$. The distribution of mesh (L × W) for the proposed investigation is shown in Table 1. L^U = 8d, L^D = 25d and W = 16d is shown to be a suitable computational domain.

The Lattice Boltzmann numerical algorithm simulates flow over a single square polygon, three square polygons in tandem and side by side, and now staggered polygons. Simulations are carried out for flow over two staggered square polygons at G = 1.5 for grid sizes d = 10, 20, and 30. The computational domains for d = 10, 20, and 30 grid sizes are chosen to be (366 × 116, 731 × 231, and 1,096 × 346). Table 2 calculates mean drag coefficient for different grid sizes. Increased grid size shows that CDMEAN monotonically decreases until d = 30. Grid size refinement can increase computing cost and impact physical parameter critical values. Thus, analysis shows that d = 20 is the best grid size in terms of accuracy, efficiency, and computing cost see Figure 2B.

The flow experienced no-slip boundary conditions (u = v = 0) on the walls of the polygons. The no-slip boundary condition is applied using the bounce-back boundary condition (Namvar and Leclaire, 2023) when using LBM. The bounce-back technique states that distributed particles return to their original node after a given time. Fitting the unknown density distribution function on the wall node is most manageable with the bounce-back approach. The mathematical expression of the bounce-back scheme is derived from the kinetic equation of modulo 8. By taking distribution functions f_4, f_7, and f_8 at nodes 4, 7, and 8, particles impact the solid surface, are reflected in opposite directions, and occupy the space of particles with distribution functions f_2, f_5, and f_6 by the following expression

$$f_i(\mathbf{x_i} + \mathbf{e_i}, t + 1) = f_{i+6}(\mathbf{x_i}, t).$$

The flow enters the system with a uniform inflow velocity (u = Uo, v = 0 and Uo = 0.04385964). The viscous nature of the fluid causes it to separate into parts. It spins through the polygons and proceeds towards the exit of the channel. There, the fluid encounters the convective boundary conditions in the form of the discretized distribution function is given as follows

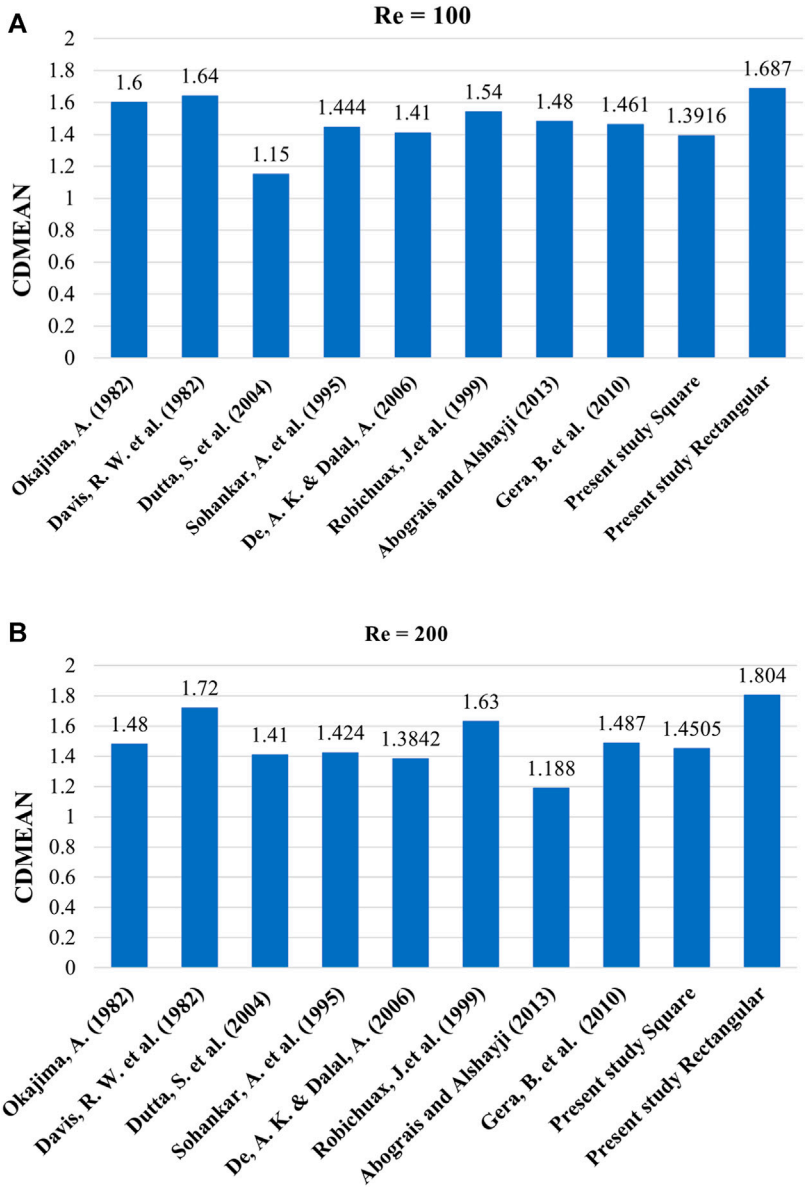

FIGURE 3
Code validation analysis.

$$\frac{f_i(\mathbf{x}, t+\Delta t) - f_i(\mathbf{x}, t)}{\Delta t} + U_o \frac{f_i(\mathbf{x}+\Delta \mathbf{x}, t+\Delta t) - f_i(\mathbf{x}, t+\Delta t)}{\Delta \mathbf{x}} = 0$$

which are employed to restrict the flow of the opposite direction in the channel. Because the width of the rectangular flow stream needs to be chosen carefully, such that the lower and the higher walls do not affect the flow before and after the Fluid Dynamical system, periodic boundary conditions are imposed. Generally it is demonstrated as

$$f_{in} = f_{out}$$

4 Code validation analysis

The lattice Boltzmann Method (LBM) has been utilized to investigate flow characteristics over various arrangements of bluff bodies, including single, numerous aligned in tandem, side-by-side (SBS), and staggered configurations. To assess the accuracy of the current code, simulations were performed on an isolated square polygon and an isolated rectangular polygon, both at a Reynolds number of 150. Two parameters that hold practical significance, namely, the drag coefficient (CD) and the Strouhal number (St) are computed. The results obtained from the simulations are compared with the findings reported in the existing scholarly literature, see Figures 3A, B.

The obtained results at Re = 100 and 200 Figures 3A, B concur highly with the previously conducted experimental and numerical investigations of Okajima, A., (Okajima, 1982), Davis, R. W. et al., Dutta, S. et al., Sohankar, A. et al., Robichuax, J. et al., and Gera, B. et al. (Davis and Moore, 1982; Sohankar et al., 1995; Robichaux et al., 1999; Dutta et al., 2004; Gera et al., 2010). Minor disparities are apparent due to variations in experimental and numerical setups

TABLE 3 Code Validation analysis.

Re = 73: G = 4	CDMEAN	St
Staggered (Rectangle 1) Present	1.9616	0.0833
Staggered (Rectangle 2) Present	1.8768	0.0948
SBS (Square 1) Present	1.6252	0.1531
SBS (Square 1) Present	1.6252	0.1531
Staggered (Square 1) Islam, S. U. Islam et al. (2019)	1.5592	0.1552
Staggered (Square 2) Islam, S. U. Islam et al. (2019)	1.4393	0.1635
SBS (Square 1) Agarwal et al. Agrawal et al. (2006)	1.7501	0.1661
SBS (Square 2) Agarwal et al. Agrawal et al. (2006)	1.7501	0.1661

TABLE 4 Comparison between Square and Rectangular polygons.

Re	Square CDMEAN	Rectangle CDMEAN	Square CDRMS	Rectangle CDRMS	Square CLRMS	Rectangle CLRMS	Square St	Rectangle St
50	1.5565	1.7605	0.37063	8.19E-05	0	0.00031	0.0602	0.0667
100	1.445	1.7897	0.37677	0.15472	0.19362	0.26538	0.1543	0.0908
150	1.4577	1.9342	0.37801	0.24641	0.24761	0.46434	0.1608	0.0974
200	1.5059	2.094	0.38152	0.3357	0.39535	0.63235	0.1565	0.1039

employed by different scientists. These variations can introduce changes to the outputs of the problems, such as modifications to boundary conditions, channel length, width, mesh resolution, and the choice of fluid. The characteristics can influence the CD and St of the situation under consideration.

Simulations were carried out for two square polygons in both side-by-side (SBS) and staggered arrangements to validate the code further. The simulations were conducted at a Reynolds number 73 and a gap ratio 4. The outcomes are compared with the research conducted by Islam, S. U (Islam et al., 2019). and Agarwal, A (Agrawal et al., 2006). presented in Table 3. This comparison highlights the substantial influence of various configurations of bluff bodies in a crossflow on the physical properties of the fluid. The present discourse has established that utilizing the 2D Lattice Boltzmann code is a reliable approach for examining the fluid dynamics of the flow through two rectangular polygons arranged in a staggered configuration.

A comparative table is constructed between square and rectangular polygon at different Re to validate the code further. Remarkable results are observed. Values of CDMEAN for different Reynolds numbers are greater for rectangular polygon as compared to square polygon. Similar behavior is obseved by CLRMS. On the Contrary, values of St for different Reynolds number are greater for Square polygon as compared to rectangular polygon see Table 4. Similar behavior is observed for CDRMS.

5 Results and discussion

This numerical study examines the flow characteristics of two rectangular polygons positioned vertically in a staggered arrangement in a two-dimensional flow field. The Reynolds Number ($Re = \frac{Uod}{\nu}$, Uo is flow velocity, d is a size of polygon and v is kinematic viscosity of fluid) is fixed at 150, while the spacing between the rectangular polygons varies (growing) from 0 to 6. The findings are provided in the form of Vortex Shedding Mechanisms (VSM) which is describe in term of Strouhal number ($St = fd/Uo$, where f is a vortex shedding frequency, u is velocity of fluid and d is th size of the object), the analysis of the temporal evolution of drag and lift coefficients, and the examination of the power spectrum energy of the lift coefficient.

The calculation of VSM involves the utilization of the two-dimensional vorticity equation. The mathematical expression for the vorticity at a specific place inside a flow field is given by the curl of the linear velocity vector, denoted as $\boldsymbol{\omega} = \nabla \times \boldsymbol{v}$. To the inherent viscosity of the fluid, two significant fluid forces, namely, drag and lift, manifest. The calculation of the drag force (FD) and lift force (FL) coefficients ($CD = 2FD/\rho Uo^2d$ and $CL = 2FL/\rho Uo^2d$, respectively) is performed using the momentum exchange method (Chen et al., 2013) during the contact between the fluid and the solid. Finally, the power spectrum is computed using the Fast Fourier Transform (FFT) algorithm.

Before examining the flow characteristics surrounding two staggered vertically positioned rectangular polygons, we investigated the flow interaction with a square and vertically positioned rectangular polygon at a Reynolds number 150. Figures 3A–L presents the results as a vortex snapshot, time histories of CD and CL plots, power spectrum plots of CL, velocity and pressure plots.

The phenomenon of vortex shedding is apparent in Figures 4A, B, wherein both square and vertically positioned rectangular polygons exhibit the shedding of vortices alternately. Solid lines

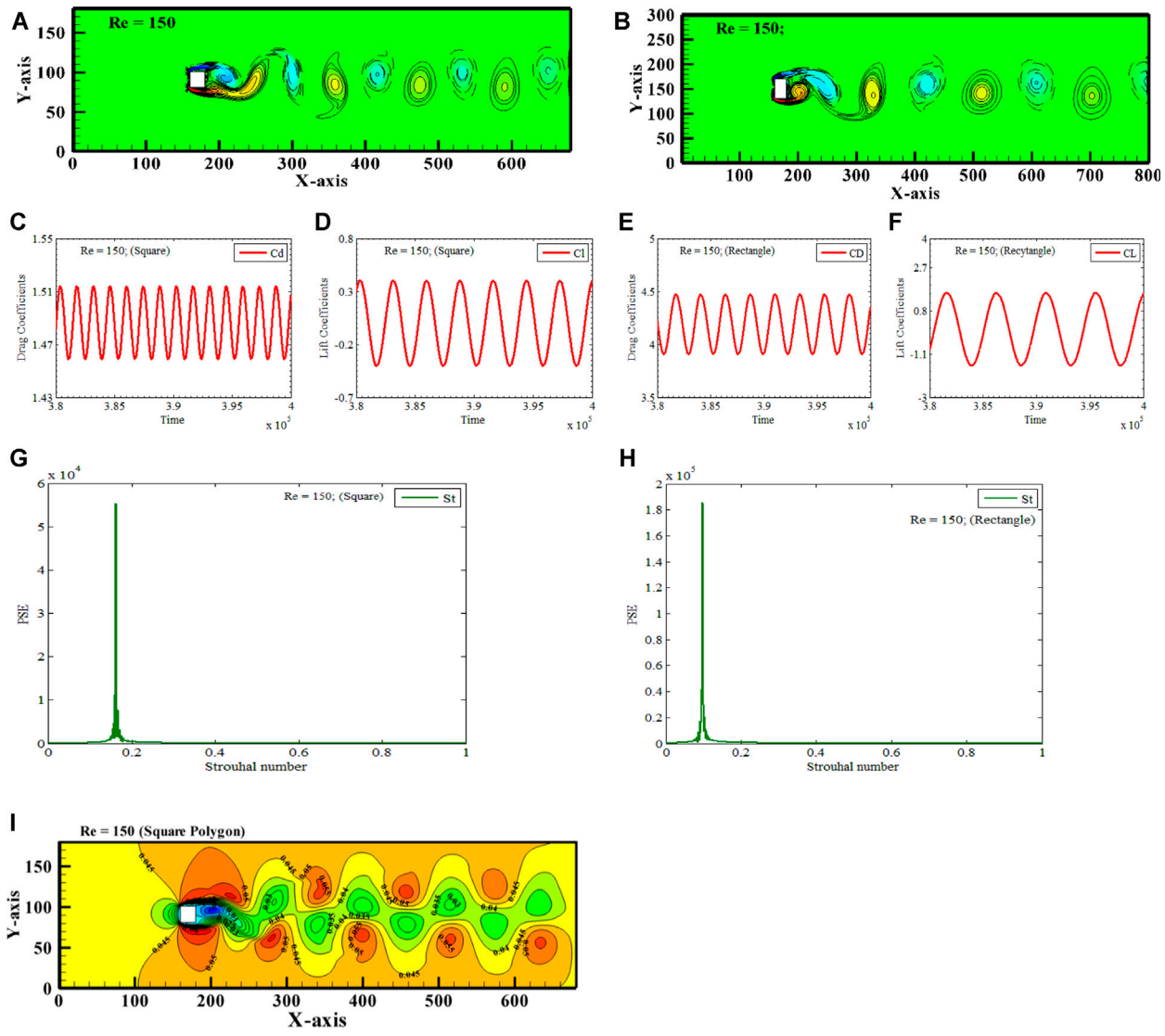

FIGURE 4
Von Karman Vortex Street **(A, B)** Vorticity contours **(C–F)** Time-trace signals of CD and CL **(G, H)** Power Energy Spectrum of CL, **(I, J)** Velocity profile and **(K, L)** Pressure profile for circular and vertically positioned rectangular polygons.(a), (b).

indicate that negative vortices are being shed from the top left corner of the polygons. In contrast, positive vortices, represented by dashed lines, are being shed from the bottom left corner. The vortices exhibit vertical movement and alternate motion within the distant region, forming a consistent pattern known as the Von Karman Vortex Street (VKVS). This flow regime is exclusive to a specific range of velocities, as it limits the range of Reynolds numbers employed.

The periodic behavior of the alternate shedding of vortices is confirmed by the time-history plots of CD and CL, as shown in Figures 4C–F. It has been found that the time of CL is consistently double that of CD. The spectrum graphs exhibit a single peak for square and vertically positioned rectangular polygons. The peak of utmost elevation guarantees the presence of rhythmic characteristics in the flow, as depicted in Figures 4G, H. The laminar flow subjected to square and vertically positioned rectangular polygons has St values of 0.1608 and 0.1630, correspondingly.

Due to viscosity, fluid sticks to the square and rectangular polygons (Fig, 4 (i-l) and has almost little velocity. Fluid velocity increases as it flows away from the polygon's surface, causing a velocity gradient in the boundary layer. The boundary layer forms as fluid travels along a polygon surface. Viscous forces slow fluid in the boundary layer. This slowdown is more significant near solid surfaces. The velocity profile over the boundary layer is usually parabolic, with the maximum velocity at the free stream (far from the polygon surface) and zero at the polygon surface. The boundary layer's polygon-fluid interface has a shear stress, which measures the fluid's force per unit area on the polygon. The fluid experiences a pressure gradient at square or rectangular polygons due to viscous forces. Pressure gradients occur from velocity gradients in the boundary layer, the fluid layer next to the solid surface, where viscous effects are significant. The fluid motion-describing Navier-Stokes equations link shear stress and pressure gradient. Pressure gradient and shear stress interact in the boundary layer. Viscous

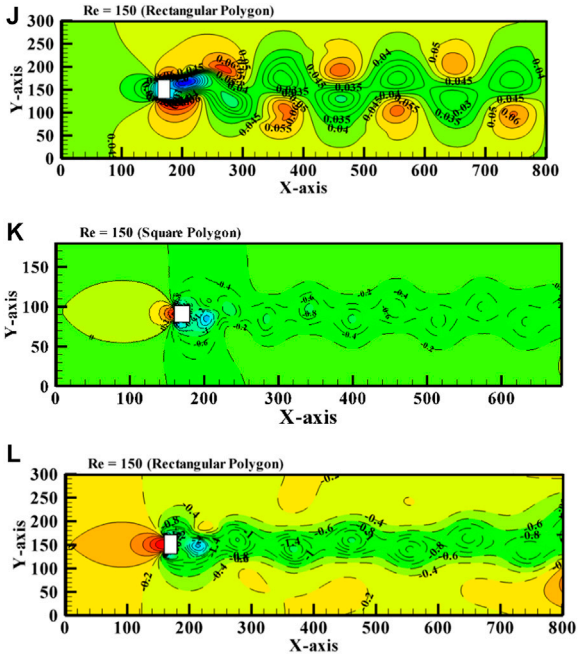

FIGURE 4
Continued.

forces may cause a pressure drop when the fluid flows along the polygon surface, especially in the boundary layer. This pressure reduction is caused by fluid kinetic energy to internal energy conversion. As fluid flows across a polygon surface, the boundary layer may separate. This separation may alter pressure distribution and flow patterns. Reattaching the boundary layer can restore pressure. Pressure is usually highest at the stagnation point when fluid meets the polygon. When the fluid rests, pressure energy becomes kinetic energy. This pressure behavior depends on fluid viscosity, flow velocity, and solid object geometry.

In the subsequent sections, we will examine the unique flow characteristics that arise when fluid flows through two horizontally positioned rectangular polygons in a staggered pattern. The primary objective of this study is to examine the impact of flow separation and re-attachment phenomena after interaction. CD1 and CD2 show the drag coefficients of R^{P1} and R^{P2}, CL1 and CL2 show the Lift coefficients of R^{P1} and $R^{P2,}$ and St1 and St2 show the Strouhal number of R^{P1} and R^{P2}, respectively.

5.1 Solitary Contorted Bluff Body Vortex Street

In this numerical study, the Reynolds number is fixed at 150, and the XY-gap is varied from 0–6, so distinct vortex streets are observed at different combinations of Re, X^G, and Y^G. A Solitary Contorted Bluff Body Vortex Street occurs at Reynolds number 150, X-gap spacing 0, and Y-gap spacing 0, respectively. (Re, X^G, Y^G) = (150, 0, 0) is the only combination of chosen physical parameters for which this vortex street is obtained see Figures 5A–E. Two rectangular polygons, R^{P1} and R^{P2}, are placed vertically along the center line of the computational domain. Since the XY-gap spacings between the polygons are zero, due to which two polygons are acting as a solitary bluff body, see Figure 5A. Also, when R^{P1} and R^{P2} are visualized individually, they appear as regularly shaped polygons, but at zero spacing between them, both R^{P1} and R^{P2} combinedly act as a single bluff body having an irregular structure called a contorted bluff body. The vortex shedding process for Solitary Bluff Body flow is represented in the gyre snapshot see Figure 5A. The uniform and laminar flow interacts with R^{P2} firstly due to the staggered alignment of polygons. It is observed that flow separation takes place in the form of negative and positive vortices. The stagnation point is relatively observed for R^{P2}, but for R^{P1}, no clear separation is visible. A clear negative vortex is shedding from the top corner of R^{P2}. The positive vortex separating from the bottom corner of R^{P2} is re-attached with the incoming flow behind R^{P1}, so no flow separation occurs from the top corner of R^{P2}. No flow is observed passing between the polygons due to zero gap spacing. The positive vortices shedding from the bottom corners of R^{P2} and R^{P1} are mixing, and a significant positive vortex is shedding from the bottom of R^{P1}. An alternate movement of the single positive and negative vortices is observed throughout the computational domain. Due to the vertical alignments of polygons, the wake of flow is centralized and widened. Both negative and positive vortices are round and oval. This type of vortex street is also observed for square and rectangle single polygons, which generate Von Karman Vortex Street. Here, we conclude that when two solid obstacles in the shape of rectangular polygons are nearby, i.e., they act as a single obstacle and generate a flow like a single solid obstacle with an expanded wake.

The above observations regarding the shedding pattern can also be verified by looking into the time series of the drag and lift coefficients of two vertically aligned polygons, R^{P1} and R^{P2}, respectively. Figures 5B, C for (Re, X^G, Y^G) = (150, 0.0, 0.0) shows that both (CD1 & CD2) and (CL1 & CL2) have a periodic behavior. The magnitude of CD1 is observed to be greater than that of CD2. The amplitudes of CL1 for the first rectangular polygon is 1.5, and that for the second polygon is 3.3,

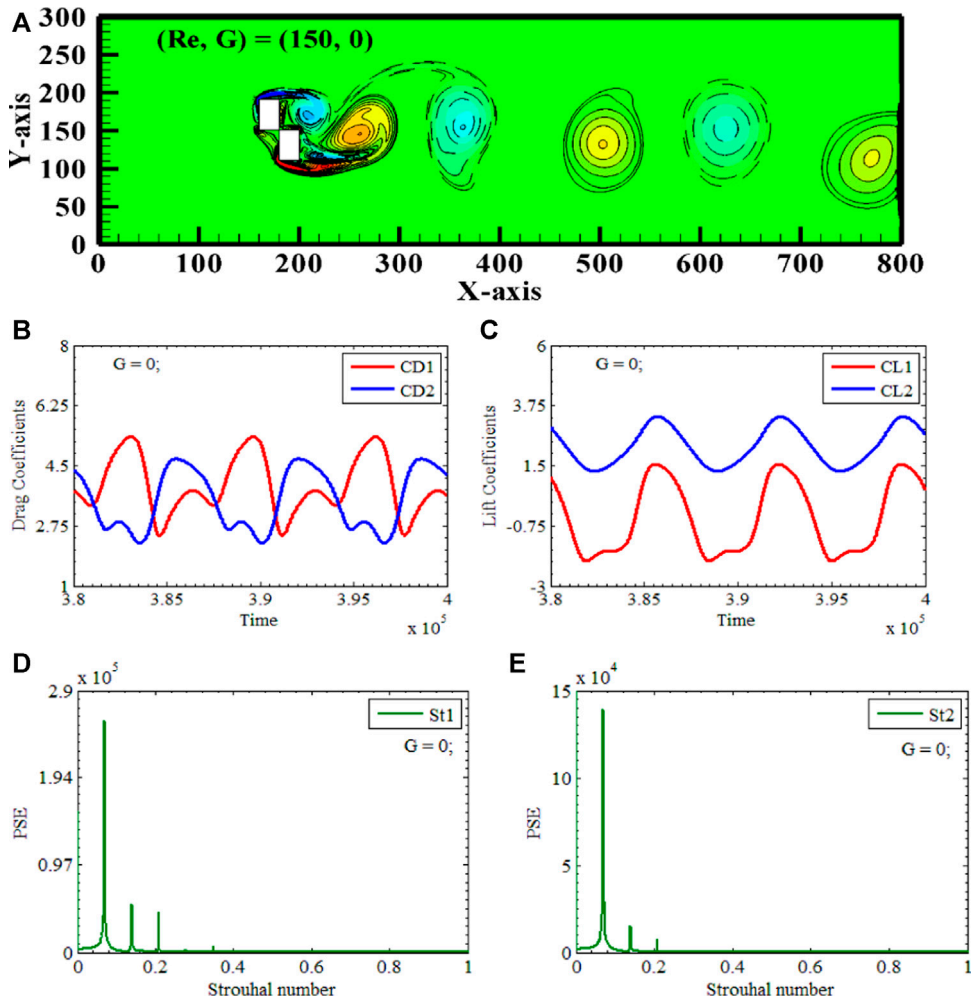

FIGURE 5
Solitary Contorted Bluff Body Vortex Street **(A)** Vorticity contours **(B, C)** Time-trace signals of (CD1 & CD2) and (CL1 & CL2) **(D, E)** Power Energy Spectrum of CL1 and CL2.

implying that the lift coefficient of the second polygon is greater than the first one. In contrast, the amplitude of CD1 and CD2 for the first rectangular polygon is 5.486 with a, and that for the second polygon is 4.9. The frequency of oscillation for both drags and lift coefficients is the same. This finding aligns with the empirical evidence indicating that the occurrence of an extremum in lift is also associated with the highest level of drag. The phenomenon is further explained by the power spectrum analysis of CL1 and CL2, respectively see Figures 5D, E. For (Re, X^G, Y^G) = (150, 0.0, 0.0), single cylinder interaction frequency is observed for both polygons. Two baby peaks along with the primary are observed at the right side of the single cylinder interaction frequency, indicating the amalgamation of shear layers.

5.2 Contorted descending bluff body vortex street

A Contorted Descending Bluff Body Vortex Street appears at Reynolds number 150, with X-gap spacing of 0.1 and Y-gap spacing of 0.1, respectively. (Re, X^G, Y^G) = (150, 0.1, 0.1) is the only combination of physical parameters to obtain this vortex street. Two rectangular polygons, R^{P1} and R^{P2}, are again placed vertically along the center line of the computational domain, having XY-gap spacings 0.1 between the polygons, due to which two polygons are acting as non-solitary bluff bodies, see Figure 6A. Also, when R^{P1} and R^{P2} are visualized individually, they appear as regularly shaped polygons, but at minimal gap spacing (0.1) between them, both R^{P1} and R^{P2} again combinedly act as a bluff body having an irregular structure called a contorted bluff body. Figure 5A depicts the vortex shedding process during the Contorted Descending Bluff Body movement as seen in the gyre photograph. Uniform and laminar flow initially interacts with R^{P2} due to the asymmetrical arrangement of polygons. Observations indicate that flow separation occurs in terms of negative and positive vortices. For R^{P2}, the stagnation point is quite evident, whereas for R^{P1}, no distinct separation is observed. A distinct negative vortex emanates from the upper corner of R^{P2} near 340d. The positive vortex that separates from the bottom corner of R^{P2} stretches and rejoins with the incoming flow behind R^{P1}. There is a slight flow between the top corner of R^{P1} and the lower corner of R^{P2} due to minimal gap spacing. The positive vortices shedding from the bottom extremities of R^{P2} and R^{P1} combine, and a giant positive vortex is shedding from the bottom of R^{P1}. The alternate movement of positive

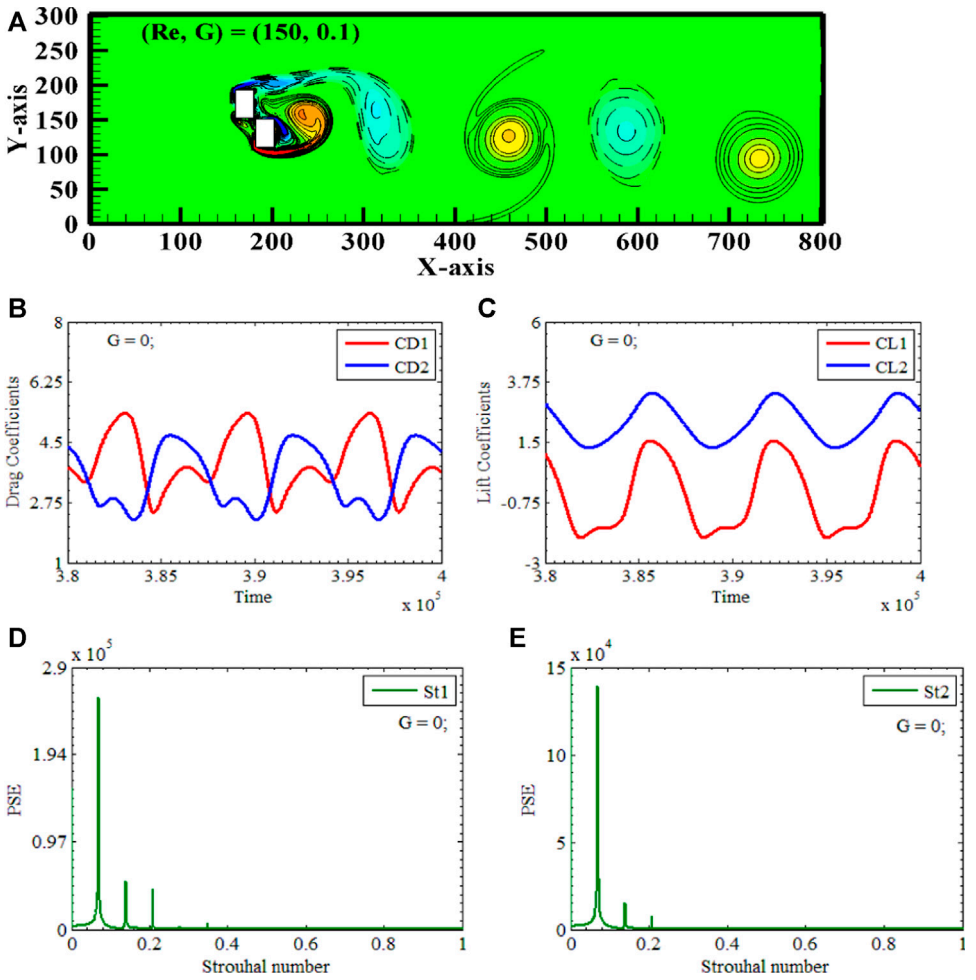

FIGURE 6
Contorted Descending Bluff Body Vortex Street **(A)** Vorticity contours **(B, C)** Time-trace signals of (CD1 & CD2) and (CL1 & CL2) **(D, E)** Power Energy Spectrum of CL1 and CL2.

and negative vortices is observed throughout the computational domain see Figure 6A. Due to the vertical alignment of polygons and 0.1 gap spacing between polygons, the flow wake is widened and deflected to the computational domain's lower wall. Both negative and positive vortices are round, oval, and spike shaped. This type of vortex street is to Von Karman Vortex Street flow with two differences, i.e., wake is descending, and vortex is showing spiked behavior at 450d.

The temporal histories are discussed for drag and lift forces. Here, CD1 and CD2 are highly periodic signals. The amplitude of CD1 is much higher when compared to CD2 because R^{P1} interacts with already disturbed flow. The behavior of the lift coefficient is opposite to that of drag. In Figure 4B, in-phase fluctuations for both drag and lift are observed for both polygons. The sinusoidal behavior of lift is observed for an upstream polygon. Primary Vortex shedding frequency (PVSF) and secondary cylinder frequencies (SCF) are observed for rectangular polygons. The facts about the shedding pattern can be corroborated by examining the time series data of the drag and lift coefficients for two vertically aligned polygons, denoted as R^{P1} and R^{P2}, respectively. In Figures 6B, C, it can be shown that for the given values of (Re, X^G, Y^G) = (150, 0.1, 0.1), CD1, CD2, CL1, and CL2 show a periodic behavior, while CL2 exhibits a sinusoidal pattern with amplitude of 3.2. The CD1 continuously shows a linear increase, with the highest value of 5.375. The drag coefficient for CD2 has a constant increase in amplitude, indicating that the maximum value is identical for each cycle. CL2 is clearly greater than CD2. The phenomenon can be further elucidated by utilizing power spectrum analysis on CL1 and CL2. When the values of (Re, X^G, Y^G) are set to (150, 0.1, 0.1), it is noticed that the single cylinder interaction frequency occurs for both polygons see Figures 6D, E. Two small peaks can be detected on the right side of the frequency at which the interaction of a single cylinder occurs. These peaks suggest that a small gap significantly impacts flow due to jet flow that affects the flow and deflects the wake towards the lower boundary.

5.3 Solitary contorted bluff body distorted vortex street

A Distorted Von Karman Street Vortex Street appears at Reynolds number 150, with X-gap spacing of 0.25 and Y-gap spacing of 0.25, respectively. (Re, X^G, Y^G) = (150, 0.25, 0.25) is the

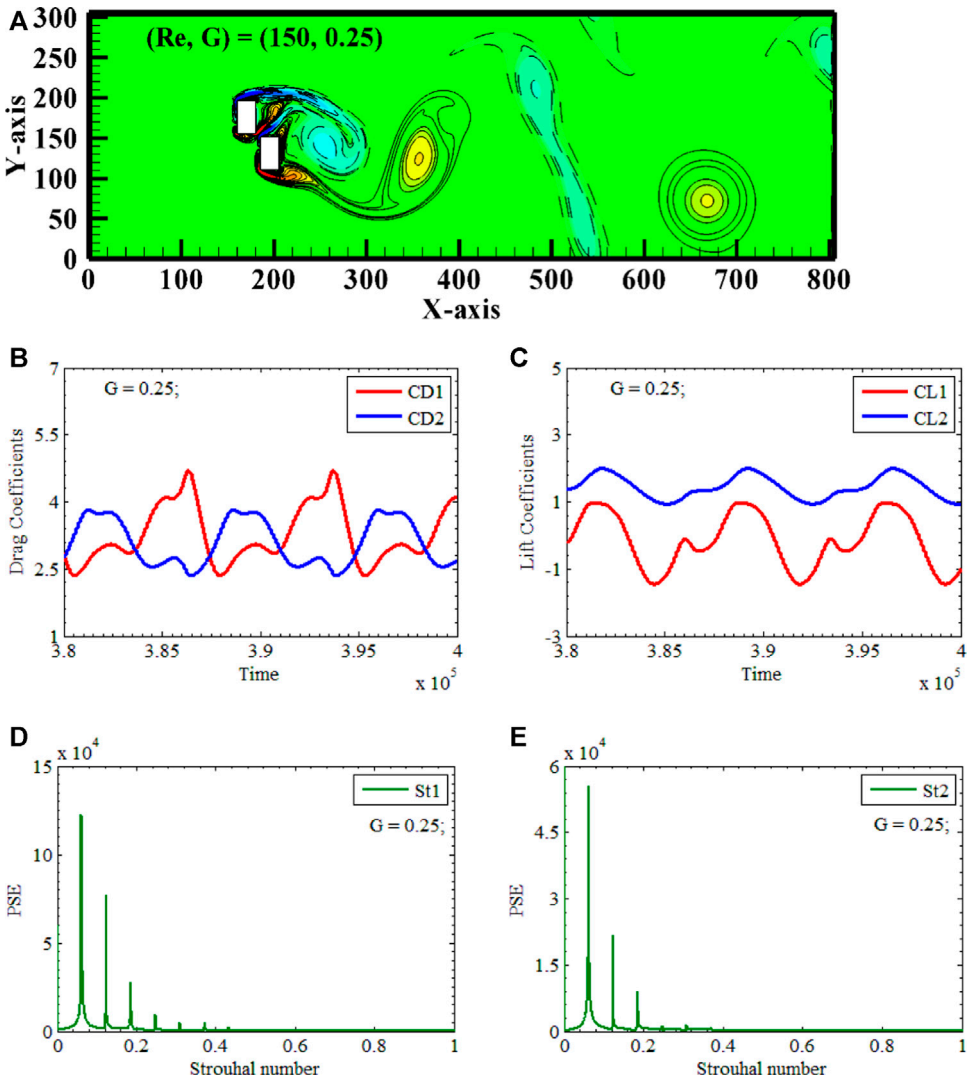

FIGURE 7
Solitary Contorted Bluff Body Distorted Vortex Street **(A)** Vorticity contours **(B, C)** Time-trace signals of (CD1 & CD2) and (CL1 & CL2) **(D, E)** Power Energy Spectrum of CL1 and CL2.

only combination of physical characteristics to obtain this vortex street. Figure 7A demonstrates that R^{P1} and R^{P2} are positioned vertically along the center line of the channel. The XY-gap spacings are increased to 0.25 between the polygons, due to which two polygons act as independent bluff bodies. In addition, when R^{P1} and R^{P2} are viewed separately, they appear as regularly shaped polygons. However, at minimal gap spacing (0.25) between them, both R^{P1} and R^{P2} function as two independent bluff bodies with a regular structure. In the gyre snapshot, independent fluid separation occurs from upstream and downstream polygons. The floe separation from the lower corner of R^{P2} and the upper corner of R^{P1} is intermixing, creating a jet flow. The jet flow between the cylinders affects the wake of flow. The sizeable positive vortex is shedding near 400d. We observe that vortices have damaged their size and shape in the far domain. Now, vortices are scattered toward the lateral walls. The alternate shedding mechanism is present in the near wake but has lost its occurrence in the far wake. Vortices are distorted, slender, rounded, and dispersed in the domain. A minimal gap spacing can change the vortex street.

Figure 7A depicts the vortex-shedding process during the Contorted Descending Bluff Body movement. R^{P2} initially interacts with uniform and laminar flow due to the asymmetrical arrangement of polygons. Observations suggest that negative and positive vortices characterize flow separation. For R^{P2}, the stagnation point is quite apparent, whereas for R^{P1}, there is no discernible separation. A distinct negative vortex emanates from the upper corner of R^{P2} near 340d. Behind R^{P1}, the positive vortex that separates from the bottom corner of R^{P2} stretches and rejoins the incoming flow. Due to minimal gap spacing, there is a minor flow between the upper corner of R^{P1} and the lower corner of R^{P2}. Positive vortices emanating from the bottom extremities of R^{P2} and R^{P1} combine, and a massive positive vortex emanates from the bottom of R^{P1}. The movement of positive and negative vortices alternates throughout the computational domain. The flow discharge is widened and deflected towards the lower wall of the

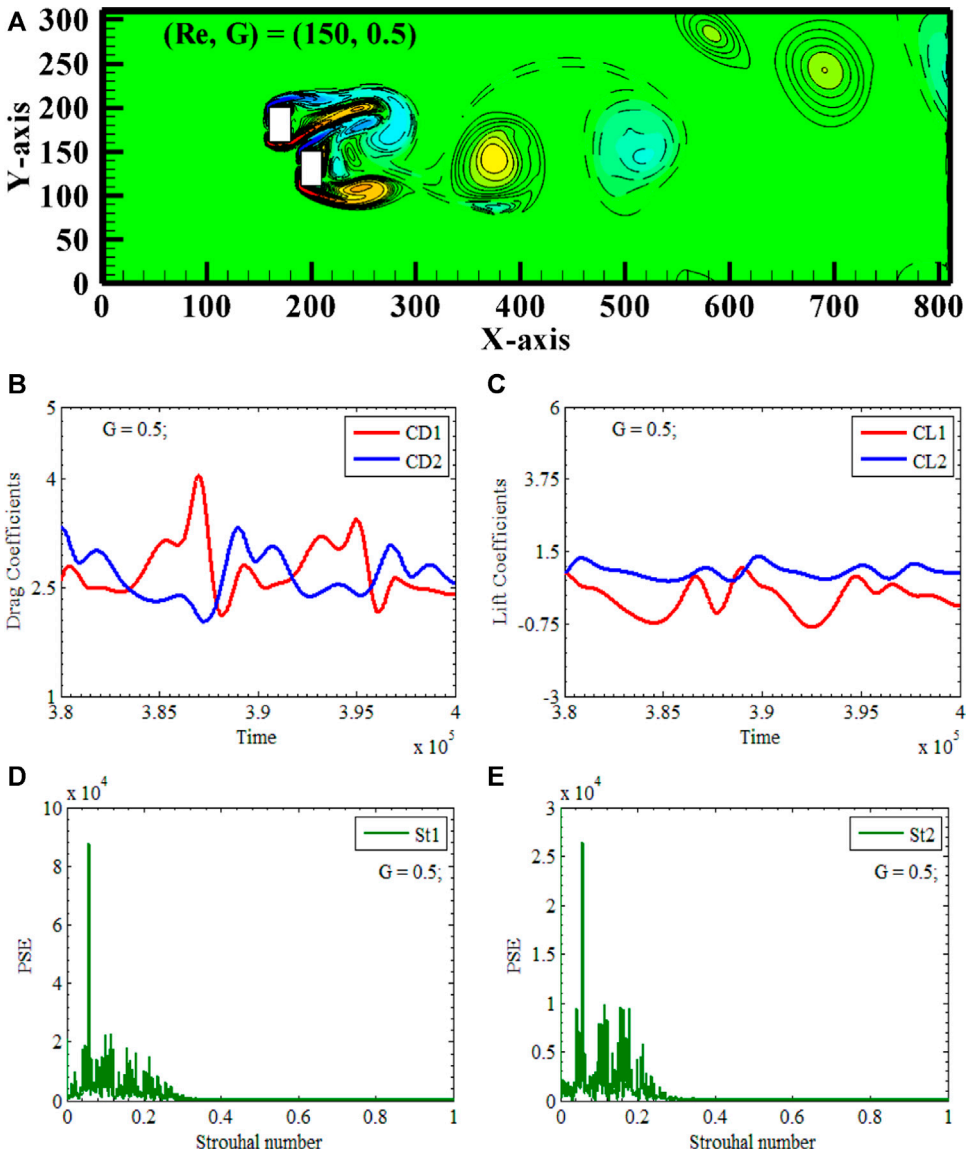

FIGURE 8
Contorted Ascending Bluff Body Vortex Street **(A)** Vorticity contours **(B, C)** Time-trace signals of (CD1 & CD2) and (CL1 & CL2) **(D, E)** Power Energy Spectrum of CL1 and CL2.

computational domain due to the vertical alignment of polygons and 0.1 gap spacing between polygons. Both positive and negative vortices are spherical, oval, and spiked. This vortex street differs from Von Karman Vortex Street flows in two ways: the wake is descending, and the vortex exhibits spiked behavior at 450d. Examining the time series data of the drag and lift coefficients for two vertically aligned polygons, designated as R^{P1} and R^{P2}, respectively, is a method that can provide supporting evidence for the assertions made concerning the shedding pattern. It can be seen in Figures 7B, C that CD1, CD2, CL1, and CL2 show periodic behaviors for the values of (Re, X^G, Y^G) equal to (150, 0.25, 0.25). CD1 has an amplitude of 4.75, while CD2 has 4. The drag curves of both polygons are attractive to each other. At the same time, the lift curve of the second polygon is higher than the lift curve of the first polygon. Due to a small gap between the polygons, we can see the distorted vortices in a far domain.

It is seen that the single cylinder interaction frequency is present for both polygons when the values of (Re, X^G, Y^G) are set to (150, 0.25, 0.25), respectively. On the right-hand side of the SCF, there are visible signs of two minor peaks. These peaks are more significant than those occurring for X^G, Y^G = 0.1. These peaks imply that a relatively tiny gap substantially impacts the flow due to jet flow, which influences the flow and directs the wake toward the lower and upper boundaries of the computational domain see Figures 7D,E.

5.4 Contorted ascending bluff body vortex street

A Contorted Ascending Bluff Body Vortex Street appears at Reynolds number 150, with X-gap spacing of 0.1 and Y-gap spacing of 0.1, respectively. (Re, X^G, Y^G) = (150, 0.5, 0.5) is the only

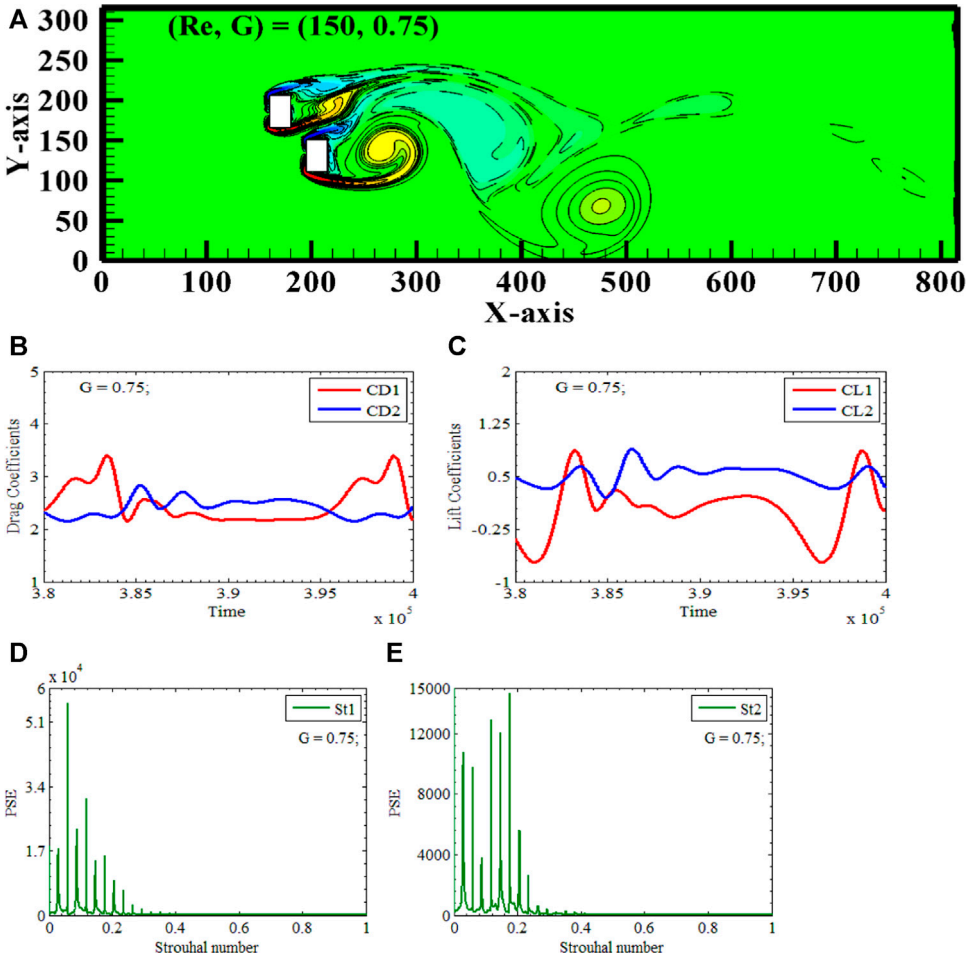

FIGURE 9
Jumbled Vortex Street **(A)** Vorticity contours **(B, C)** Time-trace signals of (CD1 & CD2) and (CL1 & CL2) **(D, E)** Power Energy Spectrum of CL1 and CL2.

combination of physical parameters to obtain this vortex street. Two rectangular polygons, R^{P1} and R^{P2}, are again placed vertically along the center line of the computational domain, having XY-gap spacings 0.5 between the polygons, due to which two polygons are acting as non-solitary bluff bodies, see Figure 8A. Figure 8A depicts the vortex shedding process during the Contorted Ascending Bluff Body movement as seen in the gyre photograph. Uniform and laminar flow initially interacts with R^{P2} due to the asymmetrical arrangement of polygons. When R^{P1} and R^{P2} are visualized keenly, they appear as regularly shaped independent polygons. However, the presence of nominal stream-wise and transverse-wise gaps of 0.5 between them dramatically impacts the development of the vortex street. We can see that an independent separation of flow is taking place from both polygons. Flow is separated from the top and bottom corners of the polygons. But it is also visible that the negative vortex detaching from the upper corner of R^{P2} is growing into a well-established negative vortex visible with dotted lines. Similarly, the positive vortex separating from the lower edge of R^{P1} is sprouting into a well-established positive vortex visible with solid lines. We will highlight the impact of the 0.5 gap between the polygons. The flow is well separated from the lower corner of R^{P2} and the upper corner of R^{P1} see Figure 8A. However, due to minimal gap spacing, the formation of positive and negative vortices is completely suppressed, so we see the sandwiching behavior of the vortices. Due to this combining mechanism of vortices, a jet flow impact appears, pushing the sandwich vortices toward the upper boundary. All this mechanism appears near the wake of two polygons. In the far domain, we see that alternate vortices are moving, which are slightly enlarged, having spikes and irregular shapes. This type of flow behavior is called Von Karman Vortex Street Flow (VKVSF), a benchmark of a single square cylinder. Here, two isolated rectangular polygons give a flow phenomenon of a single cylinder in ascending VKVSF; that's why this flow is called the Contorted Ascending Bluff Body Vortex Street. Due to the vertical alignment of polygons and 0.5 gap spacing between polygons, the flow wake is widened and deflected to the computational domain's upper wall.

The time series of the drag and lift coefficients of two vertically aligned polygons can confirm the shedding pattern. Figures 8B,C shows that (CD1 & CD2) and (CL1 & CL2) are strongly modulated curves at (Re, X^G, Y^G) = (150, 0.5, 0.5). R^{P1} interacts with the disturbed flow; CD1 amplitude is 4.0, compared to CD2, which is 3.2. Both lift coefficient curves interact at this gap spacing, indicating the same lift coefficient at some places. Lift curves did not interact before this gap. Rectangular polygons have primary vortex shedding frequency and multiple secondary cylinder interaction frequencies

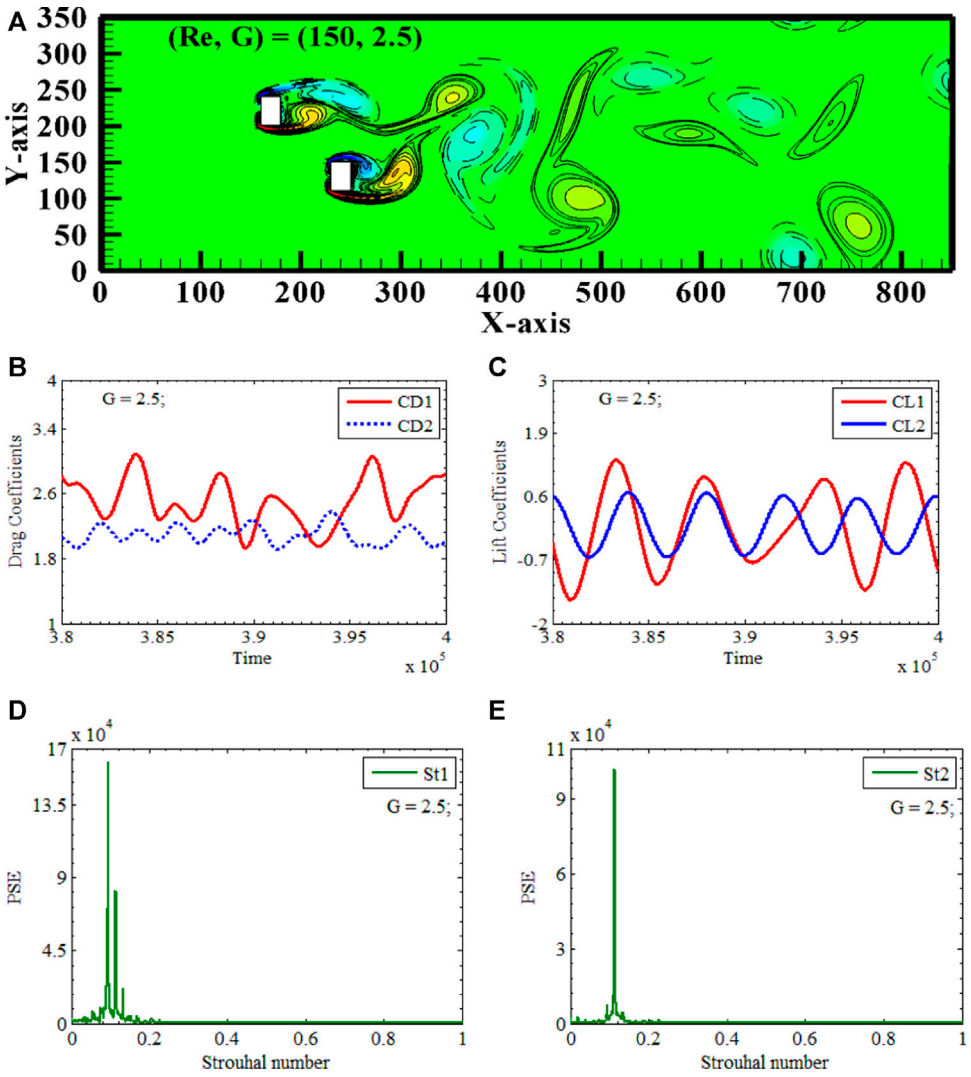

FIGURE 10
Anti-Phase Jumbled Vortex Street **(A)** Vorticity contours **(B, C)** Time-trace signals of (CD1 & CD2) and (CL1 & CL2) **(D, E)** Power Energy Spectrum of CL1 and CL2.

before and after the PVSF see Figures 8D,E. The enlargement of vortices and the spread of the wake toward the upper wall of the computational domain confirm the ascending feature of the flow.

5.5 Jumbled vortex street

A Jumbled Vortex Street appears at Reynolds number 150, with X-gap and Y-gap spacing of 0.75, 1, & 1.5, respectively. (Re, X^G, Y^G) = (150, 0.75, 0.75) is the only case we will discuss in detail. Two rectangular polygons, R^{P1} and R^{P2}, are again placed vertically along the center line of the computational domain, having increased XY-gap spacings of 0.75 between the polygons, due to which two polygons are acting as independent bluff bodies, see Figure 9A. This flow is distinguished by the absence of any discernible flow structure see Figure 9A. Independent flow separation occurs from R^{P1} and R^{P2} in the form of upper and lower shear layers, which then re-attach themselves to the horizontal surfaces of both polygons. These shear layers are spreading downward in a near computational domain. In the near domain of the channel, a chaotic flow is produced because of the upper shear layer of R^{P1} combining with the lower shear layer of R^{P2} through intermixing. The vortices shedding from the lower corner of R^{P1} is well defined. Still, the vortices shedding from the upper corner of R^{P1} & R^{P2} and the lower corner of R^{P2} are amalgamated to form a triangular-shaped vortex deflected to the lower boundary of the domain. No alternate shedding is visible in the far domain. Between 400d and 500d, the independent positive vortex is present, followed by the mixture of negative and positive vortices. Because of the expansion and amalgamation of the shear layer, the normal shedding of vortices is disrupted, which ultimately results in chaos; due to this character, the flow is named as the jumbled Vortex Street. The observations about the shedding pattern can be corroborated by examining the time series of the drag and lift coefficients of two vertically aligned polygons, denoted as R^{P1} and R^{P2}, respectively. In Figures 9B, C, it can be shown that for the given values of (Re, X^G, Y^G) = (150, 0.75, 0.75), both (CD1 & CD2) and (CL1 & CL2) exhibit a highly modulated behavior. The amplitude of

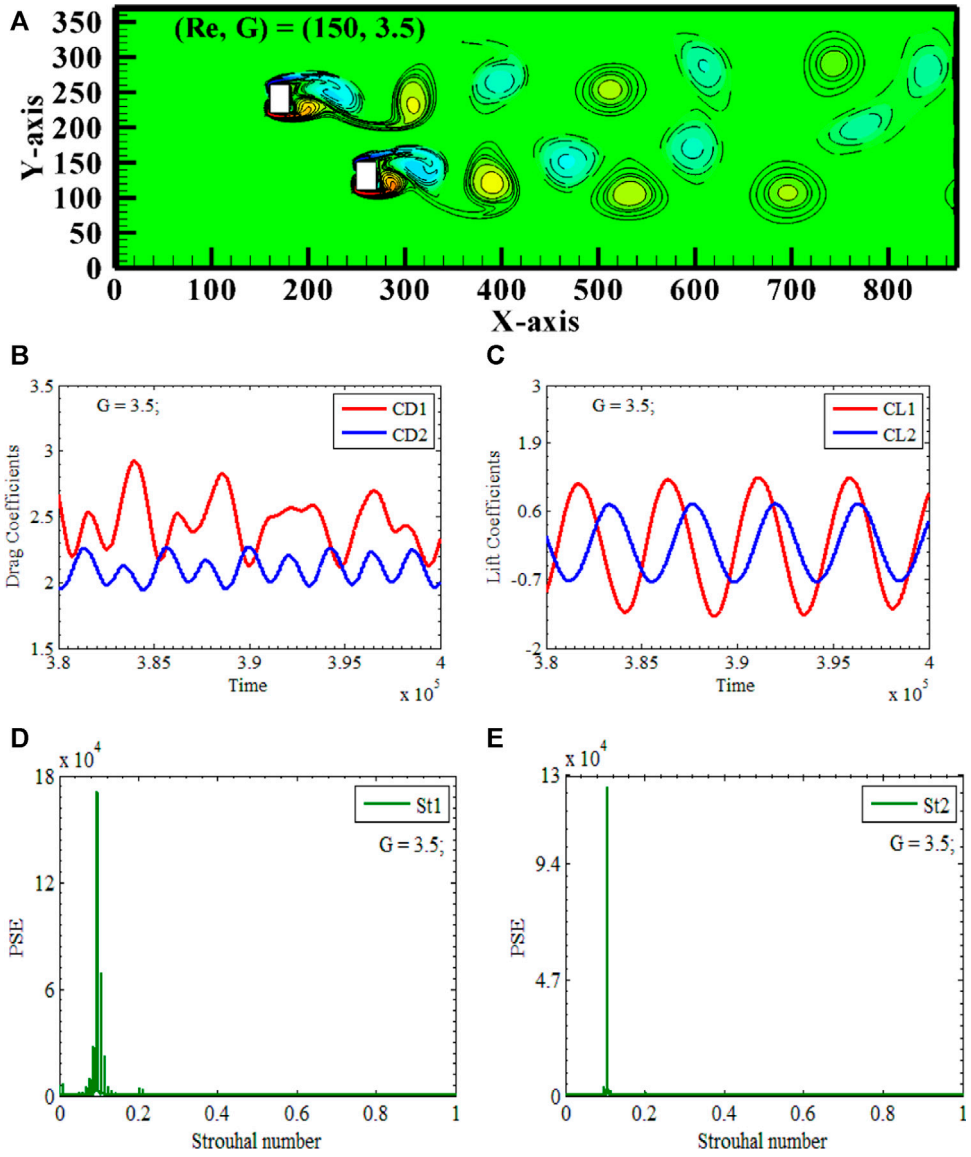

FIGURE 11
In-Phase Jumbled Vortex Street **(A)** Vorticity contours **(B, C)** Time-trace signals of (CD1 & CD2) and (CL1 & CL2) **(D, E)** Power Energy Spectrum of CL1 and CL2.

CD1 is 3.1, much higher when compared to CD2, which is 2.8 because R^{P1} interacts with already disturbed flow. Both lift coefficient curves interact at this gap spacing, showing that they have a standard lift coefficient at some points. Before this gap spacing, lift curves did not interact with each other. Primary Vortex shedding frequency and multiple SCF are observed for rectangular polygons see Figures 9D, E. It is observed that modulation and multiple peaks before and after PVSF indicate complete Jumbled flow. The distortion of vortices and amalgamation of vortices support Jumbled flow.

5.6 Anti-phase jumbled vortex street

An Anti-phase Jumbled Flow appears at Reynolds number 150, with X-gap spacing and Y-gap spacing of 2 & 2.5, respectively. (Re, X^G, Y^G) = (150, 2.5, 2.5) is the case we will discuss in detail. Two rectangular polygons, R^{P1} and R^{P2}, are again placed vertically along the center line of the computational domain, having XY-gap spacings 2.5 between the polygons, due to which two polygons are acting as independent bluff bodies, see Figure 10A. Again, the distance between the polygons is sufficient for the independent shedding of vortices from both polygons (see Figure 10). (a). It is clear from the vorticity snapshot that flow is separating from the polygons, reattaching, and then shedding negative and positive vortices. The shedding mechanism is delayed for R^{P1} as there exists a gap of 2.5 between two polygons. Additionally, the two polygons are arranged in a staggered alignment, which results in a delay in the process of separation of R^{P1}. We can see when R^{P2} is shedding its positive vortex, R^{P1} is shedding its negative vortex. There is a time-lapse due to staggered alignment in the shedding process. Also, different types of vortices are shedding simultaneously, so the flow is called Anti-phase in nature. If we

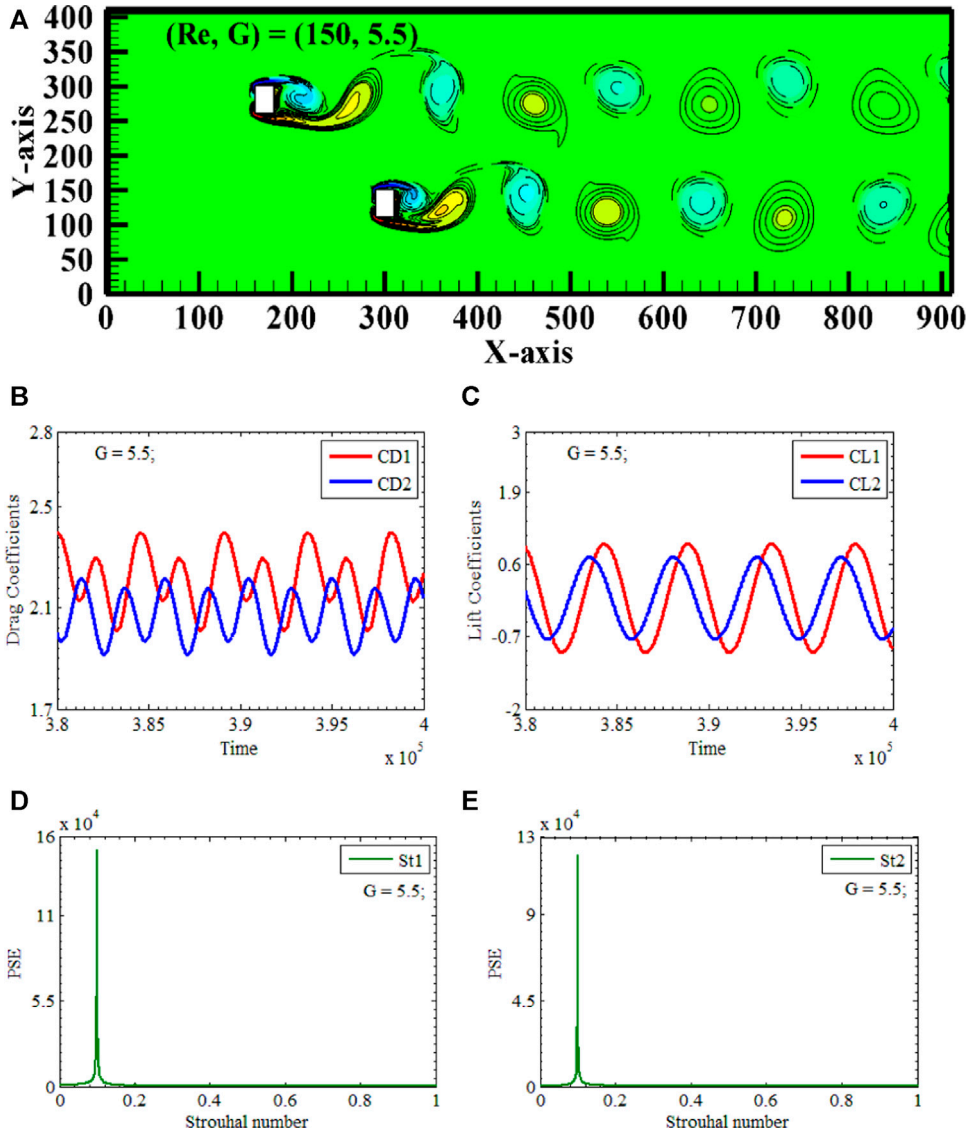

FIGURE 12
In-Phase Two Independent Row Vortex Street **(A)** Vorticity contours **(B, C)** Time-trace signals of (CD1 & CD2) and (CL1 & CL2) **(D, E)** Power Energy Spectrum of CL1 and CL2.

see the vortices in the far domain, it has been seen that shed vortices are amalgamating and becoming distorted. Now that the shedding process has taken longer than expected, a merger of vortices has occurred, which has led to anti-phase jumbled flow in the flow domain. Therefore, this flow is known as the Anti-phase Jumbled Flow because, despite its staggered nature, the shedding can be seen as anti-phase when observed simultaneously.

The previous observations regarding the shedding pattern can also be validated by looking at the drag and lift coefficients of the R^{P1} and R^{P2} time series, respectively. It can be shown in Figures 10B,C that both CD1 and CD2 have modulated signals, while CL1 and CL2 have continuously varying sinusoidal behaviors with changing amplitude. The maximum amplitude that is observed exists for CD1, having the value of 3.08 is regulated when (Re, X^G, Y^G) is equal to (150, 2.5, 2.4). Figure 5 depicts a time series of the lift and drag coefficients for two adjacent cylinders under the gap spacing of 2.5 is less than 3.08. It has been shown that CD1 has a magnitude that is larger than that of CD2. It may be deduced that the amplitudes of CL1 for the first rectangular polygon are 1.38 and that for the second polygon, they are 0.6, and the lift coefficient of the first polygon is higher than that of the second polygon. The drag and lift coefficients have no same oscillation frequency in motion. This discovery is consistent with the empirical evidence, which suggests that the occurrence of an extremum in lift is also related to the maximum amount of drag. The power spectrum study of CL1 and CL2 further explains the phenomenon. The probability of a single cylinder interaction frequency is seen for both polygons when (Re, X^G, Y^G) = (150, 2.5, 2.5). The merging of shear layers may be indicated by two baby peaks on the right-hand side of the single-cylinder interaction frequency for CL1. No, baby peaks are observed for CL2, indicating a single polygon behavior confirming the sinusoidal behavior of the lift coefficient see in Figures 10D, E.

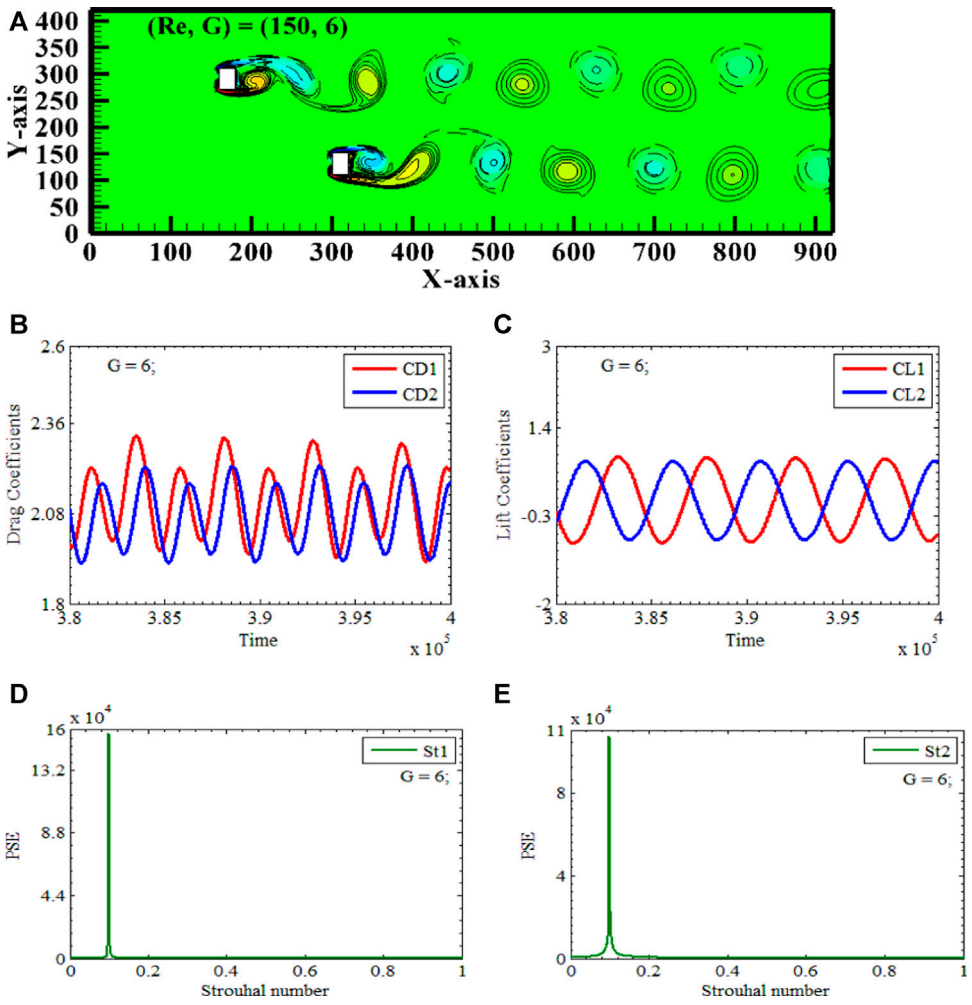

FIGURE 13
Anti-Phase Two Independent Row Vortex Street **(A)** Vorticity contours **(B, C)** Time-trace signals of (CD1 & CD2) and (CL1 & CL2) **(D, E)** Power Energy Spectrum of CL1 and CL2.

5.7 In-phase Jumbled Vortex Street

At a Reynolds number of 150, In-phase Jumbled flow manifests itself with X-gap spacings of 3, 3.5, 4, 4.5, and 5 and Y-gap spacings of 3, 3.5, 4, 4.5, and 5, respectively. The chosen scenario in which In-phase Jumbled flow (Re, X^G, Y^G) = (150, 3.5, 3.5) occurs is the one that will be the subject of our in-depth discussion. Again, two rectangular polygons, R^{P1} and R^{P2}, are placed vertically along the center line of the computational domain. This time, however, the XY-gap spacings between the polygons are set to 3.5, which results in the two polygons functioning as independent bluff bodies see Figures 11A–E. Again, the distance between the polygons is adequate for the independent shedding of vortices from both polygons see Figure 11A. The snapshot of the vorticity makes it clear that the flow is detaching from the polygons, reattaching itself, and then releasing both negative and positive vortices. Because there is a space of 3.5 between the two polygons, the shedding mechanism is delayed for this R^{P1}. In addition, the two polygons are placed in a staggered alignment, which causes a delay in the process of R^{P1}'s flow separation. When R^{P2} is shedding its positive vortex, we can see that R^{P1} is also shedding its positive vortex. In the process of shedding, there is a delay caused by the staggered alignment of the Polygons. Additionally, since the same kind of vortices are shedding simultaneously, the flow is referred to as In-phase when it occurs in nature. Looking at the vortices in the distant domain, we can see that the shed vortices combine into larger ones and become distorted. A merging of vortices has taken place, which has resulted in In-phase jumbled flow within the flow domain as a direct consequence of the shedding process taking significantly more time than was anticipated. Therefore, this flow is known as the In-phase Jumbled Flow because, although the shedding occurs staggered, it is possible to see the shedding as In-phase when observed simultaneously. The conclusions pertaining to the shedding pattern can be further substantiated by examining the Time series of drag and lift coefficients for R^{P1} and R^{P2}, correspondingly.

Figure Figures 11B, C demonstrates that CD1 exhibits modulated signals while CD2 has a periodic nature with the highest amplitude oh 2.25. CL1 and CL2 display sinusoidal behaviors with constant amplitude. The highest observed amplitude is found in CD1, with a value of 2.9, when the values of (Re, X^G, Y^G) are equal to (150, 3.5, 3.5).

Outcomes clearly demonstrated that the magnitude of CD1 is greater than that of CD2. It can be inferred from the given

information that the amplitudes of CL1 for the initial rectangular polygon are 1.12, whereas, for the subsequent polygon, they are 0.8. Additionally, it is evident that the lift coefficient of the first polygon surpasses that of the second polygon. The oscillation frequencies of the drag and lift coefficients coincide when they are in motion. This finding aligns with the empirical data, indicating a correlation between the presence of a peak in lift and the highest level of drag. The examination of the power spectrum of CL1 and CL2 offers additional elucidation into the observed event. The occurrence rate of interactions between individual cylinders is seen for both polygons under the conditions of (Re, X^G, Y^G) = (150, 3.5, 3.5). The indication of independent shedding is observed by the highest peaks and merging is observed through the existence of two smaller peaks located on the left side of the interaction frequency for CL1, which corresponds to a single cylinder see Figures 11D,E.

5.8 In-phase two independent row vortex street

An In-phase Two Independent Vortex Street occurs at Reynolds number 150, with X-gap spacing and Y-gap spacing of 5.5, respectively. (Re, X^G, Y^G) = (150, 5.5, 5.5) is the only case we will discuss in detail. Two rectangular polygons, R^{P1} and R^{P2}, are again placed vertically along the center line of the computational domain, having XY-gap spacings 5.5 between the polygons, due to which two polygons are acting as independent bluff bodies, see Figure 12A. When G equals 5.5, the distance between two polygons is sufficient to prevent interaction. As the interaction between the fluid and the polygon continues, it is possible to observe the independent shedding of both positive and negative vortices. See Figure 12A for an illustration of the two independent Von Karman Vortex Ttreets that can be seen in the whole computational domain. Both polygons shed negative vortices at the same time, which resulted in in-phase behavior. Because of these flow characteristics, this type of flow is known as In-phase Two Rows Independent Vortex Street Flow. The positive and negative vortices initially are spike-shaped, but as the flow continues through the channel, they change to an oval and round shape.

The conclusions about the shedding pattern can be further substantiated by examining the time series of drag and lift coefficients for R^{P1} and R^{P2}. Figures 12B, C demonstrates that CD1 and CD2 have a periodic nature with the highest amplitude, of 2.25. CL1 and CL2 display sinusoidal behaviors with constant

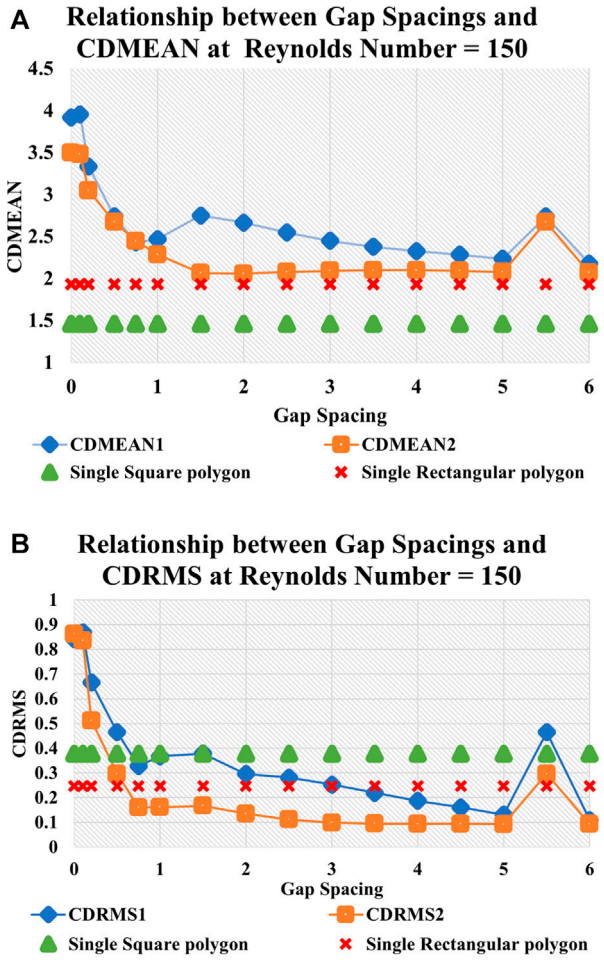

FIGURE 14
Statistical analysis. Effect of g on **(A)** CDMEAN, **(B)** CDRMS, **(C)** CLRMS, and **(D)** St.(a), (b).

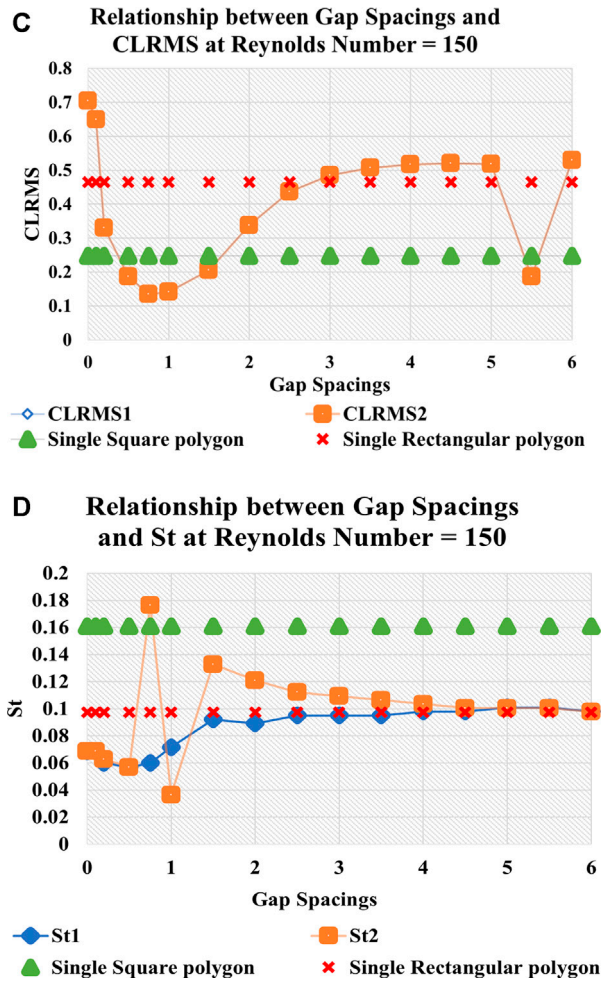

FIGURE 14
Continued.

amplitude. The highest observed amplitude is found in CD1, with a value of 2.25, when the values of (Re, X^G, Y^G) are equal to (150, 5.5, 5.5). Outcomes clearly demonstrated that the magnitude of CD1 is greater than that of CD2. It can be inferred from the given information that the amplitudes of CL1 for the initial rectangular polygon are 1.0, whereas, for the subsequent polygon, they are 0.8. Additionally, the lift coefficient of the first polygon surpasses that of the second polygon. The oscillation frequencies of the drag and lift coefficients coincide when they are in motion. This finding aligns with the empirical data, indicating a correlation between a peak in lift and the highest level of drag. Examining the power spectrum of CL1 and CL2 offers additional elucidation into the observed event. The occurrence rate of interactions between individual cylinders is seen for both polygons under the conditions of (Re, X^G, Y^G) = (150, 5.5, 5.5). The highest peaks observe the indication of independent shedding. No merging is observed since there is no existence of smaller peaks see Figures 12D, E. The power spectrum is narrow like a single polygon clearly indicating the effect of Von Karman Street on the other. The gap is vast enough that the effect of the wake of one polygon does not affect the wake of another.

5.9 Anti-phase two independent row vortex street

An Anti-phase Two Independent Vortex Street occurs at Reynolds number 150, with X-gap spacing and Y-gap spacing of 6, respectively. (Re, X^G, Y^G) = (150, 6, 6) is the only case we will discuss in detail. Two rectangular polygons, R^{P1} and R^{P2}, are again placed vertically along the center line of the computational domain, having XY-gap spacings 6 between the polygons, due to which two polygons are acting as independent bluff bodies, see Figures 13A–E. When G equals 6, the distance between two polygons is insignificant and prevents the interaction between polygons. As the interaction between the fluid and the polygon continues, it is possible to observe the independent shedding of both positive and negative vortices. See Figure 13(8) for an illustration of the two independent Von Karman Vortex Ttreets that can be seen in the whole computational domain. R^{P1} shed a negative vortex, and R^{P2} shed a positive vortex simultaneously, which resulted in Anti-phase behavior. Because of these flow characteristics, this type of flow is known as Anti-phase Two Rows Independent Vortex Street Flow. The positive and negative vortices initially are spike-shaped, but as the flow

TABLE 5 Maximum values of drag and lift coefficients for two rectangular polygons.

G	CD1	CD2	CL1	CL2
0	5.50	4.85	1.73	2.85
0.1	5.55	4.68	1.60	3.28
0.25	4.75	3.89	1.00	2.00
0.5	4.75	3.60	1.30	1.40
0.75	3.40	2.90	0.95	0.95
1	3.73	2.75	1.20	8.83
1.5	3.50	2.60	0.78	0.60
2	3.29	2.44	1.60	0.70
2.5	3.09	2.36	1.38	0.60
3	2.47	2.30	1.38	0.60
3.5	2.95	2.30	1.25	0.73
4	2.65	2.29	1.24	0.88
4.5	2.63	2.24	1.24	1.08
5	2.64	2.27	1.01	0.79
5.5	2.42	2.22	1.12	0.86
6	2.33	2.22	0.81	0.81

continues through the channel, they change to an oval and round shape. Further evidence supporting the conclusions regarding the shedding pattern may be obtained by analyzing the time series data of the drag and lift coefficients for R^{P1} and R^{P2}. The cyclic character of CD1 and CD2 is illustrated in Figures 13B, C, with the maximum amplitude recorded at 2.3. Both CL1 and CL2 exhibit sinusoidal patterns characterized by a consistent amplitude. The maximum observed amplitude is in CD1, exhibiting a magnitude of 2.2, corresponding to the values of (Re, X^G, Y^G) = (150, 6.0, 6.0).

The results clearly indicate that the magnitude of CD1 is more significant than that of CD2. Based on the above information, it can be deduced that the amplitudes of CL1 for the initial rectangular polygon are 0.775, whereas, for the subsequent polygon, it is 0.665. Furthermore, the lift coefficient of the initial polygon exceeds that of the subsequent polygon. The frequency of oscillation for the drag and lift coefficients aligns while they are in motion. This discovery is consistent with the empirical evidence, which suggests a positive association between the maximum lift and the corresponding peak in drag.

Further analysis of the power spectrum of CL1 and CL2 provides additional clarification regarding the reported phenomenon. The frequency at which individual cylinders contact is observed for both polygons with the specified conditions of (Re, X^G, Y^G) = (150, 6.0, 6.0). The tallest peaks exhibit evidence of autonomous shedding. The absence of lesser peaks precludes the occurrence of a merger of vortices see Figures 13D, E. The power spectrum has a narrow profile, resembling that of a single polygon, which strongly indicates the comparison with Von Karman Street on adjacent elements. The spacing between polygons is sufficient to ensure that the wake generated by the second polygon does not impact the wake generated by the first polygon.

6 Force statistical analysis

The deviation of different physical entities such as CDMEAN, CDRMS, CLRMS, and St with gap spacing G at fixed Re = 150 is discussed in this section and is given in Figures 14A–D. It is observed that CDMEAN2 shows a decreasing behavior till G = 5. After that, it shows a jump towards an increase and again a sudden drop at G = 6. Since R^{P2} is positioned upstream, its mean drag coefficient smoothly changes from increasing to decreasing behavior. The maximum value of CDMEAN2 is observed at G = 0 where flow is Solitary Contorted Bluff Body Vortex Street and the smallest value at G = 6 where two bluff bodies act as single bluff bodies. CDMEAN1 also shows decreasing behavior till G = 0.75; after that, it shows increasing behavior till 1.5. After that, it shows a steady decreasing behavior till G = 5; again, it shows a sudden jump at gap spacing G = 5.5 and a sudden drop at G = 6. Since R^{P1} is positioned downstream, its mean drag coefficient is very disturbed due to presence of another bluff body in the proximity of the bluff body. The mixed trend in CDMEAN is observed For R^{P1}. Clearly, CDMEAN1 > CDMEAN2. The maximum value of CDMEAN1 is observed at G = 0, where the flow is Solitary Contorted Bluff Body Vortex Street, and the smallest value at G = 6, where two bluff bodies act as single bluff bodies. A vertical V is the observed trend in both CDMEANS at G = 5–6. This phenomenon indicates that the size, shape, and distance between the bluff bodies can change the drag. At large gap spacing CDMEAN of single and two staggered rectangular polygons coincides see Figure 14A.

Due to significant gap flow interference between two staggered polygons, upstream cylinder R^{P2} CDRMS decreases until G = 0.75. CDRMS2 decreases further monotonically up to G = 5. For downstream cylinder R^{P1}, CDRMS behaves irregularly at gap spacings G = 0 and 5. Figure 14B shows that CDRMS decreases in the $1.25 \leq G \leq 5$ gap spacing range. The analysis showed that adding an upstream cylinder

TABLE 6 Minimum values of drag and lift coefficients for two rectangular polygons.

G	CD1	CD2	CL1	CL2
0	2.40	2.23	−2.10	1.39
0.1	2.58	2.40	−2.04	1.32
0.25	2.35	2.35	−1.40	0.90
0.5	2.20	2.05	−0.98	0.60
0.75	2.20	2.20	−0.77	0.20
1	1.98	2.05	−1.05	−0.15
1.5	2.00	1.90	−1.22	−0.31
2	2.01	1.79	−1.55	−0.50
2.5	2.04	1.96	−1.48	−0.70
3	1.70	1.73	−1.48	−0.70
3.5	2.10	1.95	−1.35	−0.70
4	2.10	1.95	−1.35	−0.70
4.5	2.06	1.95	−1.28	−0.80
5	1.88	1.92	−1.06	−0.84
5.5	1.93	1.87	−0.96	−0.70
6	1.94	1.91	−0.81	−0.81

R^{P2} before downstream cylinder R^{P1} and increasing cylinder gap spacings significantly lowered CDRMS2. In Figure 14B, the upstream cylinder R^{P2} has higher CDRMS2 values than a single square cylinder, while the downstream cylinder R^{P1} has lower values for $G \geq 0.75$. Importantly, CDRMS of downstream cylinder R^{P1} and upstream cylinder R^{P2} approach single cylinder data at large gap spacings (Figure 14B). The CLRMS values of two Staggered polygons exhibit identical behavior when the gap spacings G are varied, and the Re is fixed at 150. The CLRMS exhibits a declining trend as the gap spacing increases to G = 0.75; at this point, the minimal CLRMS for both cylinders is achieved. G = 0.75 is determined to be crucial due to the presence of a Jumbled Vortex Street at this specific gap spacing. There is a noticeable upward trend in the behavior of CLRMS when G is greater than or equal to 5. Additionally, it has been shown that the CLRMS values for both Staggered cylinders with a gap spacing of $G \leq 0.25$ are more pronounced compared to the data from a single cylinder see Figure 14C. This indicates the existence of a strong interaction between the wakes of the two cylinders without any vortex-generating phenomena. Furthermore, the CLRMS values for both cylinders are lower than those for a single polygon when the gap separation G is greater than or equal to 0.1–2.5 and at 5.5. This indicates that the interaction between the wakes of the two Staggered polygons is nearly insignificant. The Fast Fourier Transform of the lift coefficient estimates the Strouhal number, which describes oscillating flow behavior. As we know, a time series power spectrum is a signal that describes power distribution as frequency components. The power spectrum energy is a statistical average of the signal's frequency. In Figure 14D, the single cylinder interaction frequency, the most prominent peak of this frequency, is shown against all gap spacings. Upstream cylinder R^{P2} has the highest value at G = 0.75 and the lowest at G = 1. Meanwhile, downstream cylinder R^{P1} increases monotonically. Strouhal numbers remain constant at significant gaps. This incident effectively isolates two Staggered polygons wakes. Thus, the two cylinders' wakes barely interact at large gap spacings. At large gap spacings, all physical entities, i.e., CDMEAN, CDRMS, CLRMS, and St of both Staggered cylinders, are almost approaching the single cylinder values CDMEAN, CDRMS, CLRMS, and St.

7 Relationship between gap spacings and maximum and minimum values of CD and CL

Table 5, 6 present the maximum and minimum drag and lift values for upstream and downstream rectangular polygons. Clearly, the values of CD and CL are not same simultaneously for any chosen case. For a pair of polygons positioned in a staggered configuration, the impact of fluid forces, that is, drag and lift, is experienced by the downstream cylinder because it always gets an impact with a disturbed flow. Outcomes clearly show that the flow's maximum values of CD1 and CD2 decrease monotonically as the gap spacing between the polygons increases with CD1 > CD2. On the other hand, maximum values of CL1 and CL2 also show decreasing behavior but follow some mixing behavior. In Table 6, both minimum values of drag and lift show increasing and decreasing behaviors for different gap spacings. All this occurs due to the presence of jet flow and the irregular shape of two polygons as a unit.

8 Conclusion

A two-dimensional numerical analysis is conducted for the flow past two vertically arranged staggered rectangular polygons. The Reynolds number is fixed at 150, while the distance between

vertical polygons differs from 0 to 6. Simulations are conducted by using SRT-LBM. Nine distinct flow regimes are identified and referred to as Solo Bluff Body Flow, Distorted Solo Bluff Body Flow, Jumbled flow, In-phase Jumbled Flow, Anti-phase Jumbled flow, In-phase Two Rows Vortex Street Flow, and Anti-phase Two rows vortex Street Flow. When two rectangular polygons are situated in proximity, the distance between them has a significant effect on the flow characteristics, resulting in the development of nine distinct flow regimes with their own characteristics. For a pair of polygons positioned in a staggered configuration, the impact of fluid forces, that is, drag and lift, is experienced by the downstream cylinder because it always gets an impact with a disturbed flow. It is observed that the configuration of a bluff body can alter the flow field. The vertical alignment of polygons favors the immediate detachment of shear layers rather than promoting their reattachment and growth. The time histories of the coefficients of drag and lift alternate between modulated and sinusoidal behavior for various gaps and among the same gaps for different polygons. Strouhal numbers remain constant at significant gaps. This incident effectively isolates two Staggered polygons wakes. Thus, the two cylinders wakes barely interact at large gap spacings. At large gap spacings, all physical quantities, i.e., CDMEAN, CDRMS, CLRMS, and St of both Staggered polygons, are almost approaching the single rectangular polygons values of CDMEAN, CDRMS, CLRMS, and St. It is also observed that values of CDMEAN for different Reynolds number are greater for rectangular polygon as compared to square polygon but for St it is totally opposite.

Data availability statement

The original contributions presented in the study are included in the article/Supplementary material, further inquiries can be directed to the corresponding author.

Author contributions

FG: Conceptualization, Writing–review and editing. GN: Writing–original draft. MS: Investigation, Writing–review and editing. SS: Formal Analysis, Writing–review and editing. SI: Supervision, Writing–review and editing.

Funding

The author(s) declare financial support was received for the research, authorship, and/or publication of this article.

Acknowledgments

I thank all my colleagues for their hard work and support.

Conflict of interest

The authors declare that the research was conducted in the absence of any commercial or financial relationships that could be construed as a potential conflict of interest.

Publisher's note

References

Abbasi, W. S., Naheed, A., Islam, S. U., and Rahman, H. (2021). Investigation of optimum conditions for flow control around two inline square cylinders. *Arabian J. Sci. Eng.* 46, 2845–2864. doi:10.1007/s13369-020-05303-x

Abdolahipour, S. (2023). Effects of low and high frequency actuation on aerodynamic performance of a supercritical airfoil. *Front. Mech. Eng.* 9, 1290074. doi:10.3389/fmech.2023.1290074

Abdolahipour, S., Mani, M., and Shams Taleghani, A. (2022a). Experimental investigation of flow control on a high-lift wing using modulated pulse jet vortex generator. *J. Aerosp. Eng.* 35 (5), 05022001. doi:10.1061/(ASCE)AS.1943-5525.0001463

Abdolahipour, S., Mani, M., and Shams Taleghani, A. (2022b). Pressure improvement on a supercritical high-lift wing using simple and modulated pulse jet vortex generator. *Flow, Turbul. Combust.* 109 (1), 65–100. doi:10.1007/s10494-022-00327-9

Abdolahipour, S., Mani, M., and Taleghani, A. S. (2021). Parametric study of a frequency-modulated pulse jet by measurements of flow characteristics. *Phys. Scr.* 96 (12), 125012. doi:10.1088/1402-4896/ac2bdf

Aboueian, J., and Sohankar, A. (2017). Identification of flow regimes around two staggered square cylinders by a numerical study. *Theor. Comput. Fluid Dyn.* 31, 295–315. doi:10.1007/s00162-017-0424-2

Agrawal, A., Djenidi, L., and Antonia, R. A. (2006). Investigation of flow around a pair of side-by-side square cylinders using the lattice Boltzmann method. *Comput. fluids* 35 (10), 1093–1107. doi:10.1016/j.compfluid.2005.05.008

Ahmad, S., ul Islam, S., Nazeer, G., and Zhou, C. Y. (2021). Numerical investigation of Strouhal number discontinuity and flow characteristics around single rectangular cylinder at low aspect ratios and Reynolds numbers. *J. Braz. Soc. Mech. Sci. Eng.* 43, 315–326. doi:10.1007/s40430-021-03040-2

Bajalan, S., Shadaram, A., Hedayat, N., and Taleghani, A. S. (2011). Experimental study of frequency behavior for a circular cylinder behind an airfoil. *World Acad. Sci. Eng. Technol. Int. J. Mech. Aerosp. Industrial, Mechatron. Manuf. Eng.* 5 (11), 2356–2360. doi:10.5281/zenodo.1078273

Boix, A. C. (2013). Application of the Lattice Boltzmann Method to issues of coolant flows in nuclear power reactors. Master's thesis. Technische Universita¨t Mu¨nchen. Available at: http://hdl.handle.net/2099.1/19944.

Chatterjee, D., Biswas, G., and Amiroudine, S. (2010). Numerical simulation of flow past row of square cylinders for various separation ratios. *Comput. Fluids* 39 (1), 49–59. doi:10.1016/j.compfluid.2009.07.002

Chen, Y., Cai, Q., Xia, Z., Wang, M., and Chen, S. (2013). Momentum-exchange method in lattice Boltzmann simulations of particle-fluid interactions. *Phys. Rev. E* 88 (1), 013303. doi:10.1103/PhysRevE.88.013303

Chopard, B., Luthi, P. O., and Masselot, A. (2002). Cellular automata and lattice Boltzmann techniques: an approach to model and simulate complex systems. *Adv. Complex Syst.* 5, 103–246. doi:10.1142/S0219525902000602

Davis, R. W., and Moore, E. F. (1982). A numerical study of vortex shedding from rectangles. *J. Fluid Mech.* 116, 475–506. doi:10.1017/S0022112082000561

Dutta, S., Panigrahi, P. K., and Muralidhar, K. (2004). Effect of orientation on the wake of a square cylinder at low Reynolds numbers. Available at: http://nopr.niscpr.res.in/handle/123456789/9325.

Fezai, S., Nefzi, R., Ben-Beya, B., and Lili, T. (2021). Analysis of the interaction in flow around Three Staggered Square Cylinders at two Different triangular arrangements. *Glob. J. Soc. Eng. Sci.* 39, 2519–2534. doi:10.33552/GJES.2021.07.000651

Gad-el-Hak, M. (2000). *Flow control: passive, active, and reactive flow management*. new york: Cambridge University Press.

Gera, B., Sharma, P. K., and Singh, R. K. (2010). CFD analysis of 2D unsteady flow around a square cylinder. *Int. J. Appl. Eng. Res.* 1 (3), 602.

Hishikar, P., Dhiman, S. K., Tiwari, A. K., and Gaba, V. K. (2021). Analysis of flow characteristics of two circular cylinders in cross-flow with varying Reynolds number: a review. *J. Therm. Analysis Calorim.* 147, 5549–5574. doi:10.1007/s10973-021-10933-w

Islam, S. U., Manzoor, R., Ying, Z. C., and Islam, Z. U. (2018). Numerical investigation of different aspect ratios for flow past three inline rectangular cylinders. *J. Braz. Soc. Mech. Sci. Eng.* 40, 410–419. doi:10.1007/s40430-018-1334-y

Islam, S. U., Nazeer, G., and Shigri, S. H. (2019). Numerical investigation of different flow regimes for square cylinders in staggered configuration. *KSCE J. Civ. Eng.* 23, 2188–2197. doi:10.1007/s12205-019-0726-6

Kumar, D., and Sen, S. (2021). Flow-induced vibrations of a pair of in-line square cylinders. *Phys. Fluids* 33 (4), 043602. doi:10.1063/5.0038714

Luo, X., Zhang, W., Dong, H., Thakur, A. K., Yang, B., and Zhao, W. (2021). Numerical analysis of heat transfer enhancement of fluid past an oscillating circular cylinder in laminar flow regime. *Prog. Nucl. Energy* 139, 103853. doi:10.1016/j.pnucene.2021.103853

Mirzaei, M., Taleghani, A. S., and Shadaram, A. (2012). Experimental study of vortex shedding control using plasma actuator. *Appl. Mech. Mater.* 186, 75–86. doi:10.4028/www.scientific.net/AMM.186.75

Mohammad, A. A. (2011a). *Lattice Boltzmann method: fundamentals and engineering applications with computer codes*. New York: Springer. doi:10.1007/978-1-4471-7423-3

Mohammad, A. A. (2011b). *Lattice Boltzmann method: fundamentals and engineering applications with computer codes*. New York: Springer.

Mohammadi, M., and Taleghani, A. S. (2014). Active flow control by dielectric barrier discharge to increase stall angle of a NACA0012 airfoil. *Arabian J. Sci. Eng.* 39, 2363–2370. doi:10.1007/s13369-013-0772-1

Namvar, M., and Leclaire, S. (2023). LaBCof: lattice Boltzmann boundary condition framework. *Comput. Phys. Commun.* 285, 108647. doi:10.1016/j.cpc.2022.108647

Nazeer, G., Islam, S. U., and Shigri, S. H. (2019). Numerical investigation of vortex shedding mechanism for staggered rows of cylinders. *Heliyon* 5 (2), e01224. doi:10.1016/j.heliyon.2019.e01224

Noori, M. S., Taleghani, A. S., and Rahni, M. T. (2020). Phenomenological investigation of drop manipulation using surface acoustic waves. *Microgravity Sci. Technol.* 32, 1147–1158. doi:10.1007/s12217-020-09839-3

Noori, M. S., Taleghani, A. S., and Rahni, M. T. (2021). Surface acoustic waves as control actuator for drop removal from solid surface. *Fluid Dyn. Res.* 53 (4), 045503. doi:10.1088/1873-7005/ac12af

Okajima, A. (1982). Strouhal numbers of rectangular cylinders. *J. Fluid Mech.* 123, 379–398. doi:10.1017/S0022112082003115

Qiu, T., Zhao, Y., Du, X., and Lin, W. (2021). Spacing effect on the two-degree-of-freedom VIV of two tandem square cylinders. *Ocean. Eng.* 236, 109519. doi:10.1016/j.oceaneng.2021.109519

Rahimi, H., Tang, X., Esmaeeli, Y., Li, M., and Pourbakhtiar, A. (2020). Numerical simulation of flow around two side-by-side circular cylinders at high Reynolds number. *Int. J. Heat Technol.* 38 (1), 77–91. doi:10.18280/ijht.380109

Rahman, H., Khan, I., Islam, S. U., Abbasi, W. S., Ullah, R., and Khan, M. U. (2022). Numerical analysis of fluid flow dynamics around two side-by-side square cylinders in the presence and absence of splitter plate. *J. Braz. Soc. Mech. Sci. Eng.* 44 (11), 552. doi:10.1007/s40430-022-03804-4

Rahni, M. T., Taleghani, A. S., Sheikholeslam, M., and Ahmadi, G. (2022). Computational simulation of water removal from a flat plate, using surface acoustic waves. *Wave Motion* 111, 102867. doi:10.1016/j.wavemoti.2021.102867

Robichaux, J., Balachandar, S., and Vanka, S. P. (1999). Three-dimensional Floquet instability of the wake of square cylinder. *Phys. Fluids* 11 (3), 560–578. doi:10.1063/1.869930

Salmasi, A., Shadaram, A., and Taleghani, A. S. (2013). Effect of plasma actuator placement on the airfoil efficiency at poststall angles of attack. *IEEE Trans. Plasma Sci.* 41 (10), 3079–3085. doi:10.1109/TPS.2013.2280612

Seyed-Aghazadeh, B., Anderson, N., and Dulac, S. (2021). Flow-induced vibration of high-mass ratio isolated and tandem flexible cylinders with fixed boundary conditions. *J. Fluids Struct.* 103, 103276. doi:10.1016/j.jfluidstructs.2021.103276

Shahab, M., Ul-Islam, S., and Nazeer, G. (2021). T-shaped control plate effect on flow past a square cylinder at low Reynolds numbers. *Math. Problems Eng.* 2021, 1–19. doi:10.1155/2021/7562460

Shams Taleghani, A., and Sheikholeslam Noori, M. (2022). Numerical investigation of coalescence phenomena, affected by surface acoustic waves. *Eur. Phys. J. Plus* 137 (8), 975. doi:10.1140/epjp/s13360-022-03175-8

Shui, Q., Duan, C., Wang, D., and Gu, Z. (2021). New insights into numerical simulations of flow around two tandem square cylinders. *AIP Adv.* 11 (4). doi:10.1063/5.0042797

Sohankar, A., Davidson, L., and Norberg, C. (1995). "Numerical simulation of unsteady flow around a square two-dimensional cylinder," in *Twelfth australasian fluid Mechanics conference* (The University of Sydney, Australia), 517–520. University of Sydney.

Taleghani, A. S., Shadaram, A., Mirzaei, M., and Abdolahipour, S. (2018). Parametric study of a plasma actuator at unsteady actuation by measurements of the induced flow velocity for flow control. *J. Braz. Soc. Mech. Sci. Eng.* 40, 173–213. doi:10.1007/s40430-018-1120-x

Viggen, E. M. (2009). The Lattice Boltzmann method with applications in acoustics. Master's thesis. NTNU, Norway.

Wang, F., and Lam, K. M. (2021). Experimental and numerical investigation of turbulent wake flow around wall-mounted square cylinder of aspect ratio 2. *Exp. Therm. Fluid Sci.* 123, 110325. doi:10.1016/j.expthermflusci.2020.110325

Zhou, C. Y., ul-Islam, S., and Ying Zhou, C. (2021). The wake and force statistics of flow past tandem rectangles. *Ocean. Eng.* 236, 109476. doi:10.1016/j.oceaneng.2021.109476

Zia ul, I., Shams ul, I., and Zhou, C. Y. (2021). Flow control around two side-by-side square cylinders using dual splitter plates. *J. Braz. Soc. Mech. Sci. Eng.* 43 (2), 90. doi:10.1007/s40430-020-02795-4

Nomenclature

R^{P1}	1st rectangular polygon
R^{P2}	2nd rectangular polygon
L1	Length of the polygon is parallel to the X-axis
L2	Length of the polygon is parallel to the Y-axis
D	Mesh size
L1	20d, L2 = 40d
L	represents the total length of the channel
W	represents the total width of the rectangular flow stream
L^U	Upstream distance from the inlet to the R^{P2} polygon
L^D	Downstream distance is the distance from the R^{P1} polygon to the outlet
G	represents the distance between two polygons. In this investigation, the
G^{XY}	G/d gives the dimensionless distance between two polygons
d	dimensions of a rectangular polygon
u	X component of velocity of incoming flow
V	Y component of velocity of incoming flow
CD	Drag coefficient of single polygon
CL	Lift coefficient of single polygon
CD1	Drag coefficient of R^{P1}
CD2	Drag coefficient of R^{P2}
CL1	Lift coefficients of R^{P1}
CL2	Lift coefficients of R^{P2}
St	Strouhal number of single polygon
St1	Strouhal number of R^{P1}
St2	show the Strouhal number of R^{P2}
X^G	Gap spacing in X-direction
Y^G	Gap spacing in Y-direction
G	Gap spacing in XY-direction (same)
G^*	Non dimensionalzed gap spacing
CDMEAN	Mean drag coefficient of single polygon
CDMEAN1	Mean drag coefficient of R^{P1}
CDMEAN2	Mean drag coefficient of R^{P2}
CLRMS	Root mean square value of lift coefficient of single polygon
CLRMS1	Root mean square value of lift coefficient of R^{P1}
CLRMS2	Root mean square value of lift coefficient of R^{P2}
CDRMS	Root mean square value of drag coefficient of single polygon
CDRMS1	Root mean square value of drag coefficient of R^{P1}
CDRMS2	Root mean square value of drag coefficient of R^{P2}

frontiers | Frontiers in Mechanical Engineering

TYPE Original Research
PUBLISHED 05 February 2024
DOI 10.3389/fmech.2024.1341618

OPEN ACCESS

EDITED BY
Arash Shams Taleghani,
Aerospace Research Institute, Tehran, Iran

REVIEWED BY
Shi Tao,
Dongguan University of Technology, China
Soheila Abdolahipour,
Aerospace Research Institute, Iran
Mahdi Sheikholeslam,
K.N.Toosi University of Technology, Iran

*CORRESPONDENCE
Waqas Sarwar Abbasi,
waqas-555@hotmail.com

RECEIVED 20 November 2023
ACCEPTED 03 January 2024
PUBLISHED 05 February 2024

CITATION
Abbasi WS, Ehsan M, Rahman H, Uddin Z, Hassan MM and Saleem K (2024), Analysis of the wake mechanism in external flow around tandem bluff bodies with different aspect ratios. *Front. Mech. Eng* 10:1341618. doi: 10.3389/fmech.2024.1341618

Analysis of the wake mechanism in external flow around tandem bluff bodies with different aspect ratios

Waqas Sarwar Abbasi[1]*, Muhammad Ehsan[1], Hamid Rahman[2], Zia Uddin[3], Mohammad Mehedi Hassan[4] and Kashif Saleem[5]

[1]Department of Mathematics, Air University, Islamabad, Pakistan, [2]Department of Mathematics and Statistics, Women University Swabi, Swabi, Pakistan, [3]Software and Service Innovation, Oslo, Norway, [4]Information Systems Department, College of Computer and Information Sciences, King Saud University, Riyadh, Saudi Arabia, [5]Department of Computer Sciences and Engineering, College of Applied Studies and Community Service, King Saud University, Riyadh, Saudi Arabia

The interaction mechanism of external flow with two inline rectangular cylinders having different aspect ratios under the impact of gap spacing (G) is the subject of this research. The gap spacing between the cylinders was varied from 0.25 to 20 times their size. Both cylinders were vertically mounted, with the first having a higher aspect ratio than the second. The results revealed five distinct flow patterns under the influence of G: single slender body, shear layer reattachment, intermittent shedding, binary vortex street, and single-row vortex street. The mean pressure on both cylinders was found to vary due to changes in flow patterns. Both cylinders bore the same shedding frequency but had different pressure variations. The second cylinder placed in the wake of first experienced negative average drag force for some spacing values, while the first cylinder had positive average drag values for all chosen G. Due to the change in flow pattern from shear layer reattachment to intermittent shedding flow, the negative drag force on the second cylinder jumped to a positive drag. It was also observed that the rms values of drag and lift force coefficients, as well as their amplitudes for the second cylinder, were mostly higher than corresponding values for the first cylinder at all selected G. This study revealed that G = 4 and 8 are the critical gap spacing values due to sudden changes in fluid force parameters.

KEYWORDS

rectangular cylinders, aspect ratio, flow structure, drag, gap spacing, lift

1 Introduction

Computational fluid dynamics (CFD) is an interesting, complex, state-of-the-art field due to the rapid development of computer technology and newly developed numerical techniques and programming languages. One of the most significant aspects of CFD is the analysis of fluid–solid interactions and resulting outcomes. Much research has examined fluid flow around bluff bodies (commonly termed “cylinders”). The study of the wake structure mechanism behind cylindrical objects is important to many practical applications in various engineering disciplines. For example, such cylindrical objects appear in most civil designs, such as high-rise buildings, chimneys, suspension bridges, and many internal and external supporting components of such structures. Electronic chips are mostly rectangular/

square in cross section, thus resembling rectangular cylinders. The flow mechanism and characteristics behind these objects depend on parameters such as the blockage ratio (B), Reynolds number (Re), inflow velocities, shape, size, arrangement, and quantity of structures in the flow field.

Many numerical and experimental studies relevant to circular and rectangular/square cylindrical structure flow characteristics are apparent from the literature. Mittal and Raghuvanshi (2001) conducted numerical analysis of vortex shedding behind circular cylinders for laminar flows by considering Re ranging from 60 to 100. They found that, as the Re increases the average drag coefficient (CD_{mean}) decreases while the Strouhal number (St) increases. Belloli et al. (2014) experimentally analyzed flow around circular cylinders at high Re up to 6×10^5 and found that drag was approximately 0.85 for the flat surface conditions at $Re = 10^5$ and dropped to 0.3 at $Re = 2.5 \times 10^5$. Kuzmina and Marchevsky (2021) simulated flow interactions with circular cylinders by considering Re ranging from 20 to 200. The two flow regimes they observed were i) stable, where the flow was symmetric, and ii) vortex shedding, where they observed the von Karman vortex street. Furthermore, the separation point changed with a variation in Re. Comparing the fluid flow features, it is apparent that the circular cylinder displayed an unfixed boundary layer detachment, but the square/rectangular cylinder displayed a stable detachment point only from its edges. Due to this detachment phenomenon, the flow modes and wake structure mechanism differ in both geometries. Zhang and Zhang (2012) analyzed low-Re flow past a square cylinder that ranged from 25 to 150. They found two stable symmetric vortices behind the cylinder at $Re = 25$ and 50, indicating steady flow. They also found that pressure gradually rose while moving toward the cylinder from the inlet and dropped in the down-wake area. Perumal et al. (2012) studied the flow around a single square cylinder by considering Re ranging from 4 to 150. They found laminar, steady, and slightly separated flow from the cylinder at extremely low Re. At higher Re, the flow split into a pair of symmetrical vortices about the channel central line. They also observed that the flow appeared uniform at low B while, for moderated $B = 10$, an instability developed within the flow field for $Re = 51$. Ahmad et al. (2021) analyzed the flow characteristics around a rectangular cylinder at low aspect ratios (AR) and Re. They found that, for $AR = 0.05$, the vortex formed instantly behind the back surface of the cylinder. They also reported the sinusoidal nature of drag coefficient (CD) for all AR. Islam et al. (2012) conducted numerical simulations of rectangular cylinder flows with distinct aspect ratios by considering $Re = 100$, 150, 200, and 250 and AR varying from 0.15 to 4. They observed that the results for $AR = 0.15$ at $Re = 100$ indicated dual parallel rows of clockwise and anticlockwise vortices. At $AR = 0.5$, the vortices appeared at the top and bottom sides of the cylinder for a shorter duration. Octavianty et al. (2016) experimentally studied the radiation of sound and flow structure around a rectangular cylinder at various Re and AR with Mach numbers ((Ma) below 0.16. According to this research, the vortex formation region was extremely close to the back surface of the cylinder where the maximum spectrum line (SPL) occurred.

In the case of multiple obstacles, gap spacing (G) is another important parameter which significantly affects flow characteristics. Several studies have examined the combined effects of Re and G on fluid flows around two inline circular or square or rectangular cylinders (Shiraishi et al., 1986; Su et al., 2002; Su et al., 2004; Kuo et al., 2008; Huang et al., 2012; Mithun and Tiwari, 2014; Gnatowska et al., 2020; Rajpoot et al., 2021; Shui et al., 2021; Wang et al., 2022). Important findings of these studies are highlighted in Table 1. From fluid–solid interaction analyses in the literature, it is well-known that bluff bodies of similar dimensions, if arranged differently, such as side-by-side, staggered, or tandem to the incoming flow, have significant differences in fluid force behavior as well as near wakes formed behind them. Chakraborty et al. (2022) analyzed the influence of gap spacing on flow past two circular cylinders placed side by side by considering $Re = 5 \times 10^5$ and $G = 2$ to 14. They observed that the pressure at the front of both cylinders was greater than the pressure on the back, resulting in a positive drag force for all G. Sarvghad et al. (2011) also conducted a numerical simulation of flow over similarly arranged cylinders by considering $Re = 100$ and 200 and $1.5 \leq G \leq 4$. They categorized the flow in different patterns they termed biased flow, flip-flopping, synchronized anti-phase vortex shedding, and in-phase asymmetric. Adeeb et al. (2018) observed the flow around two side-by-side square cylinders by considering $Re = 100$, $G = 1.5$ to 5, and corner radii (R/D) = 0 to 0.5. They observed that, for $0 \leq R/D \leq 0.5$, at $G \leq 1.5$, the wake of both cylinders joined and functioned as an isolated wake structure for all R/D choices. Ma et al. (2017) analyzed the wake of two side-by-side square cylinders at Re in the range of 16–200 and $G = 0$ to 10. It was found that, when Re was low, the wake flow after both cylinders was steady state. When Re increased, the recirculation bubbles appeared within the downstream region attached with cylinders. These bubbles grew as unstable modes and dominated the steady mode. The flow became transient and vortex shedding was then observed. Burattini and Agrawal (2013) observed the interaction of wakes of two square cylinders placed side by side by considering $Re = 73$ and $G = 0.5$ to 6. It was reported that, with changing G, vortex shedding was much affected. Lee et al. (2019) reported an isolated bluff-body flow pattern for $G \leq 0.5$, an asymmetric wake flow pattern for $0.75 \leq G \leq 1.25$, a transitional flow pattern for $1.5 \leq G \leq 1.75$, and a dual street flow pattern for $G \geq 2$ for flow-past rectangular cylinders arranged side by side. Fluid flow-past staggered cylinders strongly depended on G and inclination angle (α) between cylinders. Ye et al. (2019) observed flow induced vibrations in the case of two circular cylinders in a staggered configuration at $Re = 200$, $G = 5$ to 7 with $\alpha = 0°$ to 90 °. They reported that, at $G = 5$, the vortices' generation and attachment with the second cylinder was much influenced by an inclined angle of 0° to 35° ; however, for an inclined angle beyond these values, the flow structure was not much varied. Aboueian and Sohankar (2017) numerically analyzed the shedding frequency in the case of flow past two staggered square cylinders by considering $Re = 150$, $G = 0.1$ to 6, and $\alpha = 45°$. They reported that the variations in gap spacing are directly related to the shedding frequencies. According to Alam et al. (2016), the wake flow around two staggered square cylinders is very dependent on the angle of inclination between cylinders. Small angles greatly impact flow characteristics, while larger angles more weakly influence flow characteristics.

When multiple objects (more than two) appear in the fluid flow stream, the resulting forces and flow structure may significantly differ from those seen in case of two or a single body even at the same Reynolds number or gap spacings. Alam et al. (2017) observed the

TABLE 1 Fluid flow characteristics around two bluff bodies reported in literature.

Author(s)	Geometry and method	*Re*	*G*	Important finding(s)
Su et al. (2004)	Two tandem circular cylinders, k–ε turbulence model	$Re = 10^4$ to 10^5	G = 1.5 to 10	G = 4 was termed a "critical spacing ratio" when shear layer reattachment and two vortex streets flow patterns appeared simultaneously.
Su et al. (2002)	Two tandem circular cylinders, FEM, LBM, and experiments using laser-induced fluorescence method	Re = 200	G = 1.5 to 5	Critical spacing reported between G = 4 and 5.
				At G = 3 and 4, shear layer behavior was almost similar, but the vorticity was much stronger at G = 4 than that at G = 3.
Kuo et al. (2008)	Two tandem circular cylinders; experiments in a recirculating water channel	Re = 1,000	G = 1.5 to 7	For G = 1.5, a single vortex street appeared in the wake of the downstream cylinder only.
				For $1.5 \leq G \leq 4$, coupled separating shear layers developed fluently within the gap.
				For $G \geq 6$, coupled vortex streets appeared, one behind each cylinder.
Wang et al. (2022)	Two tandem circular cylinders of different diameters; spectral element method	$Re \leq 100$	$1.0 \leq G \leq 8.0$	The critical Reynolds number significantly influenced by the ratio of the upstream cylinder's diameter to the downstream cylinder's diameter.
Shui et al. (2021)	Two tandem square cylinders, finite element method (FEM)	Re = 100	$1 \leq G \leq 9$	For $G \leq 3.5$, a steady vortex was generated within the region between the cylinders.
				For $3.5 < G \leq 4.4$, the vortex structure lost its stability and started to oscillate, but no vortex shedding occurred between the cylinders.
				For $G \geq 4.5$, complete vortex shedding was generated behind both cylinders.
Mithun and Tiwari (2014)	Two tandem square cylinders, finite volume method (FVM)	Re = 100	G = 2 to 5	For G = 2 and 3, the range of lift oscillation magnitude was greater for the upstream cylinder while, for G = 4 and 5, the range of lift oscillation magnitude for the downstream cylinder dominated that of the upstream cylinder.
Rajpoot et al. (2021)	Tandem square cylinders, FEM	Re = 100	$0.5 \leq G \leq 8$	For wall-gap ratio g/D = 0.1, 0.2, and 0.3, the flow remained steady for all values of G; for g/D = 0.8 to 4, unsteadiness appeared for all values of G; for g/D = 0.6, vortex shedding suppressed between $1 < G < 4$; at g/D = 0.4, vortex shedding no longer existed for $G < 6$.
Huang et al. (2012)	Two 2:1 rectangular cylinders in tandem, pseudospectral method	Re = 200	$1 \leq G \leq 10$	The flow was characterized by the stagnant symmetric vortex pairs within gap between cylinders as the spacing ratio G) was smaller than 3
				Periodic shedding appeared in both wakes within range $G \geq 5$.
				RMS values of lift (CL_{rms}) and drag (CD_{rms}) for the second cylinder were greater than those for the first.
Shiraishi et al. (1986)	Two tandem rectangular structures, experimental measurements	$Re = 1.59 \times 10^4$	G = 2 to 7	St decreased with increasing G up to 4, then tended to increase gradually and approach the St of an isolated cylinder for $G > 4$.
Gnatowska et al. (2020)	Two rectangular cylinders in tandem, experimental study.	Re = 4,100, 10,310, 21,070, 32,940	G = 2 to 9	Different flow phenomena appeared as the spacing between two cylinders was progressively changed

flow around three tandem circular cylinders by considering Re = 200, gap spacing between first and second cylinder (G_1) = 3.5 to 5.25, and gap spacing between the second and third cylinder (G_2) in the range 3.6–5.5. They categorized the flow structures as in-phase, antiphase, and intermediate, depending on G_1 and G_2. Eizadi et al. (2022) analyzed the transitions in the wake of six circular obstacles placed inline at Re = 40 to 180 and G = 0.5 to 18. They concluded that wake transitions of multiple cylinders depend not only on Re but also on G. Song et al. (2017) observed the flow patterns and force variations over four inline square cylinders by considering Re = 300 and G = 1.5 to 8. They reported that, when $G < 3.5$, CD_{mean} values for the downstream cylinders increased sharply with increasing G. For $G > 3.5$, the CD_{mean} values of the downstream cylinders decreased gradually with increasing G. Islam et al. (2018) investigated different aspect ratio effects on the flow around three inline cylinders at Re = 150, AR = 0.25 to 3, and G = 0.5 to 7. They observed that, at all G, the CL_{rms} of all cylinders decreased with increasing AR. Rahman et al. (2021) numerically computed the

forces on three rectangular cylinders by considering $60 \leq Re \leq 180$, $AR = 0.25$ to 4, and $G = 1.5$. They reported that the shedding frequencies of all cylinders increased while CD_{mean} decreased due to the increase in AR at all Re.

Studies describing the fluid flow around other geometries like airfoils have also been conducted (Bajalan et al., 2011; Mirzaei et al., 2012; Rangan and Santanu Ghosh, 2022; Abdolahipour, 2023). Another aspect of fluid–solid interactions is flow control around bluff bodies. Utilizing flow control strategies, efficient devices have been designed to save energy by minimizing flow-induced forces and controlling wake flow structures. Among various available flow controlling strategies, flow control through modulated pulse jet (Abdolahipour et al., 2021; Abdolahipour et al., 2022) and plasma actuator (Salmasi et al., 2013; Mohammadi and Taleghani, 2014; Taleghani et al., 2018) are frequently studied by researchers.

It can be concluded from this literature that the flow characteristics of multiple bodies are influenced by many parameters, including Re, G, B, AR, and α. Among these, fluid flows around rectangular bodies have been less investigated, especially vertically mounted bodies. Information about cases when both cylinders have different AR is very rare. From an application point of view, bluff bodies with rectangular cross sections are particularly important because, for example, most civil structures have rectangular cross sections and are vertically assembled. Electronic devices mostly have rectangular cross-sectional internal components. Flow around such bodies differs from flow around circular/square cross-sectional bodies. Hence, the current study will explore the fluid flow characteristics around two tandem rectangular bodies with different aspect ratios. The main focus will be on the effects of aspect ratios and varying gap spacing between cylinders on vorticity patterns, pressure variations, streamline behavior, and variations in fluid forces behavior. This study will also enhance our understanding of the dependence of the flow characteristics of both bodies on each other. Furthermore, it will help in designing flow control strategies for similar bodies placed in cross flows.

2 Numerical method

The current analysis utilizes the well-known numerical methodology, the lattice Boltzmann method (LBM). The simplified nature, easy implementation, and accuracy features of LBM make it more suitable than conventional methods for simulating fluid dynamics problems (Mohammad, 2011). This method involving two main steps, streaming and collision, has several advantages over the Navier–Stokes (NS) solvers. It has an explicit nature with conditional stability conditions (Chen and Doolen, 1998). The nonlinearity appearance in the case of NS equations does not appear in this method because the Boltzmann equation (BE) is quasi-linear. Pressure can be obtained through a simple procedure from the equation of state instead of dealing with the Laplace equation in each time step. LBM contains a variety of discrete models for simulating fluid flows. The current study is based upon the well-known two-dimensional nine-velocity directions (D2Q9, D indicates dimensions and Q the number of velocity directions) model (Figure 1) (Sukop and Throne, 2006).

The discrete BE along a specified direction is

$$\frac{\partial f}{\partial t} + e_i \nabla f_i = \frac{1}{\tau}\left(f_i^{eq} - f_i\right), \tag{1}$$

where t = time, f_i = distribution function, τ = parameter for relaxation time, and f_i^{eq} = the equilibrium distribution function.

After discretization through finite differencing, the lattice Boltzmann equation (LBE) takes the following form:

$$f_i(x + \Delta x, t + \Delta t) = -\omega\left[f_i(x,t) - f_i^{eq}(x,t)\right], \tag{2}$$

where $\omega = \frac{\Delta t}{\tau}$, τ is the relaxation time, and $\Delta t = \Delta x = 1$ (Wolf-Gladrow, 2000).

For the current study, the following form of f_i^{eq} is considered:

$$f_i^{eq} = \rho w_i\left[1 + 3(e_i.u) - \frac{3}{2}u^2 + \frac{9}{4}(e_i.u)^2\right], \tag{3}$$

where ρ is density, u is fluid velocity, and w_i are weighting coefficients (see Table 2).

Here, w_0 are weight-associated with rest particle, w_a are weights for particles moving along the axis, and w_d are weights for particles moving diagonally.

Density and velocity are expressed in terms of f_i as

$$\rho = \sum_{i=0}^{i=n} f_i, \tag{4}$$

$$\rho u = \sum_{i=0}^{i=n} e_i f_i. \tag{5}$$

The fluid kinematic viscosity is expressed as

$$\nu = \frac{(2\tau - 1)}{6}. \tag{6}$$

The values of e_i are given as

$$e_i = \begin{cases} (0,0), & i = 0, \\ c\left(-\cos\frac{i\pi}{2}, -\sin\frac{i\pi}{2}\right), & i = 1\ to\ 4, \\ \sqrt{2}\,c\left(-\cos\frac{(2i+1)\pi}{2}, -\sin\frac{(2i+1)\pi}{2}\right), & i = 5\ to\ 8. \end{cases} \tag{7}$$

For some recent developments of LBM schemes regarding applications in different fields, readers are referred to Noori et al. (2019) and Noori et al. (2020).

3 Problem statement

The problem's schematic diagram considered in this study is shown in Figure 2. This figure depicts a channel containing the two tandem rectangular cylinders placed in a fluid stream to be analyzed here. The height of the first cylinder (C_1) is h_1 and of the second cylinder (C_2) is h_2, and the width of both cylinders is denoted by D. In this study, h_1 and h_2 are discretized so as to have 40 and 30 lattices, respectively, while the width D has 20 lattices. Each cylinder is of a different aspect ratio (AR = height of cylinder/width of cylinder): the first cylinder has AR = 2:1 while the second has AR = 3:2. $X_u = 10D$ is the distance from the channel entrance position to C_1, and $X_d = 20D$ is the distance from C_2 to the domain outlet. The distance from the

TABLE 2 Weighting coefficients for the D2Q9 model.

Weighting coefficient	w_0	$w_a; a = 1, 2, 3, and\ 4$	$w_d; d = 5, 6, 7, and\ 8$
	4/9	1/9	1/36

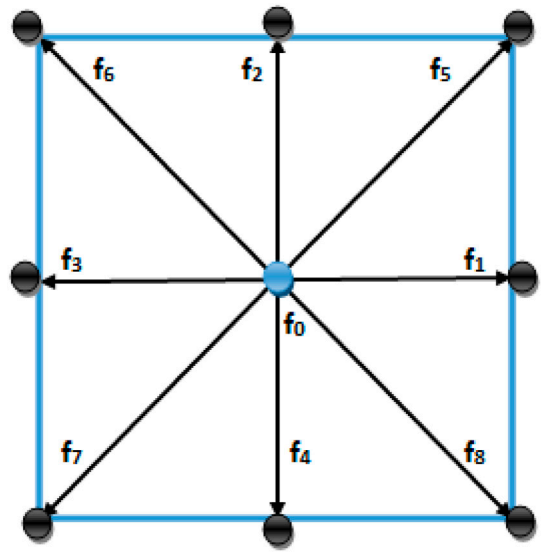

FIGURE 1
D2Q9 lattice model.

upper surface of C_1 to the upper boundary is $Y_u = 8D$, while $Y_b = 8D$ is the distance from the lower surface of $C1$ to the lower boundary of the domain. These lengths are selected based on the recommendations of previous research in order to have a minimal effect of domain size on results (Perumal et al., 2012). Channel length L varies as the gap between cylinders ($G = s/D$) varies, while the height H is fixed. All lengths in this study are non-dimensionalized using the characteristic length ($D = 20$).

The boundary conditions in this study are applied in terms of distribution functions. At the inlet position, uniform incoming flow ($u = U_{in}, v = 0$) is assumed (Islam et al., 2012). The convective boundary condition in terms of distribution functions given as $\frac{\partial f_i}{\partial t} + U_{in}\frac{\partial f_i}{\partial x} = 0$ is used at the outlet boundary (Ahmad et al., 2021). The surface of each cylinder as well as the upper and lower walls of the domain is treated through the no-slip boundary condition, mathematically expressed as ($u = v = 0$). In LBM simulations, the no-slip condition is applied in terms of the bounce back rule in which the particles which stream into the wall are bounced back in the opposite direction inside the fluid stream. For example, the particles with distribution functions f_7, f_4, and f_8 streaming toward the lower wall bounce back as $f_7 = f_5$, $f_4 = f_2$, and $f_8 = f_6$. A similar procedure was also adopted for other directions for fluid particles hitting the solid walls (Rahman et al., 2021). Although the geometry considered in the current study has smooth boundaries, LBM is also a suitable choice for curved or moving boundaries (Tao et al., 2018; Marson et al., 2021).

4 Grid independence and code validation study

4.1 Grid independence

In order to ensure grid independence, we considered three different grid sizes (10, 20, and 40 points) around the outer surface of a single square cylinder at $Re = 100$ (Table 3). In terms of percentage variation, the values of physical variables like *CDmean*, *St*, and *CLrms* are more significantly impacted by the 10-point grid than the 40-point results. In comparison, the 20-point grid produced superior outcomes relative to 10 points. Furthermore, the convergence of a 40-point grid required significantly longer time, and there was no great variation in results at 20- and 40-point grid sizes. Therefore, we considered the 20-point grid for analysis for this study. This grid size follows recommendations based on lattice Boltzmann simulations for both single and multiple objects (Islam et al., 2018; Rahman et al., 2021). Note that the uniform meshing ($\Delta x = \Delta t = 1$) is selected in the whole computational domain because the standard LBM considers such meshing for simulations without any need to use external mesh generators (Perumal et al., 2012). It is easy to apply and, in the case of rectangular obstacles, uniform meshing is an optimal choice to ensure accurate results in less computational time.

4.2 Code validation

For code validation, we performed computations for flow around a single square cylinder and quantitatively compared our results with the experimental and numerical results of other research considering $Re = 100$ (Table 4). Note that the results for the geometry considered in current work are not available in the literature. Therefore, the code validation study was performed for flow around a single square cylinder. This was based on the fact that the flow around a single cylinder serves as a benchmark problem for flow around bluff bodies. This practice was adopted in most previously published studies. Table 4 demonstrates good agreement among the current results and with those of other studies. Some minor deviations in results also appear. Note that the exact matching of results is not possible because several parameters, including the accuracy of the underlying numerical technique, mesh size, domain dimensions, and the dimensions of cylinders influence the outcomes. The overall agreement of current and previous results indicates that the current code calculated the results efficiently. Furthermore, we refer readers for the details of quantitative as well as qualitative validation in the case of flow around two and more inline arranged cylinders to Abbasi et al. (2018) and Abbasi et al. (2020).

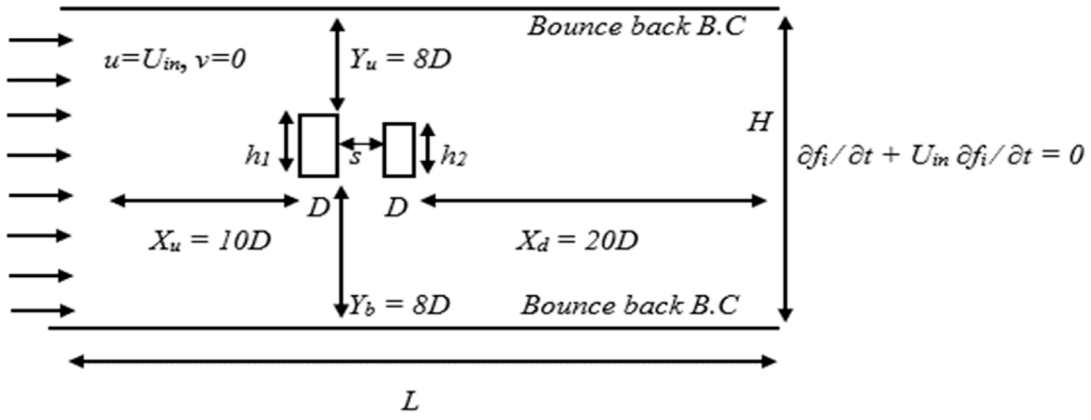

FIGURE 2
Geometry of the problem.

TABLE 3 Impact of spatial resolution on the physical properties of flow past a single square cylinder at Re = 100.

	10 points	20 points	40 points
CD_{mean}	1.4630 (1.34%)	1.4434 (0.2%)	1.4414
St	0.1498 (0.5%)	0.1491 (0%)	0.1491
CL_{rms}	0.1798 (3.1%)	0.1742 (1.2%)	0.1762

It may therefore be concluded that our code is well established and that we can use it for flow around tandem arranged cylinders, done in the present study.

5 Results and discussion

The flow around two tandem rectangular cylinders with distinct aspect ratios was simulated at Re = 100 by considering different values of G progressively varying from 0.25 to 20. From previous studies, we can conclude that the flow structure mechanism around multiple rectangular cylinders appears to be a complicated phenomenon that depends on several parameters, including Re, G, and AR (Islam et al., 2018; Rahman et al., 2021). In the current study, the resulting flow regimes are specified into different patterns in terms of the creation of different shape vortices, wake structure mechanism, and the behavior of shear layers detaching from cylinder corners and interacting with each other. These different flow patterns depend on increasing values of G in this study. The prominent flow patterns observed in this study are the single slender body (SSB) flow found in the range G = 0.25–0.75, the shear layer reattachment (SLR) flow found in the range G = 1–4, the intermittent shedding (IS) flow mode found in the range G = 4.25–5.25, and the binary vortex street (BVS) flow found for G = 5.5–20, except at G = 8 where the single-row vortex street (SRVS) flow was observed. Similar flow patterns have been reported by Zdravkovich (1987) for flow around tandem bodies with different characteristics. In the following subsections, a comprehensive illustration for each flow pattern is presented and discussed.

5.1 Single slender body

The flow pattern noticed here at smaller gaps between two tandem rectangular cylinders is the SSB flow in the range 0.25 ≤ G ≤ 0.75 (Figure 3). In Figure 3A, the corresponding vorticity contour of SSB is presented. This contour shows that the free shear layers that split off the front edges of C_1 do not rejoin with C_2 but instead roll up within the wake of C_2 while, within the space in the cylinders, a steady flow can be observed. An isolated vortex row appears within the down-wake region of the cylinders, similar to the flow around a solo body. Zdravkovich (1987) also classified such a flow pattern as a single slender body occurring in the range between 1 < G < 1.8 for coupled inline circular cylinders. This kind of flow pattern is also known as an isolated blunt body (Shui et al., 2021). Figure 3B presents the pressure and streamline contour for this flow pattern—it is obvious that the pressure is higher on the leading surface area of the C_1 and lower at the rear side of the C_2. This indicates that the existence of the C_1 has a major role in suppressing pressure on C_2. In Figure 3B, the streamlines graph shows that an elongated recirculating vortex at the upper side of C_2 is formed while, in the wake adjacent to C_2, a large D-type recirculating eddy appears. The size and shape of vortices as well as recirculating eddies are sufficiently larger than those of a single square cylinder case due to the increased aspect ratios of these cylinders. In Figure 3C, the

TABLE 4 Code validation in terms of single square cylinder at *Re* = 100.

	CD_{mean}	*St*	CD_{rms}
Saha et al. (2000)	1.510	0.159	—
Sohankar et al. (1995)	1.444	0.145	0.002
Okajima (1982)	1.600	0.141	—
Norberg (1993)	—	0.140	—
Abograis and Alshayji (2013)	1.480	0.140	0.006
Present	1.443	0.149	0.006

variation in drag coefficients with time is presented. The *CD* for C_1 is almost constant while, for C_2, it appears to be sinusoidal after some time steps. This is because the shear layers pass smoothly around C_1 but roll up in the wake of C_2. It can also be observed that the drag force is positive for C_1 and negative for C_2 acting as a thrust force. Huang et al. (2012) also observed such a drag tendency around two 2:1 rectangular cylinders. In Figure 3D, the lift coefficients for both cylinders are presented against time. The *CL* graph depicts the C_1 *CL* having higher amplitude than C_2. In that case, the flow boundary layer detaching for the C_1 corners spread over a larger region than C_2. Another reason is the impact of *AR*, which indicates that a cylinder with high *AR* tends to face more lift than a cylinder with low *AR*. Moreover, *CL* becomes periodic for both cylinders after smooth behavior at initial time steps. Figures 3E,F present the spectrum energy of lift coefficient for both cylinders. The *St* value for both cylinders (shown on peaks of spectrum graph) indicates that the shedding frequency is much dependent on *Re* and *G*. The power spectrum graphs of both cylinders depict a similar peak value, indicating the dominant wake frequency behind the cylinders. This *St* value is comparatively lower than other flow patterns found in this study. It also indicates a relatively uniform and predictable vortex shedding pattern, with vortices shedding regularly.

5.2 Shear layer reattachment

The second flow regime seen from current simulation results is SLR flow which extents in the range $1 \leq G \leq 4$ (Figure 4). In Figure 4A, the associated vorticity pattern for SLR flow is presented at $G = 1$ as a representative case. The vorticity graph depicts inner shear layers splitting from C_1 rejoin at upstream side of C_2 and also move within the gap region. The vortices shed only in the wake of C_2 like the previous flow pattern. However, now the vortices behind the rear cylinder are stronger, with reduced size and greater number compared to SSB flow. According to Zdravkovich (1987), this flow pattern appears within the range $1.2 < G < 3.4$ for coupled inline circular cylinders of same size. In Figure 4B, the pressure and streamline graph is presented for SLR flow. The pressure graph shows that, in this case, while the maximum pressure is at the front face of C_1, but C_2 is also subjected to some pressure due to the fluid being forced to flow inside the gap region as distance between cylinders increased. As the flow passes away from the cylinders, the pressure drops, implying a region of low pressure in the wake behind the cylinders. In Figure 4B, the streamline pattern shows elongated recirculating eddies developing around the upper, lower, and rear areas of C_2. In the wake adjacent to C_2, the size of the recirculating eddy appears to be smaller than the SSB case because of the reduced size of the vortices within wake region. Figure 4C presents the variation in drag coefficients with time. The *CD* graph shows almost similar behavior to the SSB flow case—higher drag on C_1 than on C_2. This might be due to the fact that the *AR* of the cylinders affects the *CD*, with the higher *AR* cylinder probably experiencing higher drag force. In Figure 4D, the lift coefficients are presented against time for the SLR flow pattern. The graph shows that *CL* is periodic for both cylinders. The amplitude of consecutive *CL* cycles is now sufficiently higher than the SSB case. This is due to the SLR and increase in the spacing ratio that results in changing the lift force signals. Figures 4E,F present the power spectrum of the lift coefficient for both cylinders. This graph of both cylinders depicts a peak value similar to the SSB flow pattern. However, here the *St* values are significantly greater than those for a SSB flow pattern. This is due to the SLR flow case, which leads to a more complicated flow pattern and a higher shedding frequency.

5.3 Intermittent shedding

With increased distance between the cylinders, the flow structure mechanism and interactions of separated flow with C_2 become entirely different from the SSB and SLR flow patterns (see Figure 5). In Figure 5A, the vorticity contour shows that the boundary layers separated out of the top and bottom sides of C_1 join to form vortices in the gap before interacting with C_2 because of the larger space between the cylinders. After that, these vortices impinge on C_2 and form a vortex street in its wake (Figure 5A). There seems no definite pattern for movement of vortices, as was in case of SSB and SLR patterns. Furthermore, the structures of vortices in street differ from each other, and it can also be observed that the strength of vortices in this case is increased more than those seen in previous flow patterns. The pressure exhibits a fluctuating pattern, with alternating regions of maximum and minimum pressure (Figure 5B). These pressure variations correspond to irregularly shedding vortices. At the back of C_1, the pressure reduces, implying the creation of a low-pressure zone, followed by a rapid increase in pressure as the flow merges to C_2. The pressure becomes minimal in the near wake zone of C_2. These alternately repeated pressure patterns generate a characteristic waviness in the pressure

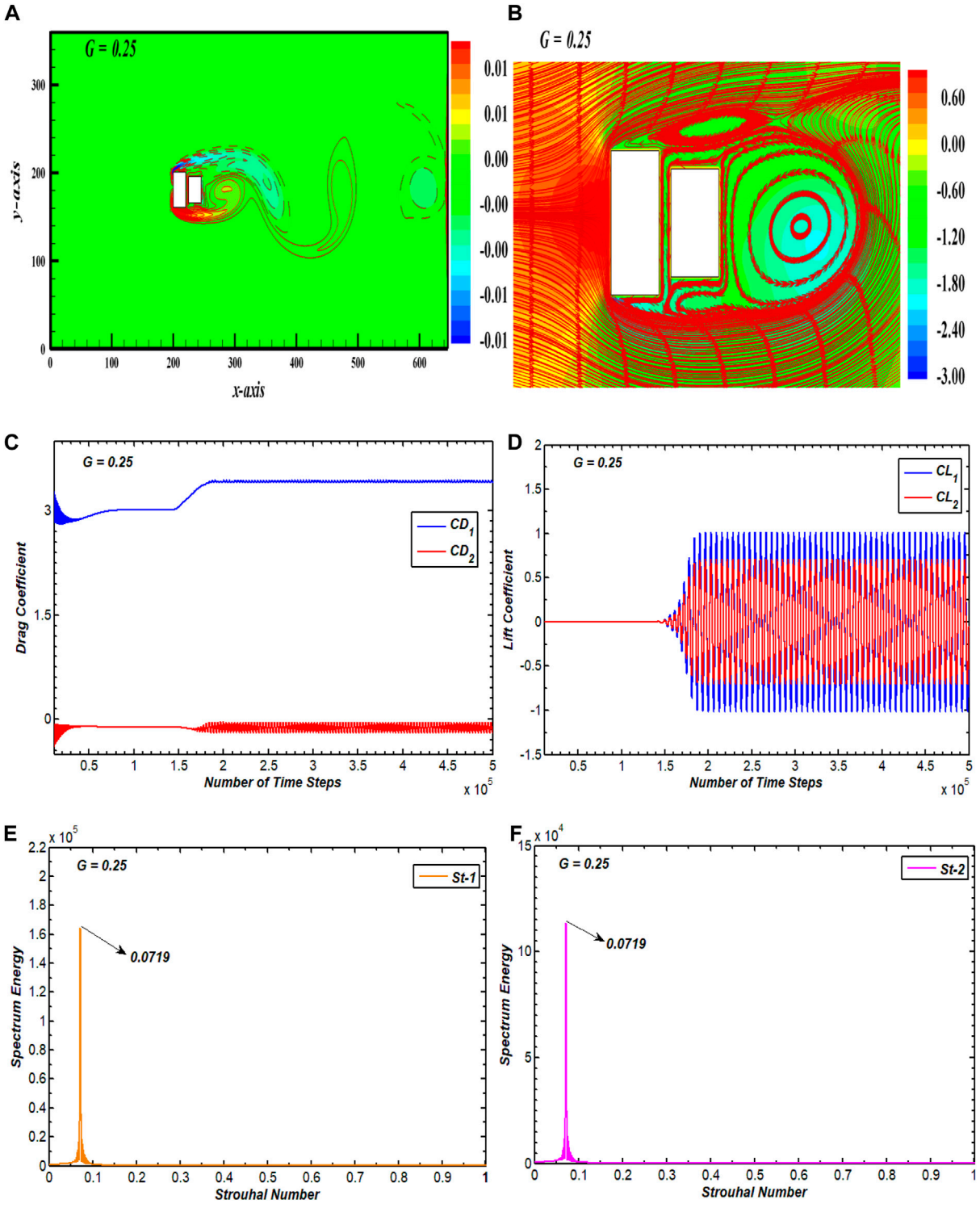

FIGURE 3
(A) Vorticity contour, **(B)** pressure streamlines, **(C, D)** drag and lift coefficients, and **(E, F)** spectral energy of *CL* for single slender body flow.

contour. From Figure 5B, the location, size, and behavior of the vortices shedding from both cylinders along with the wake pattern behind the cylinders is indicated by streamlines. These show that the fluid detachment occurs at the leading edges of C_1 and that a recirculating eddy appears behind C_1. The fluid then moves toward C_2 where it splits again, forming another recirculating eddy in the near lower corner of C_2. Both cylinders generate their own eddies because of the wider gap between them. The streamlines emerging from the bottom frontal edge of C_1 move toward the upper frontal corner of C_2, indicating irregularity of fluid movement within the gap. A similar trend prevails in the wake region, as indicated by streamlines. Due to such chaos and

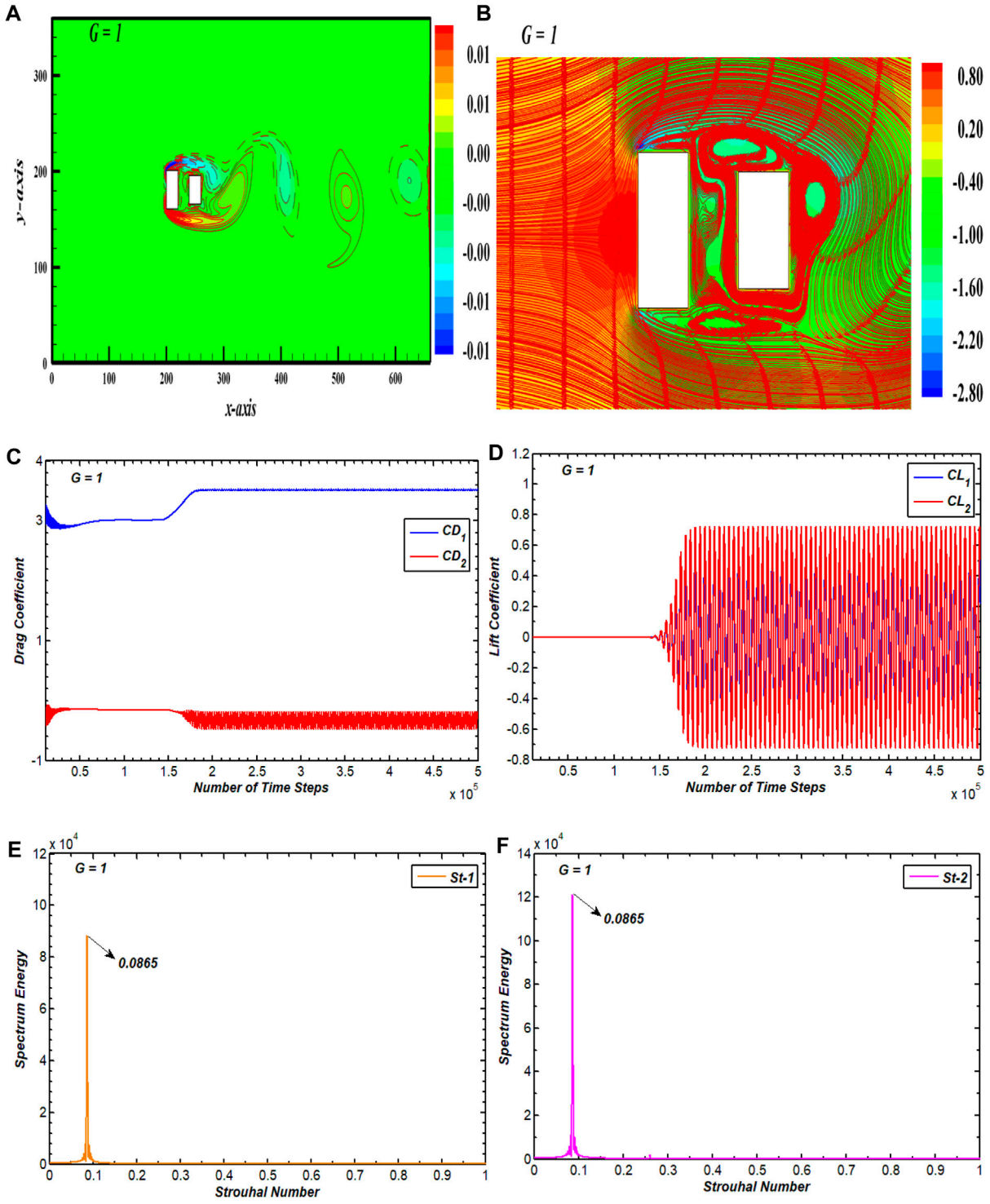

FIGURE 4
(A) Vorticity contour, **(B)** pressure streamlines, **(C, D)** drag and lift coefficients, and **(E, F)** power spectrum of *CL* for alternate reattachment flow.

amalgamation in flow, this flow pattern is classified as IS flow, and it is seen in the range $4.25 \leq G \leq 5.25$ in the current study. This disorder in flow structure also affects the drag and lift forces (Figures 5C,D). The smooth variations observed in the case of these force coefficients for SSB and SLR flow patterns no longer exist due to IS. The *CD* graph shows an irregular pattern with random dips and peaks due to the flow transitions from one vortex shedding pattern to another. The consecutive drag signals switch from low to high values onto C_2, and the amplitude of the *CD* curves increases compared to C_1 as time progresses. In Figure 5D, *CL* exhibits periodic variations, with *CL* switching from lower to higher amplitude cycles over time. Initially, the amplitude of *CL* curves

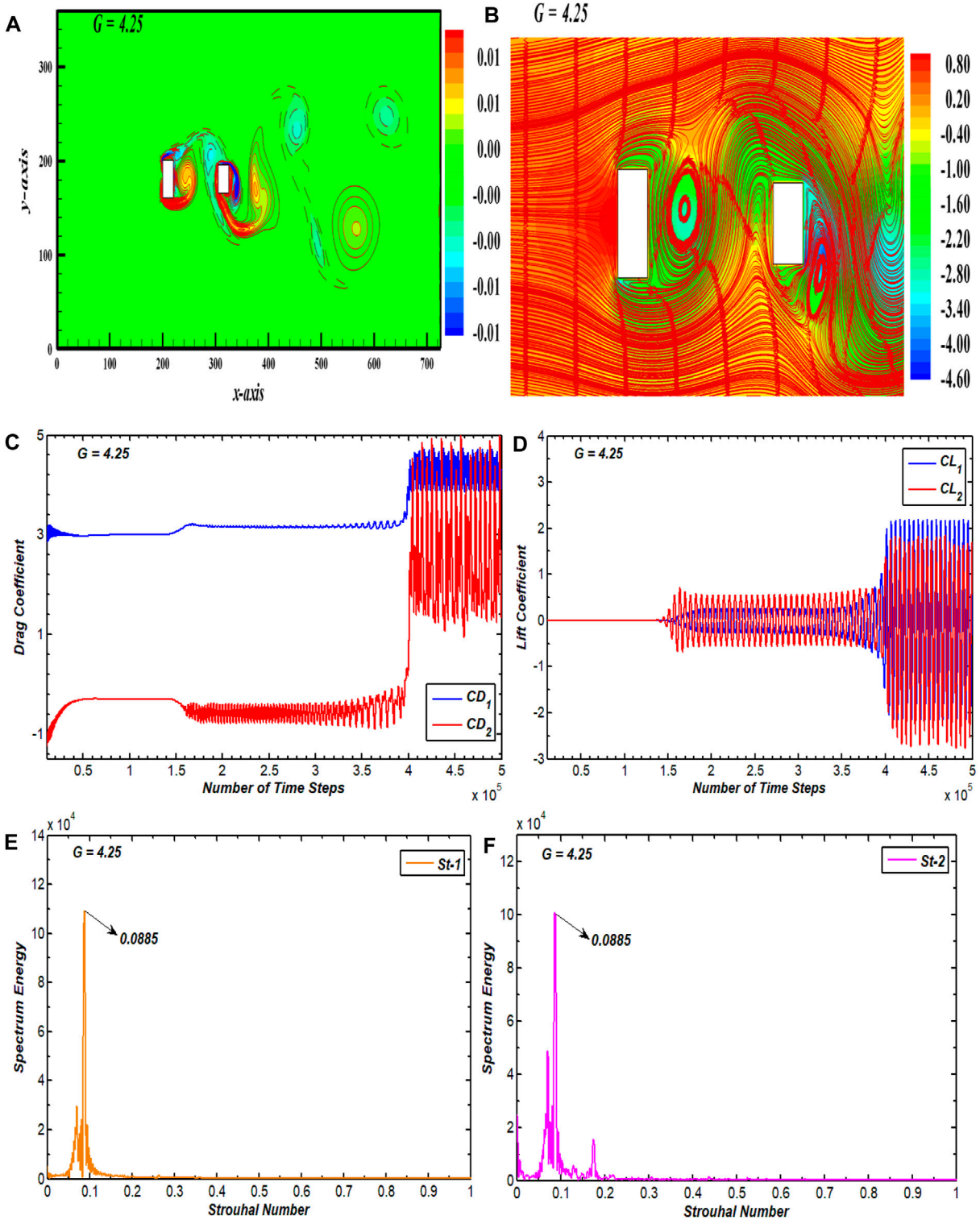

FIGURE 5
(A) Vorticity contour, **(B)** pressure streamlines, **(C, D)** drag and lift coefficients, and **(E, F)** power spectrum of *CL* for intermittent shedding flow.

for C_2 are higher than C_1, which becomes almost similar as time advances. *CL* further exhibits variations with *G* between the cylinders in this case. For lower values of *G*, the cylinders' wakes merge more strongly, leading to larger *CL* amplitude. For large *G*, the *CL* amplitude decreases, implying a weaker interaction between the cylinders' wakes. The spectral energy plots for both cylinders show a similar peak value, indicating that the vortices shed with similar frequency from both cylinders. Multiple peaks appear, indicating an irregular attachment of the shear layers and an inconsistency of shedding vortices among the cylinders and after

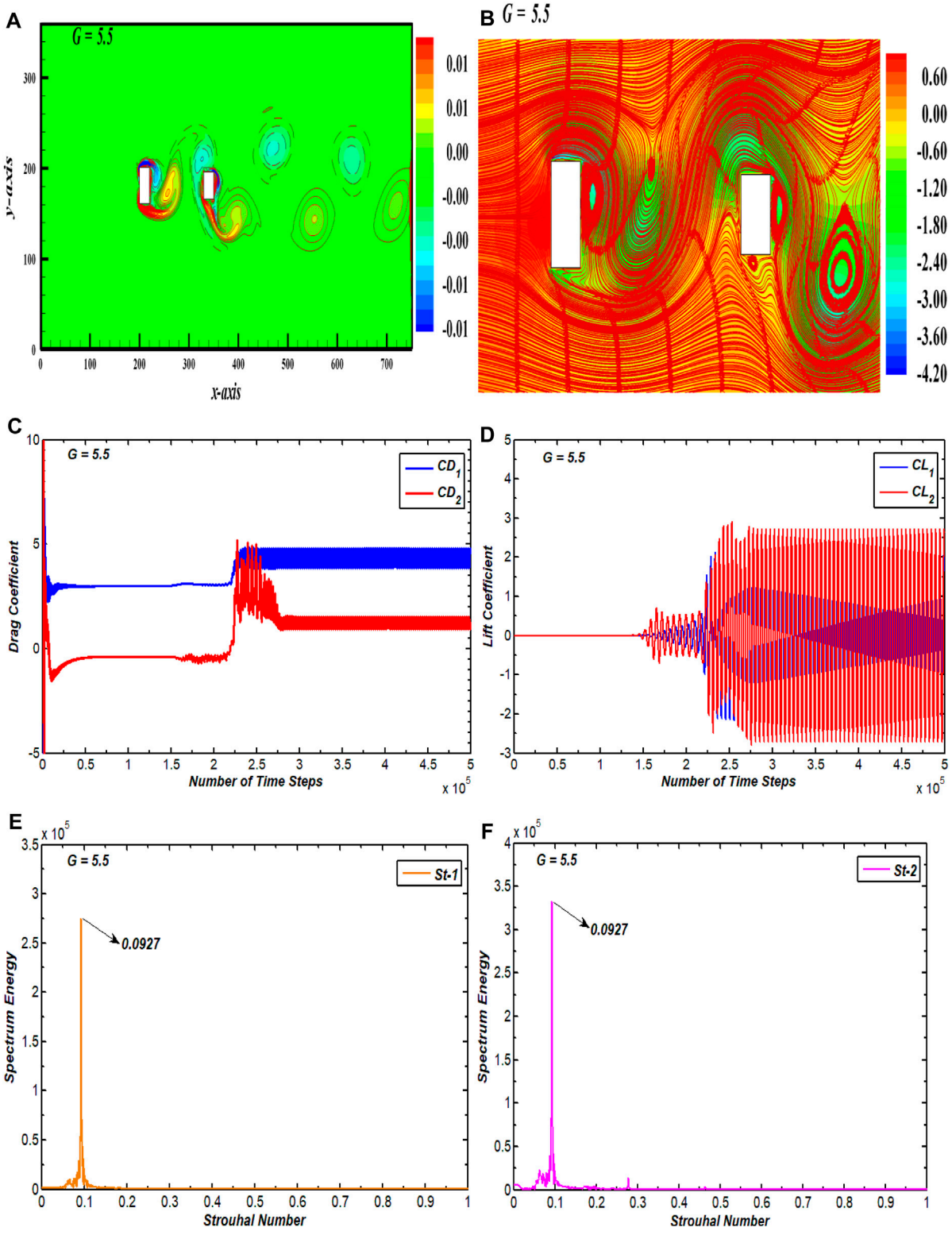

FIGURE 6
(A) Vorticity profile, **(B)** pressure streamlines, **(C, D)** drag and lift coefficients, and **(E, F)** power spectrum of *CL* for binary vortex street flow.

C_2. Islam et al. (2018) also reported such behavior in *St* for three inline rectangular cylinders. Such flow characteristics were also observed by Zdravkovich (1987) for coupled circular cylinders in tandem arrangement for the spacing range 3.4 < G < 3.8.

5.4 Binary vortex street

The BVS flow pattern ranges over the spacing values G = 5.5–20, except for G = 8, where a single-row vortex street (SRVS) pattern

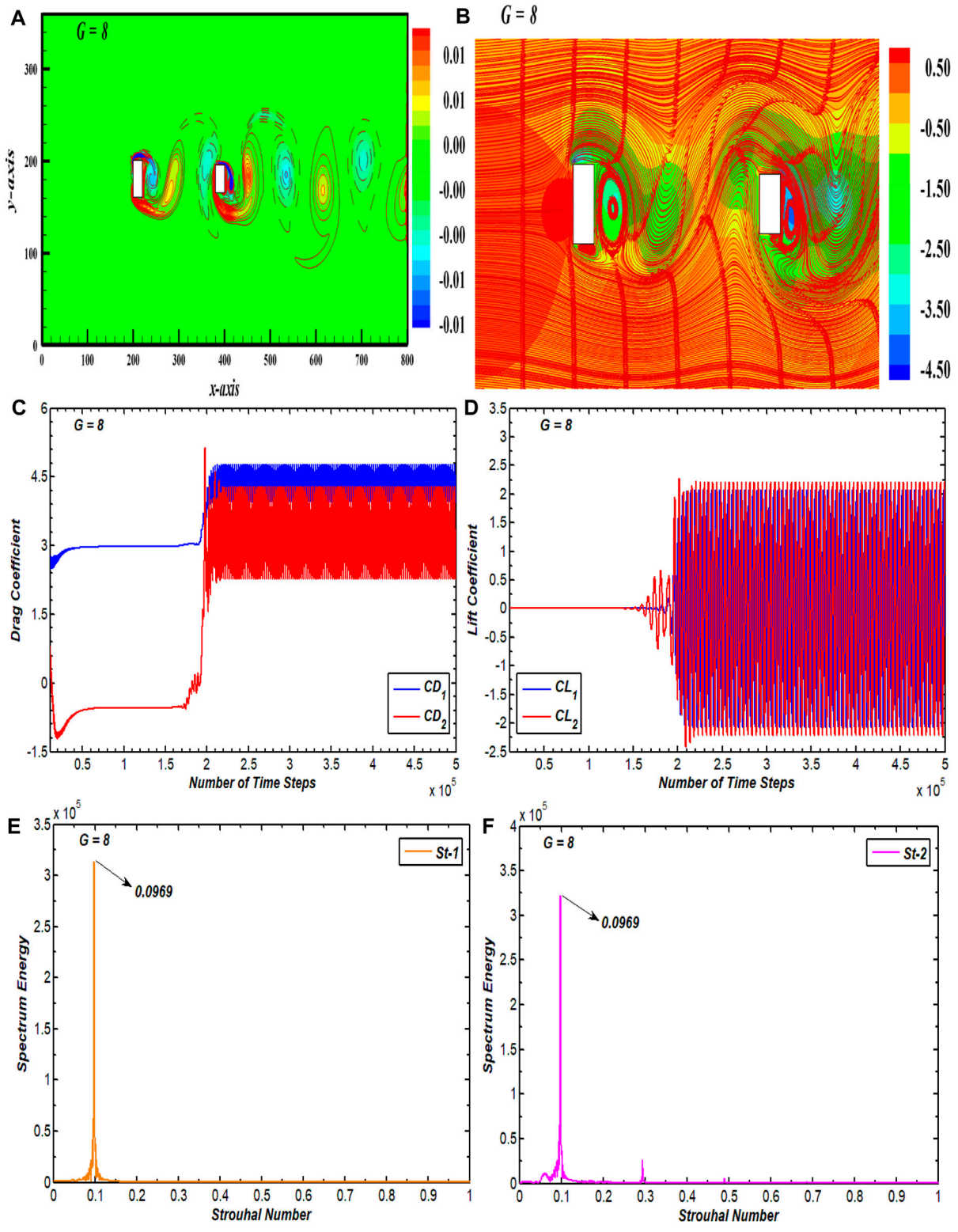

FIGURE 7
(A) Vorticity profile, **(B)** pressure streamlines, **(C, D)** drag and lift coefficients, and **(E, F)** power spectrum of *CL* for single vortex street flow.

appeared (discussed in the next section) (Figure 6). In Figure 6A, the associated vorticity pattern for BVS is given, depicting that each cylinder generates its own vortex street and that the vortex street behind C_2 is binary because the movement of the vortices is in a parallel dual line of clockwise and anticlockwise vortices. The vortices after C_2 are elliptically shaped with almost similar sizes. Zdravkovich (1987) also reported similar characteristics of BVS for flow-past coupled tandem circular cylinders for the spacing range $G > 3.4$ to 3.8. Figure 6B shows that the

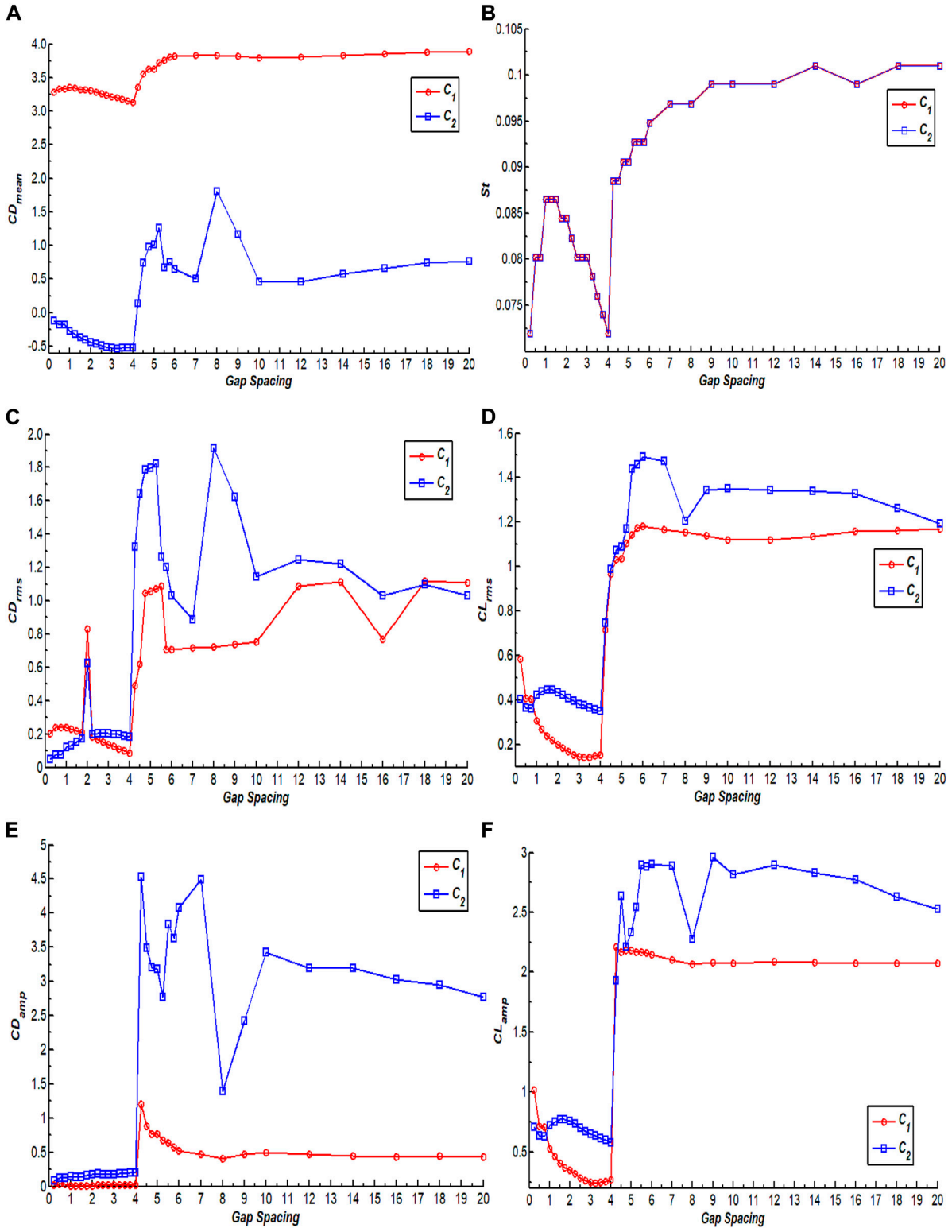

FIGURE 8
Gap spacing effect on the variation of **(A)** CD_{mean}, **(B)** St, **(C)** CD_{rms}, **(D)** CL_{rms}, **(E)** CD_{amp}, and **(F)** CL_{amp}.

pressure varies randomly inside the domain in this flow pattern. Instead of a minimal pressure zone in the back of C_2, as was seen in previous flow patterns, the pressure now seems minimal at the corners of C_1. This distribution of pressure corresponds to the single cylinder case. This can be attributed to the increased gap spacing in which wake interference effects are minimized. This phenomenon becomes more prominent in BVS flow as G further increases. The streamlines in contour show larger recirculation zones within the gaps and after C_2. In this case, the eddies

appearing within the gap region and after C_2 differ in shape and size due to changed vortex structures from the other flow patterns in this study. The *CD* for C_1 has periodic variations, while the *CD* for C_2 has initial fluctuating behavior which eventually settles to being periodic (Figure 6C). The lift coefficients become periodic for both cylinders after a short interval of linear behavior (Figure 6D). The *CL* oscillations have sufficiently higher amplitudes than SSB, SLR, and IS flow patterns due to the elliptically shaped vortices appearing after the cylinders. The periodic oscillation of the lift force demonstrates the domination of wake frequency within the spectrum energy graph (Figures 6E,F). There thus appears only a single peak in each case of the power spectrum plot.

5.5 Single-row vortex street

The SRVS flow pattern in the wake of both cylinders is observed at only one gap spacing value—G = 8 in this study (Figure 7). The corresponding vorticity contour for the SRVS flow pattern is presented in Figure 7A, which shows that the vortices travel in a single row throughout the computational domain. The vortices in the wake of each cylinder are elongated and merge in the wake of C_2. The pressure seems to be higher at the front surface of C_1 and minimal at the corners and at back surface of C_2 (Figure 7B). Here, the stagnation point is generated, showing that the flow is slowed due to the presence of the cylinder. The flow separates from the corners of the cylinders, indicating a low-pressure area. The lowest pressure value appears at back surface of C_2. This low-pressure area causes the periodic shedding of vortices in the wake of each cylinder. In Figure 7B, the streamlines depict a distinct pattern of alternating vortex shedding from each cylinder. The streamlines appear to be curvy and firmly packed together in the center of the wake, indicating the existence of strong vorticity. Due to this, the drag as well as lift coefficients appear to be significantly impacted for both cylinders (Figures 7C,D). Since each cylinder sheds its own SRVS, the lift on the second cylinder is more stabilized than the IS and BVS flow pattern. The amplitude of consecutive cycles of the lift coefficients for both cylinders lessen compared to the IS and BVS flow patterns. This can be attributed to the individual shedding of vortices from both cylinders in a single row. A comparison with the SSB and SLR flow patterns reveals a significant rise in the amplitude of consecutive *CL* cycles for both cylinders due to the elongated recirculating regions of vorticity in the wake of both cylinders. These graphs also show that the amplitude of both force coefficients is higher in the case of second cylinder than of first. This is due to wake interference effect of C_1 on the second cylinder. Due to SRVS flow pattern and the smooth passage of vortices in the domain, the power spectrum of the lift coefficient graph for both cylinders indicates a similar peak value (Figures 7E,F).

6 Force statistics

Variations of various fluid force parameters acting on both cylinders with varying gap spacing is presented in this section in order to analyze the influence of G on the forces. The parameters considered for this purpose are CD_{mean}, St, CD_{rms}, CL_{rms}, amplitude of the drag coefficient (CD_{amp}), and amplitude of the lift coefficient (CL_{amp}). Figure 8 presents the effect of G on variations of these parameters at Re = 100.

The variation of CD_{mean} for flow around two tandem rectangular cylinders with increasing G is presented in Figure 8A. It can be observed that CD_{mean} of C_1 is greater than CD_{mean} of C_2 for all chosen values of G because the incoming flow initially interacts with C_1 and thus exerts maximum drag force on C_1. Another possible reason that C_1 experiences significantly higher drag force than C_2 is that it has higher *AR*. Relating the variations of drag force coefficient, it is apparent that the change in flow patterns significantly affects the drag force. In the range G = 0.25 to 1, the average drag on C_1 slightly increases and then shows decreasing behavior until G = 4. It then increases with increasing G and approaches its maximum value at G = 20. Note that, at G = 1, the flow pattern changes from SSB to SLR, while after G = 4, the flow pattern changes from SLR to IS. The CD_{mean} of C_2 is negative and initially decreases until G = 4. Huang et al. (2012) also observed the negative value of CD_{mean} for C_2 for flowing past 2:1 rectangular cylinders in tandem at Re = 200. After G = 4, it jumps from negative to positive values due to a change in flow pattern from SLR to IS. The negative values of CD_{mean} indicate that the drag force acts as a thrust force, thus generating a backflow due to narrow gaps between cylinders. The minimum value of CD_{mean} for both cylinders can be seen at G = 4, while the maximum for C_2 occurs at G = 8, and CD_{mean} of C_1 is maximum at G = 20. Figure 8A also shows that, after G = 10, the influence of gap spacing on CD_{mean} of both cylinders decreases. Figure 8B presents the variation of St of both cylinders with G. Both cylinders have same St for all G, indicating that the vortices shed from both cylinders with same frequency notwithstanding whether both cylinders have different ARs. Rahman et al. (2021) also found similar behavior in St for flow past three rectangular cylinders. Initially for G = 0.25 to 0.75, St shows increasing behavior. SSB flow was observed in this range of gap spacing. In the range G = 1.75 to 4, it shows decreasing behavior, which indicates that the shedding frequency decreases due to the push of shear layers inside the gaps between cylinders. After that it increases with increasing G and approaches the local maximum value for both cylinders at G = 14. The minimum value of St can be observed at G = 4 for both cylinders where the SLR flow pattern was seen. The variation of CD_{rms} of both cylinders at different values of G is presented in Figure 8C. Initially, when G = 0.25 to 1, the CD_{rms} of C_1 slightly increased and then showed decreasing behavior in the range G = 1.25 to 1.75 where the SLR flow is observed. The CD_{rms} of C_2 show increasing behavior in the range G = 0.25 to 1.75. The CD_{rms} of both cylinders jump to higher values at G = 2 and then again show decreasing behavior until G = 4. After G = 4, it jumps to higher values due to a change in flow pattern from SLR to IS. The CD_{rms} of both cylinders show a mix of increasing and decreasing behaviors as G increases further. The minimum value of CD_{rms} for both cylinders can be noticed at G = 4, while the maximum value of CD_{rms} of C_1 appears at G = 18, and CD_{rms} of C_2 is maximum at G = 8 where the SRVS flow pattern was reported. The effect of varying G on CL_{rms} of both cylinders is shown in Figure 8D. This graph depicts that, in the range G = 0.25 to 4, the CL_{rms} of C_1 shows decreasing behavior. After that, it increases with increasing G and thus approaches its local maximum value at G = 6. The CL_{rms} of C_2 shows decreasing behavior initially in the SSB flow pattern regime and, after that, slightly increases and then shows

decreasing behavior until $G = 4$. The CL_{rms} curves then show an increasing trend to higher values for both cylinders. Note that the IS flow pattern is observed in this range. At $G = 4.5$ to 7.75, the value of CL_{rms} of C_2 increases and then suddenly decreases, which can be observed at $G = 8$ because of flow pattern change from BVS to SRVS flow. The variation of CD_{amp} for both cylinders with varying G is shown in Figure 8E. It can be observed that, until $G = 4$, CD_{amp} for both cylinders is almost constant, indicating little change in amplitude of drag force in this spacing range. After $G = 4$, CD_{amp} jumps to the highest values for both cylinders due to the appearance of the IS flow pattern. Note that, in this flow pattern, the vortices appear to be in an irregular pattern in the wake of both cylinders. This graph also shows that the higher spacing values result in higher amplitude drag force than the smaller spacing values. The variation of CL_{amp} of both cylinders shown in Figure 8F indicates that the C_2 bears higher amplitude than C_1 at almost all spacing values. This is due to the wake interference effects of C_1 on C_2. Shui et al. (2021) also reported similar results in CL_{amp} for flow around two tandem square cylinders. Initially, CL_{amp} corresponding to C_1 decreased until $G = 4$ but, after $G = 4$, it suddenly increased to a higher value and became almost independent of G, showing negligible modifications. In the range $G = 0.25$ to 0.75, the CL_{amp} of C_2 shows decreasing behavior. After $G = 4$, the CL_{amp} of both cylinders has sudden jumps (Figure 8F). The minimum value of CL_{amp} of both cylinders can be observed at $G = 4$ where the SLR flow pattern is observed. Its maximum value for C_1 appears at $G = 4.25$ and the maximum value for C_2 at $G = 9$.

7 Conclusion

Numerical calculations were performed to analyze the fluid flow around two vertically positioned rectangular cylinders in tandem arrangement using the lattice Boltzmann method. The cylinders considered in this study were of different aspect ratios. The main goal of this study was to determine the wake structures under the effect of gap spacing in the range $G = 0.25$ to 20 at $Re = 100$. The results were presented and discussed in the form of vorticity contour visualizations, pressure streamline contours, variation of drag, and lift coefficient against time. Fluid force parameters of average drag coefficient, Strouhal number, rms values of drag, lift coefficients, and the amplitudes of these force coefficients were also analyzed under the impact of changing gaps between cylinders. The important findings of this study are:

(1) Bearing various characteristics, five different wake flow patterns were observed in this study depending on various ranges of gap spacings: i) single slender body, ii) shear layer reattachment, iii) intermittent shedding, iv) binary vortex street, and v) single-row vortex street.
(2) The single slender body flow pattern, observed in the range $G = 0.25$ to 0.75, consists of single vortex street in the down wake area of C_2, without any gap flow, similar to the flow around a single bluff body. The fluid forces in this flow pattern varied periodically with similar amplitude as time proceeded.
(3) In the range $G = 1$ to 4, the shear layer reattachment flow was observed. In this flow pattern, the strength of vortices increased in the down wake region. The amplitude of lift force coefficient on both cylinders also increased more than single slender body flow. The secondary cylinder interaction frequency impact was also observed in this flow pattern.
(4) In the range $G = 4.25$ to 5.25, the intermittent shedding flow pattern was observed. In this flow pattern, the vortices did not exhibit any proper pattern, but instead chaos was observed in the flow structure. The CD varied irregularly with random dips and peaks due to the flow structure transitions between larger and smaller sized vortices.
(5) The binary vortex street flow pattern was found in the range $G = 5.5$ to 20 except at $G = 8$, where the single-row vortex street flow pattern was observed. In the binary vortex flow pattern, both cylinders generated their own vortex street, while the vortex street in the down wake region traveled in a double row of parallel vortices. The vortex formation region enlarged in this range of gap spacing, corresponding to both flow patterns, which resulted in higher magnitude drag and lift forces on cylinders.
(6) It was observed that C_2 experienced negative drag in the spacing range between $G = 0.25$ to 4, while C_1 had positive values of CD_{mean} for all G. The negative drag force on C_2 jumped to positive as the flow pattern changed from shear layer reattachment to intermittent shedding flow. Furthermore, the CL_{rms}, CD_{rms}, CL_{amp}, and CD_{amp} for C_2 were mostly higher than corresponding values on C_1 for all values of G.
(7) Although C_2 was shielded by C_1 and faces low pressure at smaller spacing values, it was also subjected to pressure change due to the changes in flow patterns as gap spacing progressively increased. Furthermore, the magnitude of pressure on both cylinders changed due to change in flow patterns.
(8) At $G = 4$ and 8, the fluid force parameters like CD_{mean}, St, CD_{rms}, CL_{rms}, CD_{amp}, and CL_{amp} achieved either maximum or minimum values or had sudden jumps in values. The flow structure at these spacing values also exhibits complexity. Both spacing values are hence critical for fluid flow dynamics around the geometry considered in this study.

Data availability statement

The raw data supporting the conclusions of this article will be made available by the authors without undue reservation.

Author contributions

WA: conceptualization, project administration, supervision, and writing–review and editing. ME: formal analysis, methodology,

validation, and writing–original draft. HR: visualization and writing–review and editing. ZU: funding acquisition, resources, and writing–review and editing. MH: funding acquisition, supervision, and writing–review and editing. KS: funding acquisition and writing–review and editing.

Funding

The author(s) declare that financial support was received for the research, authorship, and/or publication of this article. This work was supported by King Saud University, Riyadh, Saudi Arabia, under Researchers Supporting Project Number RSP2024R18.

Conflict of interest

The authors declare that the research was conducted in the absence of any commercial or financial relationships that could be construed as a potential conflict of interest.

Publisher's note

All claims expressed in this article are solely those of the authors and do not necessarily represent those of their affiliated organizations or those of the publisher, the editors and, the reviewers. Any product that may be evaluated in this article, or claim that may be made by its manufacturer, is not guaranteed or endorsed by the publisher.

References

Abbasi, W. S., Islam, S. U., Faiz, L., and Rahman, H. (2018). Numerical investigation of transitions in flow states and variation in aerodynamic forces for flow around square cylinders arranged inline. *Chin. J. Aeronautics* 31 (11), 2111–2123. doi:10.1016/j.cja.2018.08.020

Abbasi, W. S., Mahmood, R., and Naheed, A. (2020). On the wake interference effects for flow around tandem bodies. *J. Braz. Soc. Mech. Sci. Eng.* 42, 53. doi:10.1007/s40430-019-2137-5

Abdolahipour, S. (2023). Effects of low and high frequency actuation on aerodynamic performance of a supercritical airfoil. *Front. Mech. Eng.* 9, 1290074. doi:10.3389/fmech.2023.1290074

Abdolahipour, S., Mani, M., and Taleghani, A. S. (2021). Parametric study of a frequency-modulated pulse jet by measurements of flow characteristics. *Phys. Scr.* 96, 125012. doi:10.1088/1402-4896/ac2bdf

Abdolahipour, S., Mani, M., and Taleghani, A. S. (2022). Experimental investigation of flow control on a high-lift wing using modulated pulse jet vortex generator. *J. Aerosp. Eng.* 35 (5). doi:10.1061/(ASCE)AS.1943-5525.0001463

Abograis, A., and Alshayji, A. (2013). *Reduction of fluid forces on a square cylinder using passive control methods*. Boston, USA: COMSOL Conference.

Aboueian, J., and Sohankar, A. (2017). Identification of flow regimes around two staggered square cylinders by a numerical study. *Theory Comput. Fluid Dyn.* 31, 295–315. doi:10.1007/s00162-017-0424-2

Adeeb, E., Haider, B. A., and Sohn, C. H. (2018). Flow interference of two side-by-side square cylinders using IB-LBM- Effect of corner radius. *Results Phys.* 10, 256–263. doi:10.1016/j.rinp.2018.05.039

Ahmad, S., Islam, S. U., Nazeer, G., and Zhou, C. Y. (2021). Numerical investigation of Strouhal number discontinuity and flow characteristics around single rectangular cylinder at low aspect ratios and Reynolds numbers. *J. Braz. Soc. Mech. Sci. Eng.* 43 (315), 1–26. doi:10.1007/s40430-021-03040-2

Alam, Md. M., Bai, H., and Zhou, Y. (2016). The wake of two staggered square cylinders. *J. Fluid Mech.* 801, 475–507. doi:10.1017/jfm.2016.303

Alam, Md. M., Derakhshandeh, J. F., Zheng, Q., Rehman, S., Ji, C., and Zafar, F. (2017). "The flow around three tandem circular cylinders," in The world congress on Advances in Structural Engineering and Mechanics (ASEM 17), Ilsan(Seoul), Korea, August 28 - September 1, 2017.

Bajalan, S., Shadaram, A., Hedayat, N., and Taleghani, A. S. (2011). Experimental study of frequency behavior for a circular cylinder behind an airfoil. *World Acad. Sci. Eng. Technol. Int. J. Aerosp. Mech. Eng.* 5, 2349–2353.

Belloli, M., Giappino, S., Morganti, S., Muggiasca, S., and Zasso, A. (2014). Vortex induced vibrations at high Reynolds numbers on circular cylinders. *Ocean. Eng.* 94, 140–154. doi:10.1016/j.oceaneng.2014.11.017

Burattini, P., and Agrawal, A. (2013). Wake interaction between two side-by-side square cylinders in channel flow. *Comput. Fluids* 77, 134–142. doi:10.1016/j.compfluid.2013.02.014

Chakraborty, S., Chaterjee, S., and Kumar, R. (2022). Effect of gap ratio on flow influenced actions of two circular cylinders in side-by-side arrangement. *J. Mines, Metals Fuels* 70 (3A), 15–20. doi:10.18311/jmmf/2022/30662

Chen, S., and Doolen, G. D. (1998). Lattice Boltzmann method for fluid flows. *Annu. Rev. Fluid Mech.* 30, 329–364. doi:10.1146/annurev.fluid.30.1.329

Eizadi, H., An, H., Zhu, H., Chang, L., and Cheng, L. (2022). Wake transitions of six tandem circular cylinders at low Reynolds numbers. *Phys. Fluids* 34 (2), 1–49. doi:10.1063/5.0080268

Gnatowska, R., Sobczyk, J., and Wodziak, W. (2020). Stability of flow around two rectangular cylinders in tandem. *Appl. Phys. Mech. Material Eng.* 138 (2), 295–298. doi:10.12693/APhysPolA.138.295

Huang, Z., Xi, G., and Zhang, W. (2012). Numerical simulation of spacing effects on the flow past two 2:1 rectangular cylinders in tandem at Re = 200. *Proc. Am. Soc. Mech. Eng.* 2012, 1–9. doi:10.1115/FEDSM2012-72157

Islam, S. U., Manzoor, R., Ying, Z. C., and Islam, Z. U. (2018). Numerical investigation of different aspect ratios for flow past three inline rectangular cylinders. *J. Braz. Soc. Mech. Sci. Eng.* 40, 410. doi:10.1007/s40430-018-1334-y

Islam, S. U., Zhou, C. Y., Shah, A., and Xie, P. (2012). Numerical simulation of flow past rectangular cylinders with different aspect ratios using the incompressible lattice Boltzmann method. *J. Mech. Sci. Technol.* 26 (4), 1027–1041. doi:10.1007/s12206-012-0328-4

Kuo, C. H., Chein, S. M., and Hsieh, H. J. (2008). Self-sustained oscillations between two tandem cylinders at Reynolds number 1000. *Exp. Fluids* 44, 503–517. doi:10.1007/s00348-007-0409-9

Kuzmina, K., and Marchevsky, I. (2021). Flow simulation around circular cylinder at low Reynolds numbers. *J. Phys. Conf. Ser.* 1715, 1–7. doi:10.1088/1742-6596/1715/1/012067

Lee, S. J., Mun, G. S., Park, Y. G., and Ha, M. Y. (2019). A numerical study on fluid flow around two side-by-side rectangular cylinders with different arrangements. *J. Mech. Sci. Technol.* 33 (7), 3289–3300. doi:10.1007/s12206-019-0624-3

Ma, S., Kang, C.-W., Lim, T.-B. A., Wu, C.-H., and Tutty, O. (2017). Wake of two side-by-side square cylinders at low Reynolds numbers. *Phys. Fluids* 29, 1–23. doi:10.1063/1.4979134

Marson, F., Thorimbert, Y., Chopard, B., Ginzburg, I., and Latt, J. (2021). Enhanced single-node lattice Boltzmann boundary condition for fluid flows. *Phys. Rev. E* 103 (5), 053308. doi:10.1103/physreve.103.053308

Mirzaei, M., Taleghani, A. S., and Shadaram, A. (2012). Experimental study of vortex shedding control using plasma actuator. *Appl. Mech. Mater.* 186, 75–86. doi:10.4028/www.scientific.net/amm.186.75

Mithun, M. G., and Tiwari, S. (2014). Flow past two tandem square cylinders vibrating transversely in phase. *Jpn. Soc. Fluid Mech.* 46, 055509–055532. doi:10.1088/0169-5983/46/5/055509

Mittal, S., and Raghuvanshi, A. (2001). Control of vortex shedding behind circular cylinder for flows at low Reynolds numbers. *Int. J. Numer. Methods Fluid* 35, 421–447. doi:10.1002/1097-0363(20010228)35:4<421::aid-fld100>3.0.co;2-m

Mohammad, A. A. (2011). *Lattice Boltzmann method: fundamentals and engineering applications with computer codes*. Berlin: Springer.

Mohammadi, M., and Taleghani, A. S. (2014). Active flow control by dielectric barrier discharge to increase stall angle of a naca0012 airfoil. *Arabian J. Sci. Eng.* 39, 2363–2370. doi:10.1007/s13369-013-0772-1

Noori, M. S., Rahni, M. T., and Taleghani, A. S. (2020). Effects of contact angle hysteresis on drop manipulation using surface acoustic waves. *Theor. Comput. Fluid Dyn.* 34, 145–162. doi:10.1007/s00162-020-00516-0

Noori, S. M. S., Rahni, M. T., and Taleghani, S. A. S. (2019). Multiple-relaxation time color-gradient lattice Boltzmann model for simulating contact angle in two-phase flows with high density ratio. *Eur. Phys. J. Plus* 134, 399. doi:10.1140/epjp/i2019-12759-x

Norberg, C. (1993). Flow around rectangular cylinders: pressure forces and wake frequencies. *J. Wind Eng. Industrial Aerodynamics* 49, 187–196. doi:10.1016/0167-6105(93)90014-f

Octavianty, R., Asai, M., and Inasawa, A. (2016). Experimental study on vortex shedding and sound radiation from a rectangular cylinder at low Mach numbers. *Jpn. Soc. Aeronautical Space Sci.* 59 (5), 261–268. doi:10.2322/tjsass.59.261

Okajima, A. (1982). Strouhal numbers of rectangular cylinders. *J. Fluid Mech.* 123, 379–398. doi:10.1017/s0022112082003115

Perumal, D. A., Kumar, V. S., and Dass, K. A. (2012). Numerical simulation of viscous flow over a square cylinder using lattice Boltzmann method. *ISRN Math. Phys.* 2012, 1–16. doi:10.5402/2012/630801

Rahman, H., Islam, S. U., Abbasi, W. S., Manzoor, R., Amin, F., and Alam, Z. (2021). Numerical computations for flow patterns and force statistics of three rectangular cylinders. *Math. Problems Eng.* 2021, 1–12. doi:10.1155/2021/9991132

Rajpoot, R. S., Anirudh, K., and Dhinakaran, S. (2021). Numerical investigation of unsteady flow across tandem cylinders near a moving wall at Re = 100. *Case Stud. Therm. Eng.* 26, 1–14. doi:10.1016/j.csite.2021.101042

Rangan, M. L. N. V. K., and Santanu Ghosh, S. (2022). A face-based immersed boundary method for compressible flows using a uniform interpolation stencil. *Front. Mech. Eng.* 8, 903492. doi:10.3389/fmech.2022.903492

Saha, A. K., Muralidhar, k., and Biswas, G. (2000). Transition and chaos in two-dimensional flow past a square cylinder. *J. Eng. Mech.* 126, 523–532. doi:10.1061/(asce)0733-9399(2000)126:5(523)

Salmasi, A., Shadaram, A., and Taleghani, A. S. (2013). Effect of plasma actuator placement on the airfoil efficiency at poststall angles of attack. *IEEE Trans. Plasma Sci.* 41 (10), 3079–3085. doi:10.1109/tps.2013.2280612

Sarvghad, Hesam, M., and Navid, N. (2011). Numerical simulation of flow over two side-by-side circular cylinders. *J. Hydrodynamics* 23 (6), 792–805. doi:10.1016/S1001-6058(10)60178-3

Shiraishi, N., Matsumoto, M., and Shirato, H. (1986). On aerodynamic instabilities of tandem structures. *J. Wind Eng. Industrial Aerodynamics* 23, 437–447. doi:10.1016/0167-6105(86)90061-9

Shui, Q., Duan, C., Wang, D., and Gu, Z. (2021). New insights into numerical simulations of flow around two tandem square cylinders. *AIP Adv.* 11, 1–14. doi:10.1063/5.0042797

Sohankar, A., Davidson, L., and Norberg, C. (1995). "Numerical simulation of unsteady flow around a square two-dimensional cylinder." in. Twelfth Australasian Fluid Mechanics Conference the University of Sydney, Australia, 4-8 December 2022, 517–520.

Song, Y., Zhu, R., Simon, T. W., and Xie, G. (2017). Computational fluid dynamics modeling patterns and force characteristics of flow over in-line four square cylinders. *Therm. Sci.* 21 (00), 2553–2563. doi:10.2298/tsci170211035s

Su, Z., Liu, Y., and So, R. M. C. (2004). Numerical simulation of two tandem circular cylinders in a turbulent flow. *Flow-Induced Vib.* 2004, 297–302.

Su, Z. D., Guo, Z. L., So, R. M. C., and Liu, Y. (2002). "Two- and three-dimensional study of two tandem circular cylinders in a cross flow," in Conference on Bluff Body Wakes and Vortex-Induced Vibrations, Port Douglas, Australia, 17-20 December 2002, 1–5.

Sukop, M. C., and Throne, D. T. (2006). *Lattice Boltzmann modeling: an introduction for geo-scientists and engineers*. Berlin: Springer.

Taleghani, A. S., Abdollah Shadaram, A., Mirzaei, M., and Abdolahipour, S. (2018). Parametric study of a plasma actuator at unsteady actuation by measurements of the induced flow velocity for flow control. *J. Braz. Soc. Mech. Sci. Eng.* 40, 173. doi:10.1007/s40430-018-1120-x

Tao, S., He, Q., Chen, B., Yang, X., and Huang, S. (2018). One-point second-order curved boundary condition for lattice Boltzmann simulation of suspended particles. *Comput. Math. Appl.* 76 (7), 1593–1607. doi:10.1016/j.camwa.2018.07.013

Wang, J., Shan, X., and Liu, J. (2022). First instability of the flow past two tandem cylinders with different diameters. *Phys. Fluids* 34, 1–19. doi:10.1063/5.0098204

Wolf-Gladrow, D. A. (2000). *Lattice-gas cellular automata and lattice Boltzmann models: an introduction*. Berlin: Springer.

Ye, Z.-H., Sun, X., and Zhang, J.-Z. (2019). Flow-induced vibrations of two staggered circular cylinders at low Reynolds number. *J. Vib. Test. Syst. Dyn.* 3 (1), 39–53. doi:10.5890/jvtsd.2019.03.004

Zdravkovich, M. M. (1987). The effects of interference between circular cylinders in cross flow. *J. Fluids Struct.* 1, 239–261. doi:10.1016/s0889-9746(87)90355-0

Zhang, Z., and Zhang, X. (2012). Direct simulation of low-Re flow around a square cylinder by numerical manifold method for Navier-Stokes equations. *J. Appl. Math.* 2012, 1–14. doi:10.1155/2012/465972

10.3389/fmech.2024.1341618

Nomenclature

CFD	Computational fluid dynamics
Re	Reynolds number
CD_{mean}	Mean drag coefficient
St	Strouhal number
AR	Aspect ratio
CD	Drag coefficient
G	Gap spacing
CL_{rms}	Root mean square of the lift coefficient
CD_{rms}	Root mean square of the drag coefficient
CL	Lift coefficient
NS	No-shedding regime
CL_{mean}	Mean lift coefficient
C_1	First cylinder
C_2	Second cylinder
CD_{amp}	Amplitude of the drag coefficient
CL_{amp}	Amplitude of the lift coefficient
L	Length of the channel
H	Height of the channel
D	Width of the cylinder

frontiers | Frontiers in Mechanical Engineering

TYPE Original Research
PUBLISHED 13 March 2024
DOI 10.3389/fmech.2024.1355711

OPEN ACCESS

EDITED BY
Jian Wu,
Harbin Institute of Technology, China

REVIEWED BY
Cetin Canpolat,
Çukurova University, Türkiye
Yu Zhang,
Harbin Institute of Technology, China

*CORRESPONDENCE
Arash Shams Taleghani,
Arash.taleghani@gmail.com

RECEIVED 14 December 2023
ACCEPTED 29 February 2024
PUBLISHED 13 March 2024

CITATION
Shams Taleghani A and Ghajar A (2024), Aerodynamic characteristics of a delta wing aircraft under ground effect.
Front. Mech. Eng 10:1355711.
doi: 10.3389/fmech.2024.1355711

Aerodynamic characteristics of a delta wing aircraft under ground effect

Arash Shams Taleghani* and Arsalan Ghajar

Aerospace Research Institute, Ministry of Science, Research and Technology, Tehran, Iran

The main objective of this study is to investigate the impact of ground effects on the aerodynamic coefficients of a delta wing aircraft model. Since the flow on the delta wing exhibits vortical flow inherently, it is crucial to examine the influence of ground effects under these conditions. An experimental study was conducted to enhance understanding of the aerodynamic behavior of an aircraft model incorporating a delta wing-body-vertical tail. Experiments were conducted in a subsonic wind tunnel with a test section measuring 2.8 m × 2.2 m. Measurements were taken using a sting type balance to determine the aerodynamic forces and moments. All experimental tests were performed at a Reynolds number of 1.5×10^6, with the specific aim of examining and identifying the influence of the ground on aerodynamic coefficients. To investigate how ground effect affects the aerodynamic performance of the model, a fixed plate with an adjustable height was placed underneath it. The distance between the model and the ground was varied, and resulting data indicated that increased proximity to the ground improved longitudinal static stability. The results revealed that the presence of the ground plane resulted in a 6% increase in the maximum lift coefficient. Meanwhile, the lift increases around 25% due to ground effects at an angle of attack of 14° as it approaches the ground. The lift coefficient was enhanced across all angles of attack, while the induced drag coefficient decreased, resulting in an overall increase in aerodynamic efficiency. The lift curve slope saw a 16.9% increase when the model's height from the ground plane was less than half of the wing span. As the height decreased further, the aerodynamic center shifted backward, leading to an increase in longitudinal static stability. The rolling moment and yawing moment coefficients becomes unstable at angles of attack above 30°.

KEYWORDS

aircraft, wind tunnel, ground simulator, aerodynamic efficiency, delta wing, ground effects, vertical tail

1 Introduction

During the past decade, airplane aerodynamic designers have concentrated on enhancing the lift coefficient (Mirzaei et al., 2012; Taleghani et al., 2012; Salmasi et al., 2013; Mohammadi and Taleghani, 2014; Abdolahipour, 2023) and lowering the drag coefficient (Albers et al., 2019; Atzori et al., 2020; Rodriguez et al., 2020; Kornilov, 2021; Fahland et al., 2023) through active flow control methods in cruise phase. They have also aimed to improve the aerodynamic coefficients on high-lift devices during takeoff and landing phases (Abdolahipour et al., 2021; Abdolahipour et al., 2022a; Abdolahipour et al., 2022b). Despite the importance of the issue of ground effect during takeoff and landing,

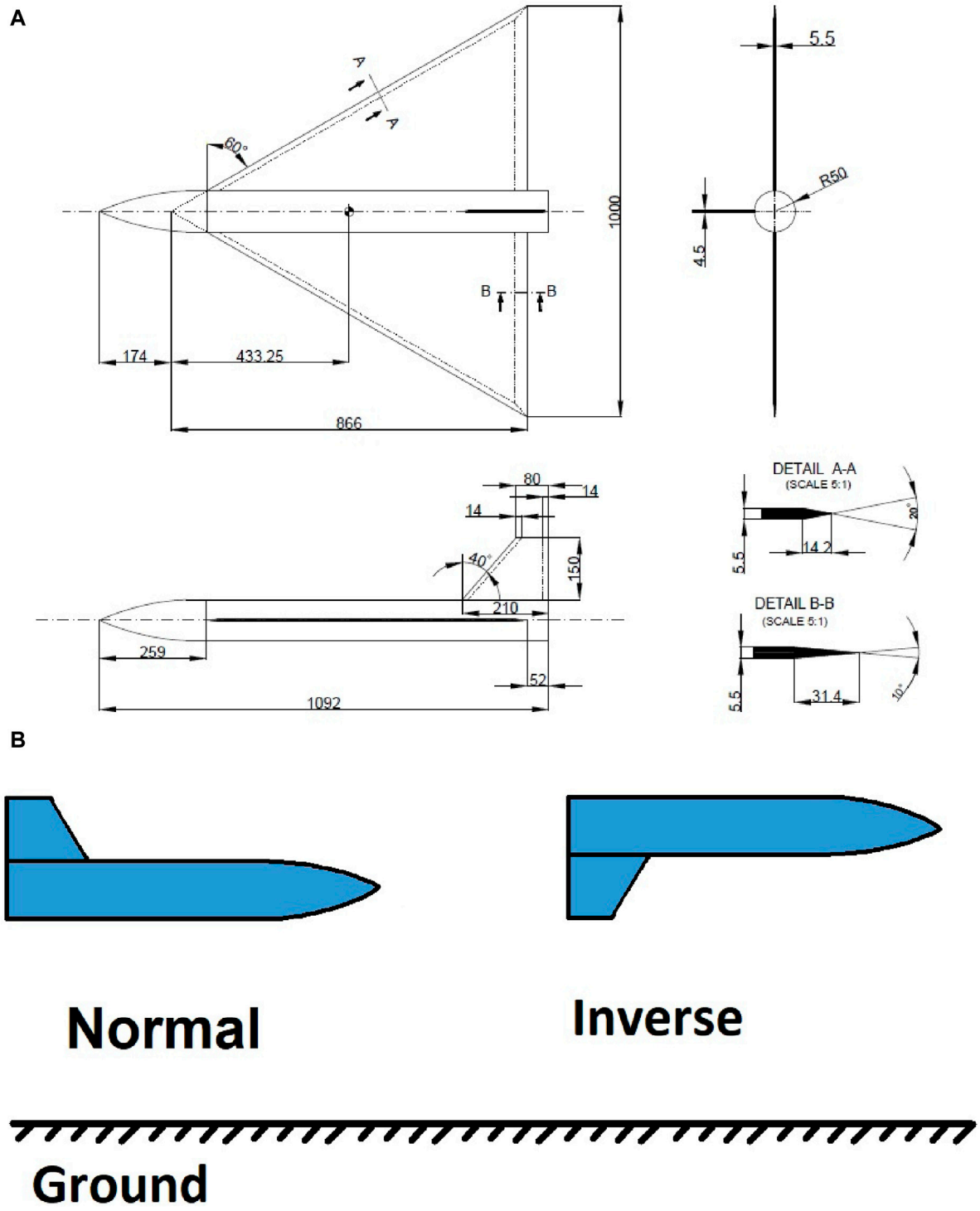

FIGURE 1
Schematic of **(A)** 60° delta wing-body-tail model (dimensions in mm) and **(B)** Model at normal and inverse positions.

recent years have seen fewer research results published, possibly due to the short duration of exposure to ground effect. A more comprehensive investigation is necessary to fully understand the impact of ground effect on aircraft performance in these critical phases of flight. When an aircraft flies at a low altitude, the airflow between the airplane and the ground aligns parallel to the surface, causing noticeable variations in the airplane's aerodynamics from flying at higher altitudes. This phenomenon is referred to as the ground effect. The ground effect has a significant impact on conventional airplanes during the landing and take-off phases, as well as on ground effect airplanes during horizontal flight. A clear comprehension of ground effects is crucial for advancing modern

FIGURE 2
Delta wing-body-tail model installation on ground simulation stand.

conventional airplane control systems, designing landing gears, and creating high-lift devices. In general, when an airplane is near the ground, the wing produces a greater amount of lift. The examination of ground effects on a wing can be separated into 2D and 3D effects. The ground induces a high-pressure distribution on the lower surface of a two-dimensional airfoil when the angle of attack is positive. This results in an increase in lift for the airfoil. A three-dimensional wing at a positive angle of attack also experiences a decrease in downwash angle and induced drag.

In a wind tunnel experiment, Ahmed et al. (Ahmed et al., 2007) studied the performance of a NACA4412 airfoil under ground effect conditions. The outcomes revealed that low angles of attack ($\alpha < 4^{\circ}$) led to reduced lift near the ground. Conversely, the lift increased in close proximity to the ground for angles of attack between 4° and 8°. Higher angles of attack result in greater lift near the ground plane due to the increased pressure on the lower surface of the airfoil. Ahmed and Sharma (Ahmed and Sharma, 2005) conducted a study on the NACA 0015 airfoil in ground effect. The study found that the aerodynamic characteristics were significantly influenced by both the angle of attack and the distance from the ground. Additionally, Zerihan and Zhang (Zerihan and Zhang, 2000) conducted a wind tunnel experiment on the Tyrrell-02 airfoil, which is an inverted airfoil with a high camber, to investigate its ground effect. The researchers observed a gradual increase in downforce as the distance from the ground plane decreased, reaching a maximum value before decreasing. An analysis of the aerodynamic and stability properties of airfoils under extreme ground effects was conducted by Nirooei (Nirooei, 2018). At low Reynolds numbers, ground effects were studied around the NACA 4415 airfoil according to He et al. (He et al., 2018). They used this data to investigate the influence of ground effects on the aerodynamic performance of the airfoil. The study, utilizing both numerical and theoretical methods, demonstrated the influential role of the ground on both primary and secondary

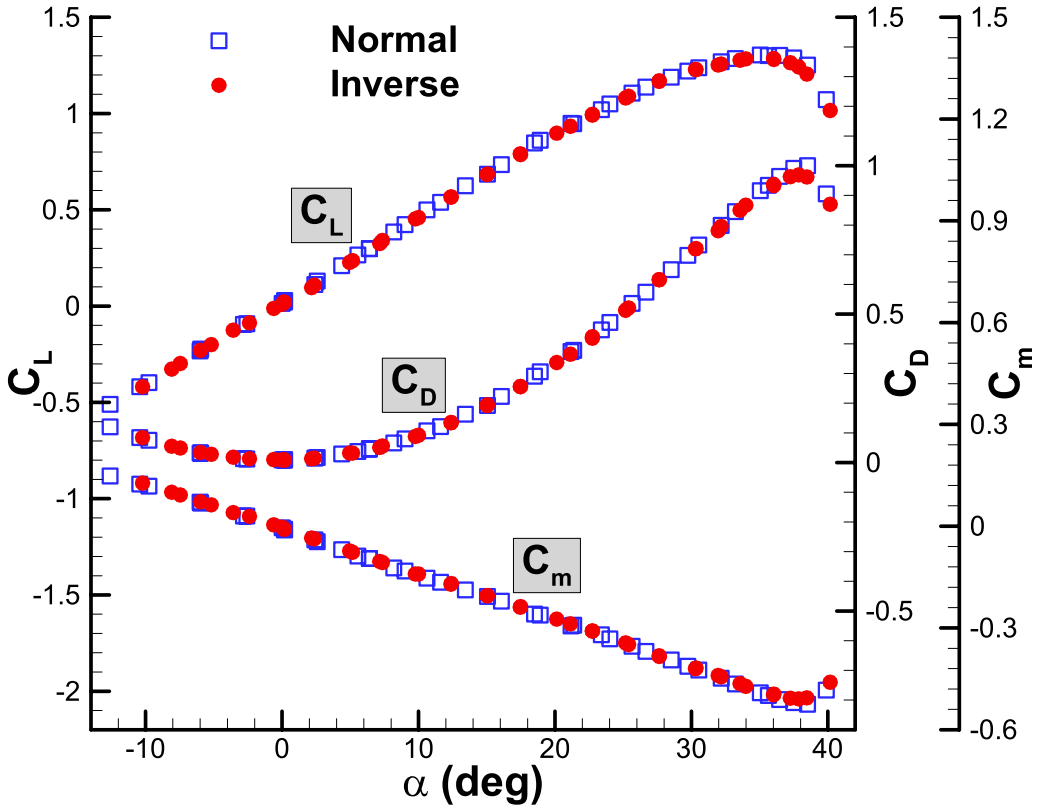

FIGURE 3
Variation of aerodynamic coefficients with angle of attack for the aircraft model without the ground plane.

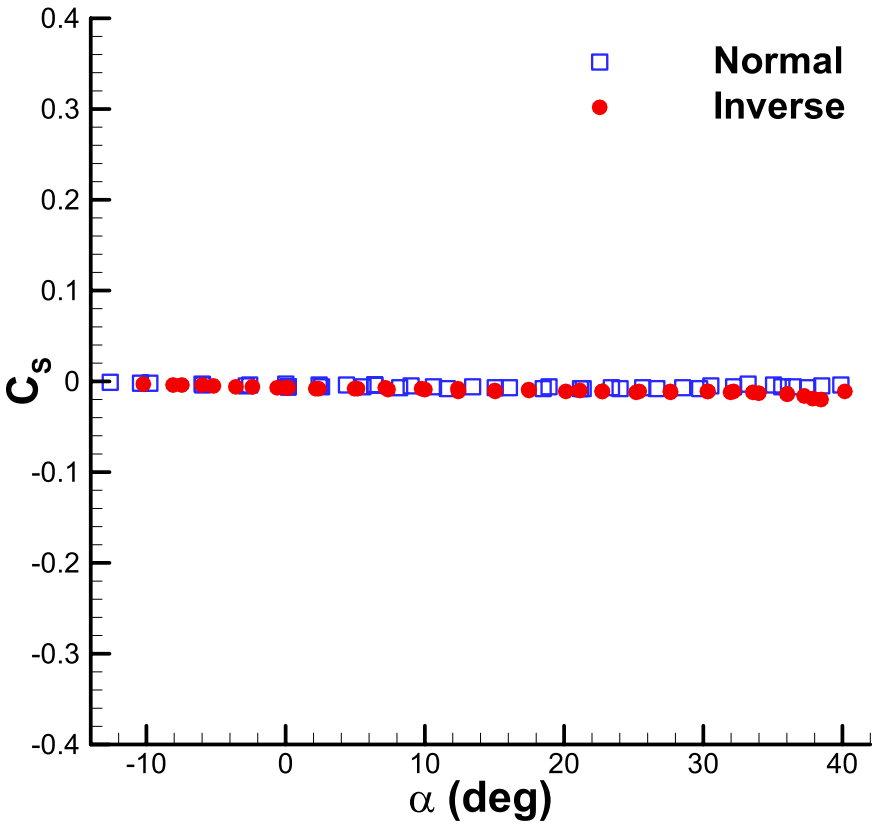

FIGURE 4
Variation of side force coefficient with angle of attack for the aircraft model without the ground plane.

instabilities of the separated flow surrounding the airfoil in low Reynolds number conditions.

A numerical simulation was performed to assess the aerodynamic features of 2D smart flaps while considering the ground effect (Djavareshkian et al., 2011). A computational simulation (Qu et al., 2014) was also performed to study the impact of dynamic ground effects on a NACA 4412 airfoil during the landing phase. The analysis revealed that at higher altitudes, the lift experienced in dynamic ground effect (DGE) remains constant despite the decrease in altitude, and is equivalent to the lift in static ground effect (SGE). On the other hand, the lift of DGE increases rapidly as the height decreases in the small height region. Furthermore, it is substantially higher than the lift in SGE with the same angle of attack. Gratzer and Mahal (Gratzer and Mahal, 1971) conducted an analysis of the aerodynamics of an STOL aircraft in ground effect through theoretical analysis and wind tunnel experiments. They found that as the height from the ground plane decreased, the slope of the lift curve decreased as well as the pressure on the upper surface. For the 3D study on ground effect, the focus has been on the aerodynamics of wingtip vortices. Chawla et al. (Chawla et al., 1990) conducted an aerodynamics experiment on a wing with an NACA4415 airfoil and aspect ratio of 2.33, utilizing a grounded plane. Their research revealed that implementing endplates improved lift at low heights from the ground plane. Lee (Lee, 2002) carried out an experimental examination of the motion of wingtip vortices of a rectangular wing in the ground effect. The study findings indicate that the presence of the ground plane causes a deceleration of downward vortices' motion and their outward motion towards the spanwise direction as a result of the ground effect.

In a wind tunnel experiment performed by Harvey and Perry (Harvey and Perry, 1971), they examined the trajectory of wingtip vortices in ground effect. Their results indicate that the vortices descended towards the ground initially before rebounding downstream. Furthermore, Dakhrabadi and Seif (Tavakoli Dakhrabadi and Seif, 2016) studied the aerodynamic properties of the compound wing-in-ground effect with both the main and outer wings. The study demonstrated that repositioning the outer wing towards the trailing edge of the main wing enhanced static height stability, leading to a decrease in tail area. In a study conducted by Rojewski and Bartoszewicz (Adam and Bartoszewicz, 2017), the impact of wing-in-ground effects was assessed on the lift coefficients of airplanes and the downforce coefficients of cars. Positive angles of attack result in a higher lift coefficient, while negative angles of attack result in a lower lift coefficient. Computational simulations were carried out by Sereez et al. (Sereez et al., 2017; Sereez et al., 2018) using CFD methods to study the aerodynamic features of the Common Research Model (CRM). This model represents a typical transport airliner in proximity to the ground. Wang (Wang, 2005) discovered significant changes in lateral-directional modes when a slender object operates close to the ground. Their study examined the body's lift and pitching moment relative to its distance from the ground plane. Their results indicate that lift decreases and nose-up

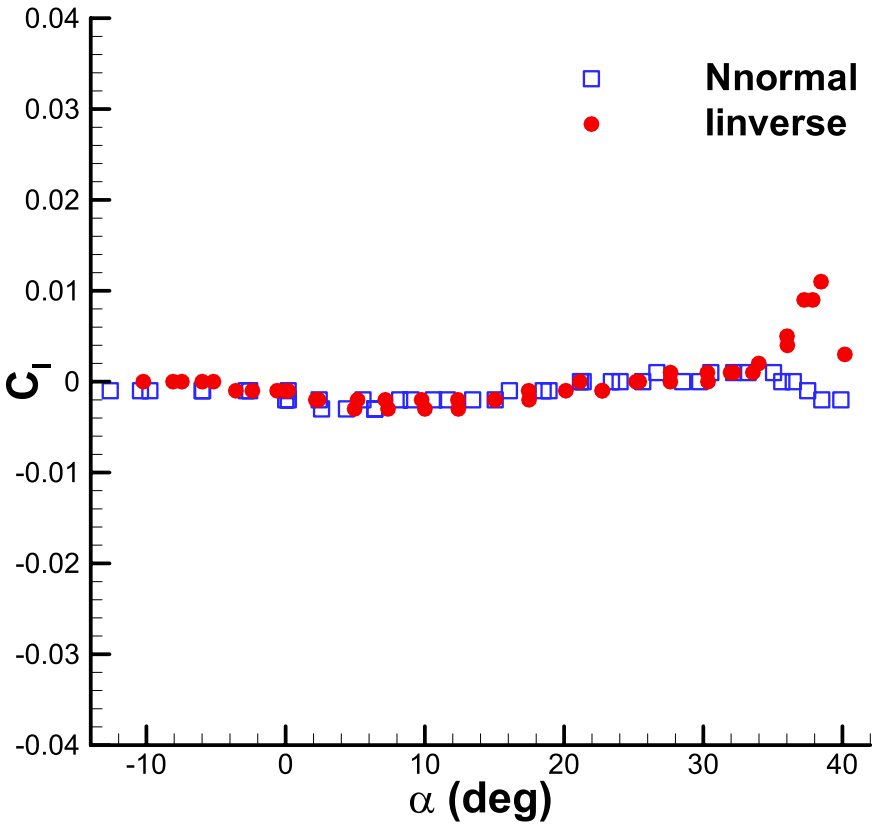

FIGURE 5
Variation of rolling moment coefficient with angle of attack for the aircraft model without the ground plane.

pitching moment increases as the distance from the ground decreases.

The ground effect was investigated by Deng (Deng, 2017) using a simulation of a three-dimensional wing-body configuration. Computations were conducted for the DLR-F6 wing-body in unbounded flow, and compared with experimental data to verify the accuracy of the simulation approach. As the wing body's height from the ground decreased while maintaining a fixed angle of attack, researchers observed an increase in lift, a decrease in drag, and an increase in nose-up pitching moment. Similarly, Deng et al. (Deng et al., 2017) studied the aerodynamics of the DLR-F6 wing body in unbounded and ground effects. It was discovered that increasing the angle of attack in the ground effect amplified the blockage effect while reducing the nose-up pitching moment. The Delayed Detached Eddy Simulation and Spalart-Allmaras turbulence model were used to investigate the aerodynamics and flow physics of a close-coupled canard configuration with a sharp leading edge in static ground effect (Qin et al., 2017), as well as a 65° sweep delta wing with a sharp leading edge in both static and dynamic ground effect (Qin et al., 2015; Qin et al., 2016).

In wind tunnel studies of ground effects, static ground effect is the most frequently used technique. This involves employing a stationary model at different heights above the ground plane to simulate the behavior of an aircraft flying at a consistent altitude near the ground. The static data obtained facilitates the simulation of an aircraft's behavior when flying at a uniform altitude close to the ground. To replicate the rate of descent of a descending airplane at a specific altitude, a wind tunnel can be utilized. The technique involves using a model that moves towards either a stationary or a moving ground plane, commonly referred to as dynamic ground effect (Chang and Muirhead, 1985; Lee et al., 1987a; Kemmerly et al., 1988; Lee et al., 1989; Paulson et al., 1990).

The results indicate that defining the ground effects numerically is complex due to the significant and variable influence of the ground effect when the height is below a certain threshold. These effects are non-linear; for instance, the increase in lift force is non-linear when the height is less than half of the wing span, and these variations differ among different aircraft. To predict and study the ground effects, analytical software is commonly employed (McDonnell Douglas Corporation and USAF Stability and Control DATCOM, 1960). This software utilizes flight data, equations, and tables to forecast control and stability characteristics.

Recently, Shams Taleghani et al. (Taleghani et al., 2020) conducted a study to examine how the ground affects aerodynamic coefficients in different situations involving the angle of attack and horizontal tail angle. Their research primarily focused on evaluating the performance of the horizontal tail by observing changes in lift, drag, and pitching moment coefficients under various conditions, including ground effect and out-of-ground effect.

Limited experimental results exist for the ground effect of delta wings, mainly focusing on airplane-like configurations (Kemp et al., 1966; Rolls and Koenig, 1966; Lockwood and Phillips, 1968; Corsiglia et al., 1969; Baker et al., 1970; Snyder et al., 1970; Katz

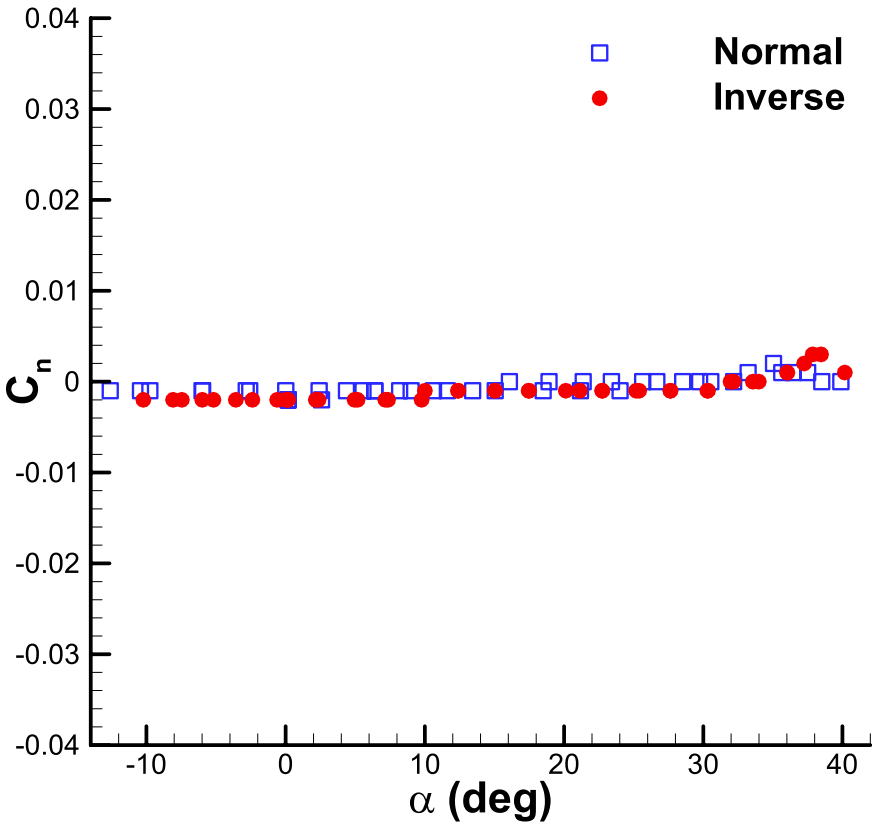

FIGURE 6
Variation of yawing moment coefficient with angle of attack for the aircraft model without the ground plane.

and Levin, 1984). This study aims to experimentally evaluate the static aerodynamic properties of a model with a 60° swept delta wing. The model includes a fuselage and vertical tail, both positioned close to and above the ground surface.

2 Experimental setup

The experiments were carried out at the National Low-Speed Wind Tunnel, which features an open test section. The rectangular test section measures 2.2 m × 2.8 m × 4 m in dimensions. The tunnel is equipped with a fixed-pitch axial-flow fan powered by a 1.2 MW electric motor, with a diameter of 4.5 m. The rotational speed of the fan can be adjusted between 60 and 560 rpm to control the airflow velocity in the test section, ranging from 10 m/s to 70 m/s. To ensure a uniform and low turbulence flow, the tunnel incorporates a six-to-one contraction following a settling chamber. The settling chamber includes one honeycomb and two metal screens. The tunnel was calibrated to ensure that the flow parameters, including turbulence level, flow uniformity, and flow angularity, were within acceptable limits for this type of wind tunnel. To measure the turbulence level of the flow in the test section and test section airflow non-uniformity in velocity, a thermal anemometer (specifically, the DANTEC 55P11 one-dimensional hot wire probe) was used. Using a traverse mechanism, the whole area is scanned by a hot wire probe at different test section flow velocities. Hot wire probe measures turbulence intensity using flow velocity fluctuations measurement. The turbulence intensity at the center of the test section remains below 0.13% for velocities exceeding 35 m/s. At a test section airflow velocity of 50 m/s, the turbulence intensity remains below 0.2%, except in regions near the free jet boundary. The test section airflow experiences a non-uniformity of less than 0.2% in velocity. The flow angle in the test section, at the same airflow velocity, was approximately 0.3°. The velocity of the airflow in the test section is determined using a pitot-static tube placed on one of the side walls. This tube is connected to both the data acquisition system and a precise differential pressure transducer. The transducer has an accuracy of 0.05% for pressure readings. The maximum error in measuring the flow velocity measured by pitot-static tube is 0.1 m/s.

A 6-component internal strain gauge balance is used to measure the aerodynamic forces and moments on the model. The maximum range of linear loading for lift, drag and side forces is 150 kg, 50 kg and 150 kg respectively, and the pitching moment, rolling moment and yawing moment are all 15 kg-m. This balance is attached to the model, which is connected to the sting mounted on the vertical and L-shaped rotated struts of the rig. A vertical strut is driven by an electric motor and gearbox located on the rotating floor plane of the wind tunnel test section, which generates the motion of the model. To conduct static tests, the model and the internal balance are placed on a test stand. The angle of attack and sideslip angle can be adjusted manually or in a pre-planned manner using potentiometers. This experimental setup covers a range of −10°–40° for the model's incidence. The setup is mounted on a special platform

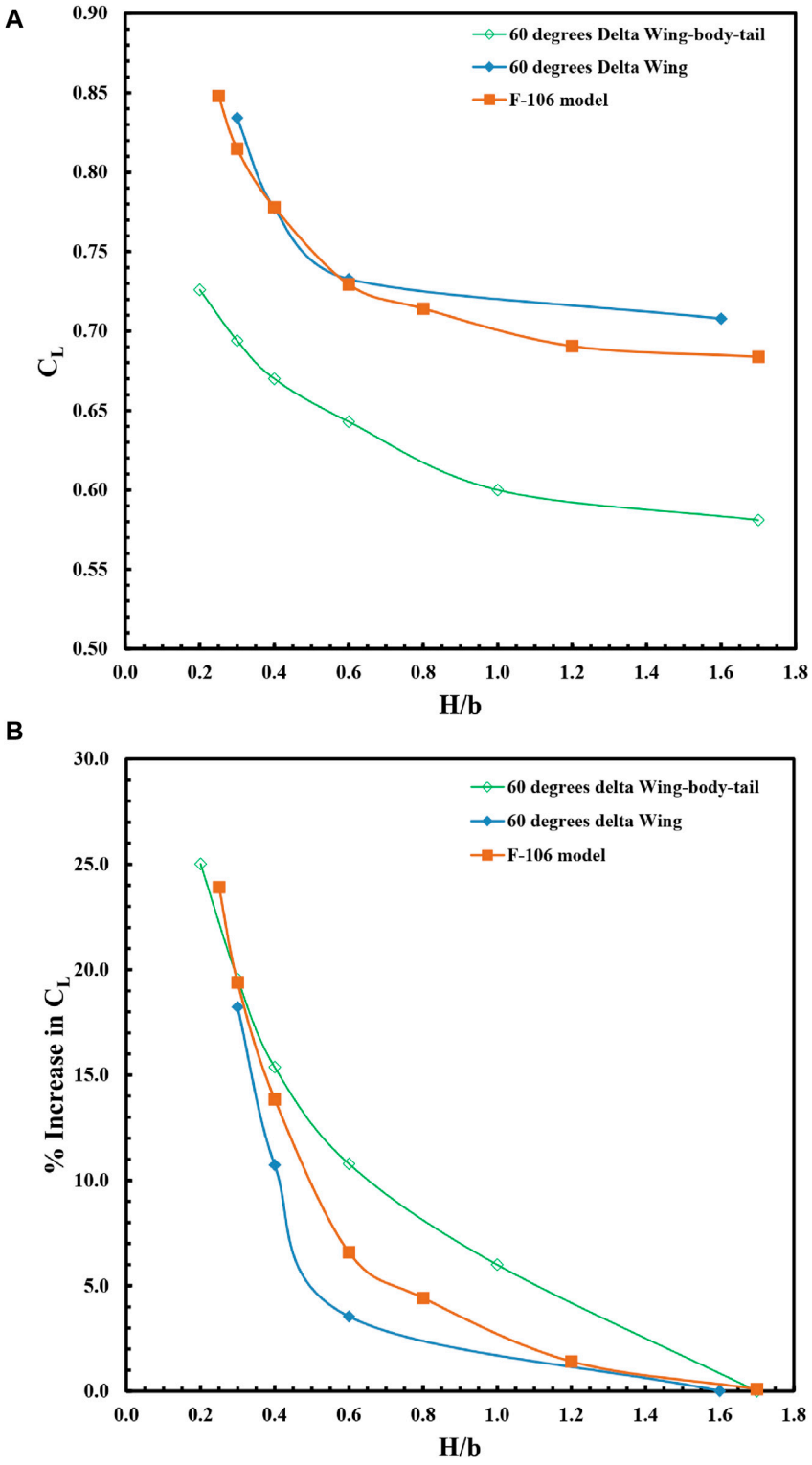

FIGURE 7
Variation of **(A)** lift coefficient and **(B)** lift increment with ground heights for the delta wing, delta wing-body-tail and F-106 model at the angle of attack of 14°.

(turntable) with a diameter of 2.0 m, installed on the wind tunnel test section's floor plane. By rotating the turntable, the mean sideslip can be changed based on the orientation of the aerodynamic model. The wind tunnel's working section turntable rotation allows for investigations of sideslip angles from −90° to +90°. All of the experiments were conducted at zero sideslip angle. This experimental setup enables the conduct of conventional steady experiments.

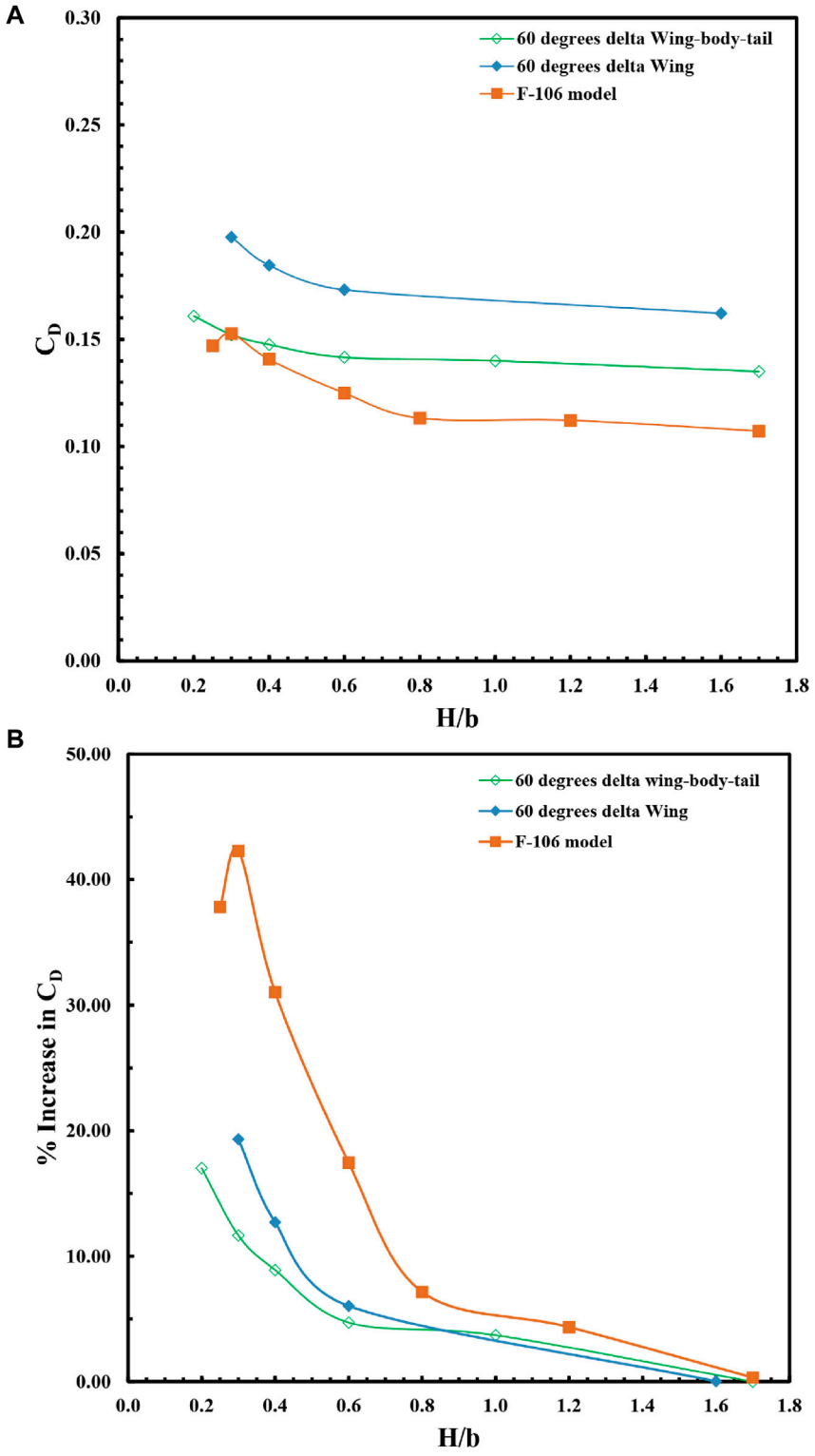

FIGURE 8
Variation of **(A)** drag coefficient and **(B)** drag increment with ground heights for the delta wing, delta wing-body-tail and F-106 model at the angle of attack of 14°.

High-speed analog-to-digital converters are used to measure the strain gauge balance signals. A 16-channel data acquisition system processes all forces and moments, as well as the angles of attack and sideslip angles, along with the dynamic pressure. These measurements are then converted to their corresponding physical quantities using calibration coefficients. The data is acquired at a frequency of 30 kHz for a duration of 10 s at each mean angle of attack. This acquisition time allows for flow stabilization, while the

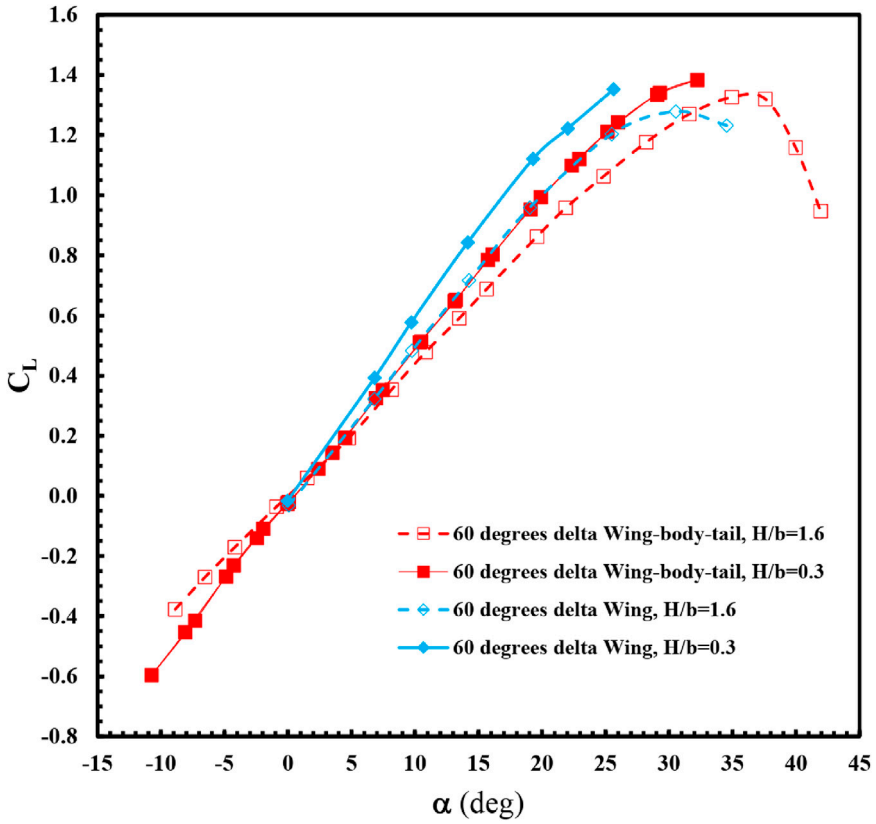

FIGURE 9
Variation of lift coefficient with angle of attack for the delta wing, delta wing-body-tail model in ground effect (H/b = 0.3) and out of ground effect (H/b = 1.6).

sampling rate is sufficient to capture the unsteady flow phenomena.

The present study utilized a model consisting of a delta wing combined with a body and vertical tail, where the wing was fixed in the middle position. The aircraft's wing featured a delta-shaped design with an aspect ratio of 2.31 and a leading edge sweep of 60°. The upper surface of the wing was flat, while the leading and trailing edges were beveled and sharp, forming a 20° angle between the lower and upper surfaces. The fuselage was cylindrical in shape with an ogive nose. It consisted of two sections: a tangent ogive nose with a semi-apex angle of 20°, and a constant diameter section measuring 0.833 m in length. The fuselage had a total length of 1.092 m and a diameter of 0.1 m. The wing was constructed from a flat plate section. The wing reference area was 0.433 m^2 and the aerodynamic mean chord was 0.577 m. The pitching moment of the model was measured at 25 percent of the mean aerodynamic chord. Figure 1A provides a schematic representation of the 60° delta wing-body-tail model. Figure 1B shows the model normal and inverse positions. At inverse position the model is rotated 180° around its body axis. The dimensions of the model were determined based on specific criteria, including the dimensions of the wind tunnel test section and the maximum allowable loads on the balance. In order to meet the limitations of the wind tunnel test section, the wing span of the model must be less than 0.80 times the width of the test section, and the frontal area of the model must be less than 7 percent of the test section area to minimize any effects from the test section walls. Based on these criteria, the model's wing span is 1.0 m, which is less than 0.80 times 2.8 m (the width of the test section). Additionally, the model's frontal area at an angle of attack of 40° is calculated as follows: Wing area × sin 40° = 0.433 × 0.6427 = 0.2783 m^2. Considering the test section area is approximately 6.0 m^2, the model's blockage ratio (0.2783/6.0 × 100) is approximately 4.6%, which is less than the allowed 7%. Regarding the maximum allowable loads on the balance, the normal force must be less than 150 kg. At a velocity of 50 m/s, the normal force is determined by 0.5× density × velocity^2 × wing area × maximum normal force coefficient (0.5 × 1.1×50^2 × 0.433×1.5). This calculation results in a normal force of 893 N, which is equivalent to 91 kg, and is less than the allowed 150 kg.

The investigation of the ground effect utilized a generic delta wing aircraft configuration derived from a delta wing-body setup. The delta wing-body-tail model was affixed to a sting balance, allowing for vertical transverse movement relative to the model. The wind tunnel test section had a rectangular cross-section, which was effectively reduced by the ground plane. Throughout the test, a constant airspeed of 50 m/s was maintained, corresponding to a Reynolds number of 1.5 × 10^6. The delta wing model featured a cylindrical center body connected to a six-component sting balance. To analyze the impact of ground effects on the longitudinal characteristics of the delta wing-body-tail model, the model was positioned at various heights above the ground simulator plate. The model was secured on a sting-type support stand in the center of the

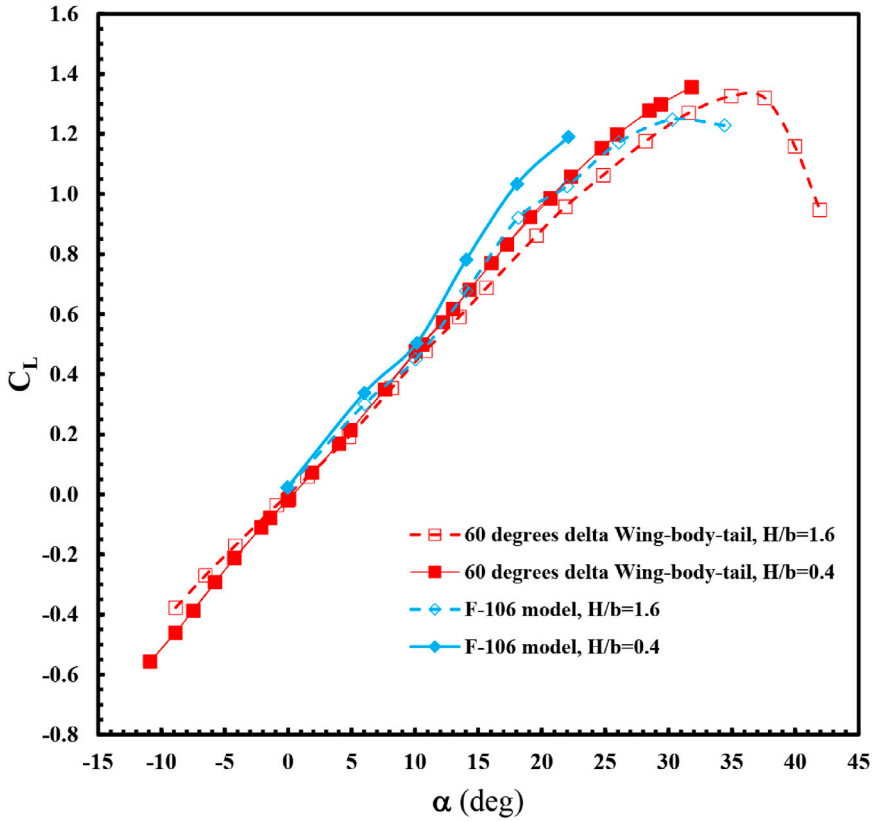

FIGURE 10
Variation of lift coefficient with angle of attack for the delta wing-body-tail, F-106 model in ground effect (H/b = 0.4) and out of ground effect (H/b = 1.6).

wind tunnel test section, while the ground plane was adjusted vertically. Figure 2 depicts the installation of the delta wing model on the ground simulation stand. The six components of the strain-gauge balance, which were installed on the stand, were capable of measuring all aerodynamic forces and moments.

Two separate potentiometers on this stand are used to measure the angle of attack and sideslip angle. The maximum error in measuring the angles of attack and sideslip angle is 0.1°. This stand incorporates a fixed plate under the central area of the test section in order to simulate the ground plane. The model was placed on the stand and tested at various ground elevations in this investigation. The measured data is compared with two basic models that were previously used for the experimental study. The 60° delta wing model was tested by Chang (Chang and Muirhead, 1987), Wentz (Wentz, 1968), and Pal Hung Lee et al. (Lee et al., 1987b), while the 1/48 scale model of the F-106 was also used.

3 Results

Delta wing-body-tail longitudinal aerodynamic coefficients are shown in Figure 3. These results are presented for conditions where the ground plane is absent. The tests were conducted in six runs, with three runs in the normal position and three runs in the inverse position of the model. The measured data demonstrate good repeatability. Model tests in normal and inverse position have been used to determine the flatness of the flow. Based on the calibration of equipment, the measurement error of the lift, drag, and side forces are 0.13%, 0.3% and 0.4% respectively and for the pitching moment and yawing moments are 0.4%, and for the rolling moment is 0.7%. To ensure the acceptable reliability of the used data, the uncertainty of the obtained data has been calculated based on the variance analysis method. Both systematic error and precision are considered in these calculations. Sensor errors, changes in flow density and velocity, changes in static pressure, data acquisition system errors, pressure sensor errors, etc. Have been investigated. The uncertainty value of the longitudinal static aerodynamic coefficient has been calculated using the results of 6 individual tests. The uncertainty of lift coefficient, drag coefficient and pitching moment coefficient at a low angle of attack is 0.0051, 0.009 and 0.0025 respectively and at a high angle of attack is 0.0160, 0.0105 and 0.0019 respectively.

In Figure 3, the lift curve slope at the linear region of the angle of attack is 0.0455 per degree. The curve remains linear up to an angle of attack of 25° but becomes nonlinear at higher angles due to the forward movement of the vortex bursting location. The angle of attack at which the stall occurs is approximately 35°. The maximum lift coefficient is 1.3. The variation of the drag coefficient with the angle of attack shows the minimum drag coefficient is 0.0095. At an angle of attack greater than 35°, a stall occurs due to full vortex bursting over the delta wing. As a result, the lift force decreases, leading to a decrease in the induced drag (drag caused by lift) and ultimately reducing the

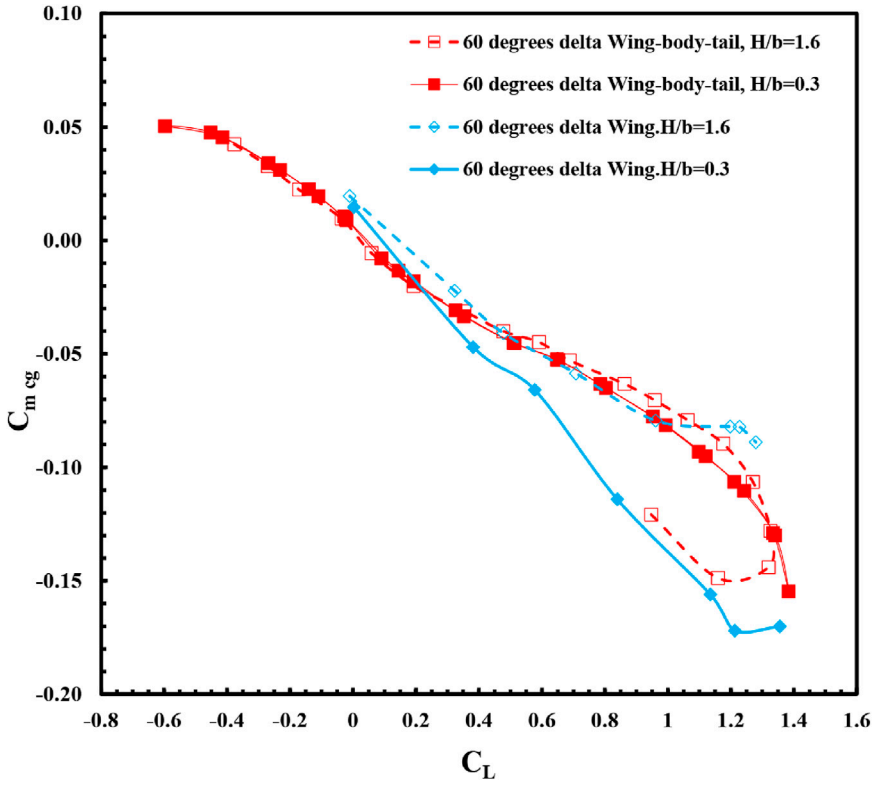

FIGURE 11
Variation of pitching moment coefficient with angle of attack for the delta wing, delta wing-body-tail model in ground effect (H/b = 0.3) and out of ground effect (H/b = 1.6).

total drag. The pitching moment coefficient is measured from 0.25 MAC. The pitching moment coefficient curve remains linear up to the stall angle of attack, with a slope of −0.0135 per degree. The curve slope with respect to the lift coefficient is −0.3, indicating that the aerodynamic center of the entire configuration is located at 0.55 MAC. Figures 4, 5, 6 display the variation of the lateral and directional aerodynamic coefficients (side force, yawing, and rolling moment) with the angle of attack, specifically at zero sideslips. Figure 4 displays the curve of the side force coefficient relative to the angle of attack at zero-degree sideslip. The side force coefficient is negligible at low angles of attack, up to approximately 20°, due to the absence of sideslip. As the angle of attack grows, the value of the side force coefficient increases, owing to the unstable vortex flow at high angles of attack. The positions of vortex bursting on the right and left wings are not consistent at a certain angle of attack, resulting in different lift forces on each side due to variations in vortex strength. The positions of vortex bursting on the right and left wings are not consistent at a certain angle of attack, resulting in different lift forces on each side due to variations in vortex strength. Consequently, the rolling moment coefficient becomes unstable at high angles of attack. Figure 5 displays the rolling moment coefficient graph with respect to the angle of attack at a sideslip angle of zero degrees. The same phenomenon is observed in the yawing moment coefficient, as demonstrated in Figure 6. This can be attributed to the instability of vortex bursting at high angles of attack. Beyond an angle of attack of 30°, the flow fields on the wing-body-tail combination become asymmetric.

Figures 7, 8 present static ground effect data. These figures compare the variations of lift and drag coefficient with ground heights for the 60° delta wing-body-tail (Figure 2) with the 60° delta wing and the F-106 model (Lee et al., 1987b) at an angle of attack of 14° (Figure 7A; Figure 8A). In Figures 7, 8 the data related to H/b larger than 1.6 are related to out-of-ground. As shown in these figures for lift coefficient for wing-body-tail configuration the lift coefficient decreases relative to wing alone configuration due to body (fuselage) presence because at wing-body-tail configuration the real wing area is less than the wing reference area because of the presence of the body. But for the F106 model, the fuselage is a lifting body so the lift coefficient is near to the wing-alone configuration ones. In other words, the lift of the fuselage compensated for the lift decreasing due to decreasing the real wing area. In Figure 7B, Figure 8B, the data are plotted as a percentage increase in lift and drag coefficient. The findings consistently demonstrate that lowering the ground height results in higher lift coefficients, lower drag coefficients, and improved longitudinal stability (as evidenced by the more negative slope of the pitching moment curve in relation to the lift coefficient). When the aircraft is not in contact with the ground, as the angle of attack increases, the delta wing leading-edge vortices tend to move towards the middle section of the wing. This reduces wing loading near the wing tips, resulting in a less negative pitching moment. However, when the ground plane is present, the power of the leading-edge vortices increases and they move towards

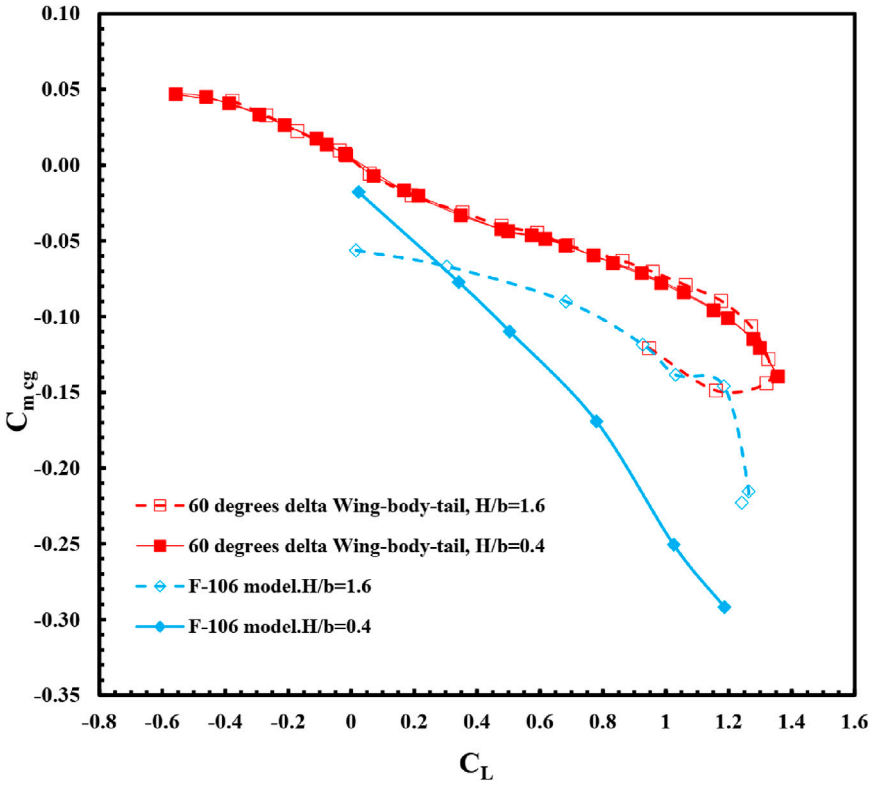

FIGURE 12
Variation of pitching moment coefficient with lift coefficient for the delta wing-body-tail, F-106 model in ground effect (H/b = 0.4) and out of ground effect (H/b = 1.6).

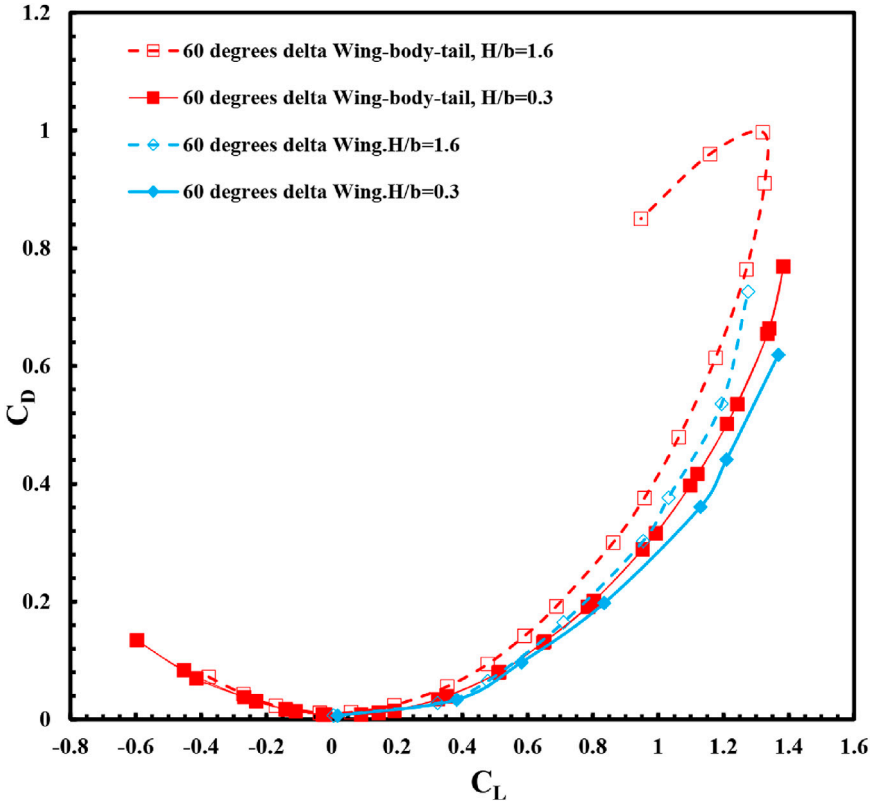

FIGURE 13
Variation of drag coefficient with angle of attack for the delta wing, delta wing-body-tail model in ground effect (H/b = 0.3) and out of ground effect (H/b = 1.6).

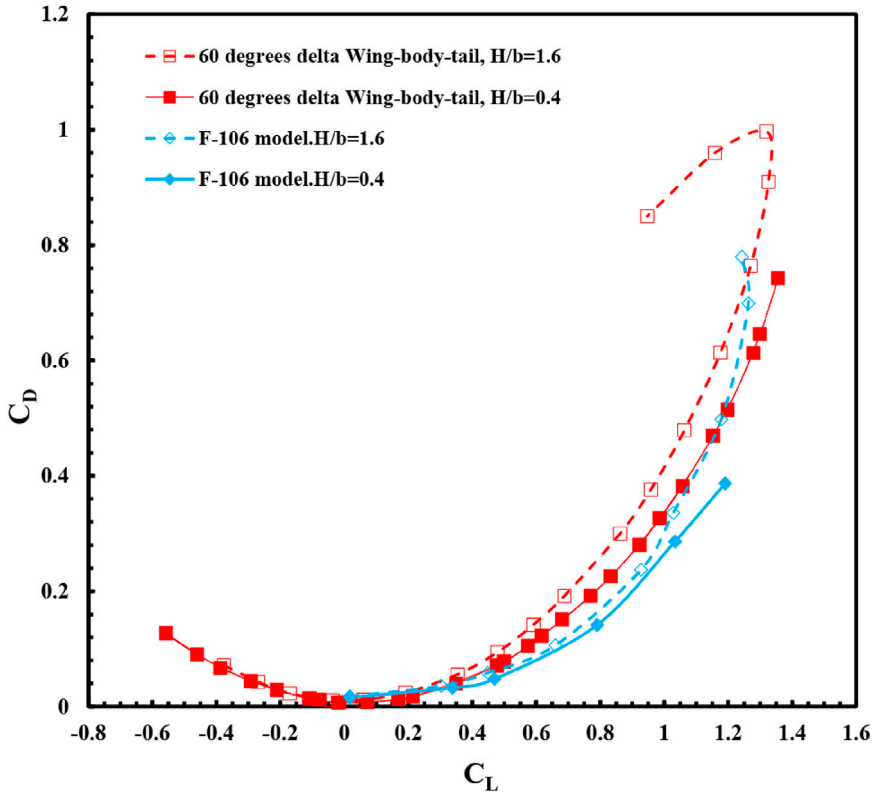

FIGURE 14
Variation of drag coefficient with lift coefficient for the delta wing-body-tail, F-106 model in ground effect (H/b = 0.4) and out of ground effect (H/b = 1.6).

the external part of the wing. Consequently, the pitching moment becomes more negative in the ground effect.

Figures 9, 10 depict the changes in lift coefficient concerning the angle of attack for the delta wing-body-tail combination under ground effect in comparison to out-of-ground effect conditions. The graph includes data from the 60° delta wing model and the F-106 model (Lee et al., 1987b). At low angles of attack, a linear relationship exists between the coefficients of lift and pitching moment and the angle of attack (Figures 11, 12). However, at higher angles of attack, the lift coefficient and moment curves become nonlinear due to the influence of leading-edge vortices. In the case of a delta wing-body-tail combination, as the height from the ground decreases at each angle of attack, the lift coefficient value and the slope of the lift curve increase. The presence of the ground increases the maximum lift coefficient from 1.3 to 1.38. Overall, the results indicate that reducing the ground height leads to increased lift coefficients and lift curve slope (Figures 9, 10), decreased drag coefficients (Figures 13, 14), and increased longitudinal stability (Figures 11, 12).

4 Conclusion

Gaining a comprehensive understanding of the aerodynamic characteristics of a delta wing aircraft in ground effect is vital for optimizing its performance and ensuring safe flight conditions. The purpose of this investigation was to examine the influence of ground effects on the aerodynamic coefficients of a model delta wing aircraft. Through conducting experiments, valuable insights were gained into the aerodynamic behavior of an aircraft model equipped with a 60° delta wing-body-vertical tail, under various ground effect conditions. The results of the experimental tests, which were carried out in a subsonic wind tunnel, unveiled a number of important findings. One key finding was that increasing the proximity to the ground led to improved longitudinal static stability. When the model's height from the ground plane was less than half of the wing span, the lift curve slope increased by 16.9%. Additionally, the study demonstrated that ground effect resulted in elevated lift coefficients at all angles of attack. Specifically, at an angle of attack of 14°, the lift increased by approximately 25% due to ground effects. When the delta wing model was in close proximity to the ground, there was a 6% increase in the maximum lift coefficient. These variations were particularly significant when the distance from the ground plane was less than half of the wing span.

Moreover, the research emphasized the importance of considering the design of the vertical tail in delta wing aircraft operating under ground effect conditions. The vertical tail plays a crucial role in maintaining stability and control, especially in the presence of altered flow patterns caused by ground effects. This study shed light on the optimal design parameters for the vertical tail, thereby contributing to the overall performance and safety of the aircraft. It further emphasized the significance of incorporating ground effects into the design and optimization of delta wing aircraft, as it has the potential to significantly enhance lift generation capabilities. The presence of a ground plane has the added benefit of strengthening the flow of leading-edge vortex towards the outboard section of the

wing. This, in turn, results in a more negative pitching moment, causing a steeper decline in the pitching moment curve. As a result, there is an increase in static longitudinal stability and a shift backward in the aerodynamic center. Additionally, reducing the distance between the ground plane and the wing leads to a decrease in the total drag coefficient for all angles of attack. This decrease is primarily due to a reduction in the induced drag coefficient. Consequently, there is a significant improvement in the aerodynamic efficiency parameter (L/D) when the distance from the ground plane is decreased. These findings have important implications for the control and stability of delta wing aircraft, especially at high angles of attack. However, it is crucial to note that the study identified a stability issue with the rolling moment and yawing moment coefficients becoming unstable at angles of attack above 30°. This highlights the necessity for further research and analysis to address this instability and ensure the safe operation of delta wing aircraft in high-angle-of-attack scenarios. Further research in this field is encouraged to explore additional variables and circumstances that may affect the aerodynamic coefficients under ground effects. This will enhance the comprehensive understanding of delta wing aircraft behavior and aid in the development of improved design strategies for heightened performance and safety in low-altitude flight operations.

Data availability statement

The original contributions presented in the study are included in the article/Supplementary material, further inquiries can be directed to the corresponding author.

Author contributions

AS: Writing–original draft, Writing–review and editing. AG: Writing–original draft, Writing–review and editing.

Funding

The author(s) declare that no financial support was received for the research, authorship, and/or publication of this article.

Conflict of interest

The authors declare that the research was conducted in the absence of any commercial or financial relationships that could be construed as a potential conflict of interest.

Publisher's note

All claims expressed in this article are solely those of the authors and do not necessarily represent those of their affiliated organizations, or those of the publisher, the editors and the reviewers. Any product that may be evaluated in this article, or claim that may be made by its manufacturer, is not guaranteed or endorsed by the publisher.

References

Abdolahipour, S. (2023). Effects of low and high frequency actuation on aerodynamic performance of a supercritical airfoil. *Front. Mech. Eng.* 9. doi:10.3389/fmech.2023.1290074

Abdolahipour, S., Mani, M., and Shams Taleghani, A. (2022a). Pressure improvement on a supercritical high-lift wing using simple and modulated pulse jet vortex generator. *Flow, Turbul. Combust.* 109 (1), 65–100. doi:10.1007/s10494-022-00327-9

Abdolahipour, S., Mani, M., and Shams Taleghani, A. (2022b). Experimental investigation of flow control on a high-lift wing using modulated pulse jet vortex generator. *J. Aerosp. Eng.* 35 (5), 05022001. doi:10.1061/(asce)as.1943-5525.0001463

Abdolahipour, S., Mani, M., and Taleghani, A. S. (2021). Parametric study of a frequency-modulated pulse jet by measurements of flow characteristics. *Phys. Scr.* 96 (12), 125012. doi:10.1088/1402-4896/ac2bdf

Adam, R., and Bartoszewicz, J. (2017). Numerical analysis of the influence of the wing in ground effect on aircraft lift coefficient and car downforce coefficient. *J. Mech. Transp. Eng.* 69 (2), 47–55. doi:10.21008/j.2449-920X.2017.69.2.06

Ahmed, M. R., and Sharma, S. D. (2005). An investigation on the aerodynamics of a symmetrical airfoil in ground effect. *Exp. Therm. Fluid Sci.* 29, 633–647. doi:10.1016/j.expthermflusci.2004.09.001

Ahmed, M. R., Takasaki, T., and Kohama, Y. (2007). Aerodynamics of a NACA 4412 airfoil in ground effect. *AIAA J.* 45 (1), 37–47. doi:10.2514/1.23872

Albers, M., Meysonnat, P. S., and Schröder, W. (2019). Actively reduced airfoil drag by transversal surface waves. *Flow, Turbul. Combust.* 102, 865–886. doi:10.1007/s10494-018-9998-z

Atzori, M., Vinuesa, R., Fahland, G., Stroh, A., Gatti, D., Frohnapfel, B., et al. (2020). Aerodynamic effects of uniform blowing and suction on a NACA4412 airfoil. *Flow, Turbul. Combust.* 105, 735–759. doi:10.1007/s10494-020-00135-z

Baker, P. A., Schweikhard, W. G., and Young, W. R. (1970). *Flight evaluation of ground effect on several low aspect ratio airplanes*. NASA TN D 6053.

Chang, R. C., and Muirhead, V. U. (1985). "Investigation of dynamic ground effect," in Proceedings of the 1985 NASA Ames Research Center's Ground-Effects Workshop, NASA CP-2462, Aug. 20, 1985, 363–393.

Chang, R. C., and Muirhead, V. U. (1987). Effect of sink rate on ground effect of low-aspect-ratio wings. *J. Aircr.* 24, 176–180. doi:10.2514/3.45413

Chawla, M., Edwards, L., and Franke, M. (1990). Wind-tunnel investigation of wing-in-ground effects. *J. Aircr.* 27 (4), 289–293. doi:10.2514/3.25270

Corsiglia, V. R., Koenig, D. G., and Morelli, J. P. (1969). *Large scale test of an airplane model with a double delta wing including longitudinal and lateral aerodynamic characteristics and ground effects*. NASA TN D 5102.

Deng, N. (2017). *Numerical study of the aerodynamics of DLR-F6 wing-body in unbounded flow field and in ground effect*. Master of Engineering thesis. Louis: Washington University.

Deng, N., Qu, Q., and Agarwal, R. K. (2017). "Numerical study of the aerodynamics of DLR-F6 wing-body in the unbounded flow field and in ground effect," in 55th AIAA Aerospace Sciences Meeting, Grapevine, Texas, 9 - 13 January 2017.

Djavareshkian, M. H., Esmaeli, A., and Parsani, A. (2011). Aerodynamics of smart flap under ground effect. *J. Aerosp. Sci. Technol.* 15 (8), 642–652. doi:10.1016/j.ast.2011.01.005

Fahland, G., Atzori, M., Frede, A., Stroh, A., Frohnapfel, B., and Gatti, D. (2023). Drag assessment for boundary layer control schemes with mass injection. *Flow, Turbul. Combust.* 2023. doi:10.1007/s10494-023-00462-x

Gratzer, L. B., and Mahal, A. S. (1971). Ground effects in STOL operation. *J. Aircr.* 19 (3), 236–242. doi:10.2514/3.58963

Harvey, J., and Perry, F. J. (1971). Flow field produced by trailing vortices in the vicinity of the ground. *AIAA J.* 9 (8), 1659–1660. doi:10.2514/3.6415

He, W., Peng, Y., Larry, K., and Li, B. (2018). Ground effects on the stability of separated flow around a NACA 4415 airfoil at low Reynolds numbers. *J. Aerosp. Sci. Technol.* 72, 63–76. doi:10.1016/j.ast.2017.10.039

Katz, J., and Levin, D. (1984). Measurements of ground effect for delta wings. *J. Aircr.* 21 (6), 441–443. doi:10.2514/3.44988

Kemmerly, G. T., Paulson, J. W., Jr., and Compton, M. (1988). Exploratory evaluation of moving-model technique for measurement of dynamic ground effects. *J. Aircr.* 25 (6), 557–562. doi:10.2514/3.45622

Kemp, W. B., Lockwood, V. E., and Phillips, W. P. (1966). *Ground effects related to landing of airplanes with low aspect ratio wings*. NASA TN D 3583.

Kornilov, V. (2021). Combined blowing/suction flow control on low-speed airfoils. *Flow, Turbul. Combust.* 106, 81–108. doi:10.1007/s10494-020-00157-7

Lee, P. H., Edward Lan, C., and Muirhead, V. U. (1987b). *An experimental investigation of dynamic ground effect*. NASA CR-4105.

Lee, P. H., Lan, C. E., and Muirhead, V. U. (1987a). *An experimental investigation of dynamic ground effect*. NASA CR-4105.

Lee, P. H., Lan, C. E., and Muirhead, V. U. (1989). Experimental investigation of dynamic ground effect. *J. Aircr.* 26 (6), 497–498. doi:10.2514/3.45793

Lee, T. W. (2002). *Experimental study of ground effect on finite-wing wake flow development*. M.S. Thesis, Aeronautics and Astronautics Dept. Tainan City, Taiwan: National Cheng Kung University. (in Chinese).

Lockwood, V. E., and Phillips, W. P. (1968). *Measurements of ground effect on a low aspect ratio ogee wing airplane model and calculations of landing flare trajectories*. NASA TN D 4329.

McDonnell Douglas Corporation, USAF Stability and Control DATCOM (1960). *U.S. Air force flight dynamics laboratory*. Ohio: Wright-Patterson AFB. Revised Apr. 1976.

Mirzaei, M., Taleghani, A. S., and Shadaram, A. (2012). Experimental study of vortex shedding control using plasma actuator. *Appl. Mech. Mater.* 186, 75–86. doi:10.4028/www.scientific.net/amm.186.75

Mohammadi, M., and Taleghani, A. S. (2014). Active flow control by dielectric barrier discharge to increase stall angle of a NACA0012 airfoil. *Arabian J. Sci. Eng.* 39, 2363–2370. doi:10.1007/s13369-013-0772-1

Nirooei, M. H. (2018). Aerodynamic and static stability characteristics of airfoils in extreme ground effect. *J. Aerosp. Eng.* 232 (6), 1134–1148. doi:10.1177/0954410017708212

Paulson, J. W., Jr., Kemmerly, G. T., and Gilbert, W. P. (1990). *Dynamic ground effects, aerodynamics of combat aircraft controls and ground effects*, 1–12. AGARD CP-465.

Qin, Y., Liu, P., Qu, Q., and Guo, H. (2016). Numerical study of aerodynamic forces and flow physics of a delta wing in dynamic ground effect. *J. Aerosp. Sci. Technol.* 51, 203–221. doi:10.1016/j.ast.2016.02.007

Qin, Y., Liu, P., Qu, Q., and Hu, T. X. (2017). Wing/canard interference of a close-coupled canard configuration in static ground effect. *J. Aerosp. Sci. Technol.* 69, 60–75. doi:10.1016/j.ast.2017.06.012

Qin, Y., Qu, Q., Liu, P., Tian, Y., and Lu, Z. (2015). DDES study of the aerodynamic forces and flow physics of a delta wing in static ground effect. *J. Aerosp. Sci. Technol.* 43, 423–436. doi:10.1016/j.ast.2015.04.004

Qu, Q., Jia, X., Wang, W., Liu, P., and Agarwal, R. K. (2014). Numerical study of the aerodynamics of a NACA 4412 airfoil in dynamic ground effect. *J. Aerosp. Sci. Technol.* 38 (6), 56–63. doi:10.1016/j.ast.2014.07.016

Rodriguez, I., Lehmkuhl, O., and Borrell, R. (2020). Effects of the actuation on the boundary layer of an airfoil at Reynolds number *Re*= 60000. *Flow, Turbul. Combust.* 105, 607–626. doi:10.1007/s10494-020-00160-y

Rolls, L. S., and Koenig, D. G. (1966). *Flight measured ground effect on a low aspect ratio ogee wing including a comparison with wind tunnel results*. NASA TN D 3431.

Salmasi, A., Shadaram, A., and Taleghani, A. S. (2013). Effect of plasma actuator placement on the airfoil efficiency at poststall angles of attack. *IEEE Trans. Plasma Sci.* 41 (10), 3079–3085. doi:10.1109/tps.2013.2280612

Sereez, M., Abramov, N. B., and Goman, M. G. (2017). "Computational ground effect aerodynamics and airplane stability analysis during take-off and landing," in 7th European Conference For Aeronautics And Aerospace Sciences (EUCASS), Milan, Italy Duration, 3 Jul 2017, 6 Jul 2017. doi:10.13009/EUCASS2017-376

Sereez, M., Abramov, N. B., and Goman, M. G. (2018). Impact of ground effect on airplane lateral directional stability during take-off and landing. *Open J. Fluid Dyn.* 08, 1–14. doi:10.4236/ojfd.2018.81001

Snyder, C. T., Drinkwater, F. J., III, and Jones, A. D. (1970). *A piloted simulator investigation of ground effect on the landing maneuver of a large tailless delta wing airplane*. NASATND6046.

Taleghani, A. S., Ghajar, A., and Masdari, Me. (2020). Experimental study of ground effect on horizontal tail effectiveness of a conceptual advanced jet trainer. *J. Aerosp. Eng.* 33. doi:10.1061/(ASCE)AS.1943-5525.0001140

Taleghani, A. S., Shadaram, A., and Mirzaei, M. (2012). Effects of duty cycles of the plasma actuators on improvement of pressure distribution above a NLF0414 airfoil. *IEEE Trans. Plasma Sci.* 40 (5), 1434–1440. doi:10.1109/tps.2012.2187683

Tavakoli Dakhrabadi, M., and Seif, M. S. (2016). Influence of main and outer wings on aerodynamic characteristics of compound wing-in-ground effect. *J. Aerosp. Sci. Technol.* 55, 177–188. doi:10.1016/j.ast.2016.06.002

Wang, Q. X. (2005). Analyses of a slender body moving near a curved ground. *Phys. Fluids* 17 (9), 097102. doi:10.1063/1.2034867

Wentz, W. H. (1968). *"Wind-Tunnel investigations of vortex breakdown on slender sharp-edge wing"*. Ph.D. dissertation. Kansas: University of Kansas.

Zerihan, J., and Zhang, X. (2000). Aerodynamics of a single element wing in ground effect. *J. Aircr.* 37 (6), 1058–1064. doi:10.2514/2.2711

Nomenclature

b	Wing span (m)
C_L	Lift coefficient
C_D	Drag coefficient
C_s	Side force coefficient;
C_m	Pitching moment coefficient
C_l	Rolling moment coefficient
C_n	Yawing moment coefficient
H	Height from Ground plane (m)
N	Fan revolution per minute (rpm)
Tu	Turbulence intensity (%)
U_o	Test section flow velocity (m/s)
α	Angle of attack (degree)
Re	Reynolds Number
WIG	Wing in Ground
MAC	Mean Aerodynamic Chord

frontiers | Frontiers in Mechanical Engineering

TYPE Original Research
PUBLISHED 15 March 2024
DOI 10.3389/fmech.2024.1371479

OPEN ACCESS

EDITED BY
Farschad Torabi,
K.N.Toosi University of Technology, Iran

REVIEWED BY
Ebrahim Afshari,
University of Isfahan, Iran
Arsalan Ghajar,
Aerospace Research Center, Iran

*CORRESPONDENCE
M. Taeibi Rahni,
taeibi@sharif.edu

RECEIVED 16 January 2024
ACCEPTED 21 February 2024
PUBLISHED 15 March 2024

CITATION
Shahrokhi SS, Taeibi Rahni M and Akbari P (2024), Aerodynamic design of a double slotted morphed flap airfoil– a numerical study. *Front. Mech. Eng* 10:1371479. doi: 10.3389/fmech.2024.1371479

Aerodynamic design of a double slotted morphed flap airfoil– a numerical study

S. S. Shahrokhi[1], M. Taeibi Rahni[1]* and P. Akbari[2]

[1]Department of Aerospace Engineering, Sharif University of Technology, Tehran, Iran, [2]Department of Electromechanical Engineering Technology, California State Polytechnic University-Pomona, Pomona, CA, United States

Introduction: The objective of this study is to develop and simulate a double slotted morphed flap with the intention of reducing drag and enhancing lift, thereby leading to a smaller flap size and reduced weight.

Methods: A flap was meticulously designed to accommodate conditions at Mach 0.2 and Reynolds numbers of 4.7×10^6. To conduct the simulation, ANSYS FLUENT flow solver and POINTWISE grid generator were utilized. The morphing technique employed involved adjusting both flap mean camber and flap slots, ensuring minimal flow interferences. By discretizing the flap mean camber line, various flap geometries were achieved.

Results and Discussions: The findings reveal a significant enhancement in the airfoil's aerodynamic efficiency attributed to the implementation of the new flap design. The study shows that utilizing double-slotted morphing in the NACA 4412 airfoil at a 30° flap deflection angle increased the lift coefficient by 82% compared to the un-morphed state. A comparison of lift coefficients between this research and the NACA 4412 split flap at a 60° deflection angle indicates that the double-slotted morphing in the NACA 4412 airfoil at a smaller deflection angle of 30° results in a 14% higher maximum lift coefficient.

KEYWORDS

morphing, double slotted flap, CFD, lift, drag, high-lift device, airfoil, flow control

1 Introduction

In recent years, there has been a notable increase in the advancement of active flow control actuators in the fields of fluid mechanics and aerodynamics. Plasma actuators (Mirzaei et al., 2012; Taleghani et al., 2012; Salmasi et al., 2013; Mohammadi and Taleghani, 2014; Taleghani et al., 2018) have demonstrated their effectiveness in enhancing aerodynamic performance by increasing lift, reducing drag, and controlling vortex shedding. This is achieved by ionizing the air near the aerodynamic surfaces, generating a micro-jet in close proximity to the surface, and utilizing a fast time response capability.

Surface acoustic waves have been utilized to manipulate water droplets on solid surfaces (Sheikholeslam Noori et al., 2020a; Sheikholeslam Noori et al., 2020b; Noori et al., 2020; Sheikholeslam Noori et al., 2021). They have been proposed as a potential technique to prevent water droplet icing on aircraft wings in areas not covered by the anti-ice system (Taeibi Rahni et al., 2022). Furthermore, fluidic actuators can inject momentum into low momentum areas, providing significant benefits (Abdolahipour, 2023). Abdolhaipour et al. have introduced a novel type of pulsed jet, known as a modulated pulse jet (Abdolahipour et al., 2021; Abdolahipour et al., 2022a; Abdolahipour et al., 2022b), and experimentally

applied it as a hybrid active control method on the flap of a high-lift device with a supercritical airfoil section to improve the wing's aerodynamic performance.

In addition to the rapid progress in flow control actuators, morphing wings have emerged as a promising flow control approach due to their lightweight nature and adjustable stiffness (Xiao et al., 2022). In the realm of aviation, morphing encompasses alterations in wing span, sweep angle, twist angle, dihedral/anhedral angles, camber line, and airfoil thickness. The aim of morphing is to enhance the performance of vehicles at different flight conditions. The aircraft exhibits varying aerodynamic characteristics in different flight conditions, including the distinct aerodynamic conditions experienced during ground effect (Shams Taleghani et al., 2020). Generally, aircrafts are designed to meet specific flight requirements, but when equipped with the ability to modify their geometry during flight, they can adapt to varying conditions and achieve exceptional performances.

To simplify the design of a morphed flap, a framework for different cruise conditions has been introduced in reference (Steenhuizen and van Tooren, 2012). Additionally, in order to enhance lift, reference (Nemati and Jahangirian, 2020) proposed a robust airfoil parameterization method for designing morphed leading and trailing edges.

Researchers have examined the aerodynamic characteristics of morphed flaps, focusing on both trailing-edge and leading-edge flaps. For example, reference (Taguchi et al., 2020) investigated the aerodynamic characteristics of a passive morphed trailing edge in a 2D wing, revealing a higher lift coefficient for the morphed airfoil. In reference (Magrini and Benini, 2017), a GA-(w)-1 airfoil with a 25% morphed leading edge was studied, demonstrating a significant reduction in drag with a slight increase in lift. Furthermore, reference (Abdessemed et al., 2018) investigated the aerodynamic performance of a NACA0012 airfoil with a time-dependent morphed trailing edge, using computational fluid dynamics (CFD), showing a 6.5% increase in aerodynamic efficiency. The effects of morphed leading and trailing edge flaps were also analyzed in reference (Aziz et al., 2019), using ANSYS FLUENT, highlighting substantial improvements in aerodynamic characteristics. Moreover, reference (Rivero et al., 2021) conducted a wind tunnel test on a NACA23012 airfoil with three configurations: base airfoil, hinged flap, and FishBAC morphed flap.

In the case of 3D wings, the aerodynamic performance of a morphed trailing edge was investigated in reference (Lyu and Martins, 2015) to explore the benefits of morphing technology. The results demonstrated a 1% reduction in drag at design and 5% reduction in off-design conditions (along with a 1% reduction in cruise fuel consumption). Reference (Burdette and Martins, 2018) illustrated that adjusting the frequency of motion of a dynamic morphed surface could effectively mitigate separation zones.

Most recently, inspired from owl's wings, reference (Harbi Monfared et al., 2022) thoroughly investigated a morphed wing from both aerodynamic and aeroacoustics points of view. Furthermore, some efforts have been done to find the best airfoil geometry for various flight conditions. In this field, an aerodynamic shape optimization using CFD was performed in reference (Secanell et al., 2006), wherein they found the best initial airfoil configuration. Their results show that the optimum airfoil configuration has a significant improvement in the performance of a UAV's. In addition, reference (Fincham and Friswell, 2015) studied optimization of an airfoil camber line in two different configurations.

In addition, morphing technology has shown the ability of delaying flow separation. In this way, reference (Chandrasekhara et al., 1998) investigated a morphed airfoil, in which the radius of its leading edge was adjustable. On the other hand, reference (Jones et al., 2018) illustrated that by adjusting the frequency of motion of a dynamically morphed surface, it is possible to eliminate the separation zone.

Morphing technology has not only improved aircraft performance, but also showcased potential for implementation in wind turbines. According to reference (Ai et al., 2019), morphed flaps provide excellent control over aerodynamic lift in turbine blades. Similarly, reference (Daynes and Weaver, 2012) focused on controlling the aerodynamic load of wind turbine blades, using morphed trailing edge flaps. They designed a morphed flap structure and conducted aeroelastic investigations, which revealed that their morphed flap, with approximately 30% less deflection compared to a conventional flap, could generate the same lift.

Furthermore, various intriguing studies have explored the vibration effects of morphed trailing edges on airfoils. Reference (Simiriotis et al., 2018) demonstrated through numerical and experimental analysis that vibration frequency has the potential to enhance aerodynamic performance and reduce noise. In a similar work focused on a transonic regime, reference (Tô et al., 2019) investigated the effects of upward motion and vibration of a trailing edge, resulting in reduced buffet and a significant increase in lift-to-drag ratio.

In this study, we aim to design a trailing edge flap with morphable camber. Additionally, we need to design two slots that minimize flow interferences. One major challenge with conventional flaps is the generation of considerable noise and drag when deployed due to vortices produced in the cove sections of their slots. Reference (Jawahar et al., 2019) experimentally demonstrated the noise reduction effect of filling the slat cove for a 30P30N airfoil. This problem also arises during retraction due to the discontinuity of wing control surfaces. Moreover, in deflected positions, conventional flaps exhibit sharp changes in geometry, resulting in poor flow quality in those regions.

In order to achieve practical morphed flaps, we have designed a mechanism capable of simultaneously changing flap camber and generating two slots. Subsequently, aerodynamic shapes were designed based on this mechanism. It is important to note that this article solely focuses on investigating the aerodynamic specifications of a morphed flap and thus the structural aspects related to this mechanism are not addressed here.

2 Solution methodology

According to reference (Abbott and Von Doenhoff, 1956), the well-documented NACA4412 airfoil was selected to be investigated in this study.

2.1 Airfoil and its flap geometry

In this study, the auxiliary spar is positioned at 63% of the airfoil chord from the leading edge, as illustrated in Supplementary Figure S1 To generate the morphed section (Supplementary Figure S2), the

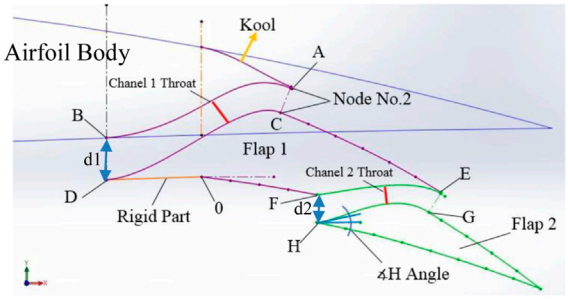

FIGURE 1
Morphed flap parts, including its channels.

flap chord is divided into 12 vertical lines (ribs). Here, the intersections of the ribs with the camber line are referred to as discretized camber line points (DCLP). The camber line is then approximated by straight lines connecting the DCLPs, with each straight line, forming an angle with its adjacent line. Considering the flap's upper and lower surfaces and ribs as a four-bar mechanism, altering the angle of the discretized camber lines results in different flap geometries. Supplementary Figure S3 demonstrates the variation of camber lines obtained using this mechanism, while Supplementary Figure S4 represents the corresponding flap geometries.

2.2 Flap nomenclature

The flap nomenclature in this study is based on the position of maximum camber (x/c') and its maximum value (t/c') relative to the flap chord (Supplementary Figure S5). As depicted in Supplementary Figure S6, our flap is named TnCy, where Tn represents t/c' = n × 100, and Cy denotes the curve number proportional to x/c' with values ranging from 1 to 5. Supplementary Table S1 provides the curve numbers and their corresponding x/c' values.

2.3 Channels

To create channels, the flap's upper surface is cut at nodes 2 and 8, while the lower surface is cut at nodes w and 4 (Supplementary Figure S2). This division results in three parts: the main airfoil body and flap parts 1 and 2. The downward vertical movement of parts 1 and 2 generates inlets and outlets of the slots (Figure 1). The slots function as channels to transfer and accelerate air from the lower surface of the flap to the upper, thereby preventing separation. The adaptability of the inlet is presumed to play an important role in facilitating smooth airflow transfer, while it is expected that the outlet area remains parallel to the flap's upper surface (to ensure airflow attachment). Consequently, the angles of the channel walls are adjustable. As depicted in Figure 1, designing the walls of the channels involves obtaining the optimum curves between the nodes (AB and CD in channel No. 1; EF and GH in channel No. 2). This aspect is of considerable importance. The airfoil comprises three parts: the airfoil body, flap parts 1 and 2, and the nearest channel to the main airfoil in channel No. 1. Note, here the area covering the slot which opens during deflection is called Kool (shoulder).

Supplementary Figure S7 illustrates three different flaps with the same maximum camber, but with different maximum camber positions. Note, when going from left to right in this figure, the maximum camber position moves towards the trailing edge.

The parameters of the morphed flap are as follows:

1. Size of the maximum camber (t/c'),
2. Position of the maximum camber (x/c'),
3. Inlet geometry of channels with A, D, F, and H angles,
4. Outlet geometry of channels,
5. Profile of channels, and
6. Position of channels' throat.

3 CFD setup

In this study, incompressible flow at Mach 0.2 and at Reynolds number of 4.7×10^6 was assumed. The solution was obtained using ANSYS FLUENT software. The pseudo-compressibility method with Roe's second-order flux splitting method was employed. Additionally, the transition SST turbulence model was used to accurately predict the transition location and thus to improve the accuracy of the drag coefficient. In addition, no-slip walls and pressure far-field boundary conditions were applied.

3.1 Computational grid

Grid generation was performed using POINTWISE software. An O-type domain with a radius of 25c was utilized. The airfoil cell size at the leading edge was set to be 0.0001c to capture high-gradient zones accurately. The cell size at the flaps' leading and trailing edges was set to be 1.047e-6c. The height of the first cell was chosen to achieve a y + value of 0.8. The quality of the grid was assessed based on mesh orthogonality, skewness, aspect ratio, etc. The number of cells in the boundary layer, wake zone, and far field was optimized to maintain a consistent lift coefficient (optimal number of cells was 210,000). Figures 2, 3 show the details of the grid and its resolution study.

3.2 Code validation

For code validation, numerical simulations were performed for the NLR7301 airfoil, which has been previously studied experimentally in reference (Vandenberg and Oskam, 1980). Figure 4A shows a comparison of the pressure coefficient (Cp) between the numerical solution of this work and the experimental data. The present lift and drag coefficients differ from the corresponding experimental data by less than about 5 percent. Figure 4B displays the velocity field around the NLR7301 airfoil. The velocity contour depicted in this figure exhibits identical characteristics to the numerical simulation conducted in reference (Narsipur et al., 2012).

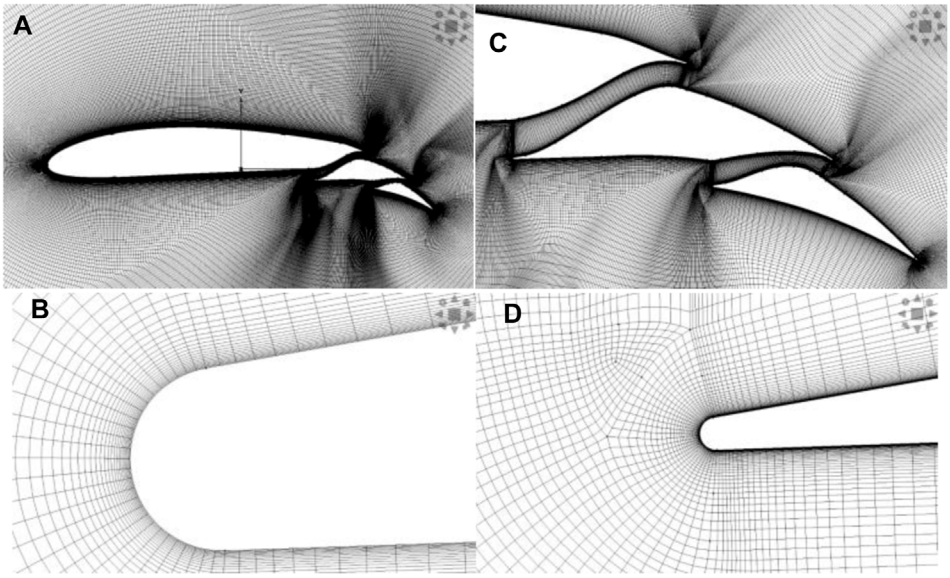

FIGURE 2
Grid details around: **(A)** the whole airfoil **(B)** the leading edge of flap number 1 **(C)** the morphed flap **(D)** the leading edge of flap number 2.

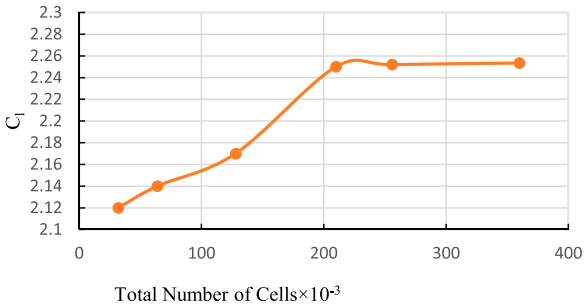

FIGURE 3
Grid resolution study.

4 Aerodynamic design

In this section, channel parameters are defined and then, while maintaining the optimal channel geometry, various flap cambers at three different angles of attack and two distinct flap deflection angles are investigated.

4.1 Channels' aerodynamic performance

Figure 5 compares the velocity contour of the morphed flap in two different configurations (with and without channels) at a 5° angle of attack. In the configuration without channels, a large separation zone is observed (even at low angles of attack). By deploying channels, a jet flow is formed, and the separation region disappears, resulting in a significant increase in lift. However, drag nearly remains the same in both configurations. Note, in the configuration without channels, drag is mainly caused by high pressure resulting from separation. With channels, separation is minimized, and thus the pressure drag is considerably reduced (but the channels themselves become the main sources of drag). These two sources of drag appear to have significant interactions, resulting in a relatively consistent total drag. Table 1 presents the aerodynamic characteristics of the two configurations. The pitching moment coefficient is calculated about the quarter-chord point.

4.2 Channel shape investigation

The following tests were conducted to design the channels' shapes at three different angles of attack: 0°, 5°, and 10°, to analyze the intake of channels. Notation "∡A" represents the angle of the channel wall with respect to the horizon at point "A" (e.g., the angle of point "H" in Figure 1). The following cases were studied:

case 1. intake angle suitable for AOA = 0°:

∡B = ∡D = ∡F = ∡H = 0°, case 2. Intake angle suitable for AOA = 5°:

∡B = ∡D = ∡F = ∡H = 5°, case 3. Intake angle suitable for AOA = 10°:

∡B = ∡D = ∡F = ∡H = 10°, case 4. angle of the lower wall is 10° and the upper wall is tangent to the airfoil surface:

∡D = ∡H = 10°.

∡B = ∡F = tangent to the airfoil surface, and

case 5. angle of the lower wall is 10° and angle of the upper wall is 5°:

∡D = ∡H = 10°.

∡B = ∡F = 5°.

Figure 6 displays the aerodynamic characteristics of these cases, in which case 3 demonstrates the best performance. (Figures 7A, C) depict the velocity field of case 1, where even at zero angle of attack, a separation region is present in the leading edge of flaps 1 and 2, resulting in reduced aerodynamic performance. As the inlet angle

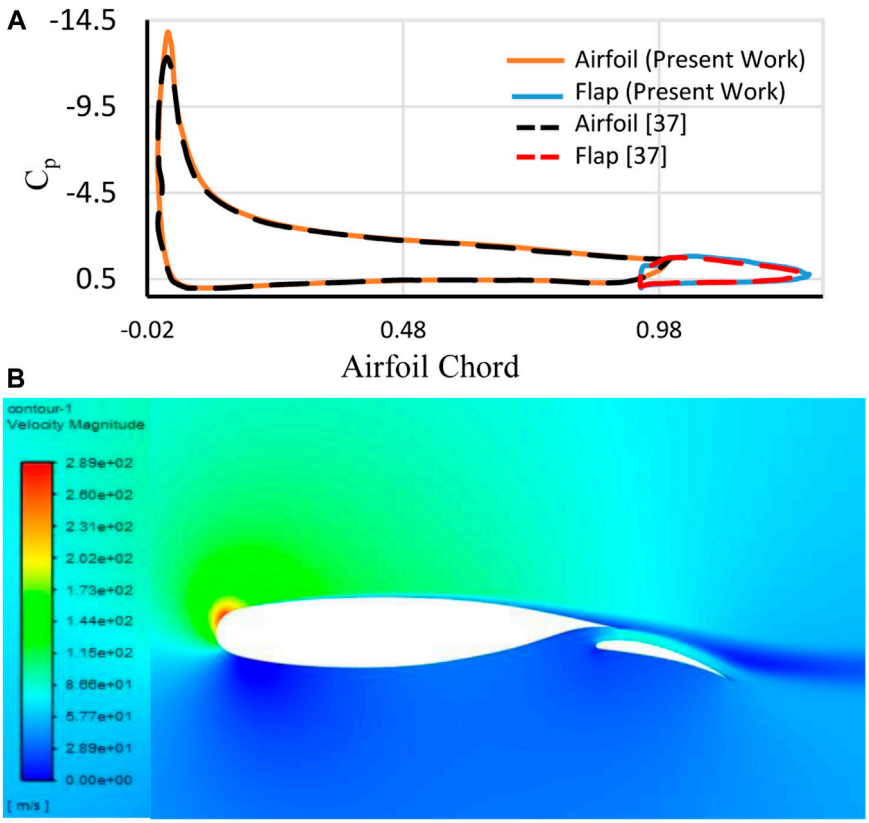

FIGURE 4
(A) Cp comparison between numerical solotion of the peresent work and the expemental data of reference (Vandenberg and Oskam, 1980) and **(B)** present velocity field around NLR7301 airfoil (at 13.1° angle of attack).

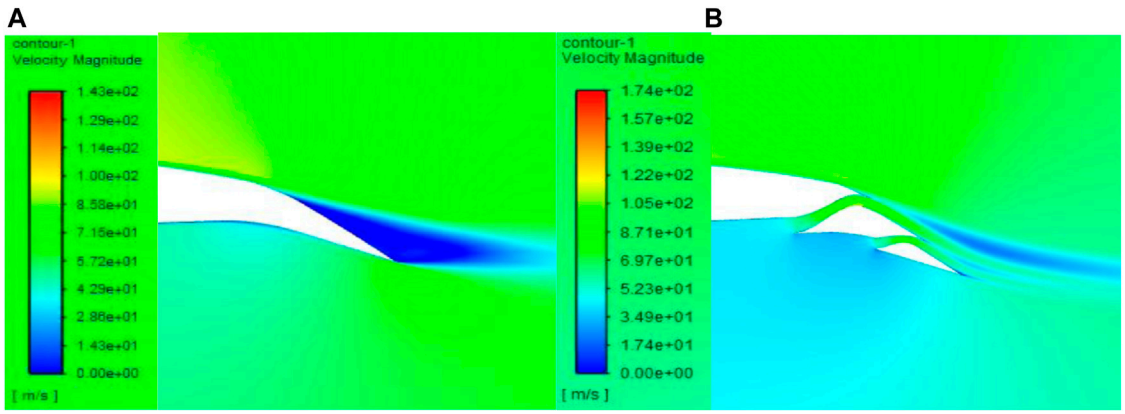

FIGURE 5
Velocity field of the morphed flap: **(A)** without channel and **(B)** with channel.

increases (cases 2 and 3), this separation region becomes smaller, leading to a reduction in drag. (Figures 7, D) present case 3 at 10° and 0° angles of attack, respectively. Increasing the inlet angle causes the channel throat to move towards the outlet, resulting in an increase in lift. Case 4 exhibits the worst performance due to the channel profile moving the throat towards the inlet. Apart from the aerodynamic advantages of the fixed inlet shape in case 3, it also reduces the related mechanism's complexity, production cost, and the overall weight of the airfoil.

The channels' profiles were studied considering the following cases:

1. Normal case, with d1 being 3 and d2 being 2 percent of the airfoil's chord,

TABLE 1 Aerodynamic characteristics of the morphed flap in two different configurations of "with" and "without" channels.

Aerodynamic characteristics	Without channel	With channel
C_l	1.664	2.21
C_d	0.028	0.027
C_m	−0.21	−0.32

2. Case 6, similar to the normal case, but with a 25 percent decrease in both d1 and d2,
3. Case 7, similar to the normal case, but with a 25 percent increase in both d1 and d2, and
4. Case 8, where the throat of the channel is moved towards the outlet.

Figure 8 demonstrates that increasing the width of the channel leads to an increase in lift and a decrease in drag until an optimum point is reached. Further increasing the channel width reverses these effects. Additionally, increasing the channel width results in an increase in the moment coefficient, which does not reverse. Moving the throat towards the outlet increases lift, drag, and pitching moment, but reduces aerodynamic efficiency. The normal case exhibits the highest aerodynamic efficiency (lift-to-drag ratio), while case 6 shows the lowest.

4.3 Morphed flap at 15 degrees deflection

(Figures 9A–C) illustrate the lift coefficient *versus* maximum camber position for three different maximum camber values and three different angles of attack (0°, 5°, and 10°). When the maximum camber position is moved towards the trailing edge, the lift coefficient initially increases and then decreases, with the best position being at 50 percent of the flap chord. Increasing the maximum camber at a fixed maximum camber position also results in an increase in Cl.

(Figures 9D–F) represent changes in drag coefficient with maximum camber position for three different maximum camber values and three different angles of attack (0°, 5°, and 10°). Moving the maximum camber position towards the trailing edge leads to an increase in Cd. At a fixed maximum camber position, increasing maximum camber causes Cd to increase (independent of the angle of attack). The maximum camber position at 16.67 percent exhibits a cove that creates a dead air area, resulting in a large Cd value. Increasing maximum camber further increases both the dead air area and Cd. The maximum camber position at 33.33 percent with a camber of 4 percent shows the minimum Cd, regardless of the angle of attack.

For x/c' = 66.67 percent, both Cl and Cd are lower than those for x/c' = 83.33 percent due to an effect called hook-like (Supplementary Figure S8). This effect occurs when the camber position moves to 83.33 percent of the flap chord, resulting in an aerodynamic behavior similar to a gurney flap of references (Papadakis et al., 1996; Papadakis et al., 1997), leading to higher Cl and Cd.

(Figures 10A–C) depict aerodynamic efficiency *versus* maximum camber position for three different maximum cambers and for three different angles of attack. The optimal lift-to-drag ratio is found to be independent of maximum camber position and angle of attack always occurring at 33.33 percent of the flap chord (curve No. 2; C2). Generally, increasing maximum camber reduces l/d and the difference in l/d for various camber values decreases at higher angles of attack.

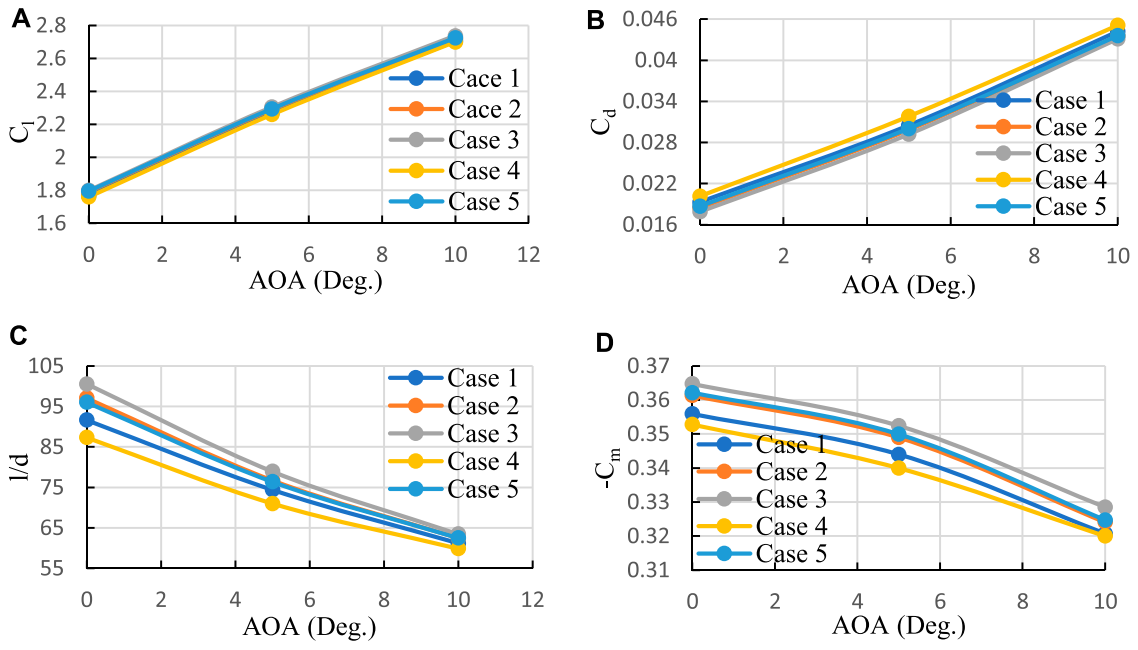

FIGURE 6
Aerodynamic characteristics of the channels' intake *versus* angle of attack. **(A)** C_l, **(B)** C_d, **(C)** l/d, and **(D)** C_m.

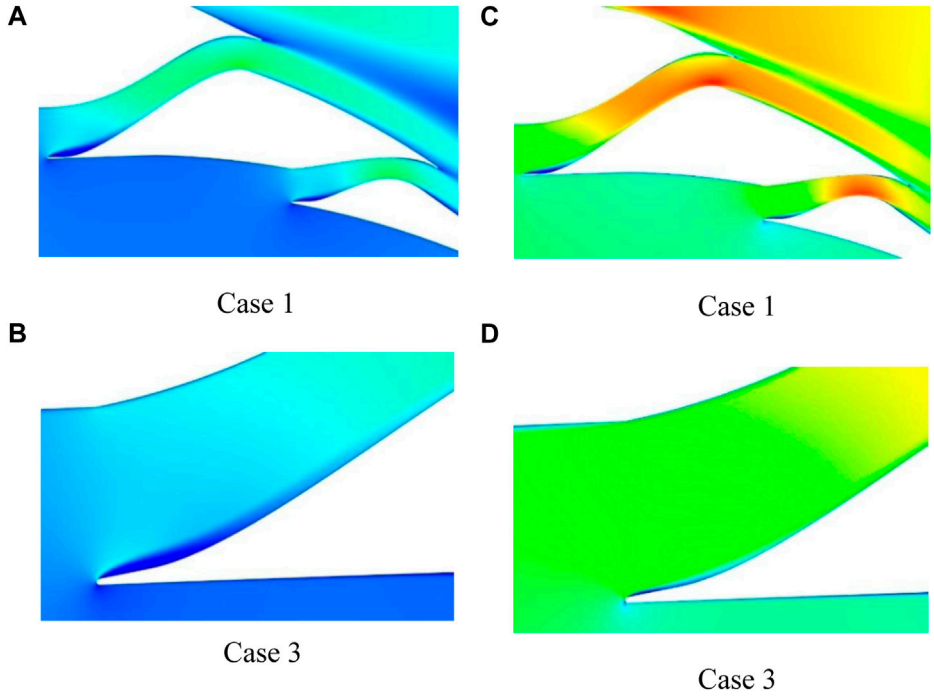

FIGURE 7
Channels' intake velocity fields at different intake angles and at: **(A)** and **(B)** AOA = 10°; **(C)** and **(D)** AOA = 0°.

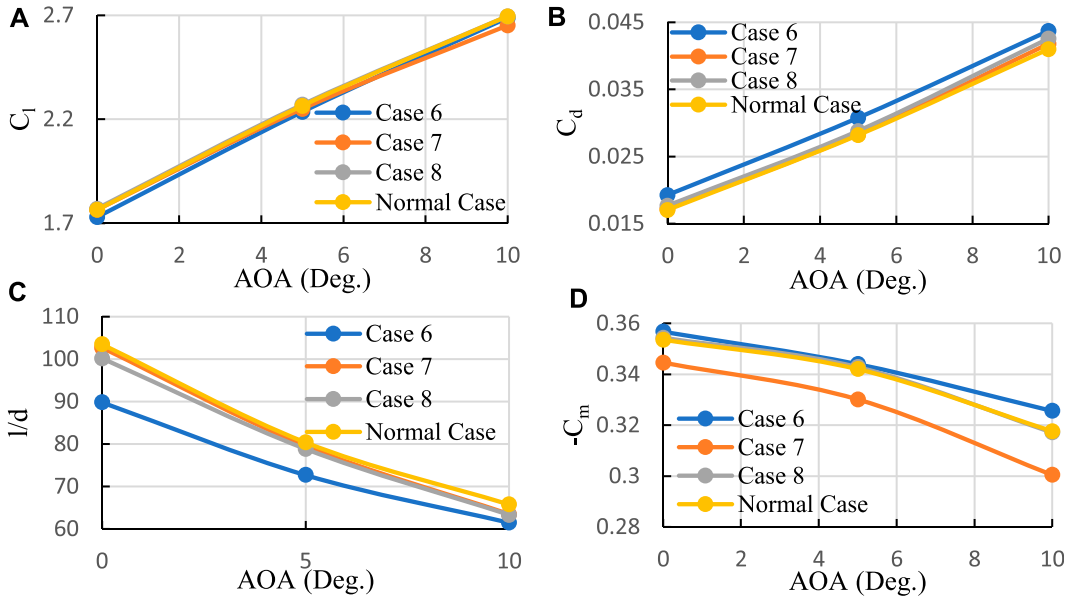

FIGURE 8
Aerodynamic characteristics *versus* AOA of channels' profile: **(A)** C_l, **(B)** C_d, **(C)** l/d, and **(D)** C_m.

(Figures 10D–F) demonstrates the pitching moment coefficient *versus* maximum camber position for three different maximum cambers and for three different angles of attack. C_m behaves similarly to C_l, showing a *hook-like* effect as well. Lower maximum camber values result in lower C_m. Moving the camber position towards the flap's leading edge leads to a smaller C_m. The minimum C_m is associated with the maximum camber position closest to the flap's leading edge.

Supplementary Tables S2, S3 provide the best and worst camber positions and camber values for various aerodynamic

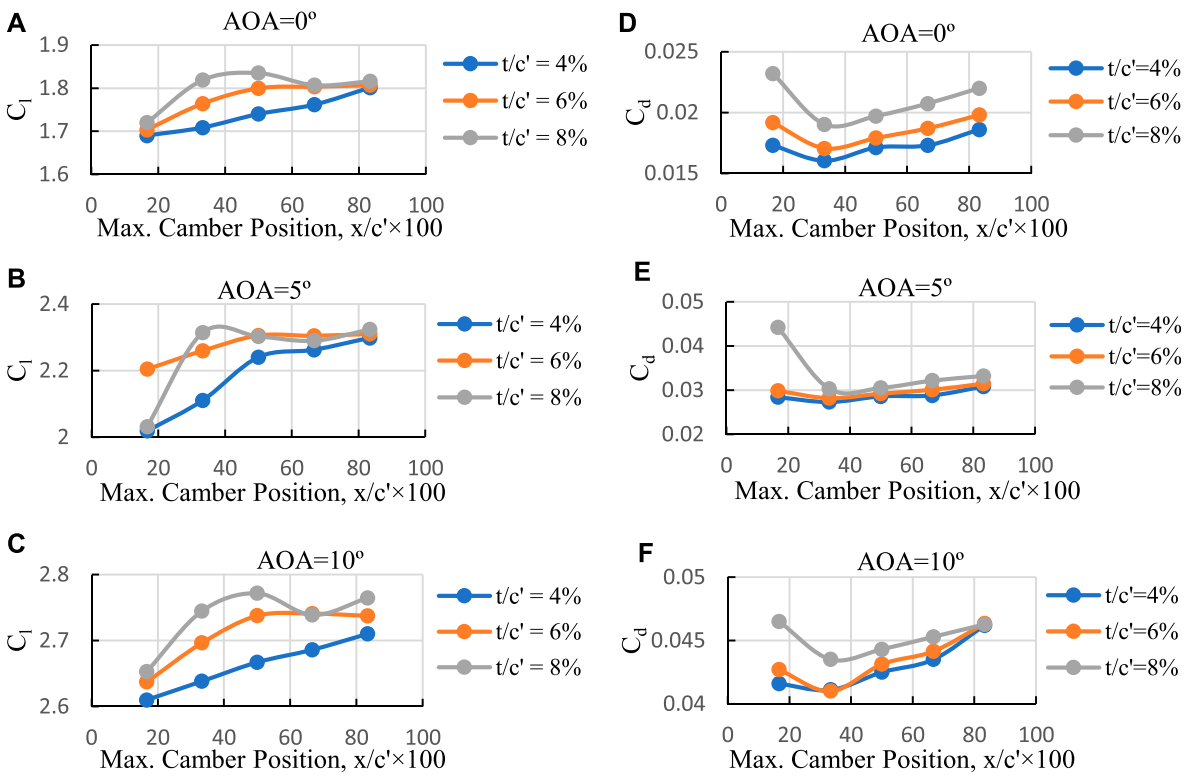

FIGURE 9
Cl and Cd *versus* maximum camber position for three different maximum cambers and three different angles of attack. **(A)** AOA = 0°, **(B)** AOA = 5°, **(C)** AOA = 10°, **(D)** AOA = 0°, **(E)** AOA = 5°, **(F)** AOA = 10°.

characteristics, respectively. The desired flap geometry for each aerodynamic specification is also listed.

Figure 11 presents a comparative analysis of four distinct desired flaps, demonstrating a reduction of approximately 5 percent in the l/d difference at higher angles of attack. It is important to note that the selection of flaps may vary depending on the aircraft and its flight type. For example, during take-off and landing configurations, quantities related to higher angles of attack hold significant importance. In such scenarios, emphasis is placed more on Cl rather than Cd, Cm, and l/d. Consequently, the T8C3 flap is considered suitable for shorter runways.

To provide a practical example, let's consider an aircraft that prioritizes drag reduction. Despite the higher Cl value of the T8C3 flap, an aircraft with specifications M = 300tons, SW = 511 m^2, AR = 7, and e = 0.8 lead to a take-off speed that is 3.28 km/h higher compared to the T6C3 flap. However, the T8C3 flap results in 3 percent higher drag force. On the other hand, the T4C2 flap exhibits a take-off speed that is 5.4 km/h higher, but a drag force that is 4.5 percent lower than that of the T8C3 flap. Additionally, the T4C2 flap's smaller Cm leads to a reduced size of the horizontal tail, resulting in less drag and a negative lift force.

Figure 12 showcases the Cp distribution of the T8C3 flap, where fluctuations in Cp are observed on the upper surface of the flaps. These fluctuations are likely a result of interactions between the separation zone and the jet flow formed by the channels, leading to a mixing layer flow.

Figure 13 provide insight into the velocity field of the T8C3 flap. The geometry exhibits a separation zone at the trailing edge of flap No. 2. As the angle of attack increases, the separation zone remains constant due to the presence of the jet flow formed by channel No. 2, which inhibits separation. This behavior persists until the angle of attack reaches a limit where flow separation occurs at the Kool area.

4.4 Morphed flap at 30 degrees deflection

At 30° flap deflection, Figures 14A–C depict the relationship between maximum camber position and Cl for two different maximum cambers and three different angles of attack. At this deflection angle, the camber position that yields maximum Cl shifts towards the trailing edge, precisely at half the flap chord (x/c' = 50%). It should be noted that a maximum camber of 6 percent, compared to 8 percent at zero angle of attack, demonstrates superior performance. However, as the angle of attack increases, a reversing phenomenon occurs. The reason behind this is that the lower maximum camber (6 percent) causes the Kool area to have larger angles relative to the flow, resulting in enhanced flow separation. Moreover, a flap with 6 percent maximum camber at 7° angle of attack experiences a deep stall.

(Figures 14D–F) showcase Cd *versus* maximum camber position for two different maximum cambers and three different angles of attack. Similar to Cl, the reversing phenomenon is observable here as well. While maximum camber position movement has a minimal

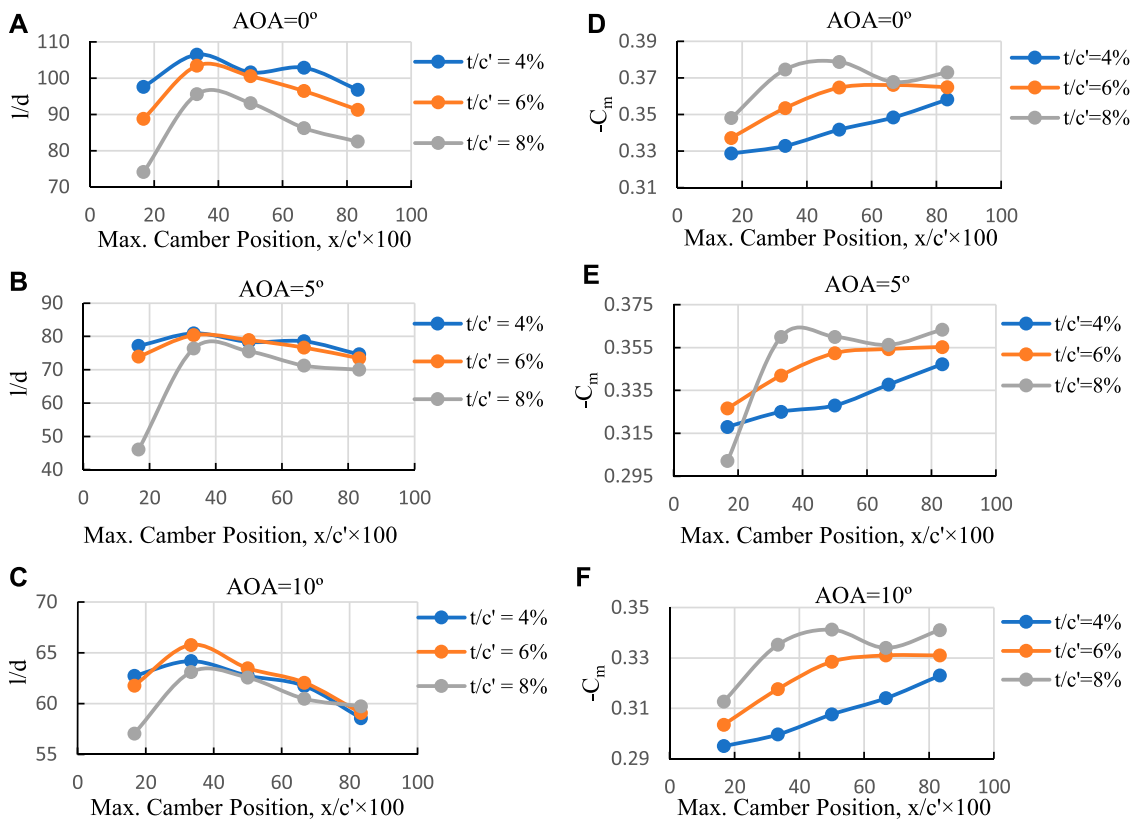

FIGURE 10
l/d and C_m *versus* camber position for three different camber values and for three distinct angles of attack. **(A)** AOA = 0°, **(B)** AOA = 5°, **(C)** AOA = 10°, **(D)** AOA = 0°, **(E)** AOA = 5°, **(F)** AOA = 10°.

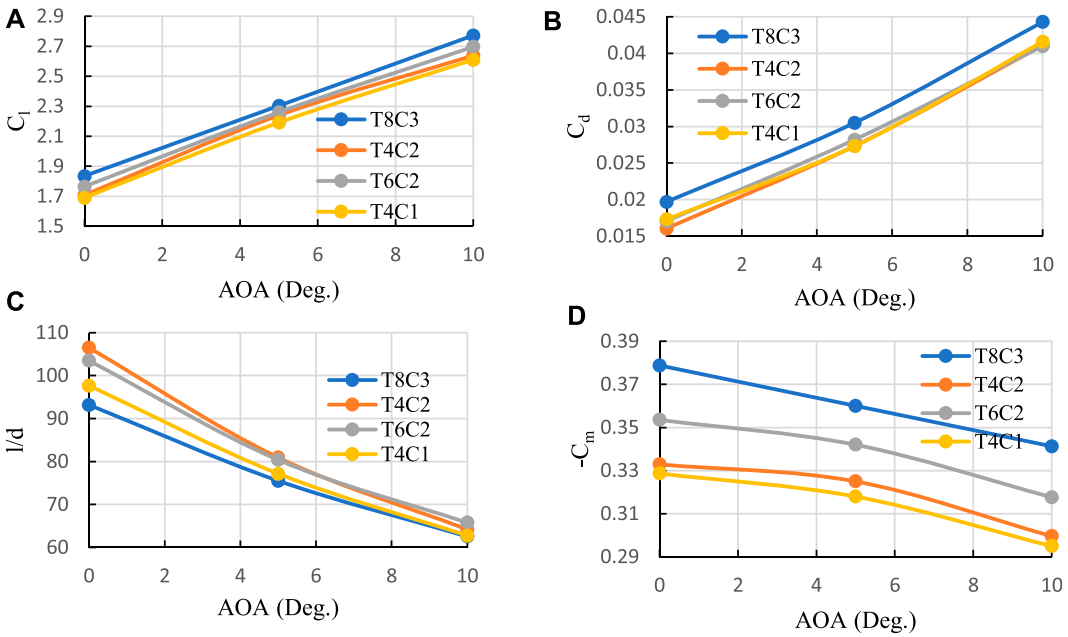

FIGURE 11
Comparison of aerodynamic performance for four desired morphed flaps. **(A)** Cl, **(B)** Cd, **(C)** l/d ratio, and **(D)** Cm.

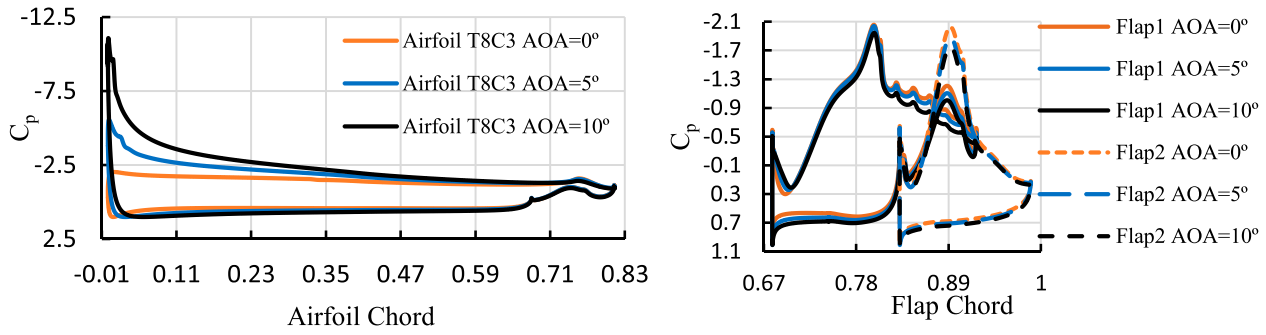

FIGURE 12
Cp distribution of the flap T8C3 for three different angles of attack.

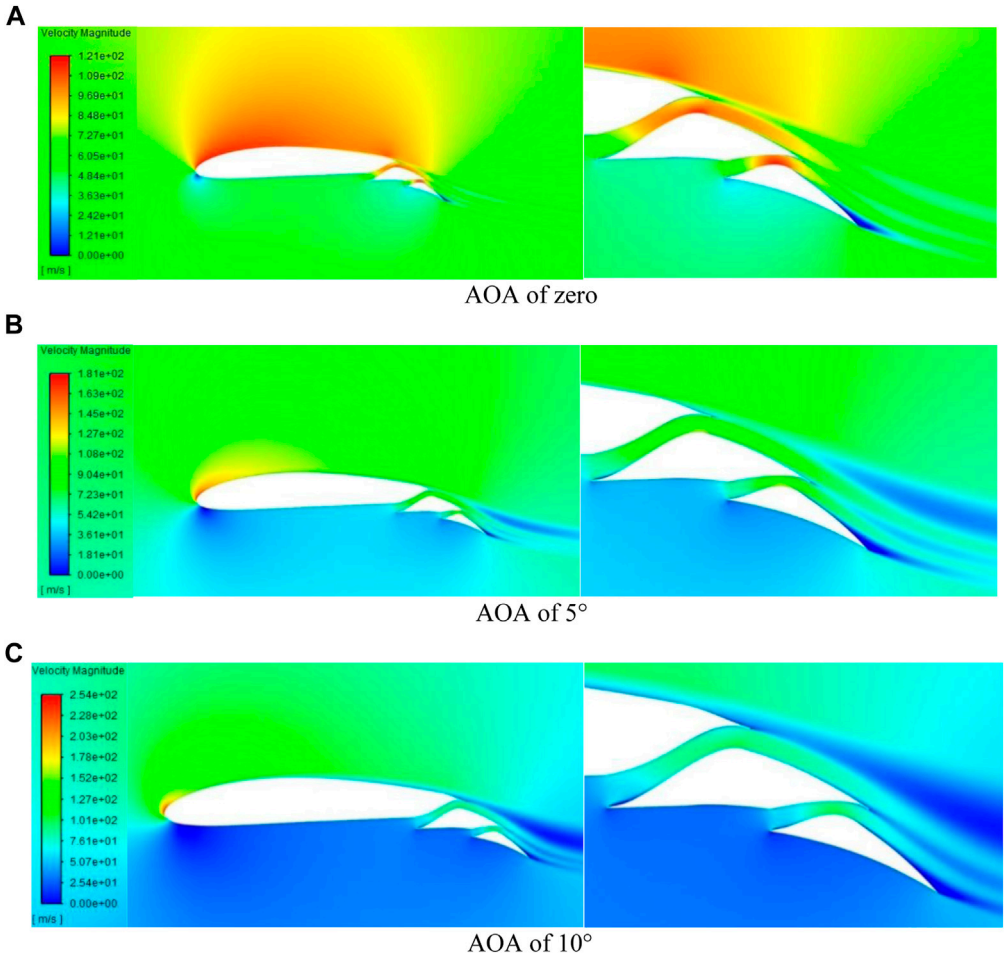

FIGURE 13
T8C3 flap velocity field at AOA of 0, 5° and 10°. **(A)** AOA of zero, **(B)** AOA of 5°, **(C)** AOA of 10°

impact on drag value, it generally leads to an increase in Cd as it approaches the trailing edge. For angles of attack below stall, the optimal maximum camber position is at the flap mid chord.

Figure 15, presented in panels a) to c), illustrates the relationship between l/d and maximum camber position for two different maximum cambers at three distinct angles of attack. Similar to Cl and Cd, smaller maximum camber values exhibit better performance at lower angles of attack. Although the movement of the maximum camber position has a slight impact on l/d, generally, when it shifts towards the trailing edge, l/d decreases. In comparison to the 15° deflection, the position of maximum l/d has shifted from 33.33 to 50 percent of the flap chord.

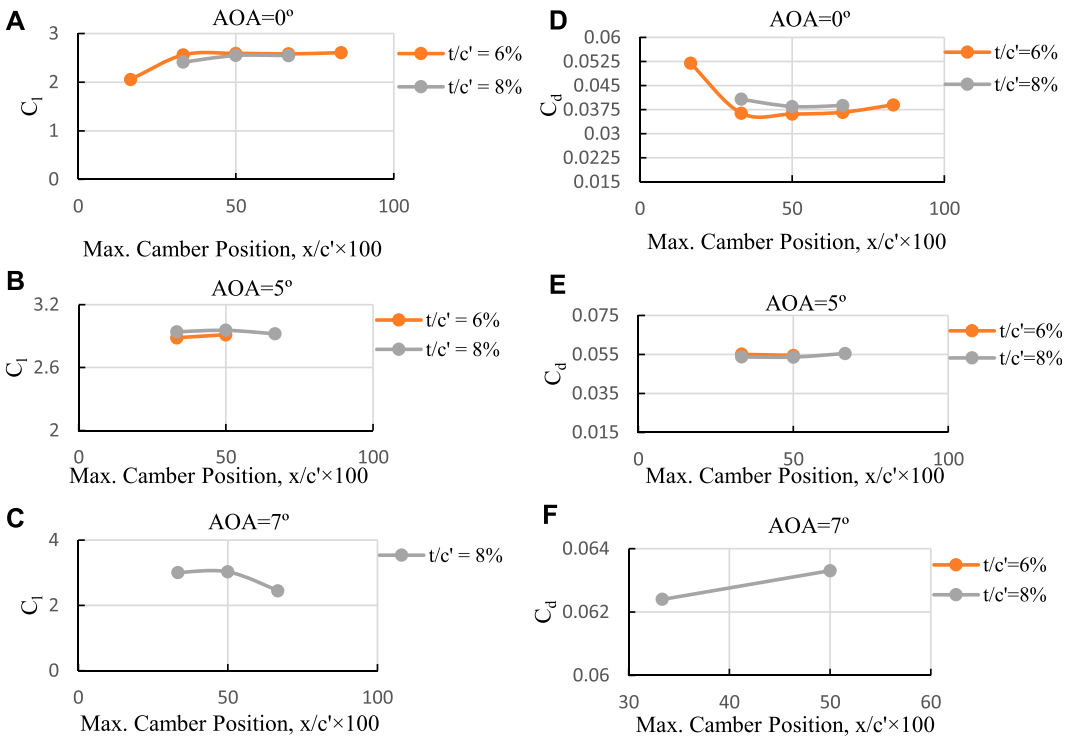

FIGURE 14
C_l and C_d *versus* camber position for three different cambers at three different angles of attack (at 30° Deflection). **(A)** AOA = 0°, **(B)** AOA = 5°, **(C)** AOA = 7°, **(D)** AOA = 0°, **(E)** AOA = 5°, **(F)** AOA = 7°.

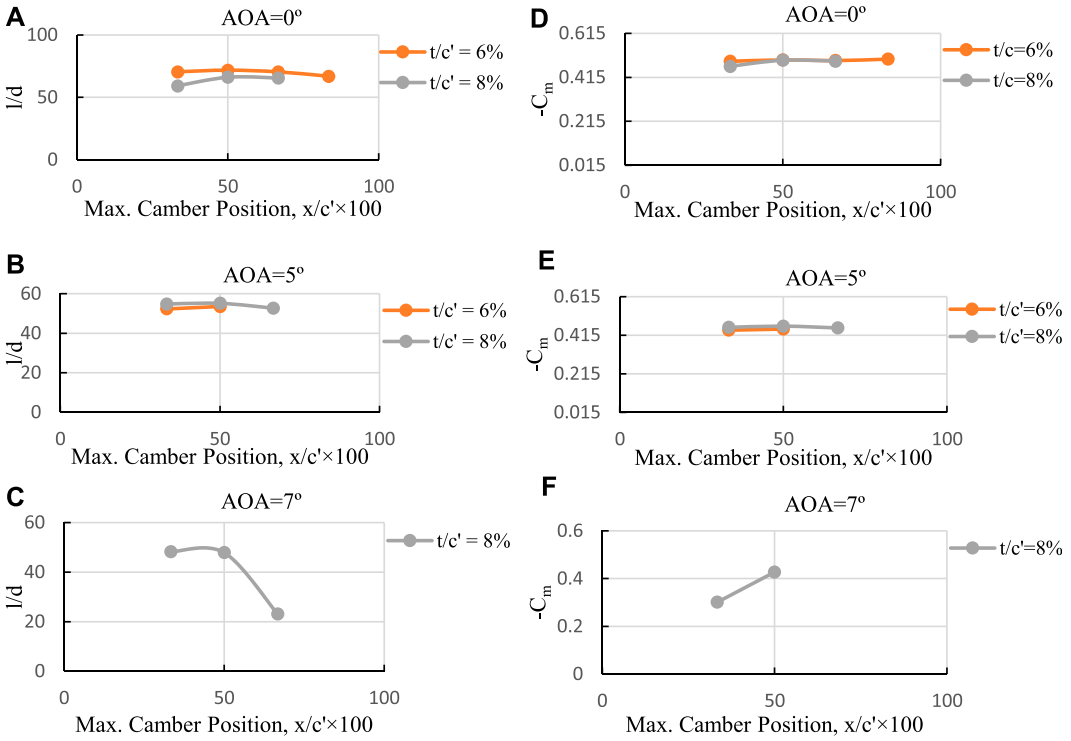

FIGURE 15
l/d and C_m *versus* maximum camber position for three different maximum cambers at three angles of attack (at 30° deflection). **(A)** AOA = 0°, **(B)** AOA = 5°, **(C)** AOA = 7°, **(D)** AOA = 0°, **(E)** AOA = 5°, **(F)** AOA = 7°.

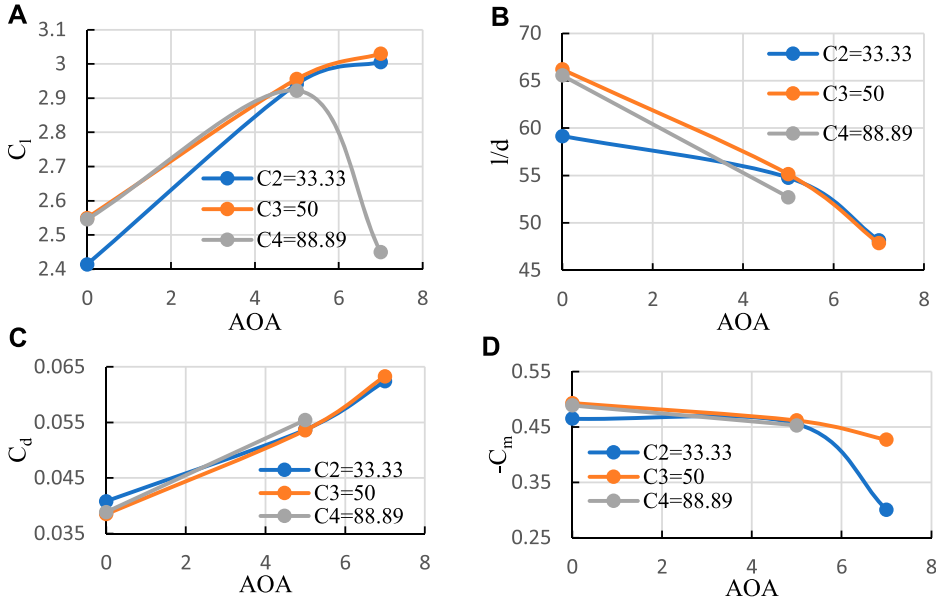

FIGURE 16
(A) C_l, **(B)** l/d *versus* angle of attack, **(C)** C_d, and **(D)** C_m *versus* AOA when t/c˙x100 = 8 and x/c˙ varies from 33.33 to 88.89 percent.

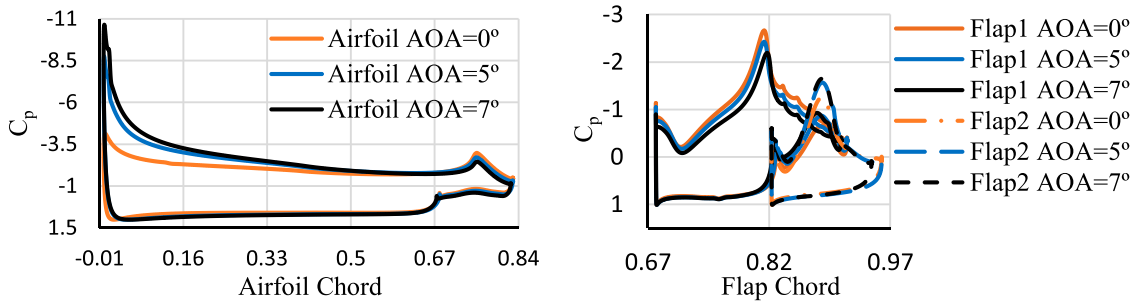

FIGURE 17
C_p for 30° deflection of the flap T8C3 at three different angles of attack.

(Figures 15D–F) depict the behavior of Cm in relation to maximum camber position. The behavior of Cm aligns with other aerodynamic characteristics. For instance, there is a small difference between the 6 percent and 8 percent maximum camber values, and a reversing phenomenon is observed as well.

Figure 16 provide a comparison of the aerodynamic performance of flaps with varying maximum camber position. It is evident that the flap maximum camber position located in the middle of the flap chord yields the best performance. Hence, for the 30° morphed flap deflection, the desired configuration is the T8C3 flap.

Figure 17 displays Cp distribution over the airfoil surface for three different angles of attack, highlighting the fluctuations resulting from the mixing layer flow on the upper surface of the flap.

Figure 18 showcase the flow field, even at zero angle of attack, indicating a separation zone at the trailing edge of flap "2"due to the steep slope of the upper surface in that area. Additionally, a larger dead region is observed at the leading edge of flap "1"caused by the alteration in the channel path, where the separated flow needs to travel a longer distance to reach the channel wall. In all angles of attack, the presence of the jet flow generated by channel number 2 maintains the trailing edge separation unchanged. At 7° angle of attack, corresponding to the stall angle of attack, separation initiates at the flap Kool area.

4.5 Modified T4C3 flap at 30 degrees deflection

(Figure 19A) demonstrates that even at zero angle of attack, flow separation occurs for the T4C3 flap. To delay separation in the Kool zone, modifications were implemented. Reducing the angle of the Kool zone increases the outlet width of channel "1," and thus, a third part was added to maintain the outlet width unchanged. Furthermore, to reduce the length of the Kool zone, the outlet of

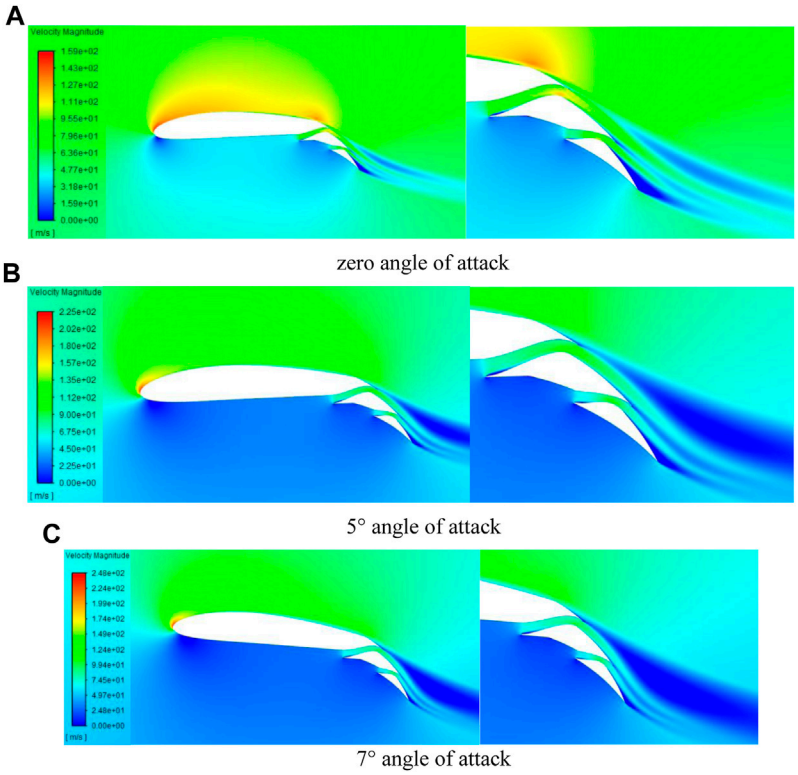

FIGURE 18
Velocity Field of the T8C3 flap at 0, 5°, and 7°. **(A)** zero angle of attack, **(B)** 5° angle of attack, **(C)** 7° angle of attack.

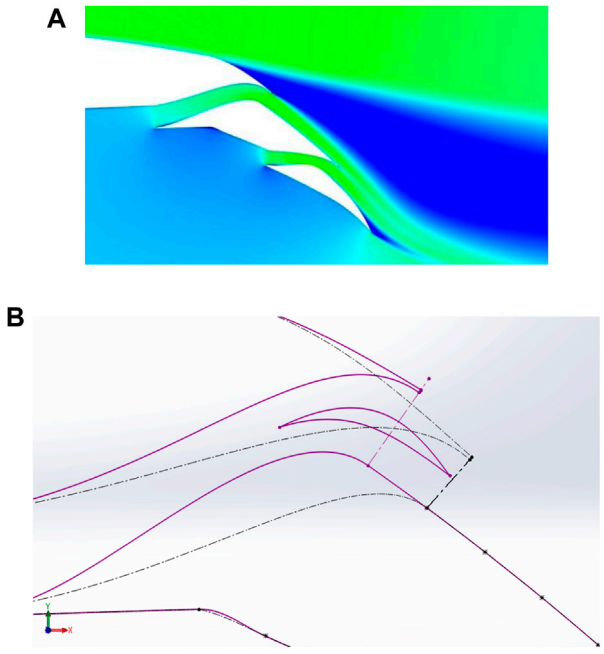

FIGURE 19
(A) Separation in Kool area and **(B)** Modified flap geometry (purple lines) and base line (dash-dotted lines).

TABLE 2 Modified flap aerodynamic specifications.

AOA (Deg.)	C_l	C_d	l/d	C_m
0	2.42	0.0436	55.5	−0.46
5	2.8223	0.057	49.51	−0.43
7	2.903	0.065	44.45	-

channel "1" was shifted from node number 2 to node number 1. (Figure 19B) visually presents the related changes, and Table 2 provides the results of the geometry modifications.

Figure 20 compares the aerodynamic characteristics of the T8C3 and modified T4C3 flaps. Although the T8C3 flap outperforms the T4C3 flap in terms of aerodynamic performance, it is worth considering that the T8C3 flap has an 8 percent maximum camber, resulting in a larger Cl. However, when considering Cl, the T4C3 flap exhibits a better improvement compared to the T8C3 flap, along with an increased stall angle of attack.

Figure 21 showcase the velocity field of the modified T4C3 flap, clearly illustrating the disappearance of separation. It is important to note that the addition of an extra part to the morphed flap introduces challenges related to increased weight, cost, and production complexities.

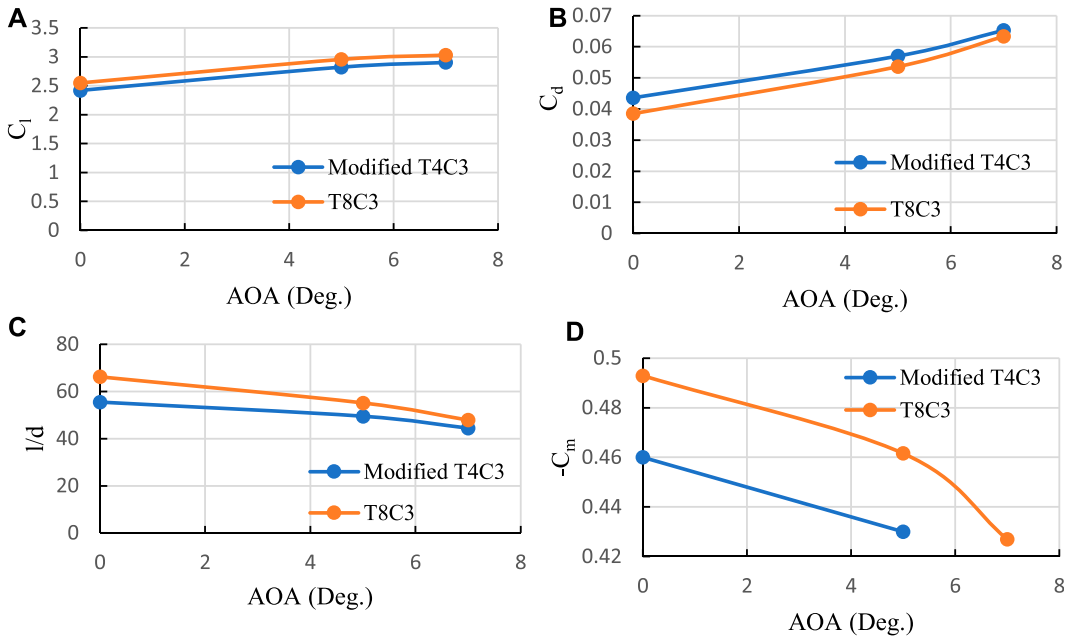

FIGURE 20
Aerodynamic characteristics comparison of the modified and T8C3 flaps. **(A)** Cl, **(B)** Cd, **(C)** l/d, and **(D)** Cm.

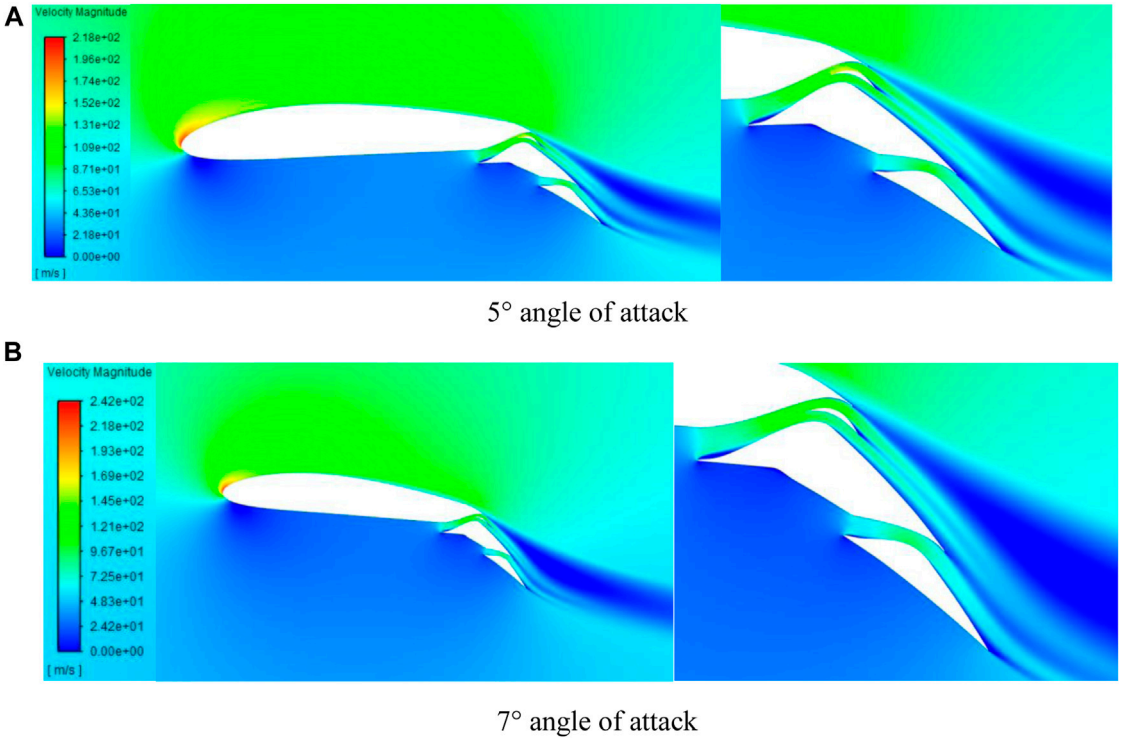

FIGURE 21
Modified flap velocity field. **(A)** 5° angle of attack, **(B)** 7° angle of attack

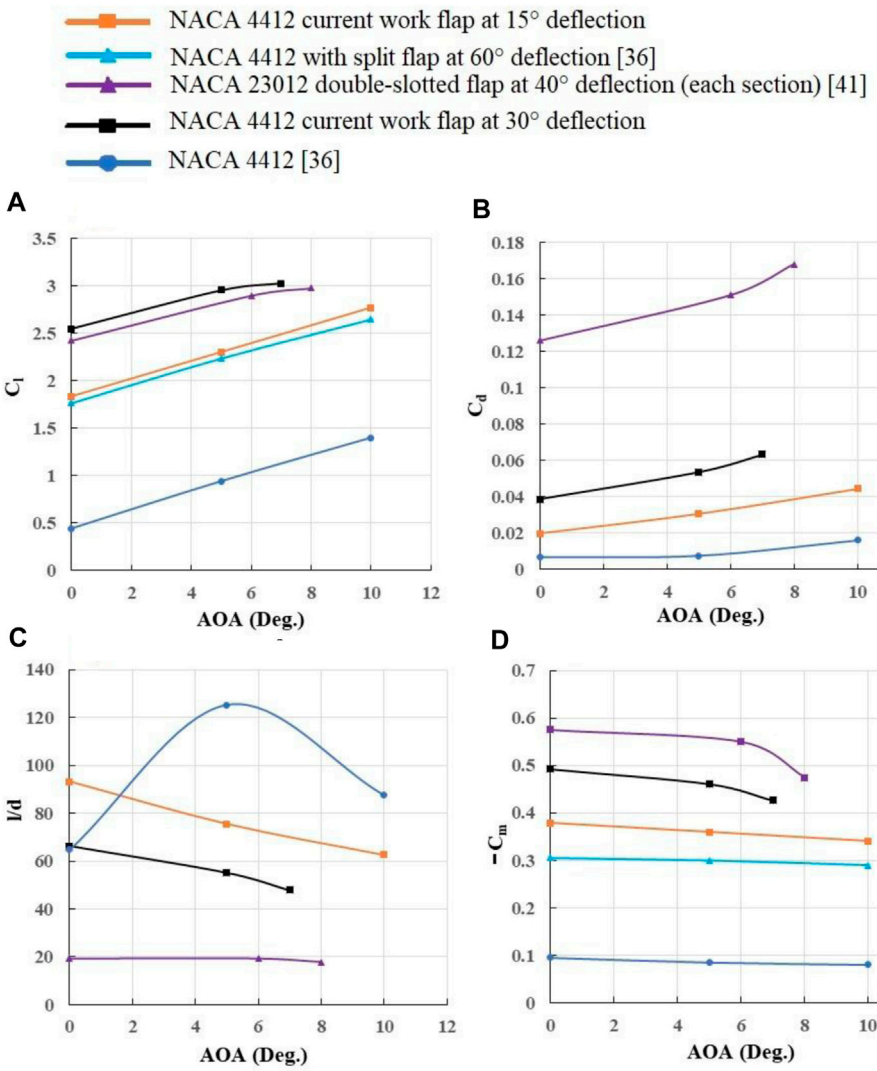

FIGURE 22
Comparison of morphed and conventional flaps: **(A)** C_l, **(B)** C_d, **(C)** l/d ratio, and **(D)** C_m.

TABLE 3 Comparison of morphed and conventional flaps.

Case	$C_{l\ max}$	$C_{d\ min}$	C_m	l/d (Max)
NACA4412 un-morphed airfoil	1.66	0.0068	−0.08	125
NACA4412 split flap at 60° flap deflection angle (Abbott and Von Doenhoff, 1956)	2.65	-	−0.29	-
NACA4412 morphing flap at 30° flap deflection angle	3.03	0.0385	−0.0427	65
NACA 23012 double-slotted flap at 40° flap deflection angle (Wenzinger and Gauvain, 1938)	2.97	0.126	−0.475	19

5 Concluding remarks

Figure 22 examines the application of a morphed flap on the NACA4412 airfoil, comparing it to a regular flap with a deflection angle of 60°. The study investigates two different deflection angles: 15° and 30°. Remarkably, despite the morphed flap having a maximum deflection angle of 30°, its performance surpasses that of the regular flap. The morphed flap exhibits a significant reduction in drag (approximately three times) and an increase in lift, resulting in a considerable improvement in the l/d ratio (approximately five times). In contrast, both the base airfoil and split flap demonstrate lower Cm values compared to the morphed flap. Table 3 shows the maximum and minimum values for these flaps. It should be noted that the results of un-morphed airfoil of the current research are the same as the results of the simple NACA4412 airfoil in reference (Abbott and Von Doenhoff, 1956).

6 Conclusion

In this study, we designed a double-slotted morphed flap with variable camber and slots, using CFD to examine its aerodynamic performance. The characteristics of the channels (slots), including width, throat position, and intake angle, were initially investigated. Subsequently, five different x/c' and three different t/c' were examined. The second step was repeated for two different flap deflections (15° and 30°) at three distinct angles of attack. The optimal flap geometry was determined and a modification was applied to further enhance the flap's aerodynamic performance. The results demonstrate an increase in lift, a reduction in drag, and a significant improvement in l/d. The maximum lift coefficient at a 30° flap deflection is 3.03, whereas the maximum lift coefficients for the un-morphed airfoil and split flap at a 60° deflection are 1.66 and 2.65, respectively. In other words, the morphed flap generates more lift (about 14% in maximum lift), despite its considerably smaller deflection angle (one of the reasons for its lower drag coefficient). According to the findings, the double-slotted modified flap has enhanced the maximum lift coefficient of the airfoil by 82.5%. While there is no available data for the drag coefficient of the split flap applied to the NACA4412 airfoil, to gain a better understanding of this coefficient, the NACA23012 airfoil with a double-slotted flap has a minimum drag coefficient of 0.126, whereas the present morphed flap exhibits a drag coefficient of 0.068 (more than three times less). Note, compared to the double-slotted flap, the morphed flap achieves a fivefold increase in l/d ratio at zero angle of attack. This study also investigated the pitching moment coefficient, which exhibits behavior similar to Cl, but with different magnitudes. Although the magnitude of Cm for the present morphed flap exceeds that of the split flap, it is lower than that of the double-slotted flap used for the NACA23012 airfoil. It appears that the magnitude of this coefficient is proportional to the lift coefficient, meaning that greater lift results in a higher pitching moment.

7 Future outlook

To enhance the practicality of the research findings, further investigation is necessary to determine the flap's weight, production cost, and manufacturing feasibility. Additionally, given the critical role of the Kool section in the flap, deeper analysis of this area is recommended. Lastly, additional investigation is suggested to identify the optimal flap shape.

Data availability statement

The original contributions presented in the study are included in the article/Supplementary Material, further inquiries can be directed to the corresponding author.

Author contributions

SS: Investigation, Methodology, Software, Writing–original draft, Writing–review and editing. MT: Conceptualization, Methodology, Supervision, Writing–original draft, Writing–review and editing. PA: Software, Writing–original draft, Writing–review and editing.

Funding

The author(s) declare that no financial support was received for the research, authorship, and/or publication of this article.

Acknowledgments

The authors would like to express their gratitude for the valuable support provided by SS, who supplied the necessary hardware for our CFD work.

Conflict of interest

The authors declare that the research was conducted in the absence of any commercial or financial relationships that could be construed as a potential conflict of interest.

The author(s) declared that they were an editorial board member of Frontiers, at the time of submission. This had no impact on the peer review process and the final decision

Publisher's note

Supplementary material

The Supplementary Material for this article can be found online at: https://www.frontiersin.org/articles/10.3389/fmech.2024.1371479/full#supplementary-material

References

Abbott, I. H., and Von Doenhoff, A. E. (1956). *Theory of wing sections*. New York: Dover.

Abdessemed, C., Yao, Y., Bouferrouk, A., and Narayan, P. (2018). Morphing airfoils analysis, using dynamic meshing. *Int. J. Numer. Methods Heat Fluid Flow* 28 (No. 5), 1117–1133. doi:10.1108/HFF-06-2017-0261

Abdolahipour, S. (2023). Effects of low and high frequency actuation on aerodynamic performance of a supercritical airfoil. *Front. Mech. Eng.* 9, 1290074. doi:10.3389/fmech.2023.1290074

Abdolahipour, S., Mani, M., and Shams Taleghani, A. (2021). Parametric study of a frequency-modulated pulse jet by measurements of flow characteristics. *Phys. Scr.* 96 (No. 12), 125012. doi:10.1088/1402-4896/ac2bdf

Abdolahipour, S., Mani, M., and Shams Taleghani, A. (2022a). Experimental investigation of flow control on a high-lift wing using modulated pulse jet vortex generator. *J. Aerosp. Eng.* 35 (5), 05022001. doi:10.1061/(asce)as.1943-5525.0001463

Abdolahipour, S., Mani, M., and Shams Taleghani, A. (2022b). Pressure improvement on a supercritical high-lift wing using simple and modulated pulse jet vortex generator. *Flow. Turbul. Combust.* 109 (1), 65–100. doi:10.1007/s10494-022-00327-9

Ai, Q., Weaver, P. M., Barlas, T. K., Olsen, A. S., Madsen, H. A., and Andersen, T. L. (2019). Field testing of morphing flaps on a wind turbine blade, using an outdoor rotating rig. *Renew. Energy* 133, 53–65. doi:10.1016/j.renene.2018.09.092

Aziz, M. A., Mansour, M., Iskander, D., and Hany, D. (2019). Combined droop nose and trailing edges morphing effects on airfoils aerodynamics. *SN Appl. Sci.* 1 (No. 9), 1033. doi:10.1007/s42452-019-0796-6

Burdette, D. A., and Martins, J. R. (2018). Design of a transonic wing with an adaptive morphing trailing edge via aerostructural optimization. *Aerosp. Sci. Technol.* 81, 192–203. doi:10.1016/j.ast.2018.08.004

Chandrasekhara, M. S., Wilder, M. C., and Carr, L. W. (1998). Unsteady stall control, using dynamically deforming airfoils. *AIAA J.* 36 (No. 10), 1792–1800. doi:10.2514/2.294

Daynes, S., and Weaver, P. M. (2012). A morphing trailing edge device for a wind turbine. *J. Intelligent Material Syst. Struct.* 23 (No. 6), 691–701. doi:10.1177/1045389X12438622

Fincham, J. H. S., and Friswell, M. I. (2015). Aerodynamic optimisation of a camber morphing aerofoil. *Elsevier Masson SAS* 43, 245–255. doi:10.1016/j.ast.2015.02.023

Harbi Monfared, R., Taeibi Rahni, M., Zareh, M., Ahmadi, G., and Etemadi Haghighi, S. (2022). Aerodynamic and aeroacoustic performance of a wing with structured surface inspired by owl's wings. *J. Appl. Fluid Mech.* 15 (4), 1243–1253. doi:10.47176/jafm.15.04.33091

Jawahar, H. K., Theunissen, R., Azarpeyvand, M., and da Silva, C. R. I. (2019). Flow characteristics of slat cove fillers. *Aerosp. Sci. Technol.* 100. doi:10.1016/j.ast.2020.105789

Jones, G., Santer, M., and Papadakis, G. (2018). Control of low Reynolds number flow around an airfoil, using periodic surface morphing: a numerical study. *J. Fluids Struct.* 76, 95–115. doi:10.1016/j.jfluidstructs.2017.09.009

Lyu, Z., and Martins, J. R. (2015). Aerodynamic shape optimization of an adaptive morphing trailing-edge wing. *J. Aircr.* 52 (No. 6), 1951–1970. doi:10.2514/1.C033116

Magrini, A., and Benini, E. (2017). Aerodynamic optimization of a morphing leading-edge airfoil with a constant arc length parameterization. *J. Aerosp. Eng.* 31 (No. 2). doi:10.1061/(ASCE)AS.1943-5525.0000812

Mirzaei, M., Taleghani, A. S., and Shadaram, A. (2012). Experimental study of vortex shedding control using plasma actuator. *Appl. Mech. Mater.* 186, 75–86. doi:10.4028/www.scientific.net/amm.186.75

Mohammadi, M., and Taleghani, A. S. (2014). Active flow control by dielectric barrier discharge to increase stall angle of a NACA0012 airfoil. *Arab. J. Sci. Eng.* 39, 2363–2370. doi:10.1007/s13369-013-0772-1

Narsipur, S., Pomeroy, B., and Selig, M. (2012). *"CFD analysis of multi-element airfoils for wind turbines," the 30th AIAA applied aerodynamics conference*. New Orleans: Louisiana. doi:10.2514/6.2012-2781

Nemati, M., and Jahangirian, A. (2020). Robust aerodynamic morphing shape optimization for high-lift missions. *Aerosp. Sci. Technol.* 103, 105897. doi:10.1016/j.ast.2020.105897

Noori, S. M. S., Taeibi Rahni, M., and Shams Taleghani, S. A. (2020). Numerical analysis of droplet motion over a flat plate due to surface acoustic waves. *Microgravity Sci. Technol.* 32 (4), 647–660. doi:10.1007/s12217-020-09784-1

Papadakis, M., Myose, R., Heron, I., and Johnson, B. (1996). *An experimental investigation of gurney flaps on a ga(W)-2 airfoil with 25% slotted flap*. AIAA-96-2437-CP. doi:10.2514/6.1996-2437

Papadakis, M., Myose, R., Matallana, S., Papadakis, M., Myose, R., and Matallana, S. (1997). *"Experimental investigation of gurney flaps on a two-element general aviation airfoil," the 35th Aerospace sciences meeting and exhibit*. Reno, NV: U.S.A. doi:10.2514/6.1997-728

Rivero, A. E., Fournier, S., Manolesos, M., Cooper, J. E., and Woods, B. K. (2021). Experimental aerodynamic comparison of active camber morphing and trailing-edge flaps. *AIAA J.* 59 (No. 7), 2627–2640. doi:10.2514/1.J059606

Salmasi, A., Shadaram, A., and Taleghani, A. S. (2013). Effect of plasma actuator placement on the airfoil efficiency at poststall angles of attack. *IEEE Trans. Plasma Sci.* 41 (10), 3079–3085. doi:10.1109/tps.2013.2280612

Secanell, M., Suleman, A., and Gamboa, P. (2006). Design of a morphing airfoil, using aerodynamic shape optimization. *AIAA J.* 44 (No. 7), 1550–1562. doi:10.2514/1.18109

Shams Taleghani, A., Ghajar, A., and Masdari, M. (2020). Experimental study of ground effect on horizontal tail effectiveness of a conceptual advanced jet trainer. *J. Aerosp. Eng.* 33 (4), 05020001. doi:10.1061/(asce)as.1943-5525.0001140

Sheikholeslam Noori, M., Shams Taleghani, A., and Taeibi Rahni, M. (2020a). Phenomenological investigation of drop manipulation using surface acoustic waves. *Microgravity Sci. Technol.* 32 (6), 1147–1158. doi:10.1007/s12217-020-09839-3

Sheikholeslam Noori, M., Shams Taleghani, A., and Taeibi Rahni, M. (2021). Surface acoustic waves as control actuator for drop removal from solid surface. *Fluid Dyn. Res.* 53 (4), 045503. doi:10.1088/1873-7005/ac12af

Sheikholeslam Noori, M., Taeibi Rahni, M., and Shams Taleghani, A. (2020b). Effects of contact angle hysteresis on drop manipulation using surface acoustic waves. *Theor. Comput. Fluid Dyn.* 34 (1), 145–162. doi:10.1007/s00162-020-00516-0

Simiriotis, N., Jodin, G., Marouf, A., Elyakime, P., Hoarau, Y., Hunt, J. C. R., et al. (2018). Morphing of a supercritical wing by means of trailing edge deformation and vibration at high Reynolds numbers: experimental and numerical investigation. *J. Fluids Struct.* 91, 102676. doi:10.1016/j.jfluidstructs.2019.06.016

Steenhuizen, D., and van Tooren, M. (2012). The implementation of a knowledge-based framework for the aerodynamic optimization of a morphing wing device. *Adv. Eng. Inf.* 26 (No. 2), 207–218. doi:10.1016/j.aei.2012.02.004

Taeibi Rahni, M., Shams Taleghani, A., Sheikholeslam, M., and Ahmadi, G. (2022). Computational simulation of water removal from a flat plate, using surface acoustic waves. *Wave Motion* 111, 102867. doi:10.1016/j.wavemoti.2021.102867

Taguchi, K., Fukunishi, K., Takazawa, S., Sunada, Y., Imamura, T., Rinoie, K., et al. (2020). Experimental study about the deformation and aerodynamic characteristics of the passive morphing airfoil. *Trans. Jpn. Soc. Aerosp. Sci.* 63 (No. 1), 18–23. doi:10.2322/tjsass.63.18

Taleghani, A. S., Shadaram, A., and Mirzaei, M. (2012). Effects of duty cycles of the plasma actuators on improvement of pressure distribution above a NLF0414 airfoil. *IEEE Trans. Plasma Sci.* 40 (5), 1434–1440. doi:10.1109/tps.2012.2187683

Taleghani, A. S., Shadaram, A., Mirzaei, M., and Abdolahipour, S. (2018). Parametric study of a plasma actuator at unsteady actuation by measurements of the induced flow velocity for flow control. *J. Braz. Soc. Mech. Sci. Eng.* 40 (No. 4), 173–213. doi:10.1007/s40430-018-1120-x

Tô, J. B., Simiriotis, N., Marouf, A., Szubert, D., Asproulias, I., Zilli, D. M., et al. (2019). Effects of vibrating and deformed trailing edge of a morphing supercritical airfoil in transonic regime by numerical simulation at high Reynolds number. *J. Fluids Struct.* 91, 102595. doi:10.1016/j.jfluidstructs.2019.02.011

Vandenberg, B., and Oskam, B. (1980). Boundary layer measurements on a two-dimensional wing with flap and a comparison with calculations. *AGARD Turbul. Bound. Layers* 14. SEE N80-27647 18-34).

Wenzinger, C. J., and Gauvain, W. E. (1938). Wind-tunnel investigation of a NACA23012 airfoil with A slotted flap and three types of auxiliary flap. *NACA Tech. Rep. No* 679.

Xiao, L., Zhao, H., Xu, Z., Li, X., Shen, C., Wang, K., et al. (2022). A new architecture of morphing wing based on hyperelastic materials and metastructures with tunable stiffness. *Front. Mech. Eng.* 7, 814446. doi:10.3389/fmech.2021.814446

Nomencalture

AR	Aspect Ratio
c	Airfoil Chord
Cd	Airfoil Drag Coefficient
Cl	Airfoil Lift Coefficient
Cm	Airfoil Pitching Moment Coefficient
Cp	Airfoil Pressure Coefficient
c'	Flap Chord
d	Airfoil Drag
d1	Flap First Channel's Entrance Length (Vertical)
d2	Flap Second Channel's Entrance Length (Vertical)
e	Oswald Efficiency Factor
l	Airfoil Lift
l/d	Airfoil Aerodynamic Efficiency
M	Aircraft Mass
SW	Wing Planform Area
t/c'	Ratio of Maximum Flap Camber to Flap Chord
x/c'	Ratio of Position of Maximum Flap Camber to Flap Cord

frontiers | Frontiers in Mechanical Engineering

TYPE Review
PUBLISHED 13 November 2024
DOI 10.3389/fmech.2024.1380675

OPEN ACCESS

EDITED BY
Farschad Torabi,
K. N. Toosi University of Technology, Iran

REVIEWED BY
Davide Lengani,
University of Genoa, Italy
Nadaraja Pillai S.,
SASTRA University, India

*CORRESPONDENCE
Soheila Abdolahipour,
sabdolahi@ari.ac.ir

RECEIVED 02 February 2024
ACCEPTED 28 October 2024
PUBLISHED 13 November 2024

CITATION
Abdolahipour S (2024) Review on flow separation control: effects of excitation frequency and momentum coefficient. *Front. Mech. Eng.* 10:1380675. doi: 10.3389/fmech.2024.1380675

Review on flow separation control: effects of excitation frequency and momentum coefficient

Soheila Abdolahipour*

Aerospace Research Institute, Ministry of Science, Research, and Technology, Tehran, Iran

This paper presents a comprehensive review of the studies and research conducted on flow separation control on lifting surfaces. In this paper, two critical parameters, namely, the momentum coefficient and excitation frequency, that significantly impact flow separation control are analyzed in detail. Through a comprehensive literature review, experimental and numerical studies are examined in order to gain insight into the underlying mechanisms of momentum injection and excitation frequency on the shear layer and wake dynamics and to quantify the impact of these parameters on the flow separation control. Effective flow control on lifting surfaces can modify the streamlines and pressure distribution, thereby increasing their aerodynamic efficiency. This paper focuses on the control of flow separation on airfoils, with particular attention paid to the benefits of such control, including lift enhancement, drag reduction, aerodynamic efficiency enhancement, performance enhancement, and other important features. This paper presents a review of studies that have employed blowing actuators, as well as zero net mass flux, plasma, and acoustic actuators, in order to provide an appropriate historical context for recent developments. The findings of this review paper will contribute to a better understanding of the optimal conditions for efficient flow separation control on lifting surfaces using unsteady excitation, which can have significant implications for improving the performance and efficiency of various aerodynamic applications. This paper aims to elucidate and emphasize the positive and negative aspects of existing research, while also suggesting new interesting areas for future investigation.

KEYWORDS

flow control, unsteady actuation, excitation frequency, momentum coefficient, blowing ratio, aerodynamic performance, airfoil, periodic excitation

1 Introduction

1.1 Flow separation phenomenon

In general, flow separation refers to the detachment of fluid flow from a solid surface, commonly referred to as a wall. The velocity of viscous fluid particles in the boundary layer adjacent to the wall decreases due to friction and shear stress exerted by the wall. On the other hand, when a viscous fluid flow encounters an adverse pressure gradient, it tends to separate. Thus, if the flow velocity undergoes a significant deceleration due to the presence of an adverse pressure gradient, the momentum of the fluid particles is concurrently reduced by both the wall shear stress and the adverse pressure gradient. From an energy

perspective, the kinetic energy gained from converting potential energy in the favorable pressure gradient region is diminished by the effects of viscosity in the boundary layer. In the region with an adverse pressure gradient, the remaining kinetic energy is converted into potential energy. However, this energy is insufficient to overcome the pressure forces, causing the movement of fluid particles near the wall to eventually cease. At this point, the viscous layer separates from the surface at a specific point (or line), and the streamlines closest to the surface separate from the wall, creating a rotational flow region near the surface. In this case, it is said that the boundary layer is separated. During the occurrence of flow separation, there is a sudden thickening of the rotational flow region close to the wall, and the normal velocity component increases to the extent that the approximations used for the boundary layer are no longer valid.

The phenomenon of flow separation is of great importance in the operation of a wide range of technological systems, including air, land, and sea vehicles, turbomachines, diffusers, and other important systems involved with fluid flow. Flow separation on the lifting surface typically occurs just prior to or at the point of maximum loading, with a significant impact on the optimal performance of the device (Gad-el-Hak, 2006). To provide further clarification, during the take-off phase of an aircraft, when the aircraft is still at low speeds, it is necessary to maximize lift by increasing the angle of attack of the wing. Elevating the angle of attack enhances the production of lift, enabling the aircraft to achieve liftoff at lower airspeeds and maximum loading. However, it is essential to exercise caution, as exceeding a certain angle of attack threshold can trigger a stall. A stall occurs when the angle of attack exceeds a critical threshold, resulting in airflow separation and the disruption of lift generation, which may result in a loss of altitude or the loss of aircraft control.

In general, the flow topology, which includes the occurrence of flow separation around an aerodynamic body or any other surface, is determined by boundary conditions such as surface geometry, Reynolds number, and Mach number. Therefore, when designing such devices, engineers optimize the effective parameters to avoid flow separation or postpone it as much as possible to increase system efficiency. For instance, delaying flow separation can reduce the pressure drag of a bluff body, increase the circulation and lift of a wing at a high angle of attack, and improve the pressure recovery of the diffuser (Gad-el-Hak, 2006). Due to significant energy losses caused by the separation of the boundary layer, the performance of numerous practical devices can be constrained by the location where separation occurs. Consequently, the utilization of flow separation control technology represents an efficient solution in many fluid dynamics applications, whereby the consumption of energy is reduced and the performance of the system is enhanced.

The field of aviation offers considerable potential for the application of flow separation control methods. Pioneering researchers in the field of aviation have investigated and employed a variety of boundary layer control methods with the objective of enhancing lift. Airfoils with conventional profiles experience significant aerodynamic performance degradation at low Reynolds numbers when $Re < 1 \times 10^6$, due to laminar boundary layer separation near the leading edge (Lissaman, 1983). Compared to high Reynolds number flows, airfoils with low Reynolds numbers experience flow separation at a lower angle of attack, even at zero angle of attack (Yarusevych et al., 2009). Downstream of the separation point, two states may occur. In the first case, the shear layer of the separated flow can reattach to the airfoil surface downstream of the separation point, creating a closed recirculation region in the time-averaged sense. This region is known as laminar separation bubble (LSB). In the second case, the flow may remain separated, which is known as stall. For flows with high Reynolds numbers, stall conditions occur after the turbulent flow separates. Compared to the airflow that remains attached to the airfoil surface along the chord, both of these phenomena typically result in a decrease in lift and an increase in drag on the airfoil. These adverse effects are more pronounced during stall and post-stall conditions, leading to high energy consumption in the aviation industry. In this regard, extensive research has been conducted on implementing boundary layer control strategies to promote flow reattachment on the airfoil surface and mitigate the unfavorable effects caused by post-stall conditions. These studies investigated the fundamental concepts underlying flow separation control and introduced various methods of momentum transfer using active and passive actuators, along with the factors influencing these methods.

The objective of this article is to present a comprehensive review of the studies and research conducted on flow separation control on lifting surfaces, with a particular focus on airfoils. Furthermore, two critical parameters that have a significant impact on flow separation control will be analyzed in detail. The main emphasis of this paper is to investigate the impact of momentum coefficient and excitation frequency as actuation parameters on flow separation control using unsteady excitation. In this study, the effective excitation frequency and the effective momentum coefficient are reported based on the objective of enhancing lift, reducing drag, or a combination of both in the pertinent research. Firstly, a concise overview of the different active separation control methods, namely, steady and unsteady, along with their respective advantages and disadvantages, is presented. Subsequently, this article reviews experimental and numerical simulation findings from recent years that highlight and emphasize the influence of the momentum coefficient and excitation frequency on active separation control. Finally, the latest developments in this field and potential applications are discussed, along with the challenges that arise from a control system perspective. Furthermore, suggestions for future research and development are provided.

1.2 Flow control

Numerous definitions have been proposed for flow control, exhibiting apparent differences, yet ultimately sharing the same concept. Fiedler and Fernholz (Fiedler and Fernholz, 1990) presented a comprehensive definition, stating that flow control is a process or operation through which certain flow properties are controlled and directed in a desired manner, based on user requirements. Among the various types of shear flow control methods available, flow separation control, historically referred to as boundary layer control, stands out as the oldest and most economically significant. Flatt's definition (Flatt, 1961) of controlling wall-bounded flows encompasses any mechanism or process that alters the behavior of the boundary layer from its

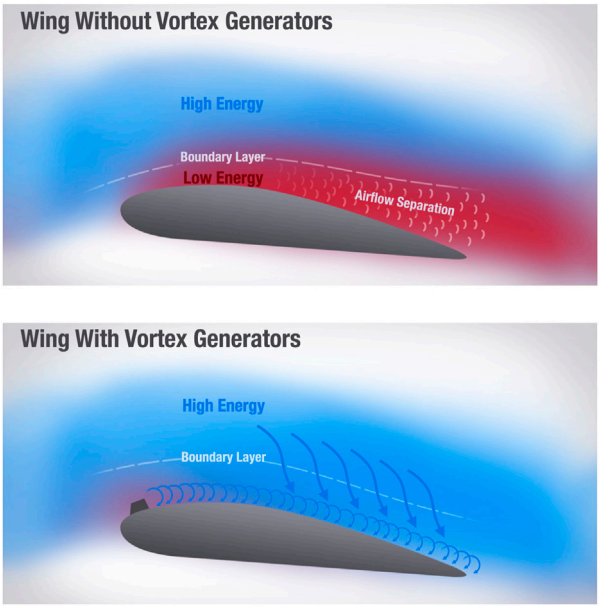

FIGURE 1
Flow separation control using a vortex generator on an airfoil (Udris, 2024).

natural state. Prandtl's introduction of boundary layer theory, accompanied by a description of several experiments involving boundary layer control, positions Prandtl as a pioneer in the field of flow control. Indeed, the earliest recognition of the potential to modify flow by influencing the boundary layer can be attributed to Prandtl's early work (Gad-el-Hak, 2006). Since then, flow control technology has been systematically researched and studied, leading to a deeper understanding of the determining parameters for the effectiveness and efficiency of flow control.

The ability to manipulate the flow pattern of the boundary layer in a desired manner holds significant practical importance across various industries. In general, methods of boundary layer control aim to either delay or accelerate the transition of the boundary layer. These actions, respectively, inhibit or enhance the generation of turbulence within the flow. This process effectively promotes or prevents flow separation, resulting in notable outcomes and achievements. Notable achievements in boundary layer flow control include the reduction of drag, augmentation of lift, enhancement of heat transfer in fluids, improved mixing, noise reduction, and the mitigation of flow-induced disturbances.

Flow control technologies can be categorized into passive and active methods. Passive control methods involve manipulating the flow without introducing external energy, relying solely on the redistribution of energy and momentum to achieve the desired flow characteristic. These methods typically impose minimal additional weight on the main system. Examples of industrially used passive flow separation control methods include vortex generators on Boeing aircraft wings, blown flaps on older generation supersonic fighters, leading edge extensions, and the implementation of strakes on newer generation airplanes. However, one drawback of passive methods is their reduced efficiency when flow conditions change, such as increasing Reynolds number or altering the angle of attack on wings and blades, which can even negatively impact overall system efficiency. On the other hand, active control methods involve the addition of energy through a control actuator. This approach utilizes an external energy source to introduce high-momentum fluid into the flow or extract low-momentum fluid from it. In essence, the active flow control method entails the exchange of energy, mass, or other auxiliary forces between the environment and the fluid. Compared to passive control, active control offers greater efficiency in flow control as it can be deactivated when not needed. Nevertheless, the implementation of active control necessitates additional weight and energy consumption.

In both active and passive control methods, various physical mechanisms are employed to achieve the desired effect, depending on the type of control. In the context of separation control, the primary challenge is to add momentum to the region close to the wall, given the applied pressure field. This is accomplished by transferring momentum from regions of the flow that are distant from the wall, where momentum is still abundant, to regions near the wall with lower momentum. Alternatively, momentum and power can be directly injected from the propulsion system. The most well-known technique for controlling flow separation is to add momentum in the near-wall region in a manner that is either active, such as tangential blowing or wall jets, or passive, such as vortex generators at different scales, as illustrated in Figure 1.

Active flow control methods can be categorized based on whether there is a net mass flux accompanied by an input of energy and momentum, as well as whether this addition occurs in a steady or unsteady manner. In the field of aviation, pioneering researchers have identified steady suction and blowing as the most commonly employed boundary layer control methods. In the case of boundary layer suction, the removal of low-momentum fluid creates a sink on the aerodynamic surface, which accelerates the flow towards the suction location and promotes a more stable boundary layer (Schlichting and Gersten, 2016). Here, both the effect of removing the low-momentum fluid and accelerating the flow are desirable in delaying the separation. In a flight test conducted by Hunter and Johnson (Hunter and Johnson, 1954), leading edge suction was utilized to eliminate flow separation occurring on a thin airfoil. Raspet (Raspet, 1951; Raspet, 1952), conducted experiments through distributed suction to control the transition of the laminar boundary layer and separation of the turbulent boundary layer. Remarkably, he was able to maintain the laminar boundary layer for over 95% of the wing chord of a TG-3A glider. Furthermore, Cornish (Cornish, 1953) employed distributed suction on the wing of a TG-3A glider and successfully increased the maximum lift coefficient from 1.38 to 2.28. In the subsequent step, this approach was employed on the L-21 motor plane, resulting in a notable enhancement of the maximum lift coefficient to 3.98 (Raspet et al., 1956).

In the case of steady blowing, an air jet, which is typically oriented tangentially or at an angle to the local curvature of the surface, injects high-momentum fluid directly into the boundary layer. This jet injects high-momentum fluid directly into the boundary layer, thereby augmenting the mixing rate of the fluid near and away from the wall and re-energizing the boundary layer (Jones et al., 2006). The combination of tangential steady blowing with the implementation of a Coanda surface, as exemplified by the

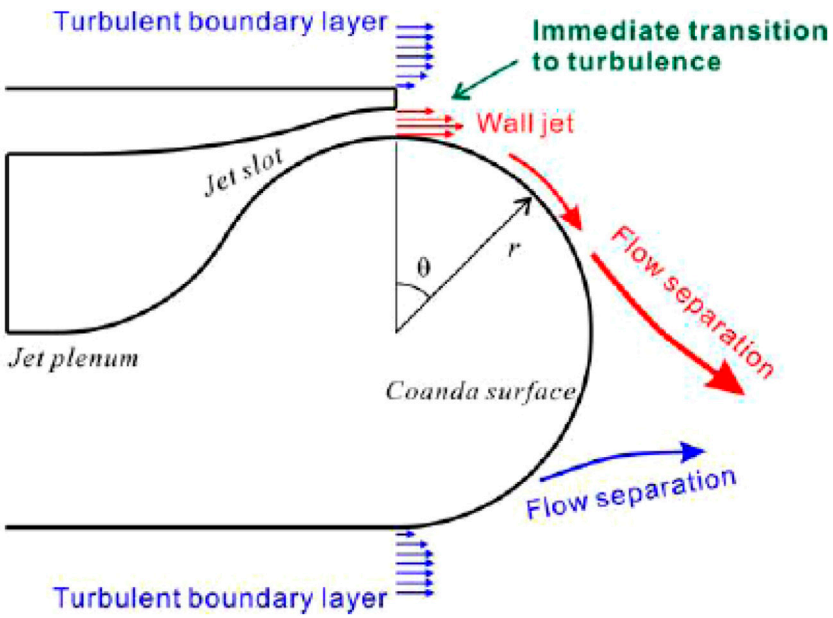

FIGURE 2
The concept of circulation control and Coanda effect influence on the airfoil's trailing edge and streamlines (Nishino et al., 2010).

design of a circular trailing edge of an airfoil in Figure 2, results in an increase in both the virtual chord length and the chamber of the airfoil. Consequently, this configuration yields a substantial boost in lift (Kweder et al., 2010; Kweder et al., 2014; Du et al., 2022).

In the 1920s, concepts of boundary layer control were investigated by aeronautical engineers for lift enhancement. Baumann (Betz and Lachmann, 1961) obtained a patent for utilizing air jets emanating from wing slots for flow separation control and lift augmentation. The first documented instance of employing a steady air jet to enhance the lift in the United States was reported by Knight and Bamber in 1929 (Knight and Bamber, 1929). Their investigation focused on the impact of air jet slot geometry, slot location and jet flow rate on lift enhancement. The experimental findings revealed a remarkable 151% increase in aerodynamic efficiency, as measured by the lift-to-drag ratio, for a two-dimensional airfoil. A concise overview of the development of boundary layer control through steady suction and blowing techniques can be found in reference (Joslin and Miller, 2009).

Currently, due to the high power and momentum requirements in the steady flow control method, the boundary layer control by the unsteady technique has been widely considered. This approach involves the application of suction and blowing, or solely blowing, in an oscillating or pulsed condition. The technique of unsteady excitation flow control exploits the phenomenon of natural flow instability, which has the potential to reduce mass flux and enhance efficiency. In contrast to steady blowing, where the momentum content and the entrainment rate of the air jets are the primary factors influencing flow control effectiveness, unsteady excitation, typically pulsed blowing, generates vortical structures that play a pivotal role. These vortices augment the mixing rate throughout the flow field, facilitating the transfer of momentum from regions of high-momentum fluid to low-momentum fluid. Research conducted by the NASA Langley comparing steady and unsteady excitation reveals that the unsteady excitation is two orders of magnitude more efficient than the steady excitation in achieving equivalent aerodynamic benefits (Sellers et al., 2002). Over several years, researchers have demonstrated that the application of local unsteady excitation on the aerodynamic surface can lead to flow reattachment and enhance aerodynamic performance (Seifert et al., 1996; Greenblatt and Wygnanski, 2000). These studies experimentally verify the effectiveness of periodic excitation on an airfoil in delaying boundary layer separation. Furthermore, studies have demonstrated that the periodic application of suction and blowing of air through a narrow slot, extending along the wing span, can effectively enhance the mixing of the shear layer and facilitate the momentum transfer between wall-near and wall-distant fluid. By employing this approach, it effectively mitigates or postpones the occurrence of boundary layer separation. Consequently, this method increases overall lift by shifting the separation point downstream and towards the trailing edge of the airfoil.

Seifert et al. (2004) stated in their research that the unsteady active control of flow separation relies on exploiting the flow's inherent instabilities that require a relatively small amplitude of excitation. Disturbances should strategically be amplified in regions prone to separation. Effective excitation frequencies consistently generate several vortices within the controlled region, irrespective of the Reynolds number. Unsteady excitation expedites and regulates the formation of large coherent structures, thereby facilitating the transfer of high-momentum fluid toward the surface. Despite the inherent unsteadiness of this process, it exhibits a stabilizing and regulating effect on flows susceptible to separation. Seifert et al. (2004) additionally emphasized that periodic excitation outperforms steady excitation in terms of performance benefits, eliminating unexpected flow responses that are undesirable from a control point of view. Moreover, it effectively mitigates separation-related

effects such as vortex shedding and buffeting, either significantly reducing their impact or eliminating them altogether.

Seifert et al. (1996) conducted experiments demonstrating that oscillatory blowing, as opposed to steady blowing, has a more pronounced impact on controlling separation and enhancing the maximum lift coefficient of a NACA 0015 airfoil. Furthermore, their research findings indicated that introducing the jet upstream of the separation point yields a more effective separation control. Similar observations were made by Greenblatt and Wignansky (Greenblatt and Wygnanski, 2000). Bernardini et al. (2014) demonstrated that the performance of an airfoil can be enhanced by employing wall-normal pulsed jets, by amplifying the inherent instabilities of the flow. In fact, in this technique, the inherent instability is exploited to achieve the desired results. They elucidated that these pulsed jets introduce disturbances to the flow corresponding to higher-order harmonics of the excitation frequency. Consequently, specific harmonics, amplified by the natural Kelvin-Helmholtz instability, facilitate the momentum absorption and transfer, and reattachment of the flow. Numerous experimental investigations have consistently shown that unsteady excitation methods are more efficient and effective in utilizing energy from the actuators. Consequently, unsteady excitation methods are often preferred in various experiments, despite requiring a more complex drive system compared to their steady counterparts. This is due to the necessity of incorporating a mechanism capable of generating unsteady flow, which is a requisite for many experiments.

As previously stated, one of the principal advantages of active flow control, in comparison to passive methods, is its adaptability and flexibility to adjust based on varying flow conditions. This adaptability is facilitated by sensor systems that are capable of providing real-time information from either the flow field or the surface flow. The utilization of a closed-loop flow control system enables users to implement specific corrections in order to achieve the desired fluid flow through control actuators. Consequently, active flow control necessitates the implementation of an actuation system capable of delivering energy, momentum, or mass flow in the desired form and quantity. Moreover, the integration of these actuators with the main system should be feasible while meeting size and weight requirements. When considering active flow control for commercial applications, it is crucial to design actuators that possess suitable power, energy conversion efficiency, cost-effectiveness, maintainability, and reliability. Furthermore, compliance with system requirements and limitations significantly influences the design of active flow control. Therefore, the design of an active flow control system always involves parameters that directly impact the effectiveness of the control effort.

2 Effective parameters in flow separation control on the surface

The most prevalent form of flow separation control mechanism employed on a surface is the utilization of fluidic actuators that employ steady and unsteady flow injection or suction. These actuators can be categorized based on their size, ranging from macro to micro jets. They can administer fluid injection continuously at a constant flow rate or periodically and pulsed to the surface. Therefore, various parameters are involved in the design of such control systems that impact their efficiency. These parameters encompass the geometric characteristics of the actuators, such as the shape and dimensions of the jet outlet slot, the location and orientation of the jet injection relative to the target surface, as well as the physical attributes of the actuators, including the actuation amplitude or momentum coefficient, jet velocity, and actuation frequency. Furthermore, flow conditions introduce a distinct set of parameters to the system design, typically encompassing similarity parameters, Mach number, and Reynolds number. The objective of this research is to investigate two key parameters in the design of fluidic actuators: the momentum coefficient or actuation amplitude, and the actuation frequency. These parameters have a significant impact on the effectiveness of the control effort. The study will provide a comprehensive review of the existing research conducted on these two parameters.

2.1 Actuation amplitude or momentum coefficient C_μ

In the context of flow control research, the actuation amplitude represents a valuable metric for the evaluation of the efficacy of suction and blowing flow control techniques. This amplitude directly contributes to enhancing the system's efficiency. The actuation amplitude is generally presented in normalized form. It is quantified by the momentum coefficient C_μ, as depicted in Equation 1 in its general form.

$$\mathbf{C_\mu} = \frac{\mathbf{J}}{\mathbf{q_\infty} \cdot \mathbf{A_{ref}}} \tag{1}$$

Based on this equation, the momentum coefficient C_μ can be defined as the ratio between the momentum flux generated by the flow control system J and the momentum flux of the oncoming flow, represented by the product of the freestream dynamic pressure q_∞ and a reference area A_{ref}. The precise formulation of the momentum coefficient is established by Poisson-Quinton (Joslin and Miller, 2009) in Equation 2.

$$\mathbf{C_\mu} = \frac{\mathbf{q_m} \cdot \mathbf{V_j}}{\mathbf{q_\infty} \cdot \mathbf{A_{ref}}} \tag{2}$$

In the given equation, the variables q_m and V_j represent the mass flow rate and jet velocity, respectively. These variables are normalized by the dynamic pressure q_∞ and the reference area A_{ref}, respectively. The following paragraphs outline the methodology employed to determine the actuation amplitude of some unsteady flow control actuators.

Synthetic jet actuators primarily depend on two operating conditions to determine their actuation amplitude: the actuation frequency and the stroke length of the synthetic jet driver. The strain of the piezoelectric diaphragm, and consequently the driver's stroke length, is adjusted by applying a voltage potential across the piezoelectric material. Once the actuation frequency is selected, the amplitude is solely determined by the voltage input to the piezoelectric material. In optimal systems, the fluidic amplitude correlates with the input voltage, although calibration is necessary to accurately assess the performance of each actuator. This calibration typically involves measuring the phase-averaged jet velocity at the

centerline of the synthetic jet orifice using a hotwire anemometer. To comprehensively quantify the fluidic amplitude of a synthetic jet actuator, it is crucial to fully map the exit velocity profile (Smith and Gregory, 2001; Holman et al., 2005). However, for calibration purposes, assuming a plug-flow exit profile with an amplitude equivalent to the measured centerline velocity is acceptable (Shuster and Douglas, 2007). By analyzing this data, two critical benchmarks of actuator effectiveness can be determined for a specific flow control application: the blowing coefficient C_b and the momentum coefficient C_μ. The blowing ratio C_b represents a valuable metric for scaling the amplitude of a synthetic jet in accordance with the prevailing freestream conditions. This ratio is defined by Equation 3, in which V_j represents the average jet exit velocity over the blowing portion of the synthetic jet cycle, as calculated by Equation 4.

$$C_b = \frac{V_j}{V_\infty} \tag{3}$$

$$V_j = \frac{1}{T}\int_0^{\frac{T}{2}} v_j(t)dt \tag{4}$$

Where $v_j(t)$ is the jet exit velocity as a function of time and T is period. While the blowing coefficient is a significant measurement, it is not enough to fully evaluate the effectiveness of a synthetic jet actuator by itself. A metric that takes into account the orifice cross-sectional area is also needed to truly compare the efficiency of similar actuators. Therefore, it can be argued that the local momentum measurement added to the system is more appropriate. As a result, the time-averaged momentum coefficient C_μ is commonly used and is defined as Equation 5. The time-averaged momentum for synthetic jet actuator can be calculated as the integral of the momentum added during the expulsion phase of the synthetic jet cycle averaged over the entire period of the cycle. The numerator of the fraction in Equation 2 for synthetic jets is derived from the Equation 5:

$$\mathbf{q_m} \cdot \mathbf{V_j} = \frac{1}{T}\int_0^{\frac{T}{2}} \rho_j A_j v_j(t)^2 dt \tag{5}$$

In the context of employing solenoid valves as an actuator to produce pulsed jets, it is possible to adjust the amplitude or momentum coefficient C_μ of the pulsed jets by varying the pressure within the compressed air duct. The mass flow rate and jet velocity can be regulated by pressure regulators. Furthermore, the momentum coefficient can be determined from Equation 2 using anemometry, or calculated using a flow meter and jet's cross-section area.

The actuation amplitude of plasma actuators can be adjusted by the input voltage applied to the actuator (Taleghani et al., 2012). The output actuation amplitude of the plasma actuator can typically be determined by measuring the velocity of the produced microjet or by measuring the momentum of the jet (Taleghani et al., 2018). Experimental results indicate that the dominant frequency of the flow vortices generated by the plasma actuators precisely corresponds to the excitation frequency of the input electric wave (Taleghani et al., 2018). In addition to voltage amplitude, other geometric and electrical parameters play a significant role in determining the amplitude of plasma actuator output excitation (Taleghani et al., 2012; Taleghani et al., 2018; Mohammadi and Taleghani, 2014; Salmasi et al., 2013; Mirzaei et al., 2012). After measuring the velocity profile of the generated microjet in a quiescent environment, the numerator of the fraction in Equation 2 is determined by Equation 6. In Equation 6, A_j represents the cross-section area of the microjet.

$$\mathbf{q_m} \cdot \mathbf{V_j} = \int \rho_j V_j^2 dA_j \tag{6}$$

The amplitude of acoustic excitation in flow control methods refers to the magnitude or strength of the acoustic signals generated by the actuator to influence the fluid flow. This amplitude can be measured in various ways, including through sound pressure level (in decibels, dB), microphone recordings, or vibration measurements. The amplitude of acoustic excitation plays a crucial role in determining the effectiveness of flow control methods, as it directly impacts the intensity of the acoustic forces exerted on the fluid flow.

It is important to note that while the momentum coefficient is commonly used to quantify the actuation amplitude, it is not an appropriate parameter for comparing the benefits of flow control across different parameter settings and configurations (Stal nov and Seifert, 2010). The momentum coefficient C_μ is calculated by multiplying the mass flow rate and the velocity of mass propagation, which leads to the formation of the jet momentum flux J, as indicated in the numerator of Equation 1. This definition of C_μ reveals that numerous combinations of mass flow rate and jet velocity can yield the same value for the momentum coefficient. To address this crucial distinction between the two quantities, the parameter of jet velocity ratio VR or blowing ratio (as previously mentioned), is employed. This is defined in Equation 7.

$$\mathbf{VR} = \frac{\mathbf{V_{jet}}}{\mathbf{V_{ref}}} \tag{7}$$

The jet velocity ratio VR, represents the ratio of the velocity of the air jet exiting the actuator V_{jet} to the reference velocity V_{ref}. The reference velocity can be the local V_x, the impingement velocity, or the freestream flow velocity V_∞ of the controlled flow. Consequently, the magnitude of the air jet velocities emitted from the active flow control system is expressed through the velocity ratio or blowing ratio.

Experimental results obtained from flow control on a two-dimensional airfoil with a plain flap indicate that, when exciting the flow with the same momentum coefficient, employing a higher jet velocity ratio yields superior outcomes compared to conditions where the mass flow rate is higher and the jet velocity ratio is lower (Thomas, 1962). In the context of flow injection, it can be demonstrated that a positive effect on the flow can be achieved by ensuring that the velocity ratio of the actuation exceeds unity. (Greenblatt and Wygnanski, 2000). Otherwise, the momentum content of the boundary layer may be decreased, leading to an increased likelihood of flow separation. This detrimental effect adversely impacts aerodynamic performance (Bauer et al., 2010; Mueller-Vahl et al., 2013).

The blowing ratio has been commonly employed in studies investigating two-dimensional flow control as a means to measure the actuation amplitude, instead of the momentum coefficient. In general, for both objectives of flow control, namely, delaying flow separation or reattachment of separated flow, it has been observed

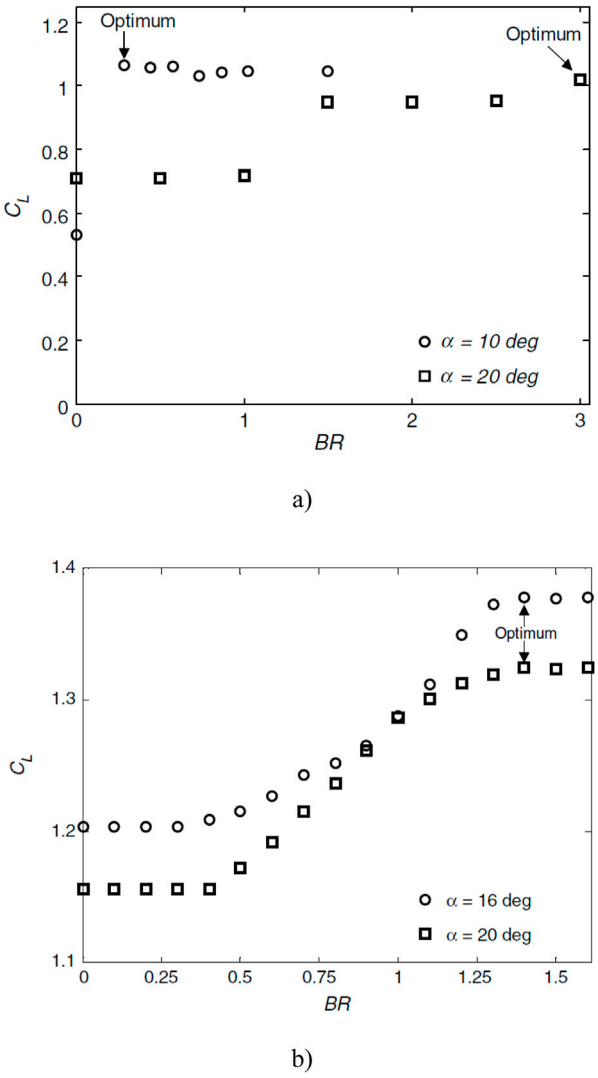

FIGURE 3
Variation of Lift coefficient with different blowing ratio **(A)** at angle of attack of 10° and 20° and Re = 6.4 × 10^4 **(B)** at angle of attack of 16° and 20° and Re = 4×10^6 (Packard et al., 2013).

that increasing the actuation amplitude or blowing ratio beyond a certain threshold limit (i.e., introducing additional input momentum) has a diminishing effect on the attached flow. This phenomenon is well-documented through the saturation of the increase in lift coefficient, as demonstrated by Packard et al. (2013) for the steady normal blowing actuation on a NACA 643-618 airfoil at two different Reynolds numbers as depicted in Figure 3. Furthermore, Packard et al. research (Packard et al., 2013) has demonstrated that the optimal blowing ratio varies in flows with different Reynolds numbers. By comparing Figures 3A,B, it is evident that at an angle of attack α = 20°, a blowing ratio BR of approximately 1 has negligible impact on the lift coefficient in the low Reynolds number flow (6.4 × 10^4), thus failing to improve the aerodynamic characteristics. Conversely, in the high Reynolds number flow (4 × 10^6), the blowing ratio BR ≈ 1 enhances the lift coefficient and approaches its peak performance. Consequently, it can be inferred that maintaining a constant blowing ratio for different Reynolds numbers is not ideal. The physics of flow around lifting surfaces undergoes significant changes with variations in the Reynolds number. As a result, the optimal values of flow control parameters, such as the blowing ratio, will also vary in accordance with these alterations in freestream flow characteristics.

In various studies, the momentum coefficient C_μ has been identified as a crucial parameter in determining the effectiveness of active flow control. It has been observed that increasing the momentum coefficient leads to enhanced control benefits. According to the research conducted by Jones and Englar (2003) on high-lift systems, actuation with a low momentum coefficient typically indicates separation control (boundary layer control), while actuation with a high momentum coefficient suggests circulation control. Their study focused on the development and testing of two-dimensional airfoil design for potential general aviation use. This model was based on 17% supercritical-type section with a circular trailing edge as a Coanda surface. They utilized dual-slot blowing on a Coanda surface for high-lift operations in both the steady state and the pulsed modes. Testing was conducted at Reynolds number of approximately 5 × 10^5 in the wind tunnel, focusing on high lift, cruise, and mass flow optimization modes. In Jones and Englar (2003) study, the lift performance characteristics of the model in high-lift mode demonstrate the difference between separation control (boundary layer control) and super-circulation, as illustrated in Figure 4. When the jet blows with low momentum coefficients, it entrains the outer flow, causing the boundary layer to attach to the Coanda surface and turn the local streamlines (see Figure 5A). As the blowing level increases, the separation point moves around the Coanda surface towards the maximum x/C of the airfoil (i.e., x/C = 1) as shown in Figure 5B. This results in the higher momentum jet entraining with the oncoming low momentum flow from the under-surface flow field. The jet penetration creates a virtual or pneumatic flap that turns the streamlines. Increasing the blowing results in more jet penetration and entrainment, leading to greater streamline turning beyond the maximum x/C, Figure 5C. The magnitude of the jet momentum governs the penetration into the trailing edge flow field once the separation is fixed. As momentum increases, the penetration depth (length) also increases, leading to increased streamline turning and circulation. This increased circulation causes the leading edge stagnation point to move aft along the lower surface, resulting in an increase in the leading edge suction pressure and lift enhancement.

From a phenomenological perspective, the threshold momentum coefficient that distinguishes these two regimes, separation control (boundary layer control) and super-circulation, is the momentum coefficient that just suffices to suppress flow separation completely. Experimental findings indicate that the threshold momentum coefficient falls within the range of 3% < C_μ < 5% (Greenblatt and Wygnanski, 2000). As depicted in Figure 4, the transition between these two regimes is gradual and is accompanied by a decrease in actuation efficiency, as indicated by the dC_L/dC_μ ratio.

The experimental results demonstrate that optimal flow control benefits, in terms of drag reduction and lift enhancement, are achieved when a specific momentum coefficient is attained. Across various systems, there exists a saturation point where the control benefits reach a plateau, and further changes in aerodynamic coefficients are not observed. This

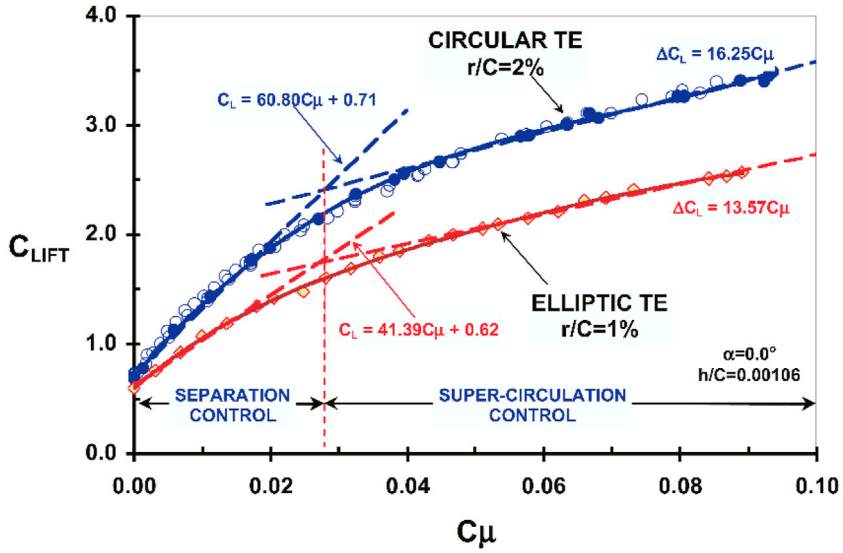

FIGURE 4
Effect of momentum coefficient on lift coefficient and transition from separation control (boundary layer control) to circulation control (Jones and Englar, 2003).

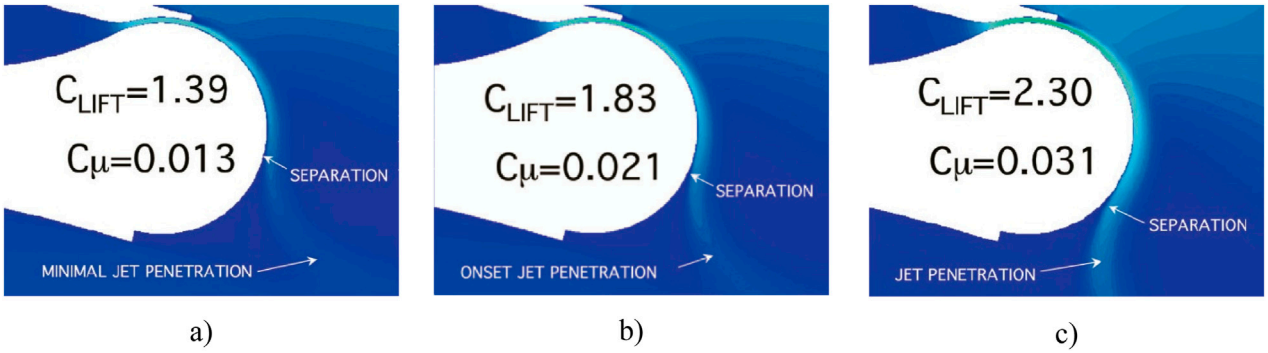

FIGURE 5
CFD simulation of the jet penetration around a Coanda surface for different momentum coefficientsCμ =, **(A)** 0.013, **(B)** 0.021, **(C)** 0.031 (Jones and Englar, 2003).

saturation occurs when the momentum coefficient surpasses a threshold value. The threshold value represents the required momentum coefficient to establish a fully attached flow on the surface. The specific threshold value of the momentum coefficient is influenced by other actuation parameters, such as the actuation frequency F^+ and the actuator's location (Feero et al., 2017). In the case of a low-Reynolds airfoil with actuator operating within a moderate range of momentum coefficient, prior to the onset of saturation, the lift coefficient increases while the drag coefficient decreases. This beneficial effect is attributed to the formation of a laminar separation bubble on the suction wing's surface, as evidenced by the pressure distribution on the airfoil's suction surface. However, once the momentum coefficient reaches a threshold value, the flow becomes fully attached to the surface. Beyond this point, further increases in the momentum coefficient do not yield improvements in the airfoil's lift and drag coefficients.

The saturation of the drag coefficient has also been observed in experiments conducted by Feero et al. (2015), as illustrated in Figure 6. These experiments involved unsteady excitation using a synthetic jet on a NACA 0025 airfoil at a Reynolds number of 1×10^5 and an angle of attack of 10°. Figure 6 shows the impact of increasing the momentum coefficient C_μ on the flow pattern around the airfoil under the influence of excitation with dimensionless frequency of 58. As illustrated in Figure 6B, the boundary layer remains separated from the surface when $C_\mu < 0.34\%$. Consequently, the drag coefficient experiences minimal changes. However, when the momentum coefficient is increased to $C_\mu = 0.34\%$ as depicted in Figure 6C, the boundary layer becomes attached to the surface, resulting in a narrow wake. This configuration leads to a significant reduction of approximately 45% in the drag coefficient. Conversely, a marginal reduction in the drag coefficient is observed when the momentum coefficient is further increased to $C_\mu = 3.72\%$. This small

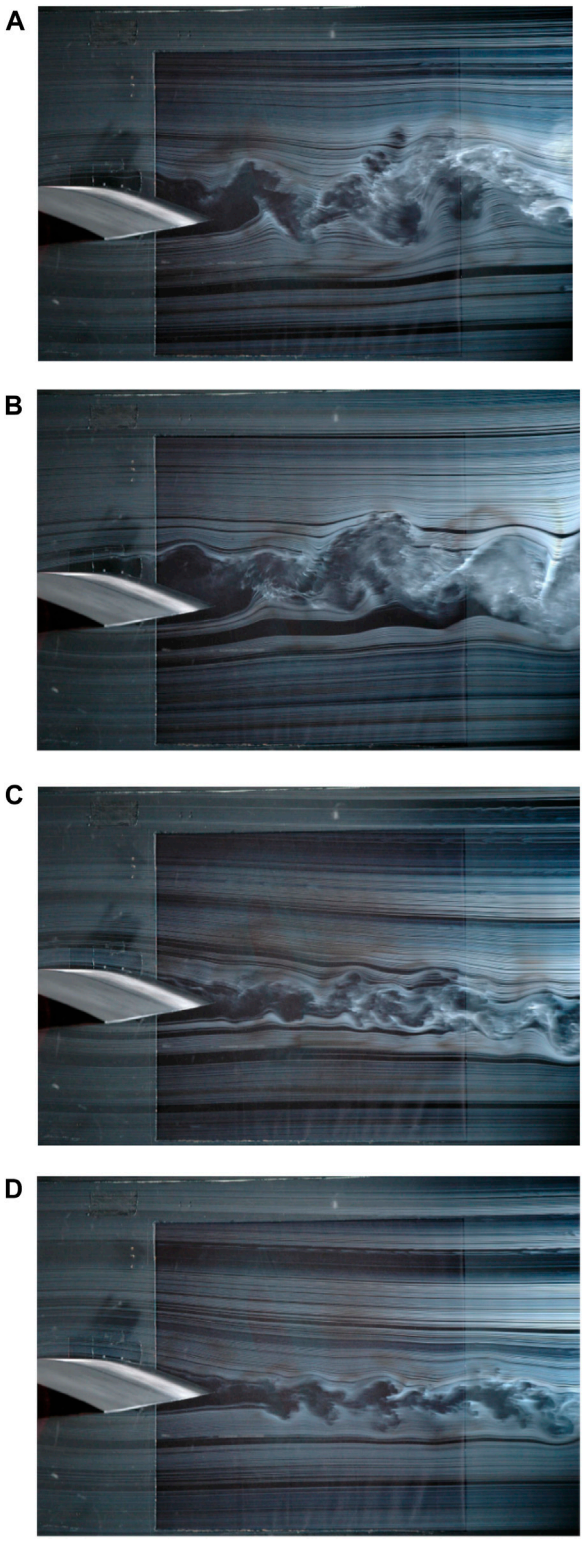

FIGURE 6
Flow visualization in near wake of the airfoil and investigating the effect of different momentum coefficients on the changes in the flow structure under the influence of unsteady excitation, **(A)** basic model $C_\mu = 0$, **(B)** $C_\mu = 0.12\%$, **(C)** $C_\mu = 0.34\%$, **(D)** $C_\mu = 3.72\%$ (Feero et al., 2015).

change in the drag coefficient for higher values of C_μ can be attributed to the flow already being attached, with only reduced spatial scale structures as illustrated in Figure 6D. These findings highlight that the effectiveness of control actuation in reducing airfoil drag basically relies on surpassing the threshold value of C_μ.

Munday and Taira (2018) utilized the modified momentum coefficient parameter as a metric to assess the effectiveness of flow control. Their study focused on numerically investigating the impact of momentum injection on mitigating flow separation on a NACA 0012 airfoil operating at an angle of attack of 9° and Reynolds number of $Re = 2.3 \times 10^4$. Under these conditions, the airfoil experienced a significant separation, resulting in the detachment of the shear layer from the leading edge and the formation of large spanwise vortices. The breakdown of these vortices resulted in the generation of turbulent flow downstream. In this study, momentum is incorporated into the separated flow in two distinct forms through the use of swirling jets: wall-normal momentum and angular momentum. The investigation and analysis have focused on assessing the effects of different combinations of actuator inputs on the flow field and surface vorticity fluxes. The experiments revealed that the injection of wall-normal momentum resulted in a reduction in flow separation. Furthermore, the addition of angular momentum injection, in conjunction with wall-normal momentum injection, led to an enhanced reduction in flow separation. Accordingly, the modified momentum coefficient, as defined in Equation 8, was employed in this article. In this context, the correction function S, as described in Equation 9, represents the ratio of the velocity in the angular momentum mode $u_{\theta,\max}$ to the velocity in the vertical mode $u_{n,\max}$, while k denotes a constant value.

$$C_\mu^* = (1 + S)^2 C_\mu \tag{8}$$

$$S = k\left(u_{\theta,\max}/u_{n,\max}\right) \tag{9}$$

In the investigation conducted by Munday and Taira (2018), the responses of the flowfield and the surface vorticity fluxes to a range of actuation input combinations were examined in detail in order to evaluate the value of the modified momentum coefficient S. An illustrative example of the research findings is presented in Figure 7. The results illustrate the effectiveness of combining wall-normal and angular momentum in controlling flow separation and eliminating it along the suction surface of the airfoil. Figure 7 depicts the lift and drag forces as a function of C_μ^*. Moreover, this figure presents time-averaged flow visualisations utilizing the time-averaged zero streamwise velocity $\bar{u}_x = 0$ isosurface, colored with spanwise Reynolds stress τ_{xy}. In Figure 7, three broad classifications of flow can be identified with different colors. These categories include separated flow for $C_\mu^* \leq 1.5\%$, transitional flow for $1.5\% < C_\mu^* \leq 2\%$, and reattached flow for $2\% < C_\mu^*$. For low values of $C_\mu^* \leq 1.5\%$, as shown by the blue region in Figure 7, the flow remains separated and the time-averaged recirculation region has approximately the same size as in the baseline case. The control injection modifies the shear layer around the leading edge, yet this is insufficient to achieve reattachment. Conversely, values of $C_\mu^* \leq 1.5\%$ result in a detrimental impact on the flow, leading to a decrease in lift in comparison to the baseline case (as indicated by

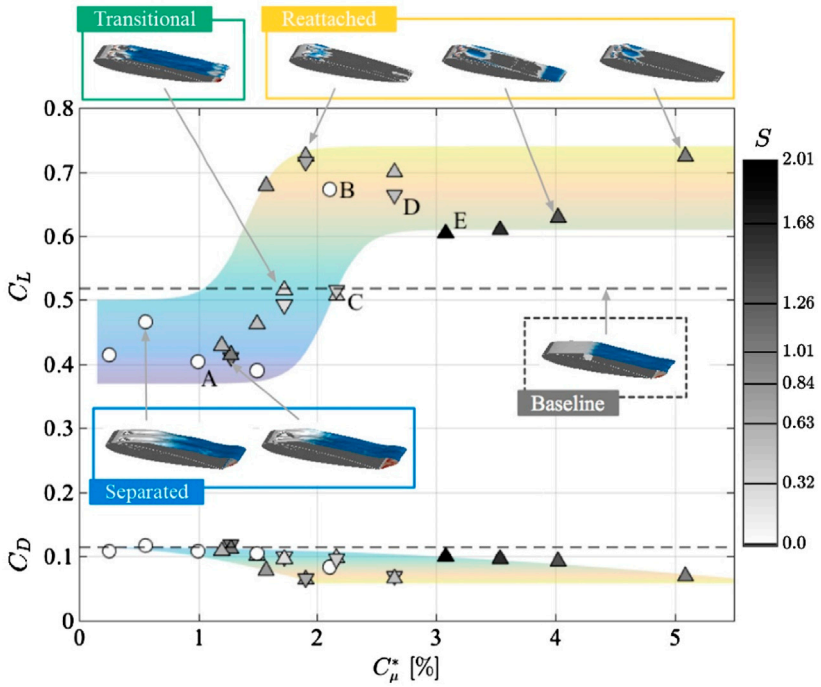

FIGURE 7
The effect of modified momentum coefficient on lift (top) and drag (bottom) coefficients. Values without flow control are indicated by dashed lines. Controlled cases include: injection of wall-normal momentum with pure blowing (○), injection of angular momentum with corotating (∇) and injection of angular momentum with counter-rotating (Δ) (Munday and Taira, 2018).

the dashed lines). The second region, indicated in green in Figure 7, depicts transitional flow cases for $1.5\% < C_\mu^* \leq 2\%$, wherein the lift and drag coefficients exhibit a notable increase and decrease, respectively. In this region, the control input modifies the separated flow, which remains separated behind the actuators. Variations in the modified momentum coefficient between $1.5\% < C_\mu^* \leq 2\%$ show different effects on the flow and lift. The variation of lift and drag in this region illustrates that the flow becomes sensitive to changes in the control input within transitional region. The third region, defined by the modified momentum coefficient of $2\% < C_\mu^*$, is represented by the yellow area in Figure 7. In this region, the controlled flow downstream of the actuators is reattached. This results in enhanced aerodynamic performance. Furthermore, the greatest enhancements in lift and reductions in drag are observed in this region, which is characterized by reattachment. However, it is important to note that excessively high values of S should be avoided; for cases where S > 1.5%, a significant increase in the lift coefficient is observed, but it is accompanied by unstable behavior due to dynamic stall.

2.2 Dimensionless frequency or reduced frequency F^+

One of the crucial design parameters for the control actuator in situations involving unsteady oscillatory or pulsed excitations is the excitation frequency. Numerous studies have represented the excitation frequency as the dimensionless frequency F^+, which is defined in a manner similar to the Strouhal number, as shown in Equation 10.

$$\mathbf{F^+ = St = \frac{f.l_{ref}}{u_{ref}}} \tag{10}$$

The dimensionless frequency serves to adjust the physical time scale of the excitation, whereby the excitation frequency f is made dimensionless by incorporating the characteristic velocity u_{ref} and length scale l_{ref}. Typically, the incidence velocity or freestream velocity is considered as the characteristic velocity u_{ref}. In the case of airfoils, the length scale l_{ref} is defined as the length of the airfoil chord. Some studies have determined the length scale l_{ref} for calculating F^+ based on the length of the separation region. In the context of an airfoil, when separation occurs at the leading edge, the length scale l_{ref} is equal in both cases, and selecting the chord length of the airfoil facilitates comparison with other experimental results.

To achieve optimal flow separation control, experiments have identified different dimensionless frequency bands F^+ as the most effective values, depending on the underlying physical mechanism of flow control. For improved performance of the control system, when the excitation amplitude reaches a threshold value, the actuator should operate at an appropriate excitation frequency. The unsteady actuator produces varying effects on the flow depending on the time scale and frequency of excitation.

A comprehensive analysis of airfoil flow control studies conducted by Greenblatt and Wygnanski (Greenblatt and Wygnanski, 2000; Wygnanski, 2000) reveals that, in the majority of cases, the optimal dimensionless frequency F^+ for controlling flow separation in poststall conditions falls within the range of $0.3 \leq F^+ \leq$

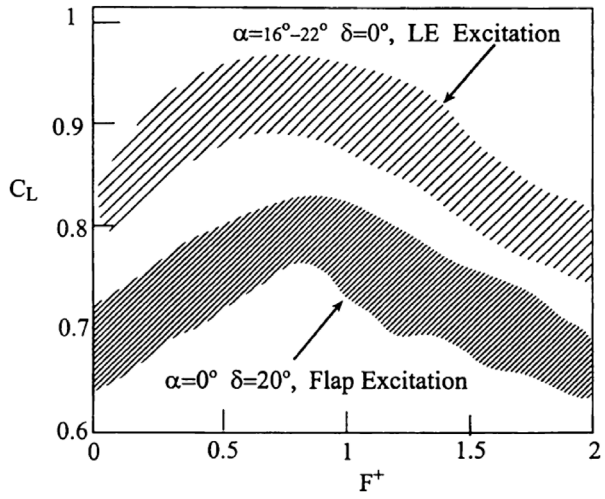

FIGURE 8
The lift response of a NACA 0015 airfoil to periodic excitation at either the leading edge or flap shoulder at different frequencies for C_μ = 0.08% and 1.5 × 10^5 ≤ Re ≤ 6 × 10^5 (Seifert et al., 1996).

4. Their findings also indicate that this range applies to excited shear layer and deflected flap. However, alternative research, particularly the work of Glezer et al. (Smith et al., 1998; Amitay et al., 2024), suggests that higher magnitude dimensionless frequencies, such as F^+ = 10 or 20, can also effectively control separated flow. The wide range of effective frequencies in flow separation control can be attributed to factors such as surface curvature, upstream conditions, boundary layer conditions, excitation methods, and the utilization of different momentum coefficient values ($C_\mu > C_{\mu,min}$) (Greenblatt and Wygnanski, 2003). Seifert et al. conducted experiments to examine the impact of dimensionless frequency F^+ on the increase in lift coefficient for a NACA 0015 flapped airfoil across a wide range of Reynolds numbers and two different excitation locations (Seifert et al., 1996). The results of their research are presented in Figure 8. One case depicted in the figure pertains to airfoil tests at angles of attack ranging from 16° to 22° in the poststall regime, conducted at the leading edge of the excitation. The second experiment involves testing the airfoil at a zero angle of attack and a deflection flap angle of 20°. In this case, the control actuation is carried out on the shoulder of the flap. The figure demonstrates that, for both experiments, the effective excitation frequency for this airfoil falls within the range of 0.5 ≤ F^+ ≤ 1. Another study (Seifert and Pack, 1999) also concluded that the effective excitation frequency for high Reynolds number flow lies within the range of 0.5 ≤ F^+ ≤ 1. Furthermore, the research conducted by Hecklau et al. (Hecklau et al., 2011; Hecklau et al., 2013) indicates that in scenarios where large-scale disturbances directly transport high-momentum fluid within the boundary layer in low Reynolds flow, the minimum excitation frequency required to prevent the onset of flow separation between each controlled pulse is approximately F^+ ≈ 0.5.

The effectiveness of separation control typically relies on the receptivity of the mean flow to the external excitation. In this technique, the characteristic timescale of flow physics and its instabilities play a significant role. Previous research has demonstrated that enhancing flow instabilities can be an effective approach to control separation (Wu et al., 1998). When dealing with a separated flow, the excitation frequency can be adjusted based on the frequency of natural instabilities in the shear layer. Consequently, disturbances introduced by the active flow control system within the medium range have undergone by maximum amplification until they reach the model's trailing edge, therefore providing the highest mixing rate. As a result, the mixing rate along the shear layer experiences a substantial increase, leading to the highest mixing ratio (Wygnanski, 2000). In this technique, a greater amount of momentum is transferred to the flow near the surface.

Several studies (Wu et al., 1998; Kotapati et al., 2010; Mccullough and Gault, 1951; Chang, 1976), provide a comprehensive analysis of the natural frequencies of flow on an airfoil, which play a crucial role in determining the excitation frequency. For flow over a thin airfoil at a certain Reynolds number, three natural frequencies can be observed depending on the angle of attack. At a low angle of attack, the flow over the airfoil remains attached to the surface despite an adverse pressure gradient. Consequently, the dominant phenomenon in the flow is wake instability, and the frequency of these instabilities can be referred to as the wake frequency f_{wake}. As the angle of attack increases, separation may occur near the leading edge due to the adverse pressure gradient. However, the separated shear layer may reattach before reaching the trailing edge. In such cases, three natural frequencies are present: the roll-up frequency of vortices in the shear layer f_{sl}, the frequency of fluctuations caused by unsteady flow in the separation bubble f_{sep}, and the frequency of fluctuations caused by unsteady flow in the wake f_{wake}. At high angles of attack, where separation is significant and post-stall flow dominates, the flow behaves similarly to passing through a bluff body. In post-stall conditions, two primary instabilities are observed: the roll-up of vortices in the separated shear layer f_{sl} and the release of large-scale vortices in the wake f_{wake} and the fluctuations caused by the unsteady flow (Wu et al., 1998). These instabilities typically correspond to dimensionless frequencies f_{sl}^+ ≈ 10 (Boutilier and Yarusevych, 2012a; Boutilier and Yarusevych, 2012b) and f_{wake}^+ ≈ 1 (Buchmann et al., 2013), respectively. Here, the dimensionless frequency is defined as $f^+ = fc/U_\infty$, where f is the frequency of instability in separated flow and c is the chord length.

The reported effective dimensionless frequency band is largely limited to F^+ = O (1) in cases where the control mechanism relies on the resonance of inherent perturbations in flow instabilities. For example, exciting the separated shear layer at frequencies close to F^+ = 1, taking advantage of the wake instability with a frequency of f_{wake}^+ ≈ 1 (representing the frequency of shedding of large-scale vortical structures into the wake) has proven to be effective. In the excitation mode with frequency F^+ = O (1), large vortical structures are formed, which are subsequently transferred downstream near the airfoil surface. This process induces unsteady reattachment and time-periodic variation in the flow circulation on the airfoil (Amitay and Glezer, 2002a; Amitay and Glezer, 2002b). The study conducted by Amitay and Glezer (2002b) examined the impact of separation control across a broad range of F^+. However, in this particular research, the frequency range of separated flow during stall conditions was not explicitly defined. Therefore, results have not been identified when the control mechanism targets flow instabilities.

Yarusevych and Kotsonis (2017) investigated the effect of controlling the separation bubble phenomenon on a NACA 0012 airfoil for flow with Reynolds number Re = 1.3 × 10^5, in actuation frequencies $2 \leq F^+ \leq 10$ and $F^+ = 100$. The results of this study demonstrated that the most significant reduction in the size of the separation bubble was achieved at the excitation frequency of $F^+ = 6$, which corresponds to enhanced fluctuations of the separated shear layer. Wu et al. (1998) conducted two-dimensional simulations on a NACA-0012 airfoil in turbulent flow under post-stall conditions, with a Reynolds number of 5 × 10^5 and angles of attack ranging from 18° to 35°. Wu et al. (1991) put forth the idea that the fundamental principle behind the post-stall lift enhancement due to unsteady controls involves a series of interconnected mechanisms: vortex layer instability, receptivity, resonance, and nonlinear streaming. The diverse response spectrum of the shear layer to disturbances leads to varying resonant states when exposed to different actuation frequencies. These different resonant states play a crucial role in determining the lift and drag characteristics of the object. Their findings revealed that the effective dimensionless frequency F^+ is in the range of 0.3–2.0 times the frequency of the wake (0.3–2.0 f_{wake}). Specifically, when the excitation frequency was set at one and two times the natural frequency of the wake (f/f_{wake} = 1.0, 2.0), the lift-to-drag ratio increased by 49.2% and 46.7%, respectively, at an angle of attack of 25°, where harmonic resonance of vortex shedding occurred. Notably, the maximum lift increase observed in these experiments was 73.2%, which was achieved in the subharmonic resonance at half the natural frequency of vortex shedding in the wake (f/f_{wake} = 0.5).

In a separate study (Duvigneau and Visonneau, 2006), researchers simulated the two-dimensional flow over a NACA-0015 airfoil at Re = 8.96 × 10^5 and angles of attack ranging from 12° to 24°. They proposed an optimization method to maximize the lift coefficient at various angles of attack by modifying the design parameters, including the excitation frequency, velocity ratio, pitch angle. Their research indicated that the optimal dimensionless frequency F^+ was approximately 0.8 for angles of attack between 14° and 20°, while a much smaller value of $F^+ = 0.25$ was obtained for an angle of attack of 22°. They concluded that the optimal average lift is achieved at $F^+ = 0.85$ across the entire range of angle of attack variations. A similar study was conducted by You and Moin (2008) using the LES method for an angle of attack of 16.6°. It was concluded that applying control excitation with a dimensionless frequency of $F^+ = 1.284$ resulted in a 70% increase in lift. Experimental studies have also been conducted on flow separation control on the NACA-0015 airfoil (Buchmann et al., 2013; Tuck and Soria, 2008) at a Reynolds number of 3 × 10^4 and an angle of attack of 18°. The results of this research indicated that the optimal excitation frequencies for achieving maximum lift were $F^+ = 0.65$ and $F^+ = 1.3$, which correspond to the wake frequency f_{wake} and its harmonic $2f_{wake}$, respectively. Other studies have reported the optimal frequencies for an unsteady control system to reattach the flow to the deflected flap surface as $F^+ \approx 1.5$ (Darabi and Wyganski, 2004) and $F^+ \approx 1.3$ (Nishri and Wygnanski, 1998).

In situations where the flow on the airfoil experiences separation near the leading edge, the application of an appropriate control method can facilitate the reattachment of the separated flow to the surface. At the optimum frequency, the flow reattaches to the surface

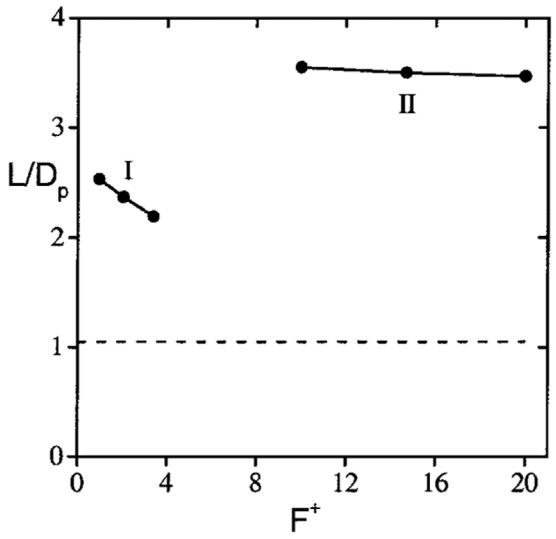

FIGURE 9
Variation of the lift to pressure drag ratio with F^+, uncontrolled value shown as dashed line (Amitay et al., 2001).

with the lowest momentum coefficient C_μ. The optimum frequency for the reattachment of the flow to a straight surface occurs at dimensionless frequency of $F^+ = 1$. Once the flow is reattached due to the effective operation of the control system, it forms a large bubble. The size of this bubble may decrease as the frequency increases. Injecting flow with a frequency higher than the natural frequencies of the flow primarily enhances the turbulent kinetic energy of the boundary layer by introducing small-scale vortical structures (Zander and Nitsche, 2013). However, injecting flow at excessively high frequencies leads to flow separation at the trailing edge, as the dimensionless frequency F^+ becomes so high that the applied fluctuations are dissipated before reaching the flap's trailing edge. Therefore, the excitation frequency must be sufficiently high to prevent flow separation from the surface between two consecutive pulses (Hecklau et al., 2011). Previous studies indicate that in cases where there is a separated flow with reattachment to the surface, the most effective frequency range shifts to higher values within the range of $3 < F^+ < 4$ in order to avoid flow re-separation (Nishri and Wygnanski, 1998).

Raju et al. (2008) conducted a numerical simulation of the NACA-4418 airfoil at a Reynolds number of 4 × 10^4 and an angle of attack of 18°. In the absence of control, the flow over the airfoil exhibits a separation bubble near the leading edge, leading to stall. Under these conditions, the uncontrolled flow is characterized by three natural frequencies: the shear layer frequency f_{sl}, the separation bubble frequency f_{sep}, and the wake frequency f_{wake}. The simulation results indicate that applying synthetic jet excitation near the frequency of oscillations caused by the unsteady flow in the separation bubble $f_{sep}^+ \sim$ O (1) (based on chord length) effectively reduces the size of the separation bubble and improves the lift-to-drag ratio. However, employing a higher excitation frequency, on the order of magnitude of the roll-up of vortices in the shear layer $f_{sl}^+ \sim$ O (10) (based on chord length), for controlling the separation is not beneficial. This is because in such cases, the vortices in the shear layer merge into a larger vortex,

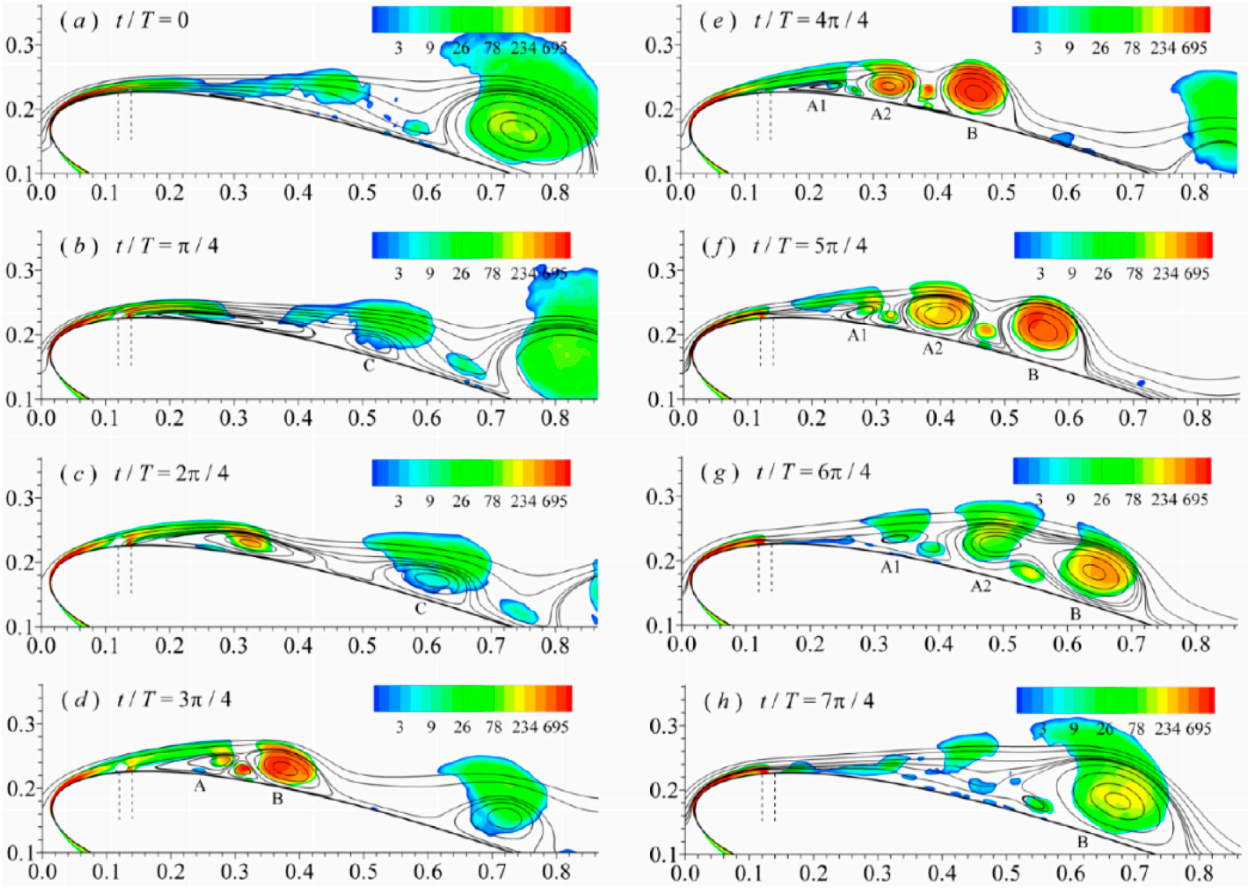

FIGURE 10
Evolutions of phase-averaged streamlines and Q criteria for excitation case with $F^+ = 0.5$. The vertical dotted line shows the location of the actuator (Zhang and Ravi, 2015).

intensifying the separation phenomenon. The occurrence of inefficient excitation at high frequencies, resulting from the merging of Kelvin-Helmholtz vortices, has been observed by Kotapati et al. (2010) in the context of flow over a flat plate with an elliptical leading edge and a blunt trailing edge.

However, contrasting findings were reported by Amitay et al. (2001) based on their experimental results. The results demonstrate the presence of two distinct regimes of dimensionless frequency that lead to an elevation in the lift to pressure drag ratio as shown in Figure 9. The first regime occurs when the excitation frequency equals with the frequency of large-scale vortex shedding in the wake f_{wake}, falling within the range of $F^+ \leq 4$. The second regime occurs when the excitation frequency surpasses the frequency of vortex shedding in the wake f_{wake} by one or more orders of magnitude, specifically within the range of $F^+ \geq 10$.

Glezer et al. (2005) demonstrated that excitation at low frequencies within the range of the natural shedding frequency, and excitation at high frequencies, at least an order of magnitude higher than the frequency of natural instabilities, yield distinct effects on the shear layer. The separated flow on the airfoil before excitation is shown in Figures 12A. When the excitation frequencies approach the natural vortex shedding frequency, the separated shear layer undergoes deflection towards the surface. At this time, a sequence of vortices can be observed that are advected downstream along the airfoil surface. These vortices persist up to the trailing edge of the airfoil, and their strength increases as they move downstream due to the potential coupling between the excitation frequency and the natural shedding frequency of the vortices in the flow (Figures 10, 11, 12B–E) (Glezer et al., 2005; Abdolahipour, 2023; Zhang and Ravi, 2015).

On the other hand, at dimensionless frequencies at least an order of magnitude higher than the natural frequency, the flow remains completely attached to the airfoil surface, with no discernible presence of large-scale coherent structures (Figures 12F) (Glezer et al., 2005; Abdolahipour, 2023; Zhang and Ravi, 2015). Glezer et al. (2005) have presented a different approach to controlling separation on lifting surfaces through high-frequency actuation. This approach underscores the fluidic modification of the aerodynamic shape of the surface, with the objective of altering the streamwise pressure gradient to achieve either partial or complete elimination of flow separation. Actuation is achieved through the establishment of an interaction domain between the actuation jet and the crossflow upstream of the separation, which can be viewed as a virtual alteration in surface shape. In this technique, the characteristic wavelength of excitation is at least an order of magnitude smaller than the corresponding length scale in the flow. Moreover, the excitation frequency is sufficiently high to ensure that the interaction between the excitation and the crossflow remains essentially time-

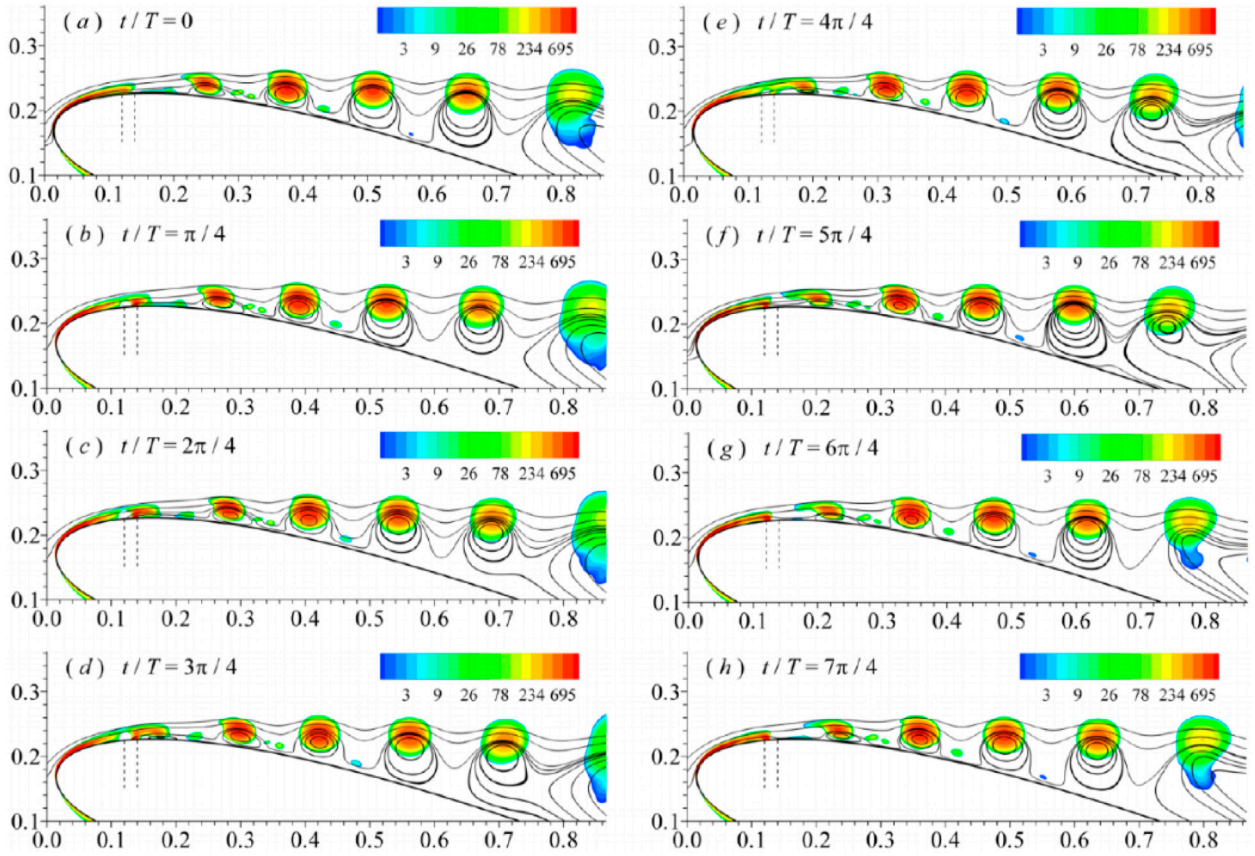

FIGURE 11
Evolutions of phase-averaged streamlines and Q criteria for excitation case with $F^+ = 4$. The vertical dotted line shows the location of the actuator (Zhang and Ravi, 2015).

invariant on the global timescale of the flow. Overall, various experiments have demonstrated flow reattachment in stall conditions and improved airfoil performance for excitation frequencies at both the scale of $F^+ = O(1)$ and the larger scale of $F^+ = O(10)$ (Feero et al., 2015; Glezer, 2011).

Further investigation into the various aspects of these two control approaches in the flow field has revealed that low-frequency excitation induces separated shear-layer flow oscillations. These flow oscillations establish a robust coupling with the wake, resulting in significant oscillations of the separation point during each excitation cycle. Consequently, these oscillations give rise to unstable aerodynamic forces. On the other hand, when the excitation frequency reaches a sufficiently high level, a small interaction region forms upstream of the separation region, causing displacement of the passing flow. These alterations create a favorable local pressure gradient, leading to the formation of a thinner and more stable boundary layer downstream of the interaction region. Ultimately, these modifications result in a significant delay in flow separation. As depicted in Figure 13, low-frequency excitation results in significant fluctuations in circulation, consequently causing fluctuations in aerodynamic forces. Conversely, when high-frequency excitation is applied, circulation undergoes a brief transition period before reaching a quasi-steady state. Consequently, the aerodynamic forces generated in this state exhibit relatively time invariant (Abdolahipour, 2023). These findings highlight a fundamental distinction between low-frequency and high-frequency excitation approaches. In the case of high-frequency excitation, the excitation becomes decoupled from the unsteady frequencies of the base flow. As a result, the resulting aerodynamic forces remain practically time invariant on a scale that is comparable to the characteristic timescale of the base flow, and overall flow fluctuations are attenuated, and possibly even damped.

In recent research (Abdolahipour et al., 2022a; Abdolahipour et al., 2022b; Abdolahipour et al., 2021), a novel method has been employed to take advantage of the benefits of both low and high excitation frequencies using a vortex generator jet actuator (VGJ). This method involves modifying the waveform of the excitation signal through the introduction of burst modulation. In the literature, burst modulation of an actuator signal refers to the controlled switching on and off of the actuator for predetermined periods. In this study, the burst modulated signal is achieved by combining two square-wave signals: a high-frequency square-wave containing the base frequency fc and a low-frequency square-wave containing the burst frequency fm, called carrier signal and modulating signal, respectively. Figure 14 illustrates the schematic representation of the signal burst modulation. This combination enables the incorporation of both high and low excitation frequencies within a single actuator driving signal. For instance, it becomes possible to simultaneously set the frequency of flow shear

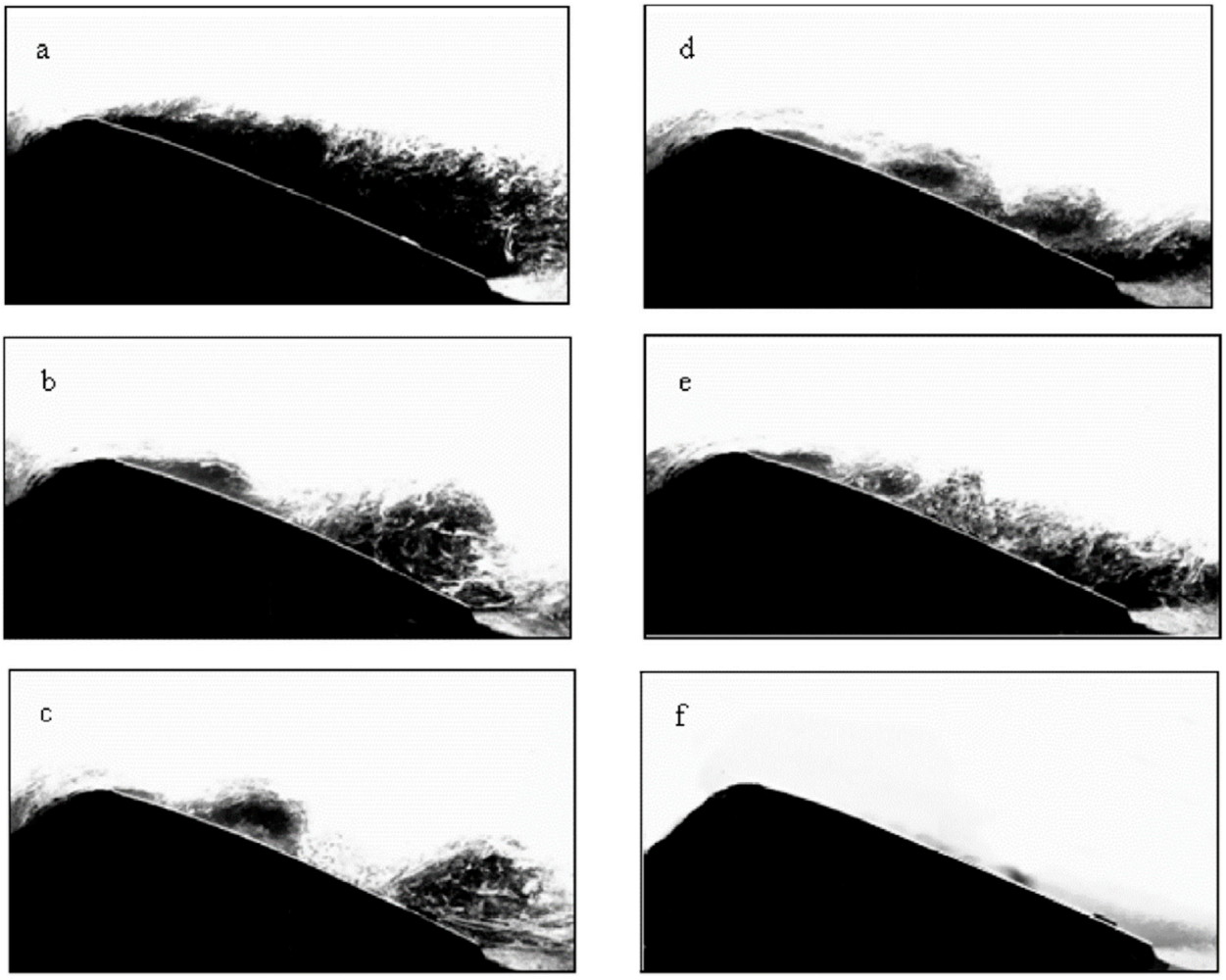

FIGURE 12
Visualization of the phase averaged flow on the airfoil surface at the angle of attack of 15°: **(A)** basic model and controlled model with dimensionless frequency F^+ = **(B)** 0.7, **(C)** 1.1, **(D)** 2.05, **(E)** 3.3, and **(F)** 10 (Glezer et al., 2005).

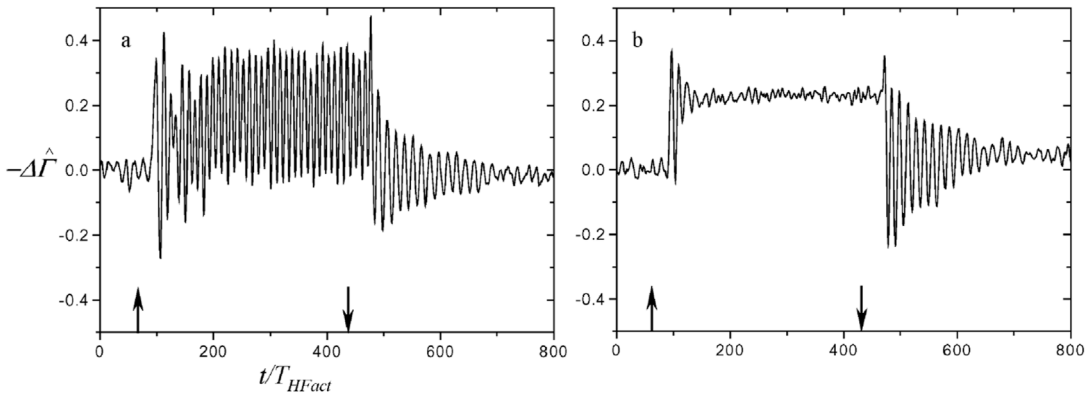

FIGURE 13
The increase in phase-averaged circulation under the influence of excitation by the control actuator with the excitation frequency a) $F^+ = 0.24$ b) $F^+ = 2.5$ (Time is dimensionless based on the period of T_{HFact}. The arrows show the time when the actuator is turned on and off) (Glezer et al., 2005).

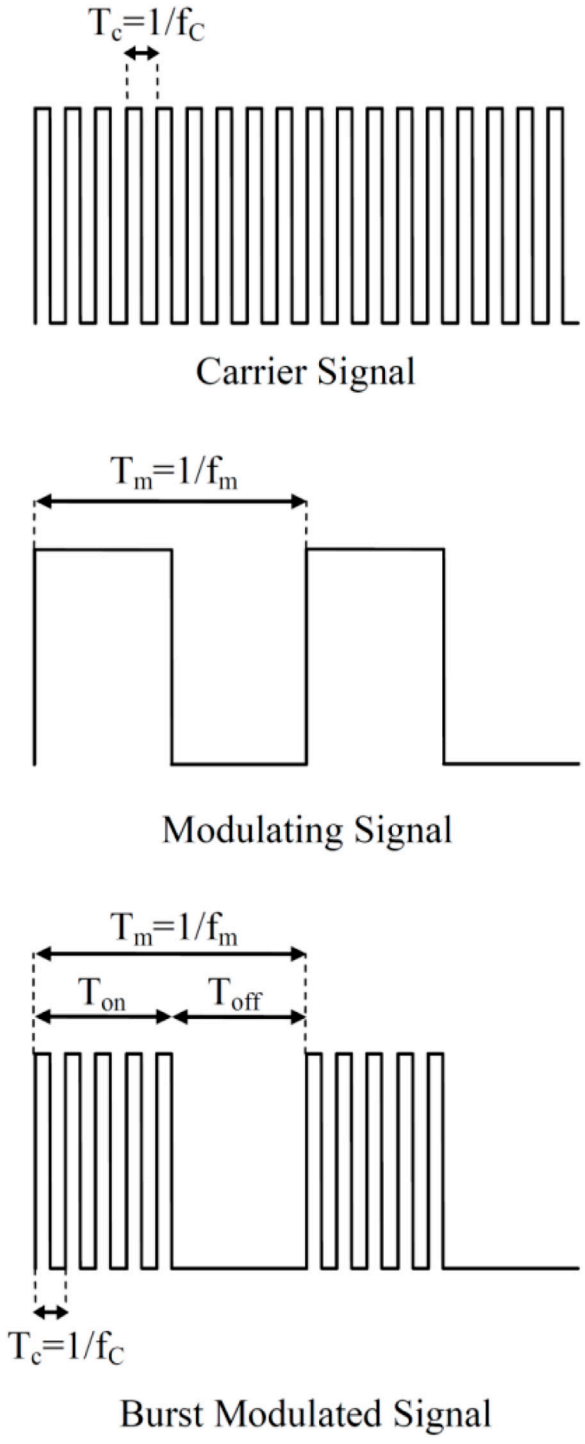

FIGURE 14
Schematic of the signal burst modulation (Abdolahipour et al., 2022b).

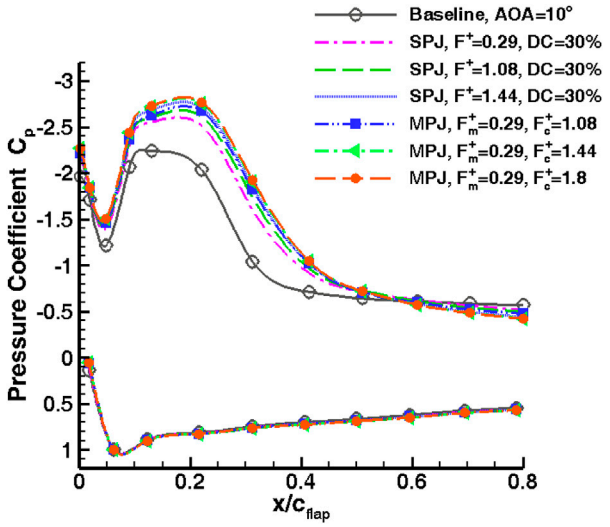

FIGURE 15
Pressure distribution on the flap surface with SPJ and MPJ actuation at AOA = 10° (Abdolahipour et al., 2022a).

layer instability, wake instability, or a frequency at least an order of magnitude larger within one excitation signal. In the context of flow control, both high and low frequencies can approximately correspond to the first-subharmonic, harmonic, and first-superharmonic of the natural vortex shedding frequency in the uncontrolled flow.

A noteworthy attribute of this signal modulation method for the generation of modulated pulse jet MPJ is its capacity to reduce air consumption by approximately 50% in comparison to a simple pulsed jet SPJ over a specific portion of the flow control period, while still producing equivalent or even greater control benefits, as illustrated in Figure 15.

The optimal excitation frequency is also influenced by the excitation location. The location of the excitation itself is a crucial parameter in designing an active flow separation control system. Previous research has generally indicated that excitation is most effective when the actuator location is positioned upstream of the separation point. However, there is no specific recommendation for the most effective actuator location. The findings of Amitay and Glezer (2002b) highlight the complexity of the problem when the excitation frequency is introduced as a variable. They used a special configuration that allowed the azimuthal position of the jet to be continuously changed relative to the airfoil chord. Their results demonstrate that if the actuator is positioned at the highest possible location on the airfoil, the excitation applied at the dimensionless frequencies of $F^+ = 3.3$ and 10, equivalent to the excitation frequency f = 246 and 740 Hz, has no measurable impact on the pressure distribution on the airfoil and does not prevent separation. Conversely, under the same conditions, excitation at the dimensionless frequency of $F^+ = 0.95$, equivalent to the frequency f = 71 Hz, leads to flow reattachment and the formation of a separation bubble on the airfoil surface. By changing the location of actuation to x/c = 0.011, the dimensionless frequencies of $F^+ = 3.3$ and 10 result in a partial reattachment. Actuation with $F^+ = 0.95$ at this particular location results in a significant increase in suction pressure followed by complete reattachment of the flow.

Amitay and Glezer (2002b) have highlighted the significant impact that different excitation methods can have on the results obtained. For instance, when $f_e \leq 300$ Hz, internally mounted acoustic speakers were employed to generate uniform jets in the span direction. However, for $f_e \geq 300$ Hz, the performance of

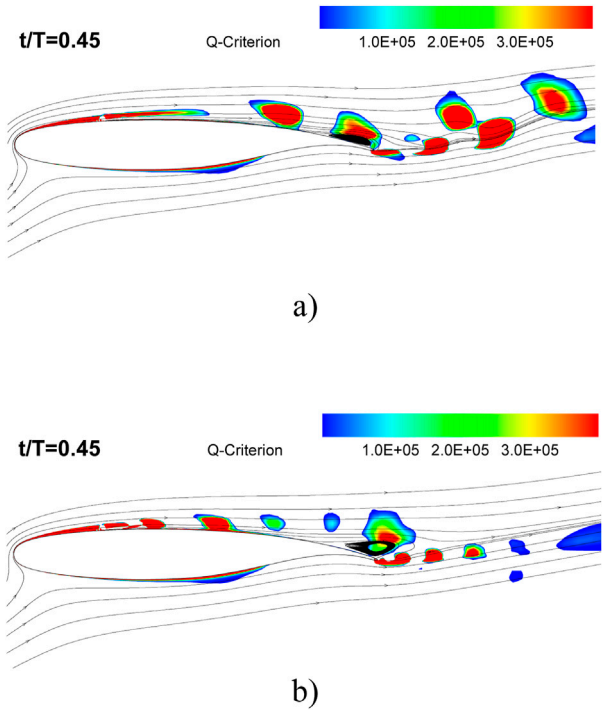

FIGURE 16
The streamlines and Q-criterion for the actuated case at AOA = 16° and at time instant t/T = 0.45 of one actuation cycle **(A)** $F^+ = 1$, **(B)** $F^+ = 6$ (Abdolahipour, 2023).

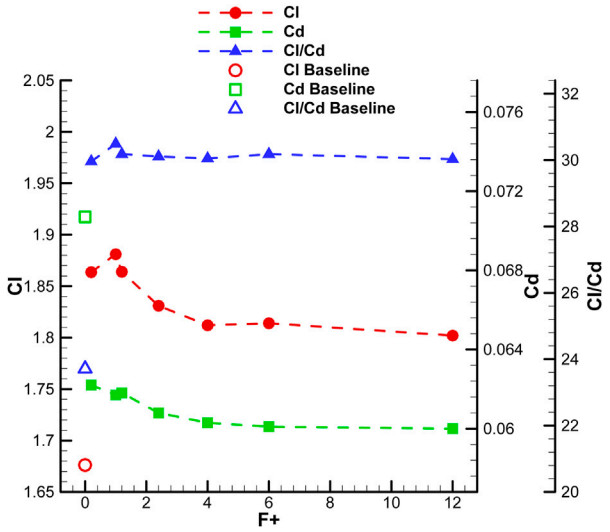

FIGURE 17
Variation of time-averaged aerodynamic forces for different actuation frequencies at AOA = 16° (Abdolahipour, 2023).

these speakers diminishes, both in the presence and absence of cross flow. In fact, in the presence of crossflow, the jet velocity decreases by over 80%, leading to a substantial reduction in the overall efficiency of the control system. Consequently, for high frequencies $f_e \geq 300$ Hz, a flow injection actuator with a small cavity was utilized.

2.3 Threshold variation of momentum coefficient and aerodynamic efficiency with excitation frequency and location

The remaining question pertains to how the threshold coefficient of momentum and aerodynamic efficiency, in terms of both lift and drag, are influenced by excitation frequency and relative slot location. To address this inquiry, a novel experimental study (Feero et al., 2017) was conducted. The research focused on investigating post-stall separated flow reattachment on a NACA 0025 airfoil at $Re = 1 \times 10^5$ and an angle of attack of 12° using synthetic jet flow control. One of the objectives of this study was to examine the impact of control parameters, specifically the momentum coefficient and excitation frequency, with varying values of $F^+ = 1$, 2, 14, and 58, on the wing's aerodynamic performance. The findings indicate that excitation at the frequency corresponding to wake instabilities f_{wake} yields the greatest lift increase, while excitation at frequencies of a higher order of magnitude within the separated shear layer instabilities range f_{sl} results in maximum drag reduction. Consequently, an excitation frequency of $F^+ = 1$ (f^+_{wake}) is more suitable when seeking lift enhancement, whereas $F^+ = 14$ (f^+_{sl}) is more appropriate for achieving the maximum lift-to-drag ratio. Furthermore, an increase in the blowing ratio or momentum coefficient positively impacts both lift and drag coefficients across all frequencies, up to a certain saturation value. This saturation value is dependent on the excitation frequency F^+ and the location of the actuator (Feero et al., 2017).

As depicted in Figure 16, the number of structures during one cycle exhibits an increase with F^+ up to a certain threshold. To achieve a greater number of vortices within a spatial domain, the size of the structures needs to be reduced, which can be accomplished by reducing the injection time. At $F^+ = 1$, it is evident that a single vortex moves downstream and away from the surface throughout one pulsed excitation cycle. During a portion of the pulse cycle, two such vortices are present on the airfoil surface. In contrast, at $F^+ = 6$, a larger number of relatively smaller vortices that remain in closer proximity to the airfoil surface are observed. This reduction in vortex size and their path along the airfoil surface leads to a narrower wake and consequently less drag as shown in Figure 17.

In a study conducted by Feero et al. (2015), the impact of excitation frequency and momentum coefficient on reattachment and subsequent drag reduction was investigated using synthetic jet actuation. Here, the dimensionless frequency expressed as a Strouhal number $St = fc/U_\infty$, where f is the frequency of excitation and c is the chord length. Figure 18A presents a comparison of the drag coefficient C_D changes with the momentum coefficient C_μ for three excitation frequencies. At a dimensionless modulation frequency of $St_m = 0.84$, an initial increase in drag coefficient is observed due to the vortex shedding at the scale of the dominant separated wake frequency. By increasing the momentum coefficient to 0.12%, the threshold momentum coefficient required for reattachment is reached at the excitation mode of $St_m = 0.84$, resulting in a 30% reduction in the drag coefficient. For $St_e = 58$, a threshold value of C_μ was reached at 0.34%, resulting in a

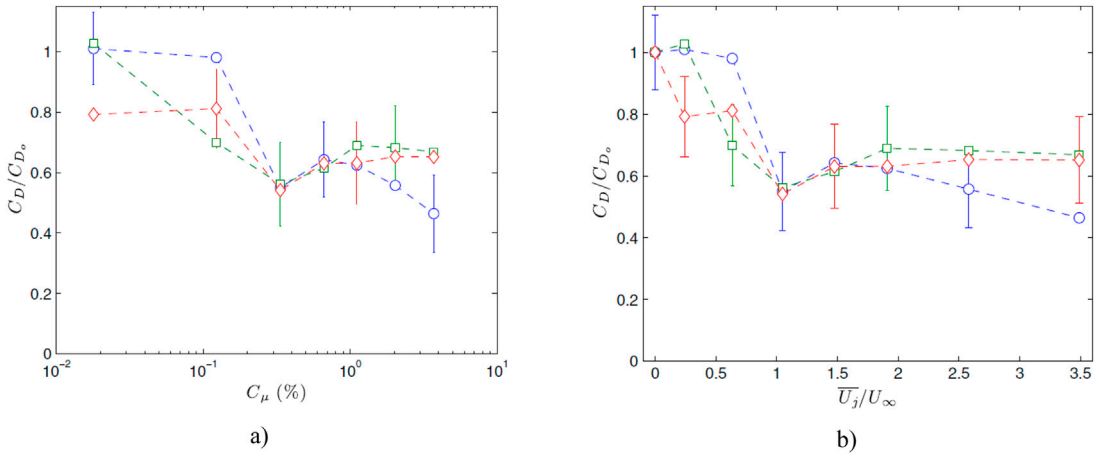

FIGURE 18
Drag coefficient as a function of **(A)** momentum coefficient C_μ **(B)** $\overline{U_j}/U_\infty$ for dimensionless frequency St_e = 58 (○), St_m = 9.9 (◇), St_m = 0.84 (□) (Feero et al., 2015)

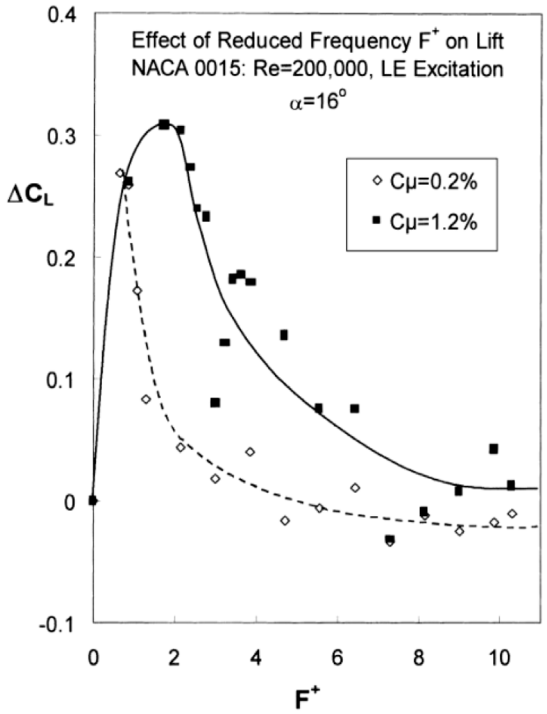

FIGURE 19
The effect of dimensionless frequency with different momentum coefficients on post-stall lift (Greenblatt et al., 1999).

narrowing and downward shift of the wake, accompanied by a decrease in C_D of approximately 45%. These changes corresponded to the steady reattachment of the boundary layer to the airfoil surface. At C_μ = 0.34%, all three excitation frequencies yield the lowest drag coefficient C_D. For a high momentum coefficient C_μ, the excitation at dimensionless frequency St_e = 58 performs slightly better. Notably, the results indicate that the momentum coefficient C_μ required for maximum drag reduction is independent of the excitation frequency. One potential explanation for the observed common maximum drag reduction for all excitation frequencis may be inferred from the unsteady blowing ratio $\overline{U_j}/U_\infty$, as illustrated in Figure 18B. The maximum drag reduction occurs at approximately $\overline{U_j}/U_\infty$ = 1, and increasing $\overline{U_j}$ beyond U_∞ initially leads to a small increase in drag coefficient C_D. These findings highlight that while flow reattachment primarily depends on reaching the threshold momentum coefficient C_μ, the blowing ratio can also play a significant role in achieving maximum drag reduction. In this study, it was observed that low-frequency excitation yields a lower threshold blowing ratio compared to high-frequency excitation. Specifically, excitation in shear layer instabilities (St_m = 9.9) requires the lowest threshold blowing ratio for flow reattachment and drag reduction.

Figure 19 illustrates the effect of frequency and momentum coefficient of pulsed excitation on the lift coefficient of a NACA 0015 airfoil. The experiment involved applying pulsed excitation at the leading edge of the airfoil under post-stall conditions (AOA = 16°) at Reynolds numbers $Re \leq 6 \times 10^5$. At a momentum coefficient of C_μ = 0.2%, it appears that high-frequency excitation within the range of $2 \leq F^+ \leq 11$ has minimal effect on the lift coefficient. The peak effectiveness is within the range of $0.5 \leq F^+ \leq 1$. As expected, at a higher momentum coefficient of C_μ = 1.2%, the effective frequency range expands to approximately $0.5 \leq F^+ \leq 3$. This is due to the reduction in hysteresis at the most effective dimensionless frequency F^+, which helps to prevent separation and promote flow reattachment (Seifert and Pack, 1999). Furthermore, it is important to highlight that even with six times more momentum input, there was no significant increase in the lift coefficient at the most effective dimensionless frequency F^+.

Table 1 presents a summary of the optimum controlling factors or parameters and the most significant airfoil performance improvements relative to the baseline, taking into account the airfoil type and Reynolds number. Additionally, a summary of selected experimental and numerical investigations dealing with active separation control applied to an airfoil model using instability exploitation, is presented in Table 2. This table

TABLE 1 Representative summary of experimental and numerical investigations on active separation control by unsteady excitation.

Author	Model	Re ($\times10^5$)	Actuator Type	C_μ (%)	F^+ (Base on chord Length	Enhancement relative to baseline (%)	Location x/c (%)	Description
Zaman 1987 (Zaman et al., 1987)	LRN-(1)-1007	0.4	Acoustic	Amplitude = 104 dB	6.5* (376 Hz)	CL_{max}: 16	Floor of the Test Section	AOA = 18° at Post-Stall
Seifert 1996 (Seifert et al., 1996)	Flapped NACA 0015	3	Continuous + Pulsed Jet	at Flap Shoulder: 0.8+<0.8> at Leading Edge: 3.2+<2.7>	2	CL_{max}: 64	at Flap Shoulder: 75 at Leading Edge: 0	Stall Delay from 12° to 14°
						CL_{max}: 64		Stall Delay from 12° to 20°
Greenblatt 1999 (Greenblatt et al., 1999)	Flapped NACA 0015	3	Periodic Excitation	0.3	0.3	CL: 53	Flap Slot	Flap Deflection Angle = 35°
Greenblatt 2003 (Greenblatt and Wygnanski, 2003)	NACA 0012	2.4	Periodic Excitation	0.09	1.5	CL_{max}: 3	5	Single Slot
				1.8	1.5	CL_{max}: 25		
Darabi 2004 (Darabi and Wyganski, 2004)	Flat Surface as a Highly Deflected Flap	1.24	Acoustic	0.08	1.5	Minimum Reattachment Time $\tau_{r,min}$ = 16	Behind the Flat Surface	Deflection Angle α = 6°
Duvigneau 2006 (Duvigneau and Visonneau, 2006)	NACA 0015	8.96	SJA	3.8* (U_{jet}/U_∞ = 1.72)	0.85	CL_{max}: 52	12	Stall Delay from 16° to 22°
You 2008 (You and Moin, 2008)	NACA 0015	8.96	SJA	1.23 (U_{jet}/U_∞ = 2.14)	1.284 (120 Hz)	CL_{max}: 70 C_D: -15 up to -18	12	AOA = 16.6°
Tuck 2008 (Tuck and Soria, 2008)	NACA 0015	0.3	SJA	0.14 ($U_{jet,\ rms}/U_\infty$ = 0.65)	1.3	CL_{max}: 34	Leading Edge	Stall Delay from 10° to 18°
Scholz 2009 (Scholz et al., 2009)	Flapped DLR-F15	20	VGJ	1.28	1.2	CL_{max}: 5	1	Flap Deflection Angle = 45°
Casper 2011 (Casper et al., 2011)	Flapped DLR-F15	42	VGJ	0.79	1.62* (100 Hz)	CL_{max}: 4	1 at Pressure Side	Flap Deflection Angle = 45°
		92		0.53	2* (100 Hz)	CL_{max}: 3		
Hecklau 2011 (Hecklau et al., 2011)	Compressor Cascade Blade	8.4	Continuous + Pulsed Jet	0.93 + 0.9	0.43 (40 Hz)	Pressure loss: -13	Continuous Blowing:10 Pulsed Blowing: 66.5	Duty Cycle = 50%
				0.93 + 1.1	1.28 (120 Hz)			
Taleghani 2012 (Taleghani et al., 2012)	NLF 0414	7.5	DBD Plasma		1.8 (100 Hz)	CL_{max}: 17%	2, 32 and 62	AOA = 18° at Post-Stall
Zhang 2015 (Zhang and Ravi, 2015)	NACA 0018	0.1	SJA	0.0213	1	CL_{max}: 210.76 C_L/C_D: 231.07	13	AOA = 10°
Yarusevych 2017 (Yarusevych and Kotsonis, 2017)	NACA 0012	1.3	DBD Plasma	2.1×10^{-4} (Forcing Amplitude Vpp = 3.5 kV)	6	Bubble Length: -40	60	AOA = 2°
Abdolahipour 2023 (Abdolahipour, 2023)	NASA SC(2)-0714	10	Pulsed Jet	0.082	1 (167 Hz)	CL_{max}: 12 C_L/C_D: 28.62	25	AOA = 16°

summarizes the frequencies associated with the instabilities present in the uncontrolled flow, f_{sl} and f_{wake}, were determined by flow characteristic measurements in the separated shear layer and wake. In these investigations, both high and low excitation frequencies approximately correspond to the subharmonic, harmonic, and superharmonic of the natural instabilities frequencies in the uncontrolled flow. All authors report a beneficial effect of the control approach, but the magnitude of the benefit varies considerably between studies. Values marked (*) were calculated based on the provided context.

The data presented in Tables 1, 2 indicate that the dimensionless frequency range of $0.8 \leq F^+ \leq 2$ is identified as the optimal frequency

TABLE 2 Representative summary of experimental and numerical investigations on active separation control by unsteady excitation using instability exploitation.

Author	Model	Re ($\times 10^5$)	Actuator Type	C_μ (%)	F^+ (Base on chord Length)	Instability frequency in Base flow	Enhancement relative to baseline (%)	Location x/c (%)	Description
Wu 1991 (Wu et al., 1991)	NACA 0012	5	Periodic Excitation	2.5	0.5 f_{wake}	f_{wake}	CL_{max}: 73.2 C_L/C_{Dp}: 49.2	Near Leading Edge	AOA = 25°
Chang 1992 (Chang et al., 1992)	NACA 63_3-018	3	Acoustic	Amplitude 110 dB	4 (200 Hz)	f_{sl} = 250 Hz f^+_{sl} = 5	CL_{max}: 18*	1.25	
Smith 1998 (Smith et al., 1998)	NACA Symmetric Airfoil-Cylindrical Leading Edge	3	SJA	0.17	10.16* (720 Hz)	f_{wake} = 75 Hz	C_L/C_{Dp} = 12 at AOA = 5° relative to $C_{L.base}$ = 0	Near Leading Edge	Cp Improvement
Amitay 2001, 2002 (Amitay and Glezer, 2002a; Amitay and Glezer, 2002b; Amitay et al., 2001; Amitay and Glezer, 2006)	NACA Symmetric Airfoil-Cylindrical Leading Edge	3.1 up to 7.25	SJA	0.35	0.95, 2.05, 3.4, 10, 14.7, 20 (71, 148, 246, 740, 1088, 1480 Hz)	f^+_{wake} = 0.7	CL: up to100 C_{Dp}: up to −45 C_L/C_{Dp}: 233	Near Leading Edge	For F^+ = 10, 14.7, 20, the C_L/C_{Dp} Is Much Larger and Invariant With the Actuation Frequency
Raju 2008 (Raju et al., 2008)	NACA 4418	0.4	SJA	1.2×10^{-2} –1.9×10^{-2} (U_{jet}/U_∞ = 0.1)	1	f^+_{wake} = 1	CL_{max}: 10 C_L/C_{Dp}: 52 Cd: -28	2.4	AOA = 18°
					2	f^+_{sl} ≈2	CL_{max}: 1 C_L/C_{Dp}: 64 C_D: -39		
Feero, 2015 (Feero et al., 2015)	NACA 0025	1	SJA	0.34 (U_{jet}/U_∞ = 1)	F^+ = 58 (970 Hz) F^+ = 0.84 (14 Hz) F^+ = 9.9	f^+_{wake} = 0.84 (f_{wake} = 14 Hz) f^+_{sl} = 9.9	C_D: -45	19	AOA = 10°
Feero, 2017 (Feero et al., 2017)	NACA 0025	1	SJA	U_{jet}/U_∞ = 0.8	F^+ = 1	f^+_{wake} = 1	C_L/C_{Lbase}: 410	(x_{jet}-$x_{separation}$)/ c = −4.3	AOA = 12°
				U_{jet}/U_∞ = 1	F^+ = 14	f^+_{sl} = 10-26	C_L/C_D: 1280		
Abdolahipour 2022 (Abdolahipour et al., 2022b)	Flapped NASA SC(2)-0714	10	VGJ Simple Pulsed Jet	0.082	0.29 (40 Hz)	f_{wake} = 40 Hz f_{sl} = 400 Hz	CL_{max}: 11 $(C_L/C_D)_{AOA=20°}$:12 $(C_L/C_D)_{AOA=0°}$: 24.5	x/c_{flap} = 0.4	AOA = 20° F^+ Range = 0.3–1.8
			VGJ Modulated Pulse Jet		F^+_m = 0.29 (40 Hz) and F^+_c = 1.8 (250 Hz)		CL_{max}: 12.6 $(C_L/C_D)_{AOA=20°}$:16 $(C_L/C_D)_{AOA=0°}$:39.5		
Abdolahipour 2022 (Abdolahipour et al., 2022a)	Flapped NASA SC(2)-0714	10	VGJ Simple Pulsed Jet	0.082	7.2 (1000 Hz) and 2.88 (400 Hz)	f^+_{wake} = 0.29 (f_{wake} = 40 Hz) f^+_{sl} = 2.88 (f_{sl} = 400 Hz)	Flap Suction Peak Cp Increase: 48	x/c_{flap} = 0.4	AOA = 20° F^+ Range = 0.3–7.2
			VGJ Modulated Pulse Jet		F^+_m = 0.29, F^+_c = 7.2and F^+_m = 0.29, F^+_c = 2.88		Flap Suction Peak Cp Increase: 53		

for enhancing aerodynamic efficiency in 76% of the research studies detailed in these tables. The analysis of the data presented in Table 2 reveals that employing an excitation frequency proximate to the wake instabilities frequency f_{wake} demonstrates enhanced effectiveness in lift improvement. Conversely, utilizing an excitation frequency near the frequencies within the range of separated shear layer instabilities f_{sl} leads to drag reduction and the optimization of the lift-to-drag ratio. Furthermore, elevating the

blowing ratio or momentum coefficient exerts a beneficial impact on both lift and drag coefficients across all frequencies, up to a defined saturation threshold.

3 Conclusion

The review presented in this paper outlined the effect of two crucial parameters in separation control by means of unsteady excitation. Among different methods, the application of unsteady excitation locally at the lifting surfaces has demonstrated the most potential as an efficient and practical means of separation control. Reviewing the literature reveals that the utilization of unsteady excitation to control flow separation is of significant interest across various applications. In this paper, an attempt was made to identify the optimal ranges of momentum coefficient and excitation frequency for achieving flow reattachment and separation delay in a shear layer flow on the lifting surfaces by means of different unsteady excitation techniques such as pulsed jets, synthetic jets, plasma, and acoustic actuators. It is important to note that the determination of the effective or optimal excitation frequency is case-dependent and relies on factors such as the actuation location, geometry of lifting surfaces, angle of attack and other freestream flow parameters. Therefore, the selection of the appropriate excitation frequency should be based on a thorough understanding of the uncontrolled flow physics in each specific case.

The research findings indicate that, elevating the amplitude or momentum coefficient of actuation exerts a beneficial impact on the aerodynamic characteristics of lifting surfaces across all frequencies, up to a defined saturation threshold. However, for flow reattachment and separation delay, there exists a saturation point where the benefits of flow control become limited once a specific momentum coefficient is reached. In other words, once a threshold momentum coefficient is achieved, further increases in momentum input have minimal impact on the attached flow.

Regarding excitation frequency, the literature primarily focuses on two distinct frequency bands. The first band corresponds to the dominant natural shedding frequencies, while the second band encompasses frequencies at least an order of magnitude higher than the natural instabilities frequencies. Several studies have shown that excitation at a dimensionless frequency in the range of $F^+ = 1$ has a positive effect on reducing flow separation and increasing lift. However, recent studies have contradicted this finding by suggesting that dimensionless frequencies an order of magnitude higher than the natural shedding frequency yield better results. One noteworthy discovery in these studies is the fundamental distinction between low-frequency and high-frequency actuation approaches. Low-frequency actuation induces pronounced oscillations in the aerodynamic forces on lifting surfaces, whereas high-frequency actuation generates time-invariant aerodynamic forces. In fact, actuating at high frequencies has been discovered to result in a more stable flow reattachment and produce better aerodynamic properties when compared to using low-frequency control methods. Recently, the excitation frequency modulation technique has emerged as a means to take advantage of both high and low excitation frequencies. A notable feature of the signal modulation was that this method can reduce the air consumption by half the amount consumed by a simple pulsed jet over a certain part of the flow control period, producing the same amount of control benefits or even more.

In this context, new research horizons are suggested for future research. The present review paper primarily focuses on studies that mainly consider the optimization of one parameter such as the efficiency of flow separation control, and lift enhancement. However, future investigations could consider multi-objective optimization, taking into account all performance metrics such as drag reduction, lift enhancement, and energy consumption. This approach would provide a more comprehensive understanding of the trade-offs and potential synergies between different control parameters, leading to more efficient and practical flow separation control strategies.

While the present review paper examines both experimental and numerical studies, future research could focus on conducting more extensive experimental investigations to validate the findings and explore practical applications. The experiments on scaled models or full-scale prototypes can provide valuable insights into the effectiveness of different excitation frequencies and momentum coefficients in flow separation control techniques, facilitating their implementation in practical engineering applications. While the current review paper examines periodic excitation and momentum injection as active flow control techniques such as synthetic jets, pulsed jets, and plasma actuators, future investigations could explore the effectiveness of other control strategies, such as sweeping jet actuators or adaptive control algorithms. Comparing the performance of these strategies can help identify more efficient and reliable approaches for separation control. In addition to excitation frequency and momentum coefficient, the surface characteristics of lifting surfaces can also play a crucial role in flow separation control. Future research could focus on studying the effects of surface modifications, such as compliant coatings, on the efficiency of unsteady flow separation control. Understanding how these surface modifications interact with excitation frequency and momentum coefficient can provide valuable insights into optimizing flow control techniques.

Author contributions

SA: Investigation, Methodology, Resources, Writing–original draft, Writing–review and editing.

Funding

The author(s) declare that no financial support was received for the research, authorship, and/or publication of this article.

Conflict of interest

The author declares that the research was conducted in the absence of any commercial or financial relationships that could be construed as a potential conflict of interest.

Publisher's note

References

Abdolahipour, S. (2023). Effects of low and high frequency actuation on aerodynamic performance of a supercritical airfoil. *Front. Mech. Eng.* 9, 1290074. doi:10.3389/fmech.2023.1290074

Abdolahipour, S., Mani, M., and Arash, S. T. (2022b). Experimental investigation of flow control on a high-lift wing using modulated pulse jet vortex generator. *J. Aerosp. Eng.* 35 (5), 05022001. doi:10.1061/(asce)as.1943-5525.0001463

Abdolahipour, S., Mani, M., and Shams Taleghani, A. (2021). Parametric study of a frequency-modulated pulse jet by measurements of flow characteristics. *Phys. Scr.* 96 (12), 125012. doi:10.1088/1402-4896/ac2bdf

Abdolahipour, S., Mani, M., and Shams Taleghani, A. (2022a). Pressure improvement on a supercritical high-lift wing using simple and modulated pulse jet vortex generator. *Flow, Turbul. Combust.* 109 (1), 65–100. doi:10.1007/s10494-022-00327-9

Amitay, M., and Glezer, A. (2002a). Controlled transients of flow reattachment over stalled airfoils. *Int. J. Heat. Fluid Flow.* 23 (5), 690–699. doi:10.1016/s0142-727x(02)00165-0

Amitay, M., and Glezer, A. (2002b). Role of actuation frequency in controlled flow reattachment over a stalled airfoil. *AIAA J.* 40 (2), 209–216. doi:10.2514/3.15052

Amitay, M., and Glezer, A. (2006). "Aerodynamic flow control using synthetic jet actuators," in *Control of fluid flow* (Berlin, Heidelberg: Springer Berlin Heidelberg, 45–73. doi:10.1007/978-3-540-36085-8_2

Amitay, M., Smith, B., and Glezer, A. (1998). Aerodynamic flow control using synthetic jet technology. *AIAA Pap. 98-0208, 36th Aerosp. Sci. Meet. Exhib*. doi:10.2514/6.1998-208

Amitay, M., Smith, D. R., Kibens, V., Parekh, D. E., and Glezer, A. (2001). Aerodynamic flow control over an unconventional airfoil using synthetic jet actuators. *AIAA J.* 39 (3), 361–370. doi:10.2514/3.14740

Bauer, M., Peltzer, I., Nitsche, W., and G¨olling, B. (2010). Active flow control on an industry-relevant civil aircraft half model. *Act. Flow Control II, Notes Numer. Fluid Mech. Multidiscip. Des.* 108, 95–107. doi:10.1007/978-3-642-11735-0_7

Bernardini, C., Benton, S. I., Chen, J. P., and Bons, J. P. (2014). Pulsed jets laminar separation control using instability exploitation. *AIAA J.* 52 (1), 104–115. doi:10.2514/1.j052274

Betz, A. (1961). "History of boundary layer control in German,". *Boundary layer and flow control*. Editor G. V. Lachmann (New York: Pergamon Press), 1, 1–20.

Boutilier, M. S., and Yarusevych, S. (2012a). Parametric study of separation and transition characteristics over an airfoil at low Reynolds numbers. *Exp. Fluids* 52 (6), 1491–1506. doi:10.1007/s00348-012-1270-z

Boutilier, M. S., and Yarusevych, S. (2012b). Separated shear layer transition over an airfoil at a low Reynolds number. *Phys. Fluids* 24 (8), 084–105. doi:10.1063/1.4744989

Buchmann, N., Atkinson, C., and Soria, J. (2013). Influence of ZNMF jet flow control on the spatio-temporal flow structure over a NACA-0015 airfoil. *Exp. fluids* 54 (3), 1485. doi:10.1007/s00348-013-1485-7

Casper, M., Scholz, P., Radespiel, R., Wild, J., and Ciobaca, V. (2011). "Separation control on a high-lift airfoil using vortex generator jets at high Reynolds numbers," in *41st AIAA fluid dynamics conference and exhibit*. Honolulu, Hawaii. No. AIAA 2011-3442.

Chang, P. K. (1976). *Control of flow separation*. McGraw-Hill.

Chang, R., Hsiao, F.-B., and Shyu, R.-N. (1992). Forcing level effects of internal acoustic excitation on the improvement of airfoil performance. *J. Aircr.* 29 (5), 823–829. doi:10.2514/3.46252

Cornish, J. J., III (1953), "Prevention of turbulent separation by suction through a perforated surface," Aerophysics Dept., Mississippi State Univ., Research Report No. 7.

Darabi, A., and Wyganski, I. (2004). Active management of naturally separated flow over a solid surface. Part 1. The forced reattachment process. *J. Fluid Mech.* 510 (7), 105–129. doi:10.1017/s0022112004009231

Du, H., Yang, L., Chen, S., Zhang, W., and Han, S. (2022). Effect of multistage circulation control on blade aerodynamic performance. *Energies* 15 (19), 7395. doi:10.3390/en15197395

Duvigneau, R., and Visonneau, M. (2006). Optimization of a synthetic jet actuator for aerodynamic stall control. *Comput. and fluids* 35 (6), 624–638. doi:10.1016/j.compfluid.2005.01.005

Feero, M. A., Goodfellow, S. D., Lavoie, P., and Sullivan, P. E. (2015). Flow reattachment using synthetic jet actuation on a low-Reynolds-number airfoil. *AIAA J.* 53 (7), 2005–2014. doi:10.2514/1.j053605

Feero, M. A., Lavoie, P., and Sullivan, P. E. (2017). Influence of synthetic jet location on active control of an airfoil at low Reynolds number. *Exp. Fluids* 58 (8), 99. doi:10.1007/s00348-017-2387-x

Fiedler, H. E., and Fernholz, H.-H. (1990). On management and control of turbulent shear flows. *Prog. Aerosp. Sci.* 27 (4), 305–387. doi:10.1016/0376-0421(90)90002-2

Flatt, J. (1961). "The history of boundary layer control research in the United States of America," *Boundary Layer and Flow Control*. Editor G. V. Lachmann (New York: Pergamon Press) Vol. 1, 122–143.

Gad-el-Hak, M. (2006). *Flow control: passive, active, and reactive flow management*. New York, United States: Cambridge University Press.

Glezer, A. (2011). Some aspects of aerodynamic flow control using synthetic-jet actuation. *Philosophical Trans. R. Soc. A Math. Phys. Eng. Sci.* 369 (No.1940), 1476–1494. doi:10.1098/rsta.2010.0374

Glezer, A., Amitay, M., and Honohan, A. M. (2005). Aspects of low-and high-frequency actuation for aerodynamic flow control. *AIAA J.* 43 (7), 1501–1511. doi:10.2514/1.7411

Greenblatt, D., Darabi, A., Nishri, B., and Wygnanski, I. (1999). "Some factors affecting stall control with particular emphasis on dynamic stall," in *30th AIAA fluid dynamics conference* (Norfolk, VA: AIAA Paper), 99–3504.

Greenblatt, D., and Wygnanski, I. (2003). Effect of leading-edge curvature on airfoil separation control. *J. Aircr.* 40 (3), 473–481. doi:10.2514/2.3142

Greenblatt, D., and Wygnanski, I. J. (2000). The control of flow separation by periodic excitation. *Prog. Aerosp. Sci.* 36 (7), 487–545. doi:10.1016/s0376-0421(00)00008-7

Hecklau, M., Salazar, D. P., and Nitsche, W. (2013). "Influence of the actuator jet angle on the reattachment process with pulsed excitation," in *New results in numerical and experimental fluid mechanics VIII*. Berlin: Springer, 143–150.

Hecklau, M., Wiederhold, O., Zander, V., King, R., Nitsche, W., Huppertz, A., et al. (2011). Active separation control with pulsed jets in a critically loaded compressor cascade. *AIAA J.* 49 (8), 1729–1739. doi:10.2514/1.j050931

Holman, R., Utturkar, Y., Mittal, R., Smith, B. L., and Cattafesta, L. (2005). Formation criterion for synthetic jets. *AIAA J.* 43 (10), 2110–2116. doi:10.2514/1.12033

Hunter, P. A., and Johnson, H. I. (1954). *A flight investigation of the practical problems associated with porous-leading-edge suction*. United States: NACA TN-3062.

Jones, G., and Englar, R. (2003). "Advances in pneumatic-controlled high-lift systems through pulsed blowing," in *21st applied aerodynamics conference*. Orlando, Florida. No. AIAA 2003-3411.

Jones, G., Yao, C.-S., and Allan, B. (2006). "Experimental investigation of a 2D supercritical circulation-control airfoil using particle image velocimetry," in *3rd AIAA flow control conference, CA*, 2006–3009.

Joslin, R. D., and Miller, D. N. (2009). *Fundamentals and applications of modern flow control* (American Institute of Aeronautics and Astronautics).

Knight, M., and Bamber, M. J. (1929). *Wind tunnel tests on aerofoil boundary layer control using a backward opening slot*. United States: NACA TN–323.

Kotapati, R. B., Mittal, R., Marxen, O., Ham, F., You, D., and Cattafesta, L. N. (2010). Nonlinear dynamics and synthetic-jet-based control of a canonical separated flow. *J. Fluid Mech.* 654, 65–97. doi:10.1017/s002211201000042x

Kweder, J., Panther, C., and Smith, J. (2010). Applications of circulation control, yesterday and today. *Int. J. Eng.* 4 (5), 411–429.

Kweder, J., Zeune, C., Geiger, J., Lowery, A., and Smith, J. (2014). Experimental evaluation of an internally passively pressurized circulation control propeller. *J. Aerodynamics* 2014, 1–10. Article ID 834132. doi:10.1155/2014/834132

Lissaman, P. B. S. (1983). Low-Reynolds-number airfoils. *Annu. Rev. fluid Mech.* 15 (1), 223–239. doi:10.1146/annurev.fl.15.010183.001255

Mccullough, G. B., and Gault, D. E. (1951). Examples of three representative types of airfoil-section stall at low speed. Technical Note, Document ID 19930083422.

Mirzaei, M., Taleghani, A. S., and Shadaram, A. (2012). Experimental study of vortex shedding control using plasma actuator. *Appl. Mech. Mater.* 186, 75–86. doi:10.4028/www.scientific.net/AMM.186.75

Mohammadi, M., and Taleghani, A. S. (2014). Active flow control by dielectric barrier discharge to increase stall angle of a NACA0012 airfoil. *Arab. J. Sci. Eng.* 39, 2363–2370. doi:10.1007/s13369-013-0772-1

Mueller-Vahl, H., Strangfeld, C., Nayeri, C., Paschereit, C., and Greenblatt, D. (2013) "Thick airfoil deep dynamic stall and its control," in *51st AIAA aerospace science meeting, grapevine, Texas, No. AIAA 2013-0854*.

Munday, P. M., and Taira, K. (2018). Effects of wall-normal and angular momentum injections in airfoil separation control. *AIAA J.* 56 (5), 1830–1842. doi:10.2514/1.j056303

Nishino, T., Hahn, S., and Shariff, K. (2010). "Calculation of the turbulence characteristics of flow around a circulation control airfoil using LES," in *48th AIAA Aerospace sciences meeting including the new horizons forum and aerospace exposition*. Florida.

Nishri, B., and Wygnanski, I. (1998). Effects of periodic excitation on turbulent flow separation from a flap. *AIAA J.* 36 (4), 547–556. doi:10.2514/2.428

Packard, N. O., Thake, M. P., Jr., Bonilla, C. H., Gompertz, K., and Bons, J. P. (2013). Active control of flow separation on a laminar airfoil. *AIAA J.* 51 (5), 1032–1041. doi:10.2514/1.j051556

Raju, R., Mittal, R., and Cattafesta, L. (2008). Dynamics of airfoil separation control using zero-net mass-flux forcing. *AIAA J.* 46 (12), 3103–3115. doi:10.2514/1.37147

Raspet, A. (1951). "Mechanisms of automatic trailing edge suction," *Engineering Research Station*. Research Rept. No. 1 (Mississippi State, MS: Mississippi State College).

Raspet, A. (1952). Boundary layer studies on a sailplane. *Aeronaut. Eng. Rev.* 11 (6), 52–60.

Raspet, A., Cornish, J. J., III, and Bryant, G. D. (1956). Delay of the stall by suction through distributed perforations. *Aeronaut. Eng. Rev.* 15 (8), 32–39.

Salmasi, A., Shadaram, A., and Shams Taleghani, A. (2013). Effect of plasma actuator placement on the airfoil efficiency at poststall angles of attack. *IEEE Trans. Plasma Sci.* 41 (10), 3079–3085. doi:10.1109/TPS.2013.2280612

Schlichting, H., and Gersten, K. (2016). *Boundary-layer theory*. 9th ed. Springer.

Scholz, P., Kaehler, C., Radespiel, R., Wild, J., and Wichmann, G. (2009). "Active control of leading-edge separation within the German flow control network," in *47th AIAA aerospace sciences meeting*. Orlando, Florida. No. AIAA 2009-0529.

Seifert, A., Darabi, A., and Israel, W. (1996). Delay of airfoil stall by periodic excitation. *J. Aircr.* 33 (4), 691–698. doi:10.2514/3.47003

Seifert, A., Greenblatt, D., and Wygnanski, I. J. (2004). Active separation control: an overview of Reynolds and Mach numbers effects. *Aerosp. Sci. Technol.* 8 (7), 569–582. doi:10.1016/j.ast.2004.06.007

Seifert, A., and Pack, L. G. (1999). Oscillatory control of separation at high Reynolds numbers. *AIAA J.* 37 (9), 1062–1071. doi:10.2514/3.14289

Sellers, W., Jones, G., and Moore, M. (2002). "Flow control research at NASA Langley in support of high-lift augmentation," in *Biennial international powered lift conference and exhibit*. Williamsburg, Virginia. AIAA 2002-6006.

Shuster, J. M., and Douglas, R. S. (2007). Experimental study of the formation and scaling of a round synthetic jet. *Phys. fluids* 19 (4). doi:10.1063/1.2711481

Smith, B., and Gregory, S. (2001). "Synthetic jets at large Reynolds number and comparison to continuous jets," in *15th AIAA computational fluid dynamics conference*, 3030.

Smith, D., Amitay, M., Kibens, V., Parekh, D., and Glezer, A. (1998). "Modification of lifting body aerodynamics using synthetic jet actuators," in *AIAA paper 98-0209, 36th aerospace sciences meeting exhibit*. Reno, NV.

Stal nov, O., and Seifert, A. (2010). On amplitude scaling of active separation control. *Act. Flow Control II , Notes Numer. Fluid Mech. Multidiscip. Des.* 108, 63–80. doi:10.1007/978-3-642-11735-0_5

Taleghani, A. S., Shadaram, A., and Mirzaei, M. (2012). Effects of duty cycles of the plasma actuators on improvement of pressure distribution above a NLF0414 airfoil. *IEEE Trans. Plasma Sci.* 40 (5), 1434–1440. doi:10.1109/tps.2012.2187683

Taleghani, A. S., Shadaram, A., Mirzaei, M., and Abdolahipour, S. (2018). Parametric study of a plasma actuator at unsteady actuation by measurements of the induced flow velocity for flow control. *J. Braz. Soc. Mech. Sci. Eng.* 40 (4), 173. doi:10.1007/s40430-018-1120-x

Thomas, F. (1962). Untersuchungen ¨uber die Erh¨ohung des Auftriebes von Tragfl¨ugeln mittels Grenzschichtbeeinflussung dutch Ausblasen. *Z. f¨ur Flugwiss.* 10 (2), 46–65. Februar. doi:10.1515/9783112527160-025

Tuck, A., and Soria, J. (2008). Separation control on a NACA 0015 airfoil using a 2D micro ZNMF jet. *Aircr. Eng. Aerosp. Technol.* 80 (2), 175–180. doi:10.1108/00022660810859391

Udris, A. (2015). *Vortex generators: preventing stalls at high and low speeds*. Available at: https://www.boldmethod.com/learn-to-fly/aerodynamics/vortexgenerators (Accessed January 9, 2015).

Wu, J. Z., Lu, X. Y., Denny, A. G., Fan, M., and Wu, J. M. (1998). Post-stall flow control on an airfoil by local unsteady forcing. *J. Fluid Mech.* 371 (1), 21–58. doi:10.1017/s0022112098002055

Wu, X.-H., Wu, J. Z., and Wu, J. M. (1991). Streaming effect of wall oscillation to boundary layer separation. *No. AIAA Pap. 91-0545*. doi:10.2514/6.1991-545

Wygnanski, I. (2000). "Some new observations affecting the control of separation by periodic excitation," in *FLUIDS 2000 conference and exhibit*. Denver, Colorado. AIAA 2000-2314.

Yarusevych, S., and Kotsonis, M. (2017). Steady and transient response of a laminar separation bubble to controlled disturbances. *J. Fluid Mech.* 813, 955–990. doi:10.1017/jfm.2016.848

Yarusevych, S., Sullivan, P. E., and Kawall, J. G. (2009). On vortex shedding from an airfoil in low-Reynolds-number flows. *J. Fluid Mech.* 632, 245–271. doi:10.1017/s0022112009007058

You, D., and Moin, P. (2008). Active control of flow separation over an airfoil using synthetic jets. *J. Fluids Struct.* 24 (8), 1349–1357. doi:10.1016/j.jfluidstructs.2008.06.017

Zaman, K., Bar-Server, A., and Mangalam, S. (1987). Effect of acoustic excitation on the flow over a low-Re airfoil. *J. Fluid Mech.* 182, 127–148. doi:10.1017/s0022112087002271

Zander, V., and Nitsche, W. (2013). Control of secondary flow structures on a highly loaded compressor cascade. *Proc. Institution Mech. Eng. Part A J. Power Energy* 227 (6), 674–682. doi:10.1177/0957650913495538

Zhang, W., and Ravi, S. (2015). A direct numerical simulation investigation of the synthetic jet frequency effects on separation control of low-Re flow past an airfoil. *Phys. Fluids* 27 (5). doi:10.1063/1.4919599

Frontiers in
Mechanical Engineering

Explores the design of mechanical systems and their applications

A multidisciplinary journal which bridges the gaps between areas of research in the mechanical engineering field, from biomechanical engineering to turbomachinery and tribology.

Discover the latest Research Topics

See more →

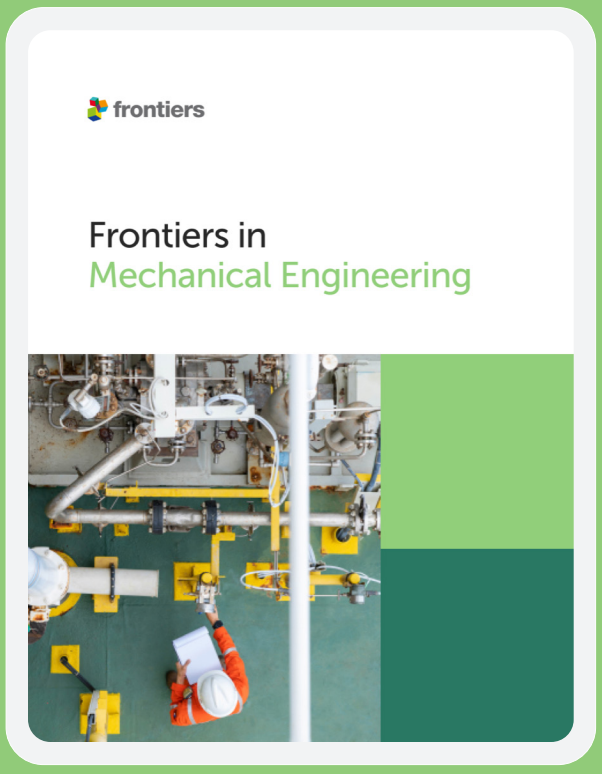

Frontiers

Avenue du Tribunal-Fédéral 34
1005 Lausanne, Switzerland
frontiersin.org

Contact us

+41 (0)21 510 17 00
frontiersin.org/about/contact